PERFORMANCE AND APPLICATION OF THE MODULAR ACOUSTIC VELOCITY SENSOR (M.A.V.S.) FOR LABORATORY MEASUREMENTS

A Thesis

by

STÉPHANE BESNARD

Submitted to the Office of Graduate Studies of
Texas A&M University
in partial fulfillment of the requirements for the degree of

MASTER OF SCIENCE

December 2004

Major Subject: Ocean Engineering

PERFORMANCE AND APPLICATION OF THE MODULAR ACOUSTIC VELOCITY SENSOR (M.A.V.S.) FOR LABORATORY MEASUREMENTS

A Thesis

by

STÉPHANE BESNARD

Submitted to the Office of Graduate Studies of
Texas A&M University
in partial fulfillment of the requirements for the degree of

MASTER OF SCIENCE

Approved as to style and content by:

Richard Mercier (Chair of Committee)	Jun Zhang (Member)
Achim Stössel (Member)	David Rosowsky (Head of Department)

December 2004

Major Subject: Ocean Engineering

ABSTRACT

Performance and Application of the Modular Acoustic Velocity Sensor (M.A.V.S) for Laboratory Measurements. (December 2004)

Stéphane Besnard, Dipl., École Spéciale des Travaux Publics, du Bâtiment et de l'Industrie, Paris, France

Chair of Advisory Committee: Dr. Richard Mercier

Every type of current meter is different and has its proper characteristics. Knowing the performance of a current meter is essential in order to use it properly either for field or laboratory measurements (such as in the Offshore Technology Research Center wave basin). A study of the MAVS (Modular Acoustic Velocity Sensor) in a wave basin is a first step essential for later deployment in real studies.

This thesis is based on data obtained from different series of laboratory measurements conducted in the OTRC wave basin. The objective of the first part of the study was to characterize the MAVS frequency response using benchmarks such as tow tests or wave tests. These benchmarks allowed us not only to characterize the sensor but also to eventually correct some of the measurement distortions due to flow blockage, vortex shedding, or vibrations of the mounting structure, for example.

After the preliminary study was done, we focused on the potential use of the MAVS in the OTRC wave basin. Indeed, in the case of a study of a scale model in the wave basin, the stresses applied to the model have to be accurately known. In the case of current-induced loads, this includes contributions from both the mean flow and the turbulence. Thus, after correcting the values measured by the MAVS, a mapping of the current jet was executed to determine its three-dimensional structure in the wave basin.

Knowing the structure of the current in the OTRC wave basin, it was then possible to define a domain in which the current can be considered uniform with a certain tolerable error. This domain of uniformity will allow us to validate the use of the OTRC wave basin to study large models such as FPSOs (Floating Production, Storage and Offloading Units).

ACKNOWLEDGEMENTS

This research was supported by the Offshore Technology Research Center (OTRC), a National Science Foundation (NSF) engineering research center.

I would also like to express my gratitude to Dr. Richard Mercier for his support during the research and for offering me the opportunity to work on one of his projects and also for his patience and his help with this thesis.

I would also thank my committee, Dr. Achim Stössel and Dr. Jun Zhang, and the rest of the ocean engineering professors at Texas A&M for providing me the knowledge that was necessary for this research.

Also, I would like to thank the whole staff of the Department of Civil Engineering and the Ocean Engineering section of the Texas A&M University and the OTRC staff for the help they often gave me.

Finally, I would also like to thank my family and my friends without whom I wouldn't have succeeded in my studies.

TABLE OF CONTENTS

Page

Page

LIST OF FIGURES

FIGURE Page

FIGURE Page

FIGURE Page

FIGURE Page

LIST OF TABLES

1. INTRODUCTION

1.1 Introduction to the Study

When a scale model is tested in the wave basin, the input environment applied to the model is expected to be a good representation of the real world. In the general case, the best representation of that will be a combination of wave, current and wind stresses.

When generating a current in a wave basin, we face such issues as:

- re-circulating flow in the wave basin;
- turbulence;
- non-uniformity of the current;
- difficulty in calibrating the desired current profile

Apart from those issues that are inherent to every test, there are other constraints that apply specifically to studies requiring measurement of current in the OTRC (Offshore Technology Research Center) wave basin:

- water is maintained crystal clear;
- electromagnetic interference from operation of motors and pumps during the wind and current tests.

The importance of such phenomena needs to be studied to determine their impact on the OTRC testing procedures.

In the past, the OTRC used electromagnetic Marsh-McByrney sensors to measure currents. Unfortunately, due to electromagnetic interference, these sensors could not provide accurate measurements for current and wind tests. There was therefore a need to

---

This thesis follows the format of the Journal of Ocean Engineering.

find another type of sensor that would satisfy OTRC's requirements (see Table 1.1). The main types of sensors available are summarized in Table 1.1 and as we can see, it appears that the MAVS best matches OTRC's requirements. However, we still need to perform some tests to verify its accuracy and its behavior in the different types of conditions it will be deployed.

First of all, it is necessary to ensure that the MAVS current meter meets the OTRC's requirements. In order to do that, a preliminary series of tests in the wave basin was conducted using a demo MAVS. The first series of tests compared the MAVS with the Marsh-McByrney electromagnetic current meter. In order to check the accuracy of the sensors, two types of benchmarks were used: tow tests and wave tests. In the tow tests, the sensors were towed in the wave basin at various constant speeds and the velocities measured by the current meters were compared with the tow speed. In the wave tests, the measured velocities were compared with the theoretical ones based on the free surface water wave elevation measured by a capacitance-type wave probe located above the current meters.

The preliminary tests confirmed the superiority of the MAVS over the Marsh-McByrney current meter for OTRC's applications. OTRC therefore purchased 9 MAVS sensors and had each of them specifically configured to output analog channels. Following receipt of the new units, a second, more comprehensive phase of tests was conducted to further verify their performance and to map the structure of the current in the OTRC basin for a representative set up of the current generator. During these tests, the behavior of the sensor regarding the measurement of the mean velocity was checked as well as its frequency response. Moreover, the sensitivity to the relative orientation between the sensor and the mean flow direction was checked in different tests. After that, inherent limitations were checked, for example, the effect of the wake from the transducer mounting (the rings), the effect of blockage from the main housing and the effect of proximity of other sensors in the array mounting.

Table 1.1: Comparison of different types of current sensors

	Essential Requirements		Desired Attributes			
	Operate in particle free environment	Insensitive to electromagnetic interference	Easy to calibrate and operate	High frequency response	Robust	3D velocity measurement
Differential Acoustic Time of Travel (MAVS)	✓	✓	✓	✓	✓	✓
Acoustic Doppler (ADV)		✓	✓		✓	✓
Electromagnetic (Marsh McByrney)	✓		✓	✓	✓	
Propeller Type	✓	✓	✓		✓	
Hot Wire	✓	✓		✓		
Laser Doppler Velocimetry (LDV)		✓		✓		✓

As expected, the flow types had different consequences on the results. The characteristics of the different flows that were investigated are:

- Tow test: steady, unidirectional and non-turbulent;
- Wave test: periodical and irrotational (=non-turbulent);
- Current test: quasi-steady and turbulent.

Moreover, the MAVS measurements were found to be sensitive to:

- the relative orientation between the sensor and the mean flow direction;
- the interference effect from the wake of the transducer mounting (the rings);
- the effect of flow blockage by the main housing on the MAVS;
- the effect of flow blockage by other sensors in close proximity and by the array mounting.

The objectives of this thesis research were to:

1) thoroughly analyze the performance of the MAVS using the previously collected test data;
2) where possible, develop procedures for calibrating the MAVS to correct for known measurement errors (e.g. due to blockage effects);
3) by applying the calibration/correction procedures to the MAVS data from the current tests, map the mean flow and turbulence structure of the current in the OTRC wave basin for the given set up of the current generator.

This thesis is divided into several parts. The first part (Section 2) is a review of the way that the real environment is modeled, including a general description of the seas, the linear and nonlinear wave theory, oceanographic current phenomena and geophysical turbulence. Spectral theory that gives us an idea of what we should expect in the frequency domain is also considered.

Section 3 explains the design and execution of the test program conducted to verify the performance of the MAVS and demonstrate its application. We first describe the OTRC wave basin and the equipment that was used for the tests. Then we focus on the design of the experiments including the way the sensors were oriented and the different arrays that were used.

Section 4 describes the processing procedures applied to the time series data to derive the standard statistical and spectral information used as the basis for the analysis. This will show some theoretical limitations that will have to be considered in the analysis and in the data processing.

Section 5 examines the results of the tests used to verify and calibrate the performance of the MAVS. We will be starting with the calm tests that show the idle state of the sensor and then we will examine the behavior of the sensors under the benchmarks that were applied: the tow and wave tests. We will also look at the results under the current tests. Finally, we will look for correction procedures and factors to apply to the MAVS measurement to obtain the most accurate results regardless of the orientation of the sensor or of the array.

Section 6 will present the results of the current mapping (including the mean current, the turbulent integral length scale, and the turbulent energy dissipation rate) under different array orientations, current speeds, etc.

Finally, Section 7 will review the major findings of the study and summarize the recommendations and the methodology that should be applied in order to test models in current environments under optimal circumstances.

1.2 The MAVS current meter

The MAVS (Modular Acoustic Velocity Sensor), shown in Figure 1.1, is a current meter manufactured by Nobska Inc. in Mashpee, Massachusetts (http://www.nobska.net).

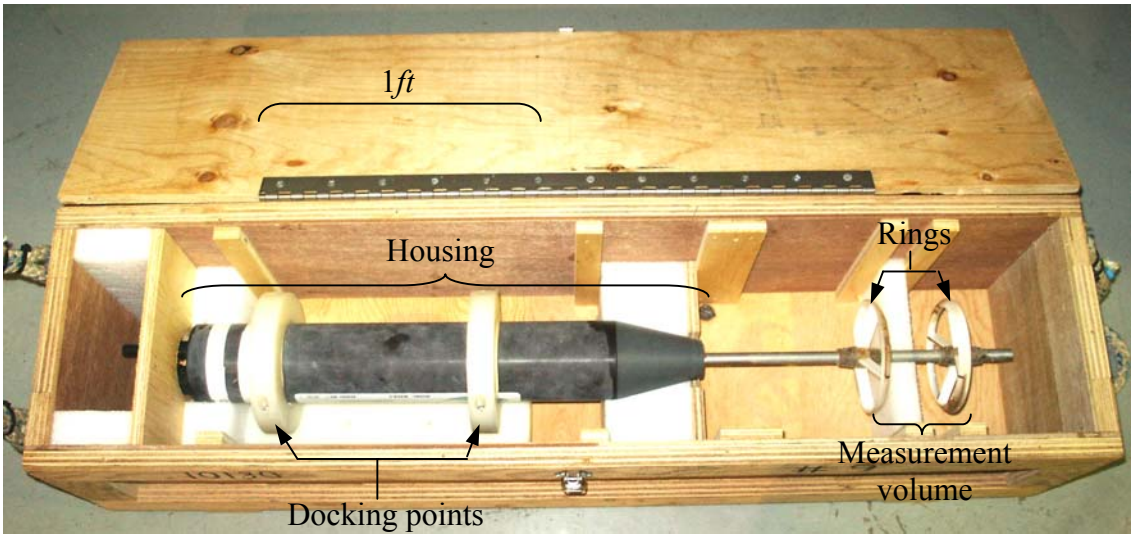

Figure 1.1: MAVS in its case

The MAVS measures the current velocity between pairs of opposing piezoceramic transducers (Figure 1.2) using the differential time of travel of simultaneously emitted acoustic pulses (Thwaites and Williams, 1996 and Williams and Thwaites, 1998).

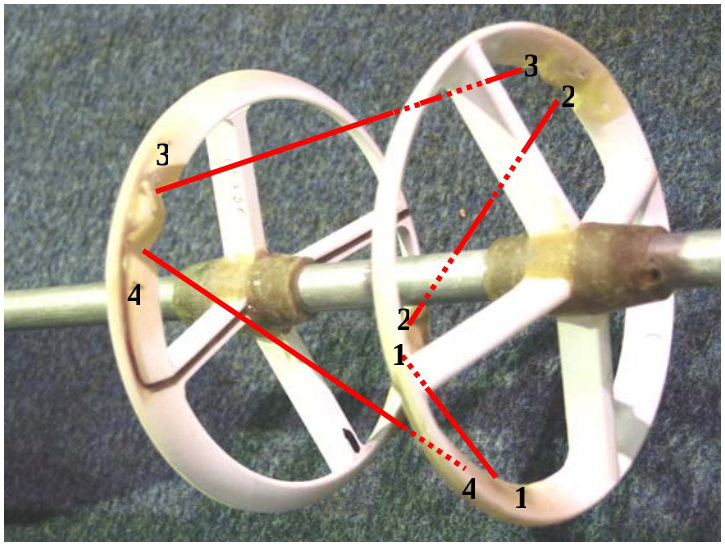

Figure 1.2: MAVS Transducers

The integration of the projection of the velocity over the travel path of the propagating pulse provides the travel time knowing the local speed of the sound (Williams, Thwaites and Morrison, 1996):

$$\delta t = \oint \frac{ds}{c(s) + \frac{\overline{v(s)}.\overline{ds}}{|ds|}} \tag{1.1}$$

where the integration is from the transducer 1 to the transducer 2 and back, and we have:

- δt : difference of travel time between the 2 transducers;
- $v(s)$: velocity of the fluid at the curvilinear position s;
- $c(s)$: local speed of the sound;
- ds : element of path

$$\delta t = \underbrace{\int_1^2 \frac{ds}{c + \frac{\overline{v(s)}.\overline{ds}}{|ds|}}}_{\delta t_{12}} - \underbrace{\int_2^1 \frac{ds}{c - \frac{\overline{v(s)}.\overline{ds}}{|ds|}}}_{\delta t_{21}} \tag{1.2}$$

The component of $\overline{v(s)}$ along the acoustic path (assumed constant along the path) captured by the transducer pair x is:

$$\frac{\overline{v(s)}.\overline{ds}}{|ds|} = V_x \tag{1.3}$$

Thus, assuming that the path is straight and reciprocal and according to the Sagnac effect, the integration gives us:

$$\begin{cases} \delta t_{12} = \dfrac{\delta l}{c + V_x} \\ \delta t_{21} = \dfrac{\delta l}{c - V_x} \end{cases} \Rightarrow \delta t = \delta t_{12} - \delta t_{21} = \frac{\delta l}{c}\left[\frac{1}{1 + V_x/c} - \frac{1}{1 - V_x/c}\right] \tag{1.4}$$

where δl is the length of the path between the transducers. Assuming that the flow velocity is much smaller than the celerity of the sound $(V_x/c \ll 1)$, we can apply the Taylor expansion:

$$f(x = x_0) = \sum_{n=0}^{+\infty} \frac{f^{(n)}(x_0)}{n!}(x - x_0)^n \tag{1.5}$$

$$\begin{cases} \dfrac{1}{1+\dfrac{V_x}{c}} \simeq 1-\dfrac{V_x}{c}+\dfrac{V_x^{\,2}}{c^2}-\dfrac{V_x^3}{c^3}+\dfrac{V_x^4}{c^4}-\dfrac{V_x^5}{c^5}+\ldots & (1.6) \\ \dfrac{1}{1-\dfrac{V_x}{c}} \simeq 1+\dfrac{V_x}{c}+\dfrac{V_x^2}{c^2}+\dfrac{V_x^3}{c^3}+\dfrac{V_x^4}{c^4}+\dfrac{V_x^5}{c^5}+\ldots & (1.7) \end{cases}$$

$$\Rightarrow \delta t = -2\frac{\delta l}{c}\left(\frac{V_x}{c}+\frac{V_x^3}{c^3}+\frac{V_x^5}{c^5}+\ldots\right) \quad (1.8)$$

So finally, up to the third order, we have:

$$\Rightarrow \left|\delta t\right| = 2\frac{V_x.\delta l}{c^2}\left(1+\frac{V_x^2}{c^2}+\ldots\right) \quad (1.9)$$

For ocean flows $\left(V_x^2/c^2 \simeq 10^{-6}\right)$, we can approximate the difference of travel time between the transducers as a function linear in t, so that the velocity measured by the transducer pair x is:

$$V_x = \frac{c^2\left|\delta t\right|}{2\delta l} \quad (1.10)$$

The MAVS measures the differential time of travel between 4 acoustic paths (beams). The beam data extracted from the MAVS then has to be converted to the three orthogonal velocity components. In the case of a sensor oriented facing the current (in the North-South orientation as we will see later), the operations to apply are:

$$\begin{cases} u = \left(-V_1 - V_2 - V_3 - V_4\right)\dfrac{\beta}{\sqrt{2}} \\ v = \left(-V_1 + V_2 + V_3 - V_4\right)\beta \\ w = \left(-V_1 - V_2 + V_3 + V_4\right)\beta \end{cases} \tag{1.11}$$

where V_1, V_2, V_3 and V_4 are the four beam velocities, and β is a constant that accounts for the geometry of the axes and any change of units.

The MAVS is known to have some limitations. First of all, the MAVS isn't capturing the detailed flow field that is between the transducers but rather an average of it. This sensor is an intrusive sensor and it will locally modify the flow field. Also, by the way the sensor is configured, we will have a turbulent wake from the rings that will interfere again with the velocity measured by the transducers. The sensor obviously cannot resolve sheared currents such as boundary layer flows, over length scales smaller than the spacing between the transducer rings. Other known sources of error are the zero offset bias and electronic noise and non-linearity (less than 1.5%). These limitations will be investigated in this thesis.

2. MODELING THE WAVE-CURRENT ENVIRONMENT

2.1 Description of the Sea

In order to find the most accurate forcing to apply to a scale model that we want to study in the wave basin, we have to understand what is happening in the real world. The sea is mainly constituted by winds, currents and waves, the latter being the more characteristic as we can see them. However, and as we can see in the Figure 2.1, the energy of the waves is not distributed evenly along the period, which indicates that some phenomena are more important than others (Dean and Dalrymple, 1984). However, we will focus our study on only two types of phenomena: the currents and the wind-generated waves.

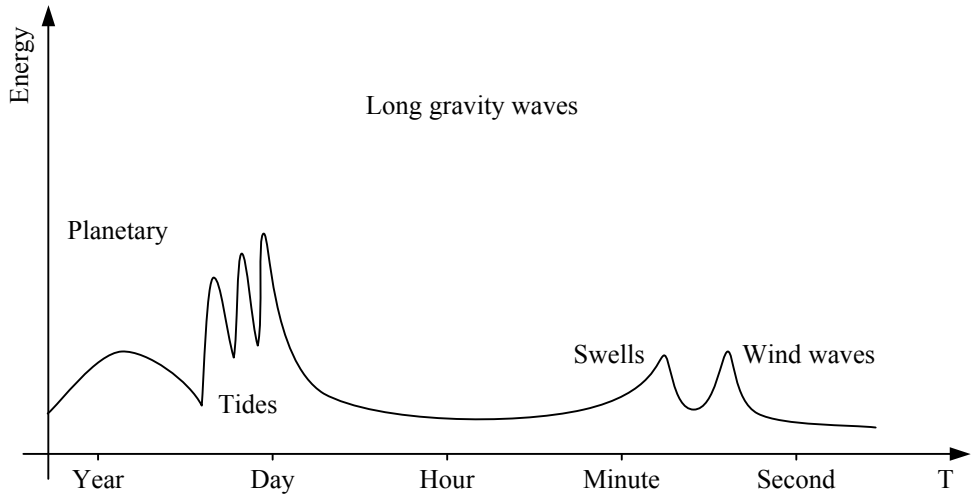

Figure 2.1: Distribution of the spectral energy of the sea surface elevation according to the period

2.1.1 Wind Waves

In wind-generated waves, the energy is transferred from the wind to the ocean, which makes the waves grow in height until a certain limit is reached (Anikouchine and Sternberg, 1973). This limit is obtained after a minimum fetch and duration of a wind stress. Then, even if the same amount of wind energy is continuously provided to the wave system, the waves do not grow anymore as energy will be dissipated by mechanisms such as viscous forces, wave breaking, etc. This state of equilibrium is often referred to as a "fully developed" sea. The waves may then be categorized according to their direction of propagation. If the waves are traveling in a single main direction, they are referred to as long-crested. However, in most conditions, the waves are not uni-directional, in which case they are referred as "short-crested". As we can see in Figure 2.2, long and short crested waves may have comparable energy but in the case of long-crested waves, the energy is more centered on the main direction whereas in the case of short-crested waves, the energy is spread among a range of directions.

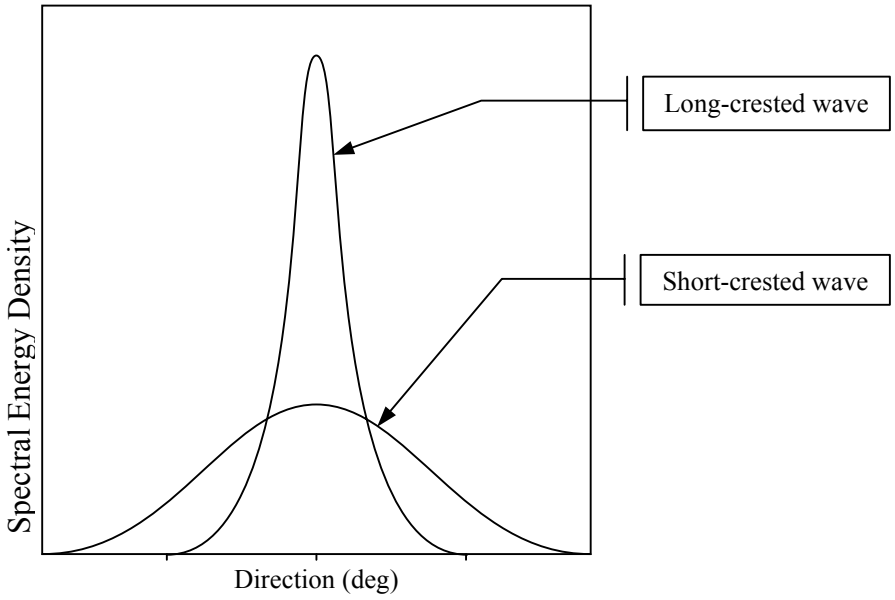

Figure 2.2: Power spectrum of the sea surface elevation for long and short crested waves at a given frequency

2.1.2 Pure Drift Currents

The friction of the wind blowing over the sea not only generates waves, it also generates pure drift current. A simple model for the relation between wind stress and surface current speed V_0 is (Anikouchine and Sternberg, 1973):

$$V_0 = \frac{T}{\sqrt{\rho_w^2 f A_z}} \tag{2.1}$$

with A_z the eddy viscosity, T the wind stress, f the Coriolis parameter and ρ_w the density of the water. The surface current then propagates to the mixed-layer through the shear stress from the top to the bottom.

2.1.3 Wind Gradient Currents

Currents at all depths in the sea can be generated by horizontal pressure gradients that arise as a result of set-up and set-down of the pure drift currents. These produce horizontal variations of ocean level that lead to a corresponding restructuring of the density field at all ocean depths.

2.1.4 Pressure Gradient Currents

Current at all depths can also be generated by variations of atmospheric pressure at the sea surface. However, these types of currents are not too significant in the sea.

2.1.5 Thermohaline currents

If the temperature of the water decreases or if the salinity increases as a result of the exchange of heat and moisture at the air-sea interface, the unstable density gradient may create mixing in the mixed layer which results in current like circulation.

Each one of these phenomena as described by Monin, Kamenkovitch and Kort (1977), and is able to generate a different type of turbulent structure from a turbulent jet in the case of a current to turbulent mixing with the breaking of a wave. Although most of these phenomena are now well known, there is still a lack of information on interaction phenomena such as wind-wave interactions, wave-wave interaction and wave-current interaction.

2.2 Wave Modeling

We first recall here the governing equations for a potential free surface flow, as given by Cohen and Kundu (2002):

$$
\begin{cases}
\nabla^2\phi = 0 & \text{in the fluid} \qquad (2.2)\\
p = -\rho\dfrac{\partial\phi}{\partial t} - \dfrac{1}{2}\rho\left(\vec{\nabla}\phi\right)^2 - \rho g z + C(t) & \text{along a streamline} \qquad (2.3)\\
\dfrac{\partial\eta}{\partial t} + \vec{\nabla}\phi.\vec{\nabla}\eta = 0 & \text{at } z = \eta \qquad (2.4)\\
\dfrac{\partial\phi}{\partial t} + \dfrac{1}{2}\left(\vec{\nabla}\phi\right)^2 + g\eta = 0 & \text{at } z = \eta \qquad (2.5)\\
\dfrac{\partial\phi}{\partial z} = 0 & \text{at } z = -h \qquad (2.6)\\
\begin{cases}\phi(x+L;t) = \phi(x;t)\\ \phi(x;t+T) = \phi(x;t)\end{cases} & \qquad (2.7)
\end{cases}
$$

where $\begin{cases} \phi = \text{fluid potential} \\ \eta = \text{free surface elevation} \\ p = \text{pressure} \\ L = \text{length period} \\ T = \text{time period} \end{cases}$

2.2.1 Linear Wave Theory

The linear wave theory is based on a linearisation of the previous set of equations (Dean and Dalrymple, 1984) valid for low wave steepness and small wave amplitude relative to water depth $\left(kh \ll 1 \text{ with } k\text{=wave number and } h\text{= water depth}\right)$. The linearized governing equations are:

$$\begin{cases} \nabla^2\phi = 0 & \text{in the fluid} & (2.2) \\ \dfrac{\partial\phi}{\partial z} - \dfrac{\partial\eta}{\partial t} = 0 & \text{at } z = 0 & (2.8) \\ \dfrac{\partial\phi}{\partial t} + g\eta = 0 & \text{at } z = 0 & (2.9) \\ \dfrac{\partial\phi}{\partial z} = 0 & \text{at } z = -h & (2.6) \\ \begin{cases} \phi(x+L;t) = \phi(x;t) \\ \phi(x;t+T) = \phi(x;t) \end{cases} & & (2.7) \end{cases}$$

From this set of equations, the solution for the potential for a regular monochromatic wave train can be derived through a separation of the variables:

$$\phi(x;y;z;t) = A\cosh\left[k(z+h)\right]\sin(kx-\sigma t) \qquad (2.10)$$

with A a constant that does not depend on x, z or t and σ the wave frequency.

Applying the dynamic free surface boundary condition, the free surface elevation is given by:

$$\eta = -\frac{1}{g}\left[\frac{\partial \phi}{\partial t}\right]_{z=0} = \frac{A\sigma}{g}\cosh(kh)\cos(kx - \sigma t) \tag{2.11}$$

If the height of the monochromatic waves is *H*, then the potential for a three-dimensional wave is:

$$\phi(x; y; z; t) = \frac{H}{2}\frac{g}{\sigma}\frac{\cosh\left[k(z+h)\right]}{\cosh(kh)}\sin\left(k_x x + k_y y - \sigma t\right) \tag{2.12}$$

Substituting the linearized dynamic free surface boundary condition into the linearized kinematic boundary condition, we obtain:

$$\frac{\partial^2 \phi}{\partial z^2} + g\frac{\partial \phi}{\partial z} = 0 \qquad \text{at } z = 0 \tag{2.13}$$

which, after substituting the expression for the velocity potential, Equation 2.12, leads to the dispersion relationship:

$$\sigma^2 = gk\tanh(kh) \tag{2.14}$$

The celerity of the wave $C = \frac{L}{T} = \frac{\sigma}{k}$ is

$$C = \sqrt{\frac{g}{k}\tanh(kh)} \tag{2.15}$$

The Bernoulli equation may be used to find the linear pressure $p = -\rho \frac{\partial \phi}{\partial t}$, leading directly to:

$$p(x;y;z;t) = -\rho g \frac{H}{2} \frac{\cosh\left[k(z+h)\right]}{\cosh(kh)} \cos\left(k_x x + k_y y - \sigma t\right) \tag{2.16}$$

We also have the static pressure that is $p_s = -\rho g z$.

The velocities are simply derived from the potential:

$$\begin{cases} u(x;y;z;t) = \dfrac{\partial \phi}{\partial x} = \dfrac{H}{2} \dfrac{g k_x}{\sigma} \dfrac{\cosh\left[k(z+h)\right]}{\cosh(kh)} \cos\left(k_x x + k_y y - \sigma t\right) & (2.17) \\ v(x;y;z;t) = \dfrac{\partial \phi}{\partial y} = \dfrac{H}{2} \dfrac{g k_y}{\sigma} \dfrac{\cosh\left[k(z+h)\right]}{\cosh(kh)} \cos\left(k_x x + k_y y - \sigma t\right) & (2.18) \\ w(x;y;z;t) = \dfrac{\partial \phi}{\partial z} = \dfrac{H}{2} \dfrac{g k}{\sigma} \dfrac{\sinh\left[k(z+h)\right]}{\cosh(kh)} \sin\left(k_x x + k_y y - \sigma t\right) & (2.19) \end{cases}$$

Deep water simplifications

In deep water, the wave length is considered very small compared to the water depth $(L \ll h)$, which can also be related to the wave number knowing that $L = 2\pi/k$. So the deep water assumption is $kh \gg 1$. Moreover, since the hyperbolic cosine can be separated in exponential functions with $\cosh(u) = \left(e^{u} + e^{-u}\right)/2$, the hyperbolic part of the potential can be simplified for $kh \gg 1$ to $\cosh\left[k(z+h)\right]/\cosh(kh) \simeq e^{kz}$.

From that, the potential can be simplified in the case of deep water into:

$$\phi(x;y;z;t;) = \frac{H}{2}\frac{g}{\sigma}e^{kz}\sin\left(k_x x + k_y y - \sigma t\right) \tag{2.20}$$

with a dispersion relationship and wave celerity:

$$\sigma = \sqrt{gk} \tag{2.21}$$

$$C = \sqrt{\frac{g}{k}} \tag{2.22}$$

2.2.2 Nonlinear Wave Theory

In the general case, the assumption of small amplitude waves that makes linear wave theory valid is too restrictive (Dean and Dalrymple, 1984). Waves in the real world are nonlinear. As long as the wave height continues to be small relative to the water depth, we can use the Stokes series expansion model (Zhang and Chen, 1999) to account for nonlinear finite wave height effects.

Up to the second order, the Stokes wave solution is:

$$\begin{cases} \phi = \dfrac{Ag}{\sigma}\dfrac{\cosh\left[k\left(z+h\right)\right]}{\cos\left(kh\right)}\sin\left(kx-\sigma t\right) \\ \quad + \dfrac{3}{8}A^2\sigma\dfrac{\cosh\left[2k\left(z+h\right)\right]}{\sinh^4\left(kh\right)}\sin\left[2\left(kx-\sigma t\right)\right] \end{cases} \tag{2.23}$$

$$\eta = A\cos\left(kx-\sigma t\right) + \frac{A^2 k}{4}\frac{\cosh\left(kh\right)}{\sinh^3\left(kh\right)}\left[2+\cosh\left(2kh\right)\right]\cos\left[2\left(kx-\sigma t\right)\right] \tag{2.24}$$

and the associated wave velocities are:

$$\begin{cases} u = \dfrac{Agk}{\sigma}\dfrac{\cosh\left[k\left(z+h\right)\right]}{\cos\left(kh\right)}\cos\left(kx-\sigma t\right)+\dfrac{3}{4}A^2\sigma k\dfrac{\cosh\left[2k\left(z+h\right)\right]}{\sinh^4\left(kh\right)}\cos\left[2\left(kx-\sigma t\right)\right] & (2.25) \\ w = \dfrac{Agk}{\sigma}\dfrac{\sinh\left[k\left(z+h\right)\right]}{\cos\left(kh\right)}\sin\left(kx-\sigma t\right)+\dfrac{3}{4}A^2\sigma k\dfrac{\sinh\left[2k\left(z+h\right)\right]}{\sinh^4\left(kh\right)}\sin\left[2\left(kx-\sigma t\right)\right] & (2.26) \end{cases}$$

The maximum horizontal velocity and wave elevation are:

$$u_{\max}\left(z\right)=\frac{Agk}{\sigma}\frac{\cosh\left[k\left(z+h\right)\right]}{\cos\left(kh\right)}+\frac{3}{4}A^2\sigma k\frac{\cosh\left[2k\left(z+h\right)\right]}{\sinh^4\left(kh\right)} \tag{2.27}$$

$$\eta_{\max}=A+\frac{A^2k}{4}\frac{\cosh\left(kh\right)}{\sinh^3\left(kh\right)}\left[2+\cosh\left(2kh\right)\right] \tag{2.28}$$

The following values are representative of the experimental conditions studied herein:

$$\begin{cases} A=10\text{cm} \\ k=2.1\text{m}^{-1} \\ \sigma=4.5\text{rad/s} \\ h=5\text{m} \end{cases}$$

Table 2.1: Comparison between linear and nonlinear wave theory

	First order	Second order
Elevation (m)	$\eta_{\max}=10\text{cm}$	$\eta_{\max}=1.03\text{cm}$
u for $z=-1\text{ft}$	$u_{\max}=24.01\text{cm/s}$	$u_{\max}=7.37\times10^{-6}\mu\text{m/s}$
u for $z=-3\text{ft}$	$u_{\max}=6.86\text{cm/s}$	$u_{\max}=6.02\times10^{-7}\mu\text{m/s}$

From Table 2.1, we can see that the second order velocity is very small and can be neglected. However, the second order elevation represents 10% of the first order one so it is pretty important. This can be seen graphically in Figure 2.3. Moreover, to compute the theoretical velocity, we extract the amplitude from the elevation measurement. Thus, if we don't take into account the importance of the nonlinear part in the elevation, we will overestimate the amplitude and it will induce an overestimation of the theoretical velocity as well. To the second order, the amplitude is:

$$A = \frac{-1 \pm \sqrt{1+2k}}{k} \tag{2.29}$$

$$A = \frac{-1 + \sqrt{1+2k}}{k} \tag{2.30}$$

We are keeping Equation 2.30 as the only reliable result for the amplitude (the second root being negative doesn't have any physical meaning).

Finally, it is important to introduce the Russell number R defined as the ratio between the second order and first order velocity.

$$R = \frac{\varepsilon\phi_1}{\phi_2} = \frac{3}{8}\frac{ka\cosh\left(2kh\right)}{\cosh\left(kh\right)\sinh^3\left(kh\right)} \ll 1 \tag{2.31}$$

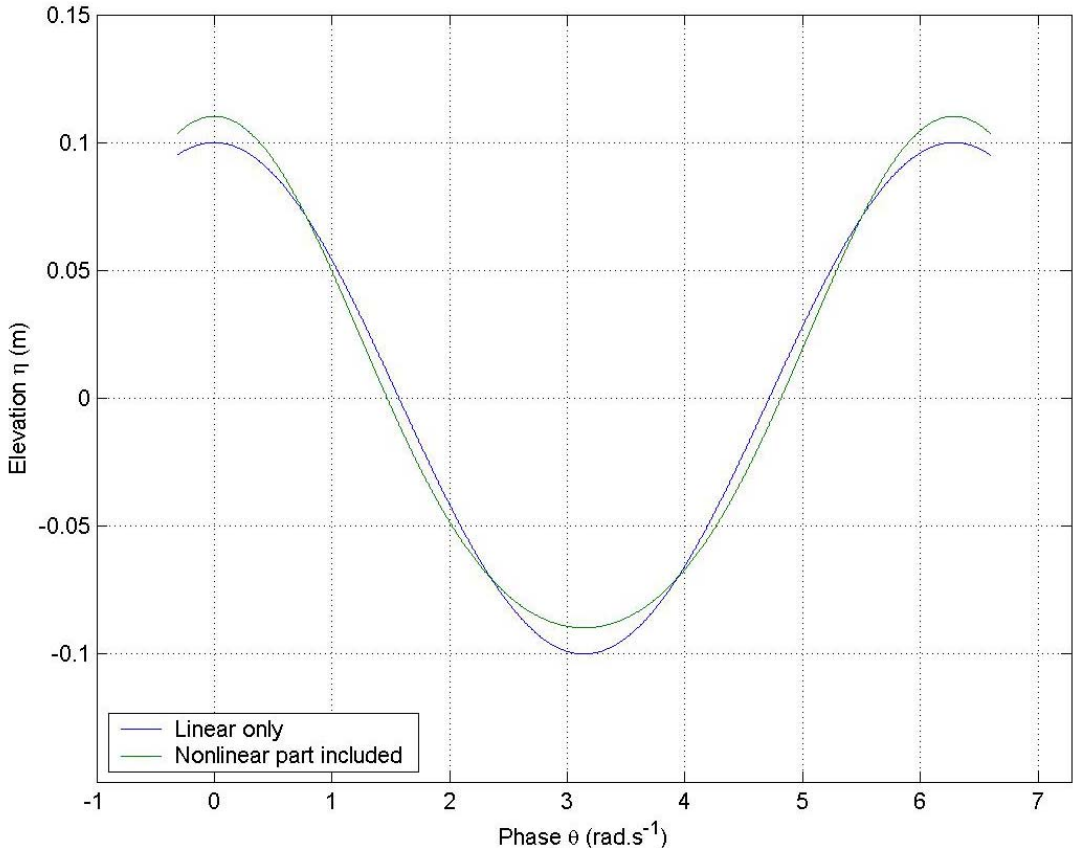

Figure 2.3: Difference between linear and nonlinear wave elevation

In the case where the Russell number is too low, the convergence of the Stokes series expansion cannot be assured. In that case, the Stokes nonlinear wave theory is no longer valid and it is necessary to use another method like the finite amplitude theory (Cokelet, 1977).

2.3 Spectral Modeling of Irregular Waves

The surface elevation of a sea may be represented as a superposition of discrete monochromatic wavelets:

$$\eta(x,y,t) = \sum_{m=-M}^{M} \sum_{l=0}^{L} A_m \cos\left(k_{mx}x + k_{my}y - \sigma_m t + \phi_m\right) \tag{2.32}$$

with the following characteristics of each wavelet $\begin{cases} A_m = \text{amplitude} \\ k_{mx} = \text{wave number in the } x \text{ direction} \\ k_{my} = \text{wave number in the } y \text{ direction} \\ \sigma_m = \text{frequency} \\ \phi_m = \text{phase lag} \end{cases}$

Equation 2.32 can also be represented as:

$$\eta(x,y,t) = \sum_{m=-M}^{M} \sum_{l=0}^{L} \frac{\alpha_{ml}}{2} e^{i\left[\sigma_m - k_m\left(x\cos(\theta_l) + y\sin(\theta_l)\right)\right] + \phi_{ml}} \tag{2.33}$$

The spectral density function $S_{\eta\eta}(f,\theta)$ of the wave elevation is obtained from the coefficients of the Fourier series.

$$\frac{1}{2}\alpha_{ml}^2 = S(f_m,\theta_l)\,df\;d\theta \text{ with } \begin{cases} f_m = m\;df \\ \theta_l = l\;d\theta \end{cases} \tag{2.34}$$

The spectrum can be separated in two parts: a frequency dependent only part and a directional part. However, it has been shown (Forristall et al. 1978) that the directional part is also dependent on the frequency and not only on the angle itself. Thus, we can write the spectrum as:

$$S(f,\theta) = S(f)D(f,\theta) \tag{2.35}$$

We will now introduce the main spectra that are commonly used. For a more exhaustive list, the reader can refer to Chakrabarti (1993) or Ochi (1998).

2.3.1 Wave Spectrum Models

Bretschneider, 1959

$$S_{\eta\eta}(f) = \frac{5H_s^2}{16}\frac{1}{\left(f/f_p\right)^5} e^{-\frac{5}{4}\left(\frac{f}{f_p}\right)^{-4}} \tag{2.36}$$

This spectrum was designed so that the variance, which is the integral of the spectrum, is related to the significant wave height according to:

$$m_0 = \sigma_\eta^2 = \int_0^\infty S_{\eta\eta}(f)\,df = \frac{H_s^2}{16} \tag{2.37}$$

This relationship is valid for a narrow band spectrum, in which case the wave heights are Rayleigh distributed. The Bretschneider model is mainly used in the case of developing seas. This spectrum is only dependent on two parameters: the peak frequency f_p and the significant wave height H_s (defined as the average of the highest one-third wave heights).

Pierson-Moskowitz, 1964

$$S_{\eta\eta}(f) = \frac{\alpha g^2}{(2\pi)^4 f^5} e^{-\frac{\beta g^4}{(2\pi u f)^4}} \tag{2.38}$$

This spectrum is used in the case of fully developed seas. The parameters are the wind speed *u*, the Phillips constant $\alpha = 8.1\times10^{-3}$ and $\beta = 0.74$. We can also notice that in this case as well $\int_0^\infty S_{\eta\eta}(f)\,df = \left(\frac{H_s}{4}\right)^2$.

JONSWAP (JOint North Sea Wave Project), 1973

$$S_{\eta\eta}(f) = \frac{\alpha g^2}{(2\pi)^4 f^5}\gamma^{\exp\left[-\frac{(f-f_p)^2}{2\sigma^2 f_p^2}\right]} e^{-\frac{5}{4}\left(\frac{f}{f_p}\right)^{-4}} \tag{2.39}$$

This spectrum, proposed by Hasselmann et al. in 1973, was firstly designed for the North Sea but it is often considered as a good approximation for the case of storm waves in other parts of the world.

The JONSWAP spectrum is a function of five parameters:

- $\alpha = 0.066\left(\frac{9F}{U^2}\right)^{-0.22} \simeq 8.1\times10^{-3}$ as before
- $f_p = 2.84\left(\frac{9F}{U^2}\right)^{-0.33}$
- F: fetch length
- γ (peak-shape parameter): often set to 3.3 although it can vary from 1 to 7
- $\sigma = \begin{cases} \sigma_a = 0.07 & \text{for } f \le f_p \\ \sigma_b = 0.09 & \text{for } f > f_p \end{cases}$

It is now more common to use the form that Goda developed (1978):

$$S_{\eta\eta}(f) = 2\pi\alpha^*\gamma^{\exp\left[-\frac{(f-f_p)^2}{2\sigma^2 f_p^2}\right]} \frac{H_s^2}{f_p} \frac{1}{\left(f/f_p\right)^5} e^{-\frac{5}{4}\left(\frac{f}{f_p}\right)^{-4}} \tag{2.40}$$

with $\alpha^* = \dfrac{0.0624}{0.230 + 0.0336\gamma - \dfrac{0.185}{1.9+\gamma}}$

Multi-modal case

We can use the superposition of different JONSWAP spectra to create a multi-modal sea state. Moreover, for the case of multi-modal spectra, we have the examples of the Ochi-Hubble spectrum (1976) and the Torsethaugen spectrum (2004).

2.3.2 Directional Spectrum Models

Generally speaking, all of the spreading function models will have a spreading parameter that spreads the energy on a broader range about a central direction.

Cosine spreading function

The cosine spreading function established in 1963 by Longuet-Higgins, Cartwright and Smith is:

$$D_1(\theta) = C(s)\cos^{2s}\left(\frac{\theta-\bar{\theta}}{2}\right) \text{ with } C(s) = \frac{2^{s-1}}{\pi}\frac{\Gamma^2(s+1)}{\Gamma(2s+1)} \tag{2.41}$$

with the over bar corresponding to the average of the variable.

We also can find other versions of the cosine spreading function that take into account the frequency dependence of the spreading parameter *s*. For more information, the reader can refer to Mitsuyasu et al. (1975), Forristall et al. (1978), Hasselman et al. (1980), Goda (1985), Niedzwecki and Whatley (1991) or Liagre (1999).

Wrapped Gaussian model

The spreading function is made to fit a Gaussian function:

$$G(\theta) = \frac{1}{\sigma_\theta\sqrt{2\pi}}e^{-\frac{(\theta-\bar{\theta})^2}{2\sigma_\theta^2}} \tag{2.42}$$

with σ_θ the standard deviation of the wave spreading

2.4 Turbulence Modeling

Turbulence is characterized by randomness, non-linearity, diffusivity (which causes rapid mixing and increases the momentum & scalar transfer), vorticity, transfer of the energy from large eddies to small eddies, and viscous dissipation of the energy in the smallest eddies.

Even if a flow has some randomness whose description will require the use of some statistical tools, we still can write some governing equations by splitting the velocity into a mean velocity and a turbulent velocity. For example, we can write the general equations of motion under the Boussinesq approximation. That approximation states that the density changes in the fluid can be neglected except in the gravity term (which is a good approximation in our case of a wave basin). The conservation of momentum, the continuity equation and the heat equation can be written using the Einstein notation (Cohen and Kundu, 2002):

$$\begin{cases} \dfrac{\partial \tilde{u}_i}{\partial t} + \tilde{u}_j \dfrac{\partial \tilde{u}_i}{\partial x_j} = -\dfrac{1}{\rho_0}\dfrac{\partial \tilde{p}}{\partial \tilde{x}_j} - g\left[1-\alpha\left(\tilde{T}-T_0\right)\right]\delta_{i3} + \nu \dfrac{\partial \tilde{u}_i}{\partial x_j x_j} & (2.43) \\ \dfrac{\partial \tilde{u}_i}{\partial x_i} = 0 & (2.44) \\ \dfrac{\partial \tilde{T}}{\partial t} + \tilde{u}_j \dfrac{\partial \tilde{T}}{\partial x_j} = \kappa \dfrac{\partial \tilde{T}}{\partial x_j x_j} & (2.45) \end{cases}$$

Under the Boussinesq approximation, the density is defined as $\rho = \rho_0\left[1+\alpha\left(T-T_0\right)\right]$ with α the coefficient of thermal expansion and all the instantaneous properties are defined with the tilde (Cohen and Kundu, 2002):

$$\begin{cases} \tilde{u}_i = U_i + u_i \\ \tilde{p} = P + p \\ \tilde{T} = T + T' \end{cases} \tag{2.46}$$

and by definition $\overline{u}_i = \overline{p} = \overline{T}' = 0$.

The equation of motion for the mean flow is:

$$\frac{\partial U_i}{\partial t} + U_j \frac{\partial U_i}{\partial x_j} = \frac{1}{\rho_0}\frac{\partial \overline{\tau}_{ij}}{\partial \tilde{x}_j} - g\frac{\overline{\rho}}{\rho_0}U_3 \tag{2.47}$$

where the stress is defined as $\overline{\tau}_{ij} = -P\delta_{ij} + 2\mu E_{ij} - \rho_0\overline{u_i u_j}$ and the main strain rate is:

$$E_{ij} = \frac{1}{2}\left(\frac{\partial U_i}{\partial x_j} + \frac{\partial U_j}{\partial x_i}\right) \tag{2.48}$$

The kinetic energy budget of the mean flow is:

$$\begin{aligned} \frac{D}{Dt}\left(\frac{1}{2}U_i^2\right) = & \underbrace{\frac{\partial}{\partial x_j}\left(-\frac{1}{\rho_0}PU_j + 2\nu U_i E_{ij} - \overline{u_i u_j}U_i\right)}_{\text{transport}} \\ & - \underbrace{2\nu E_{ij}E_{ij}}_{\text{viscous dissipation}} + \underbrace{\overline{u_i u_j}\frac{\partial U_i}{\partial x_j}}_{\text{loss to turbulence}} - \underbrace{g\frac{\overline{\rho}}{\rho_0}U_3}_{\text{loss to potential energy}} \end{aligned} \tag{2.49}$$

We can also find the kinetic energy budget of the turbulent flow by defining the fluctuating strain rate $e_{ij} = \frac{1}{2}\left(\frac{\partial u_i}{\partial x_j} + \frac{\partial u_j}{\partial x_i} \right)$, that is

$$\frac{D}{Dt}\left(\overline{\frac{1}{2}u_i^2}\right) = \underbrace{\frac{\partial}{\partial x_j}\left(-\frac{1}{\rho_0}\overline{pu_j} + \frac{1}{2}\overline{u_i^2 u_j} - 2\nu\overline{u_i e_{ij}} \right)}_{\text{transport}} - \underbrace{\overline{u_i u_j}\frac{\partial U_i}{\partial x_j}}_{\text{shear production}} - \underbrace{2\nu\overline{e_{ij}e_{ij}}}_{\text{viscous dissipation} = \varepsilon} + \underbrace{ga\overline{\omega T'}}_{\text{buoyant production}} \tag{2.50}$$

This equation is very similar to the one for the mean flow. In the latter, the shear production is equal and opposite to the loss to turbulence in the former. We also have this time a buoyant production associated with the stability of the ambient environment.

An important feature characteristic of a turbulent flow is called the turbulent cascade where the kinetic energy is cascaded down from large to small eddies in a series of small steps. The small isotropic eddies extract their energy from the larger anisotropic eddies. We recall that the term anisotropic is used to express the fact that the direction of the mean shear is important, as opposed to the isotropic medium where the direction of the mean shear has no consequences. When the so-called Kolmogorov microscale (η) is reached, the eddies are dissipated by the viscosity of the fluid. It is obvious that this microscale is then dependent on the viscosity of the fluid.

The rate of viscous dissipation is $\varepsilon = 2\nu e_{ij}e_{ij}$. Using order of magnitude scaling arguments and defining the length scale of the large eddies l and the scale of the fluctuating velocity u', then since the rate of energy transfer scales as the energy over the time, we have $u'^2 / (l/u')$ which leads to:

$$\varepsilon \sim \frac{u'^3}{l} \tag{2.51}$$

However, this is an order of magnitude estimate only and it doesn't provide the real value of the viscous dissipation. The relationship between the viscous dissipation and the microscale given by Kolmogorov (1941) is:

$$\eta = \left(\frac{\nu^3}{\varepsilon} \right)^{\frac{1}{4}} \tag{2.52}$$

In the case of a one-dimensional turbulent velocity spectrum, we should find the following characteristic power spectrum (Figure 2.4), Tennekes and Lumley (1972).

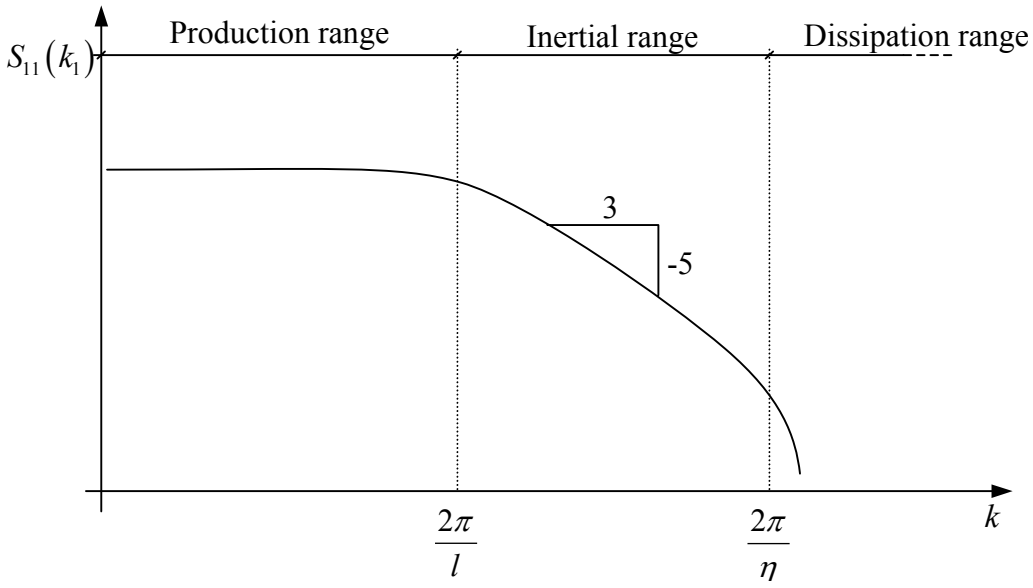

Figure 2.4: One-dimensional velocity spectrum for a turbulent flow

In the inertial range, no energy is added or subtracted in the system; we only have a transfer of energy from the low wave numbers to the high wave numbers, and the spectrum scales with $\varepsilon^{2/3} k^{-5/3}$. On the other hand, in the dissipation range, the energy of the turbulent flow is dissipated by viscosity, and the spectrum scales with ν and η so that $S_{11}(k_1) \sim \left[\nu^2 \eta \right] g_2(k_1 \eta)$. The turbulent energy is produced in the production range by transfer of energy from the larger eddies but also by absorbing energy directly from

the strain rate of the mean flow. Contrary to the dissipation range, we know that in the production range the spectrum scales with u and l so that $S_{11}(k_1) \sim \left[u^2 l\right] g_1(k_1 l)$. We should also notice that no inertial subrange can exist unless we have the turbulent Reynolds number $R_l = ul/\nu > o\left(10^5\right)$.

Since the inertial range represents an equilibrium condition where energy input from the production range is balanced by energy output to the dissipation range, we must have that:

$$\varepsilon = \frac{u^3}{l} = \frac{\nu^3}{\eta^4} \tag{2.53}$$

with u defined as the root mean square turbulent velocity fluctuation and ν as the fluid kinematic viscosity. Thus, the Kolmogorov microscale can be defined as in Equation 2.52 and the turbulent Reynolds number such as in Equation 2.53.

$$\eta = \left(\frac{\nu^3}{\varepsilon}\right)^{1/4} \tag{2.54}$$

$$R_l = \frac{ul}{\nu} = \left(\frac{l}{\eta}\right)^{4/3} \tag{2.55}$$

Tennekes and Lumley (1972) have proposed a simple model for the one-dimensional in-line velocity spectrum that we will adopt herein for describing the structure of the turbulence in the currents generated in the OTRC basin. According to that model, for the production range $\left(0 \le k_1 l \le k_0 l = 1.8\right)$:

$$S_{11}\left(k_1\right) = \frac{66}{110}\alpha u^2 l\left(k_0 l\right)^{-5/3}\left[1 - \frac{5}{11}\left(\frac{k_1}{k_0}\right)^2\right] \tag{2.56}$$

and for the inertial subrange $\left(k_1\eta < 0.55 \text{ and } k_1 l > k_0 l = 1.8\right)$:

$$S_{11}\left(k_1\right) = \frac{18}{55}\alpha u^2 l\left(k_1 l\right)^{-5/3} \tag{2.57}$$

By definition, the longitudinal integral scale is $S_{11}\left(0\right) = \frac{u^2}{\pi} l$.

Thus, with the equation for the production range, we have:

$$S_{11}\left(0\right) = \frac{66}{110}\alpha u^2 l\left(k_0 l\right)^{-5/3} = \frac{u^2}{\pi} l \tag{2.58}$$

$$\Rightarrow \alpha = \frac{66}{110\pi}\left(1.8\right)^{5/3} = 1.413 \tag{2.59}$$

Applying the frozen turbulence assumption, which states that $t = \frac{x}{U}$ if $\frac{u}{U} \ll 1$ (with U the mean flow velocity), we have $f = \frac{Uk_1}{2\pi}$. As long as the mean flow U is sufficiently strong, we can convert the wave number spectrum into a frequency spectrum according to:

$$S_{11}\left(f\right) = S_{11}\left(k_1\right)\frac{dk_1}{df} = \frac{2\pi}{U} S_{11}\left(k_1\right) \tag{2.60}$$

Using the previous equations, the model for the in-line velocity spectrum can be simplified to:

$$\begin{cases} \text{production range:} & S(f) = 2(\varepsilon l)^{2/3} \dfrac{l}{U}\left[1 - 5.5385\left(\dfrac{fl}{U}\right)^2\right] \quad (2.61) \\ \text{inertial range:} & S(f) = 0.1358(\varepsilon U)^{2/3} f^{-5/3} \quad (2.62) \end{cases}$$

Moreover, the wave number dividing the production and inertial subrange is $k_0 l = 1.8$, so the associated frequency is $f_0 = \dfrac{U k_0 l}{2\pi l} = \dfrac{1.8U}{2\pi l}$, or:

$$f_0 = 0.2865\frac{U}{l} \quad (2.63)$$

Remembering that the variance is equal to the area under the spectrum, we have the following integral relationship for the mean square turbulent velocity:

$$\sigma_u^2 = \int_0^\infty S(f)\,df = 0.9587(\varepsilon l)^{2/3} \quad (2.64)$$

3. EXPERIMENTAL DATA

3.1 Experimental Facility

The OTRC wave basin measures 150ft long by 100ft wide (45.7*30.5m) with a constant depth of 19ft (5.8m). In the center of the basin, there is a deep pit 30ft long by 15ft wide (9.1*4.6m) with a depth of 55ft (16.7m). The pit can be covered at any depth between 19ft and 55ft with a 4-inch depth increment. Figure 3.1 is a picture and Figure 3.2 shows a plan of the OTRC wave basin.

Figure 3.1: OTRC wave basin

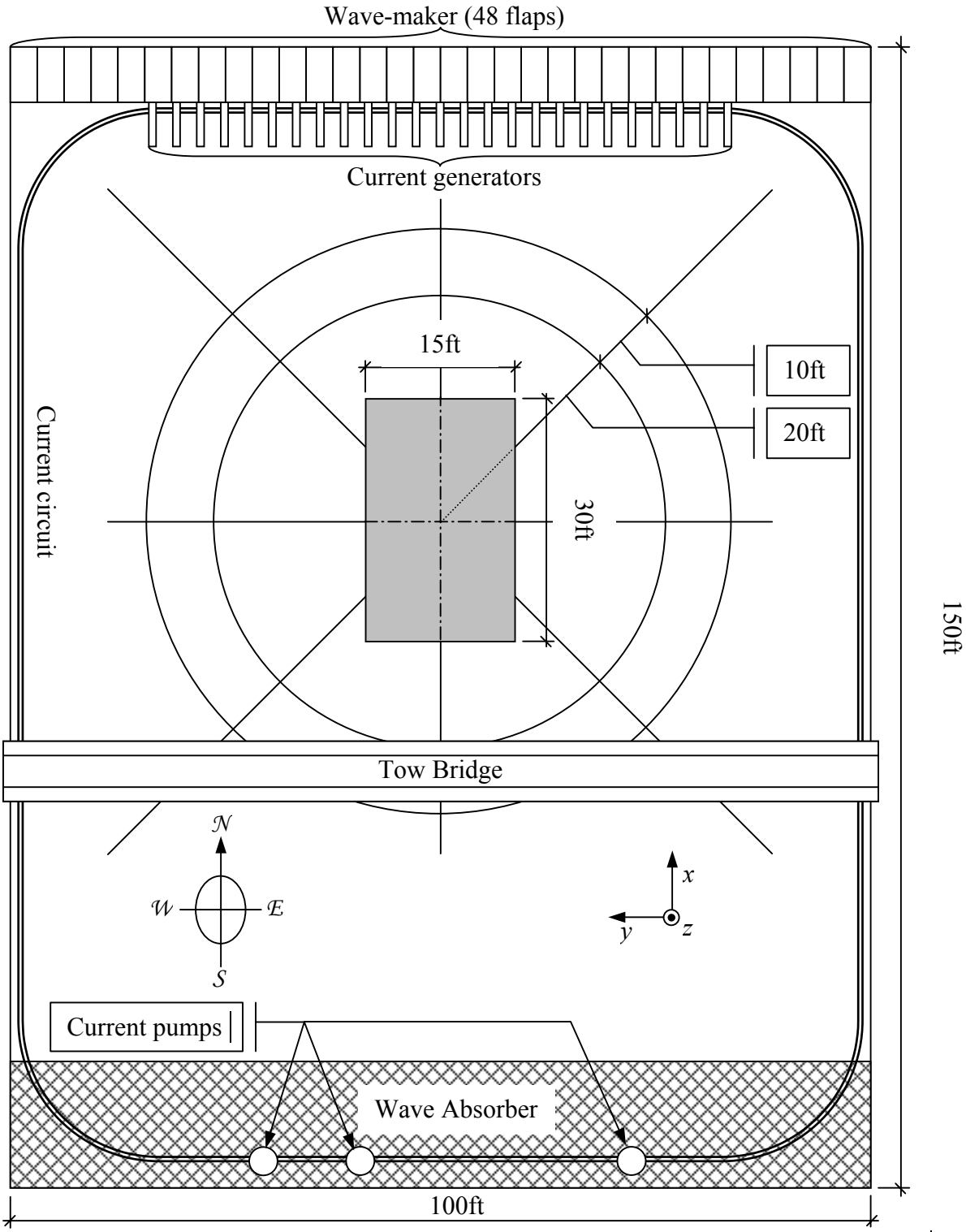

Figure 3.2: Plan of the wave basin

At the north side of the basin, there is a flap type directional wave-maker consisting of 48 flaps. Each wave board is 2ft (0.6m) wide and 11.9ft (3.6m) high, driven independently by a servo-controlled linear hydraulic actuator and attached at 8ft (2.4m) from the bottom of the basin. At the north side of the basin, there is also a current generator consisting of multiple jet nozzles set up in nine manifolds with 30 nozzles per manifold. Each nozzle is of 2in (5cm) diameter and the nozzles are spaced 9in (23cm) apart in the horizontal plane. The vertical profile of the nozzles is illustrated in Figure 3.3 and a view of the nozzles with the wavemaker in Figure 3.4.

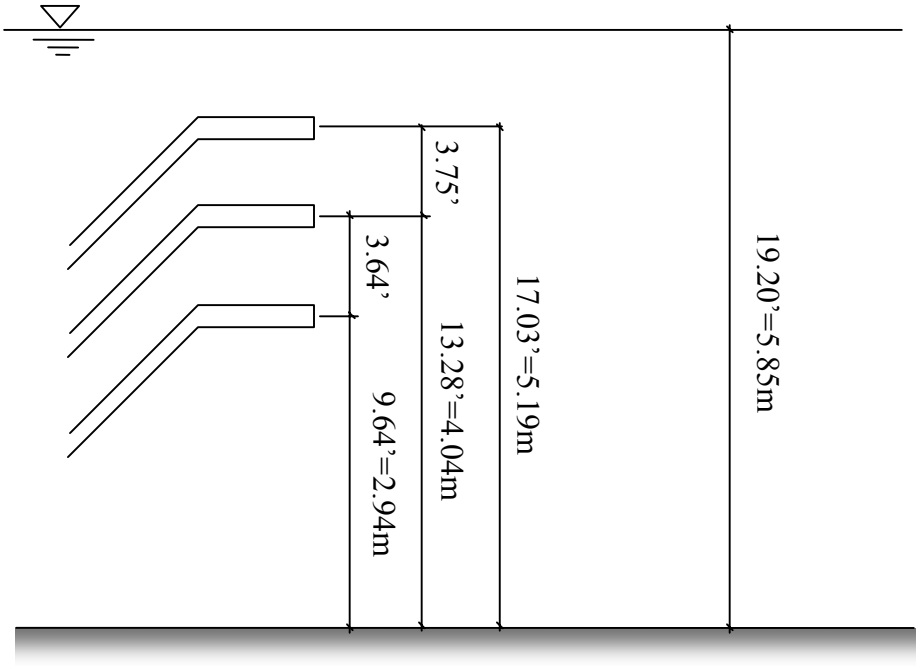

Figure 3.3: Vertical profile of the current generator

Three individual pumps are used to generate the current. The first two pumps can be set up at 0 or 100% of their capacity. The third pump has a variable frequency drive (0 to 60Hz). The pumps have a combined capacity up to 36000gpm (2250L/s) which allows a surface current up to approximately 2ft/s (0.6m/s). Pumps and pump intakes are located at the south end of the basin behind the wave absorber (Figure 3.5).

The flow is pumped to the current manifold through large pipes located on the basin floor adjacent to the east and west walls (Figure 3.2).

The basin is equipped with a traveling bridge that spans the East-West direction (Figure 3.1). The bridge may be used to support models and sensors. It has a maximum traveling velocity of 2 $ft.s^{-1}$ (0.6m/s). At the south end of the basin, there is a wave absorber that is made of expanded metal sheets that dissipate the energy of the waves. The wave absorber has a reflection coefficient of about 5% (dependent on wave period and height), so the duration of wave tests must be restricted (typically less than 30 minutes).

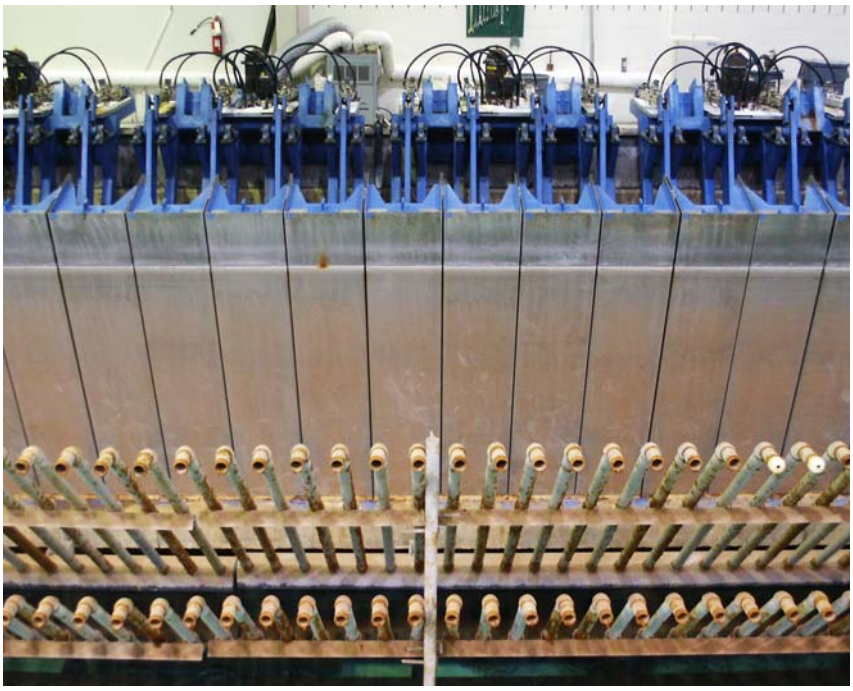

Figure 3.4: Wave maker and current generator

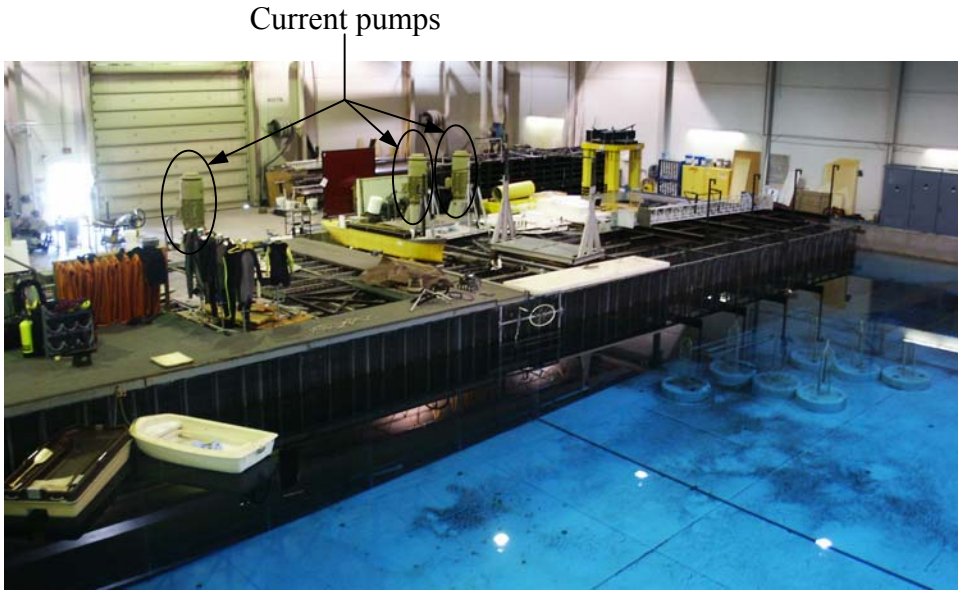

Figure 3.5: Wave absorber and three current pumps

The OTRC uses a NEFF 620 data acquisition system (Figure 3.6). It can record at a resolution of 15 bits on 64 channels at a maximum frequency of 100Hz. Also, the NEFF 620 can do individual channel conditioning, amplification and anti-alias filtering.

Figure 3.6: Data acquisition system NEFF 620

3.2 Experimental Design

The experimental program was designed to test the following aspects of the MAVS:

- sensitivity to orientation;
- frequency response characteristics;
- blockage effects (housing and mounting);

The program was also designed to test various schemes for mapping the mean flow and turbulence structure of the current in the OTRC basin. To investigate the effect of sensor orientation, three different orientations were used (Figure 3.7): one with the axis of the sensor aligned with the main current (the North-South orientation) and two with the sensor axis perpendicular to the main current, the East-West and the Vertical orientations. We expect that the Vertical orientation will have the same behavior as the North-South one in the case of a wave test.

The sensors were mounted on a beam fixed to the tow bridge; the black dots represent the docking points of the sensor on the mounting beam. Finally, the x, y & z coordinates are the absolute Cartesian coordinates of the wave basin and the x', y' & z' coordinates represent the local system of coordinates of the sensor itself. In the wave basin coordinate system, the x-axis is pointed north (toward the wave maker), the y-axis is pointed west, and the z-axis is pointed vertically upward.

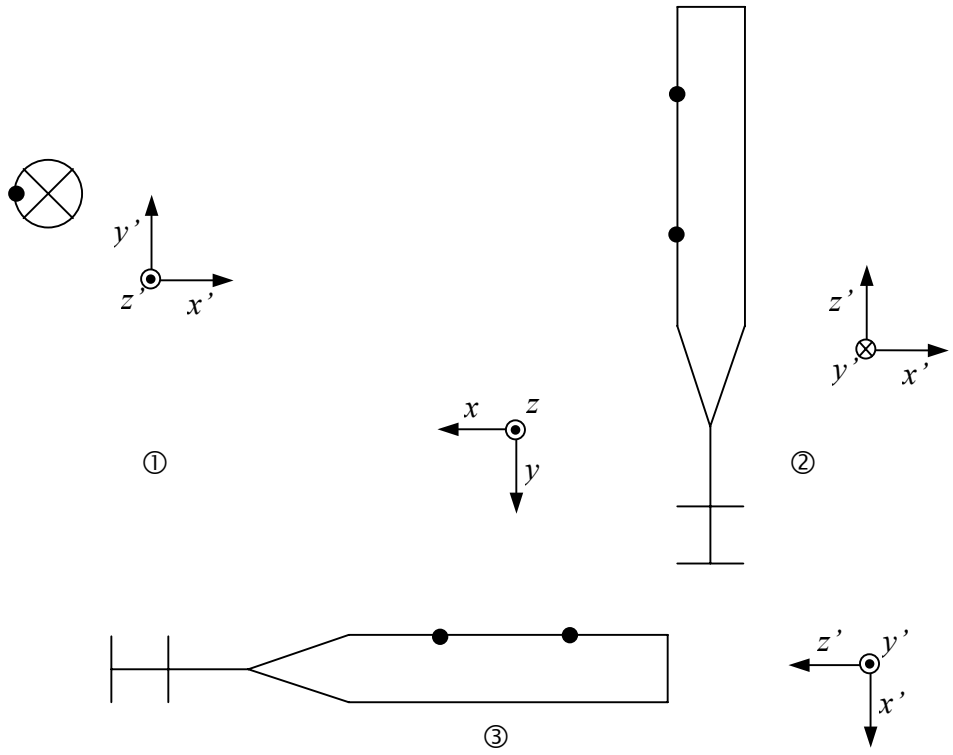

Figure 3.7: Sensor orientation. ①: Vertical orientation; ②: East-West orientation; ③: North-South orientation

Three different arrays were used to profile the structure of the current in the OTRC basin. In a first set of tests, a 3 by 3 array (Figure 3.8) centered in the centerline of the wave basin was used. Then, a horizontal array (Figure 3.9) was used to profile the surface current along the *y*-axis. And finally, a vertical array (Figure 3.10) covering the water column was used to map the velocity and turbulence profile. So as a summary:

- 3*3 arrays gives two-dimensional profile information;
- horizontal array gives a one-dimensional profile at a single depth;
- vertical array gives a one-dimensional profile at a single station.

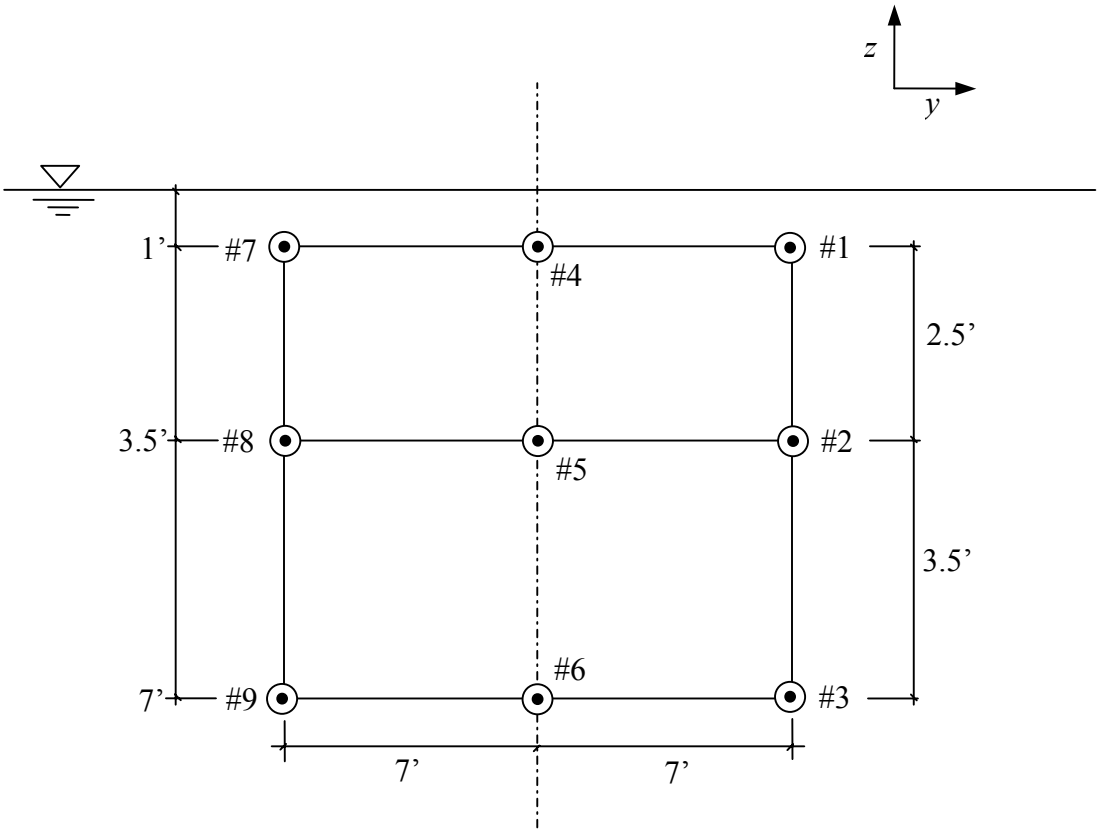

Figure 3.8: 3*3 array

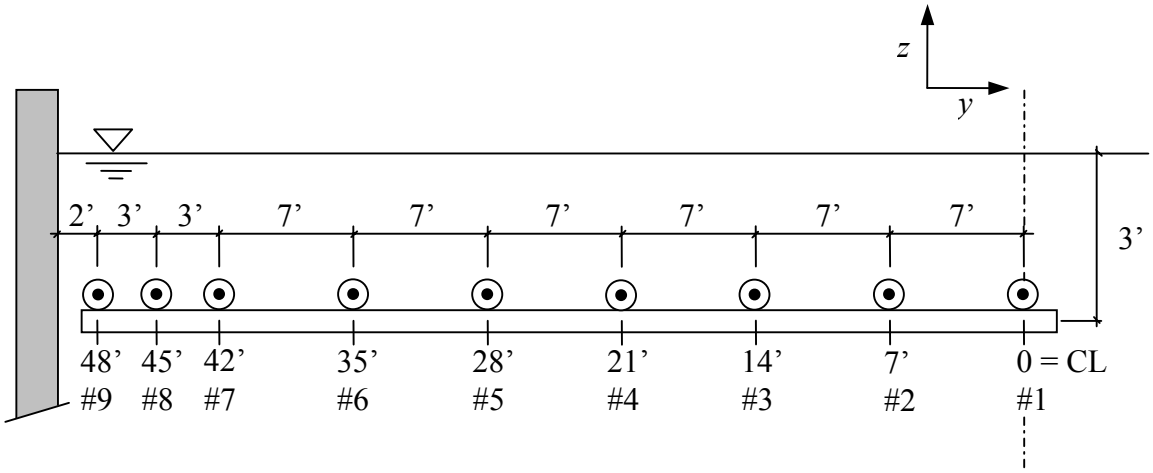

Figure 3.9: Horizontal array

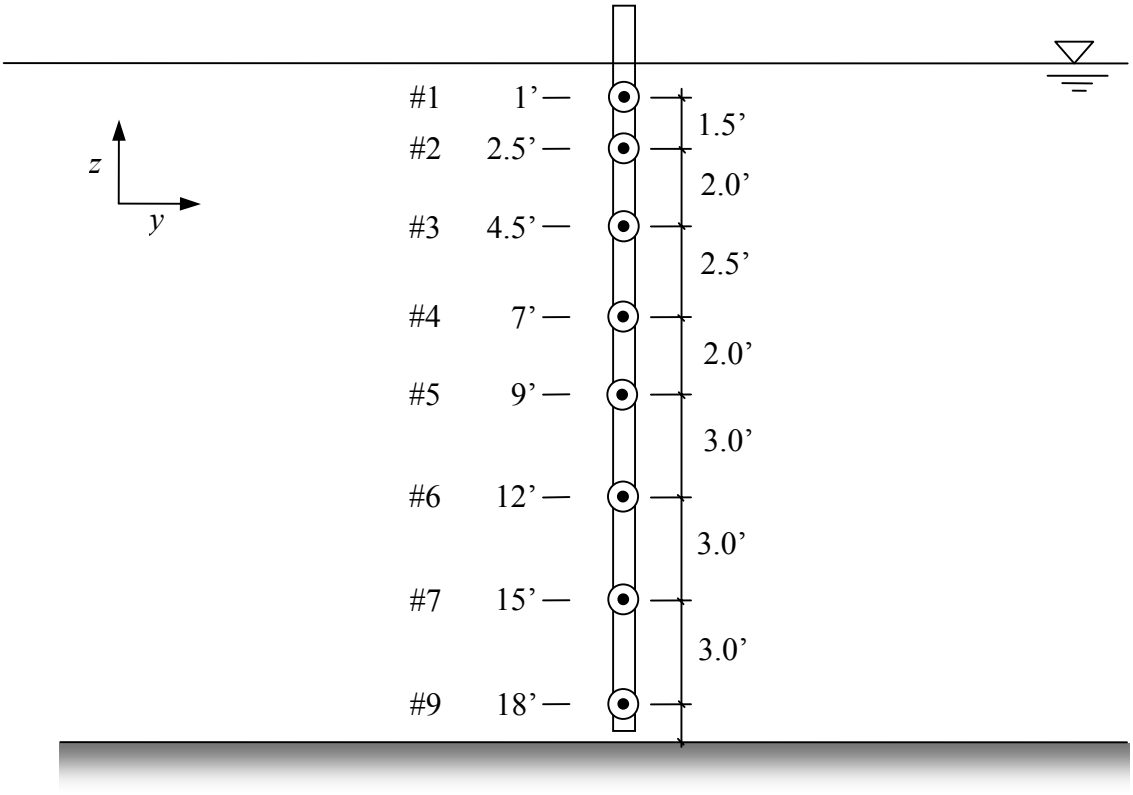

Figure 3.10: Vertical array

Tables 3.1, 3.2 and 3.3 summarize the tests that were performed for each of the three tests phases. A more detailed listing of all the individual tests is provided in Appendix E.

For the Phase I tests, a single (demonstration) MAVS sensor was deployed along with a 2-axis Marsh-McByrney current meter so that a side-by-side comparison could be made. The MAVS was tested in the three orientations and under calm, tow, current and wave tests.

The Phase II tests examined the behavior of the MAVS in an array. First, a 3*3 array was used to measure the cross-sectional current simultaneously at different stations. Then, a vertical array was used to cover the whole water depth. The vertical array was moved along the *x* and *y* direction to cover a decent surface of the wave basin. Then, a horizontal array was used to measure the surface currents simultaneously across the half-width of the basin.

The Phase III program comprised tow tests with a North-South or Vertical orientation of the sensors in the horizontal array.

Table 3.1: Test plan for Phase I

Type of test	Sensor depth	Test characteristic	Sensor orientation
Tow		15, 20, 30 and 45cm/s	VR
Calm			NS
Tow		15, 20, 30 and 45cm/s	NS
Calm			EW
Tow		15, 20, 30 and 45cm/s	EW
Calm			
Current	1ft	Current at 200%	EW
	1ft	Current at 200%	NS
	1ft	Current at 200%	VR
	6ft	Current at 200%	VR
	6ft	Current at 200%	NS
	6ft	Current at 200%	EW
Calm			
Regular Wave	1ft	Amplitude = 10cm Period = 1.4s	EW
	3ft		EW
	3ft		NS
	1ft		NS
	1ft		VR
	3ft		VR

Table 3.2: Test plan for Phase III

Type of test	Test characteristic	Sensor orientation	Array orientation
Calm		NS	EW
Tow	20, 30, 45 and 60cm/s	NS	EW
Calm		VR	EW
Tow	20, 30, 45 and 60cm/s	VR	EW

Table 3.3: Test plan for Phase II

Type of test	Test characteristic	Sensor orientation	Array orientation	Array location	
				x (ft)	*y* (ft)
Tow	20, 30, 45 and 60cm/s separated by calm tests	NS	3*3	-	0
Current	Pump #2 at 100%	NS	3*3	0	0
	Pumps #2&3 at 100%	NS	3*3	0	0
Calm		NS	3*3	0	0
Current	Pumps #2&3 at 100% & #1 at25%	NS	3*3	0	0
	Pumps #2&3 at 100% & #1 at25%	NS	3*3	-32 to 32	0
	Pump #2 at 100%	NS	3*3	32 to -32	0
Calm		NS	3*3	0	0
RG2 - Regular Wave	Amplitude = 10cm, Period = 1.4s	NS	3*3		
RG5 - Regular Wave	Amplitude = 10cm, Period = 1.5s	NS	3*3	0	0
RN - Random Wave		NS	3*3		
Calm		NS	3*3	0	0
RN Wave + Current	Current at 100%	NS	3*3		
RG2 Wave + Current	Current at 100%	NS	3*3	0 to -24	0
RG5 Wave + Current	Current at 100%	NS	3*3		
RN Wave + Current	Current at 225%	NS	3*3		
RG2 Wave + Current	Current at 225%	NS	3*3	-24 to 0	0
RG5 Wave + Current	Current at 225%	NS	3*3		
Calm		NS	V		

Table 3.3: Continued

Type of Test	Test Characteristic	Sensor orientation	Array orientation	Array loc.	
				x (ft)	*y* (ft)
Current	Current pump #2 at 100%	NS	V	0 to -24	0
	Pumps #2&3 at 100%	NS	V	0 to -24	0
	Pumps #2&3 at 100%	NS	V	-24 to 0	7
	Pumps #2&3 at 100%	NS	V	0 to -24	14
	Pumps #2&3 at 100%	NS	V	-24 to 0	21
	Pumps #2&3 at 100%	NS	V	0 to -24	28
	Pumps #2&3 at 100%	NS	V	-24 to 0	35
	Pumps #2&3 at 100%	NS	V	0 to -24	42
	Pump #2 at 100%	NS	V	-24 to 0	42
	Pump #2 at 100%	NS	V	0 to -24	35
	Pump #2 at 100%	NS	V	-24 to 0	28
	Pump #2 at 100%	NS	V	0 to -24	21
	Pump #2 at 100%	NS	V	-24 to 0	14
	Pump #2 at 100%	NS	V	0 to -24	7
	Pump #2 at 100%	NS	EW	-24 to 0	-
RG5 Wave + Current	Pump #2 at 100%	NS	EW	0 to -24	-
RN Wave + Current	Pump #2 at 100%	NS	EW		
Current	Pumps #2&3 at 100% & #1 at 25%	NS	EW	-24 to 0	-
RG5 Wave + Current	Pumps #2&3 at 100% & #1 at 25%	NS	EW	0 to -24	-
RN Wave + Current	Pumps #2&3 at 100% & #1 at 25%	NS	EW		

4. DATA PROCESSING

4.1 FFT and Spectral Analysis

Fourier analysis is a very popular method (Cooley and Tukey, 1965) used to define the energy spectrum based on a time series $f(t)$. We are assuming that this signal is periodical with a period *T* and as we will see later, the lack of periodicity can artificially create high frequency energy. First of all, we define our time series as

$$f(t) = \sum_{n=0}^{+\infty} \left(a_n \cos(n\sigma t) + b_n \sin(n\sigma t) \right) \tag{4.1}$$

where the coefficients can be obtained by using the orthogonal property of the *sin* and *cos* functions :

$$\begin{cases} \int_{t}^{t+T} \sin(n\sigma t)\cos(m\sigma t)\,dt = 0 & (4.2) \\ \int_{t}^{t+T} \cos(n\sigma t)\cos(m\sigma t)\,dt = \begin{cases} T & m = n = 0 \\ \frac{T}{2} & m = n \neq 0 \\ 0 & m \neq 0 \end{cases} & (4.3) \\ \int_{t}^{t+T} \sin(n\sigma t)\sin(m\sigma t)\,dt = \begin{cases} \frac{T}{2} & m = n \neq 0 \\ 0 & m \neq 0 \end{cases} & (4.4) \end{cases}$$

which leads us to the Fourier coefficient defined as:

$$\begin{cases} a_0 = \dfrac{1}{T}\int_t^{t+T} f(t)\,dt \\ a_n = \dfrac{2}{T}\int_t^{t+T} f(t)\cos(n\sigma t)\,dt \end{cases} \qquad \begin{cases} b_0 = 0 \\ b_n = \dfrac{2}{T}\int_t^{t+T} f(t)\sin(n\sigma t)\,dt \end{cases}$$

We notice that a_0 is the average of the signal over the period *T*. The mean square value of the function is related to the coefficients by using Parseval's theorem:

$$\frac{1}{T}\int_t^{t+T} f^2(t)\,dt = a_0^2 + \frac{1}{2}\sum_{n=1}^{N}\left(a_n^2 + b_n^2\right) \tag{4.5}$$

However, we are always dealing with discretely sampled phenomena and finite record lengths. So if we have a sampling period of *T* with N_s samples per second, we define *N* as the number of points used in the FFT. Then, using the complex series, the Fourier series itself can be represented in an easier form $f(t) = \sum_{n=-N}^{N} F(n)e^{in\sigma t}$ and we define $F(n) = |F(n)|e^{-i\varepsilon_n}$ with

$$\begin{cases} |F(n)| = \dfrac{1}{2}\sqrt{a_n^2 + b_n^2} = |F^*(-n)| & (4.6) \\ \varepsilon_n = \tan^{-1}\left(\dfrac{b_n}{a_n}\right) & (4.7) \end{cases}$$

Also, the signal can be reconstructed in a non-complex form:

$$f(t) = \sum_{n=-N}^{N} A_n \cos(n\sigma t - \beta_n) \text{ with } \begin{cases} A_n = H(\theta_n, \sigma_n)\sqrt{a_n^2 + b_n^2} = 2|F(n)| \\ \beta_n = \tan^{-1}\left(\dfrac{b_n}{a_n}\right) - H_\beta \end{cases}$$

where $H(\chi_n, \sigma_n)$ and H_β are the transfer functions which may be used to convert the equations that were established for the water surface elevation into different wave properties (see Table 4.1).

Table 4.1: Transfer function and phase lag for various wave properties

Wave Properties		$H(\chi_n, \sigma_n)$	H_β
Water surface elevation		1	0
Velocity	x	$\sigma_n \frac{\cosh\left[k_n(z+h)\right]}{\sinh(k_n h)} \cos(\chi_n)$	
	y	$\sigma_n \frac{\cosh\left[k_n(z+h)\right]}{\sinh(k_n h)} \sin(\chi_n)$	
	z	$\sigma_n \frac{\sinh\left[k_n(z+h)\right]}{\sinh(k_n h)}$	$\frac{\pi}{2}$
Acceleration	x	$\sigma_n^2 \frac{\cosh\left[k_n(z+h)\right]}{\sinh(k_n h)} \sin(\chi_n)$	
	y	$\sigma_n^2 \frac{\cosh\left[k_n(z+h)\right]}{\sinh(k_n h)} \cos(\chi_n)$	
	z	$-\sigma_n^2 \frac{\sinh\left[k_n(z+h)\right]}{\sinh(k_n h)}$	π
Pressure		$\frac{\cosh\left[k_n(z+h)\right]}{\sinh(k_n h)}$	0

The covariance function provides information on the correlation between two signals $f_i(t)$ and $f_j(t)$. This function is the mean of the product of those two signals as a function of the time lag τ between the two signals:

$$C_{ij}(\tau) = \frac{1}{T}\int_{t}^{t+T} f_i(t) f_j(t+\tau)\, dt = \sum_{n=-N/2}^{N/2} \left|F_i(n)\right|\left|F_j(n)\right| e^{i\left(\varepsilon_{j_n}-\varepsilon_{i_n}\right)} e^{in\sigma\tau} \tag{4.8}$$

The Fourier transform of the covariance function is in the case of two identical functions called the power spectrum or in the case of two different signals the cross spectrum. We are interested in the power spectrum:

$$S_{11}(n) = \frac{1}{T}\int_{t}^{t+T} C_{11}(\tau) e^{-in\sigma\tau} d\tau = \left|F_1(n)\right|^2 \tag{4.9}$$

The covariance function may also be represented as the inverse Fourier transform of the power spectrum. Moreover, this spectrum is defined as the double-sided power spectrum because it includes both positive and negative frequencies. It can be useful to have only the one-sided version of the power spectrum that is:

$$\begin{cases} S'_{11}(n) = 2\left|F_1(n)\right|^2 & n > 0 \qquad (4.10) \\ S'_{11}(0) = \left|F_1(0)\right|^2 & n = 0 \qquad (4.11) \end{cases}$$

The cross-spectrum is defined as $S_{ij}(n) = \frac{1}{T}\int_{t}^{t+T} C_{ij}(\tau) e^{-in\sigma\tau} d\tau = F_i^*(n) F_j(n)$ with the asterisk referring to the complex conjugate of the Fourier transform. The real part of it is the cospectrum and the imaginary part is the quadrature spectrum:

$$S_{ij}(n) = c_{ij}(n) + iq_{ij}(n) \tag{4.12}$$

Also, we have to notice that if we are working with cyclic frequencies *f* instead of circular frequencies σ, the spectrum is $S_{11}(f) = 2\pi S_{11}(\sigma)$.

We may check our computations by comparing the variance of the time series with the integral of the power spectrum knowing that $\sigma_1^2 = \sum_{n=1}^{+\infty} \frac{1}{2} \left| F_1(n) \right|^2$ (notice that $\sigma \neq \sigma_1$).

The Fast Fourier transform is based on the Fourier theory previously developed. The coefficients F_{jm} can be found from the signal property f_j:

$$\begin{aligned} F_{jm} &= \Delta t \sum_{n=0}^{N-1} f_j(n\Delta t) e^{-i\frac{2\pi mn}{N}} \\ &= \sum_{l=0}^{L} A_j(f_m, \chi_l) H(\chi_m, \sigma_m) e^{-i\left[k_m\left(x_j \cos(\theta_l) + y_j \sin(\theta_l)\right) + H_\beta\right]} \end{aligned} \tag{4.13}$$

where $A_j(f_m, \chi_l) = \sqrt{S(f, \chi) d\chi df}$ and the coefficient $H(\chi_n, \sigma_n)$ and H_β are the same as the ones in the Table 4.1 and where the signal property can be written in a general form as:

$$f_j(t) = \Delta f \sum_{m=-M}^{M} \sum_{l=0}^{L} F_j(f_m, \chi_l) H(\chi_m, \sigma_m) e^{-i\left[k_m\left(x_j \cos(\chi_l) + y_j \sin(\chi_l)\right) + H_\beta\right] + i\frac{2\pi mn}{N}} \tag{4.14}$$

4.2 Windowing of Time Series Data

The first processing done to the time series data is to look for the zerocrossings as it will allow us to generate artificially a periodical signal, which is good in the case of a wave test. However, in the case of a test for a non-periodical flow, as we truncate based on the zero crossing of one velocity component, the signal for the two other velocity components won't be perfectly periodic, as illustrated in Figure 4.1.

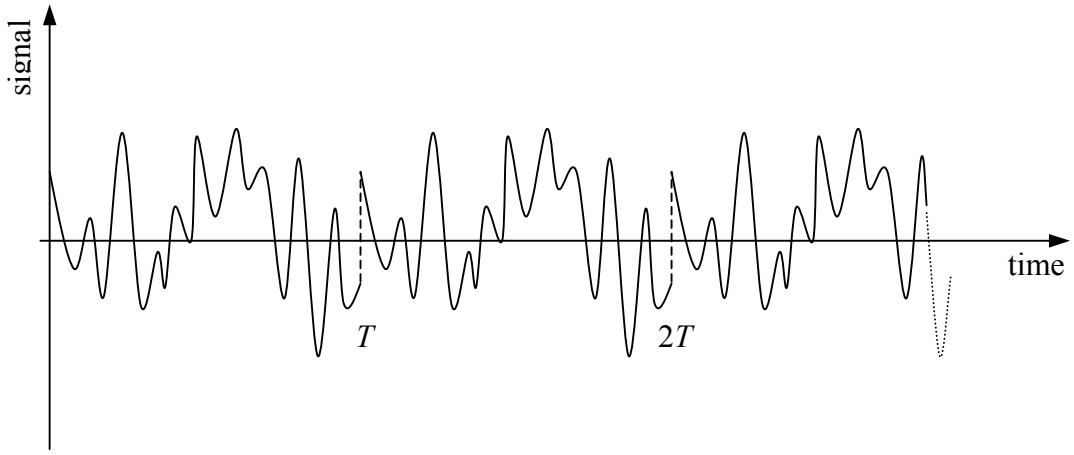

Figure 4.1: Theoretical signal generated from a signal of period T

Figure 4.2 illustrates the logarithm of the velocity spectrum in the case where we have not truncated the signal on a zero crossing. On the other hand, the truncation will generate high frequency energy above 10Hz. We also clearly see that if we truncate with the zero crossing applied on u, we will have spurious high frequency energy on v and *vice versa*. In order to correct that, we can later use an overlap function that will artificially generate a zero at the end and the beginning of the signal such as illustrated in Figure 4.3. This overlap function can avoid the numerical creation of energy at high frequency as illustrated in Figures 4.4 and 4.5.

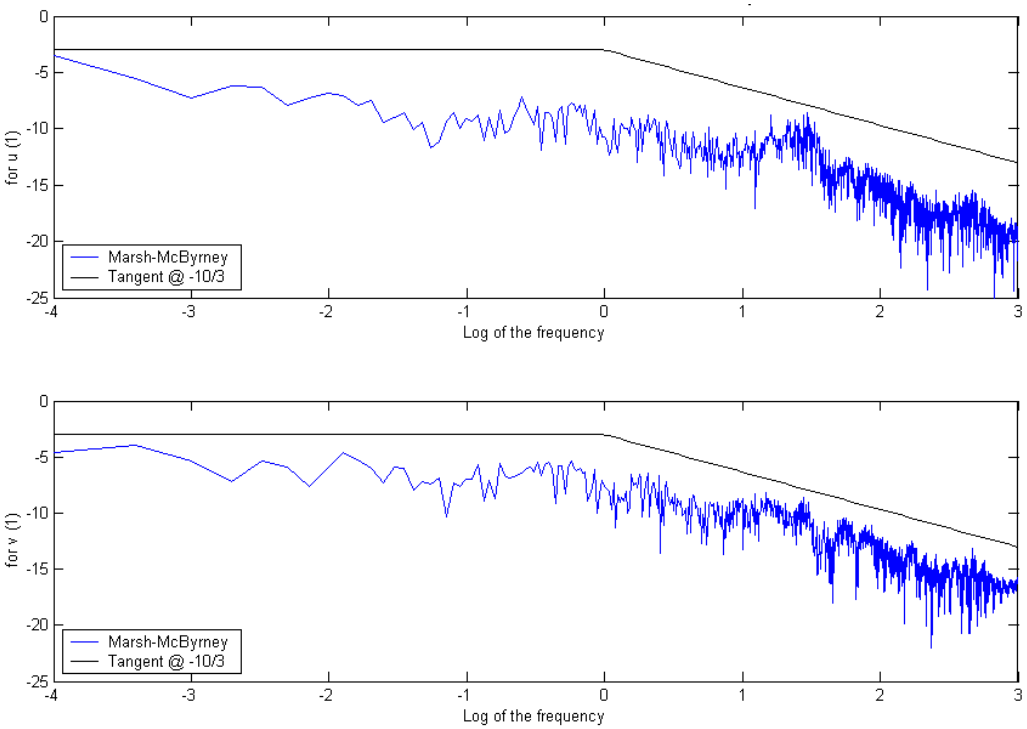

Figure 4.2: Velocity spectrum without zero crossing

Figure 4.3: Overlap function for time series windowing

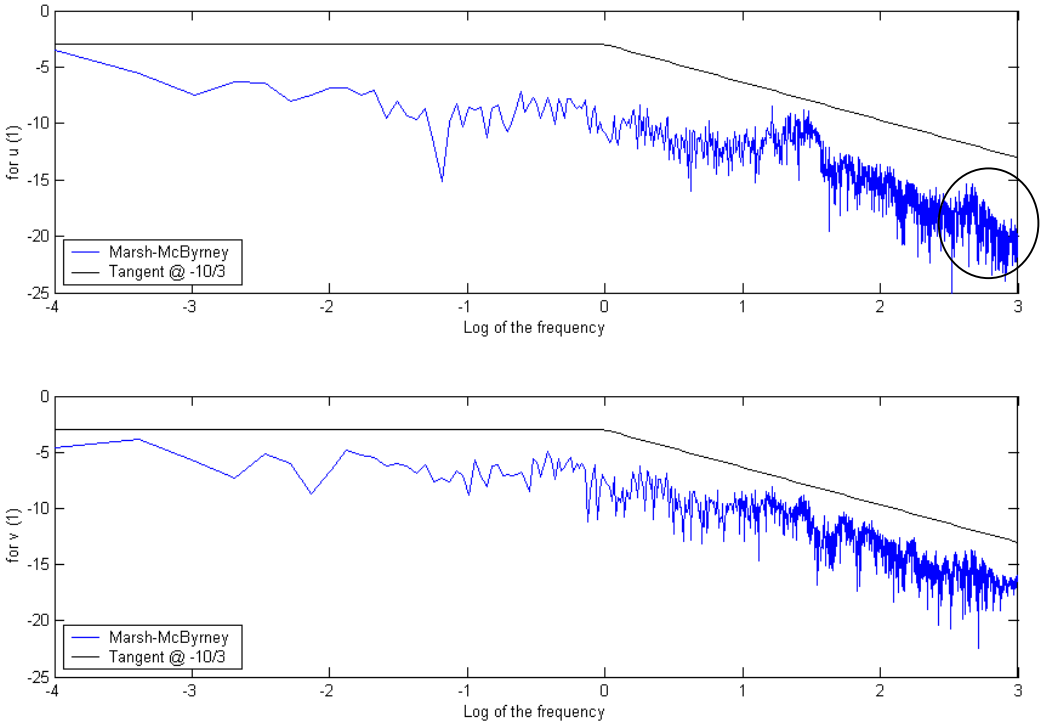

Figure 4.4: Velocity spectrum with zero crossing on *u*

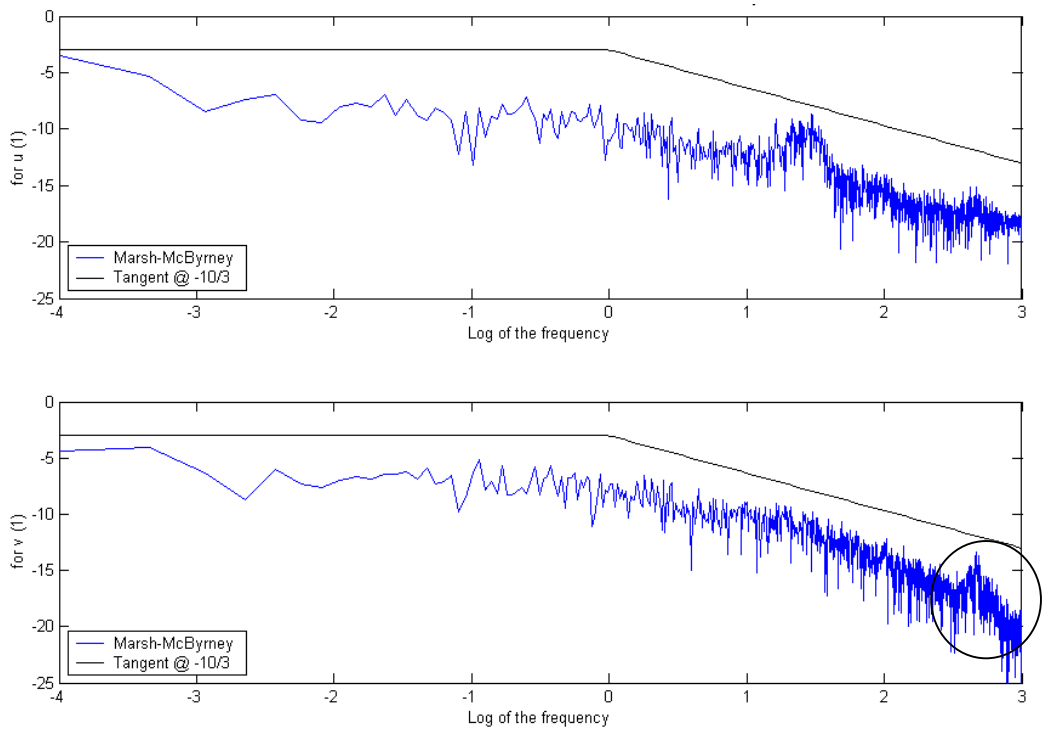

Figure 4.5: Velocity spectrum with zero crossing on *v*

4.3 Smoothing and Averaging of the Spectrum

As we have recorded sometimes a large number of samples, we may also have a large number of points to plot for the logarithm of the spectrum. However, in contrast to the regular spectrum, we now plot the logarithm of the frequency, which tends to group the points at the high frequency end and has the drawback of giving an unreadable plot. Two different methods were attempted to smooth the spectrum.

The first method attempted was a smoothing method based on a Gaussian kernel (Figure 4.6) used to weight the neighboring points.

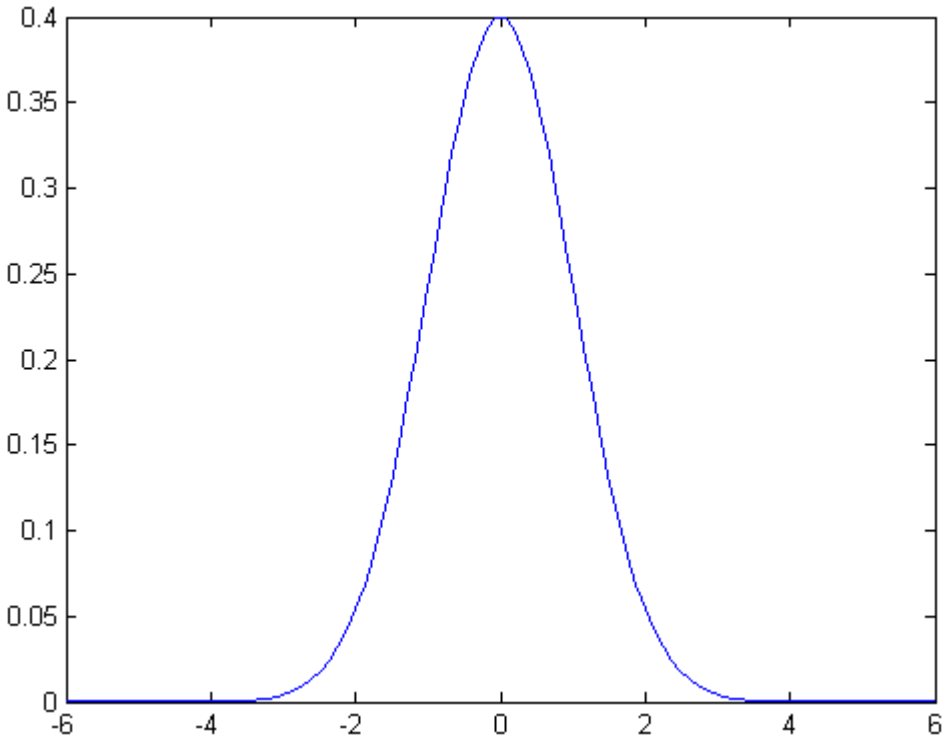

Figure 4.6: Gaussian function centered on 0 with $\sigma = 1$

The width of the Gaussian function is the full width at half maximum (FWHM) that can be related to the standard deviation of the signal on the number of points we want to smooth by $FWHM = \sigma\sqrt{8\log(2)}$.

The spectrum is processed from frequency to frequency by generating a new value that is a function of the central point and its surrounding neighbors. For example, if we are at the point #20 and we want to smooth with a FWHM of 10 points, the weighting function can be seen in Figure 4.7 (note that the integral over the whole kernel is equal to 1). So in the end, this will give us a much clearer view on the logarithm of the spectrum. However, we are generating a new signal and losing some information as we can see in the figures, especially in the case of a peak from a wave signal.

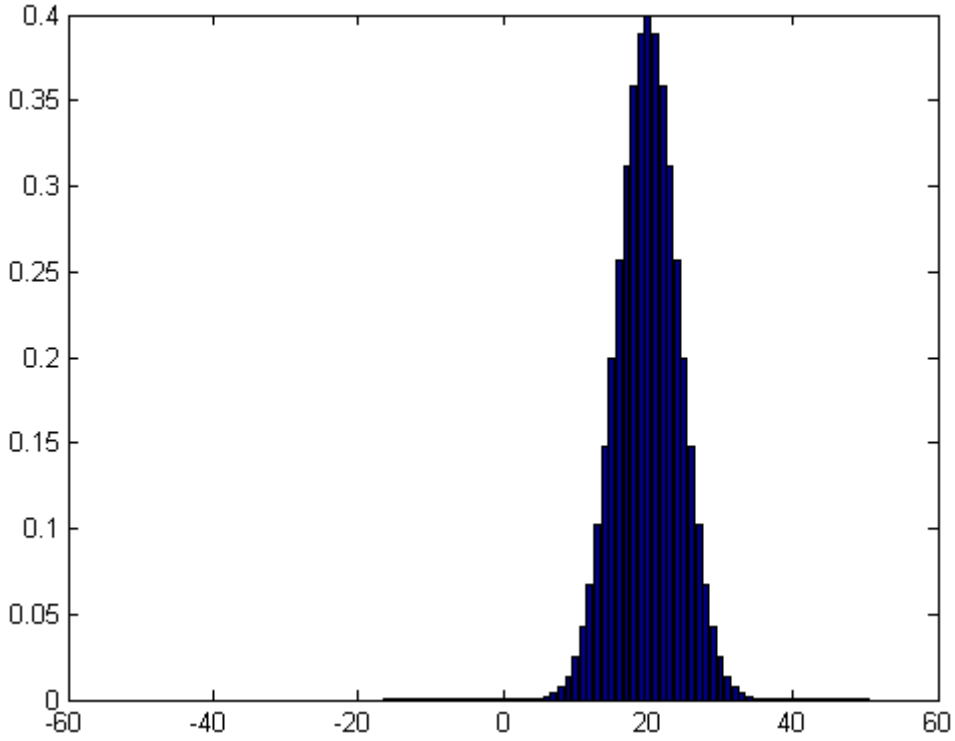

Figure 4.7: Smoothing function centered on the 20th point with FWHM=10

The second smoothing method attempted is based on the same principle but the kernel is now a simple rectangle or so-called box-car window as shown in Figure 4.8.

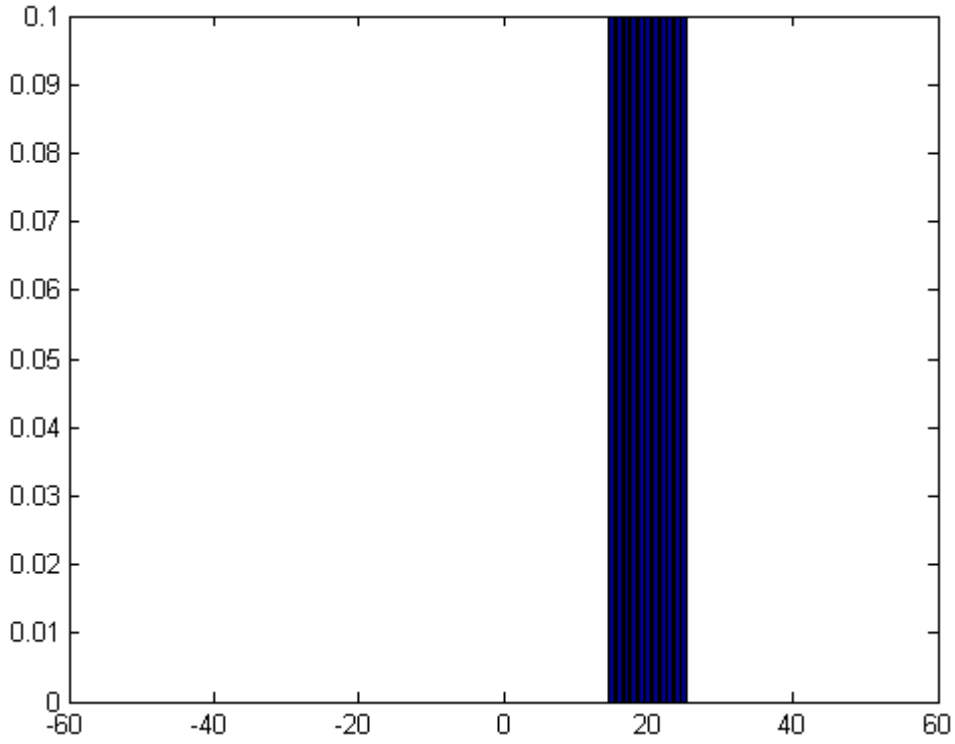

Figure 4.8: Kernel for an averaging function

Contrary to the previous case, the kernel was not applied to every point as a running window but once every 10 points as a box car average (if we use the same number as in the previous case), which yields to a much smaller number of frequency points. However, we have to take into account the fact that we have in the *x*-axis a logarithm of the frequency that will "compress" the points as we are getting to high frequencies. Therefore, the frequency range is divided into $2 * \log 10\left(n_{signal}\right)$ parcels with each parcel containing a different number of points according to $n = \frac{1}{\Delta f}$.

$$part = round\left(4 \times linspace\left(1.2, \log 10\left(n_{signal}\right), ceil\left(\frac{n_{signal}}{n}\right)\right)\right) \tag{4.15}$$

Both of these methods provide a clearer result without missing the important points as illustrated in Figure 4.9.

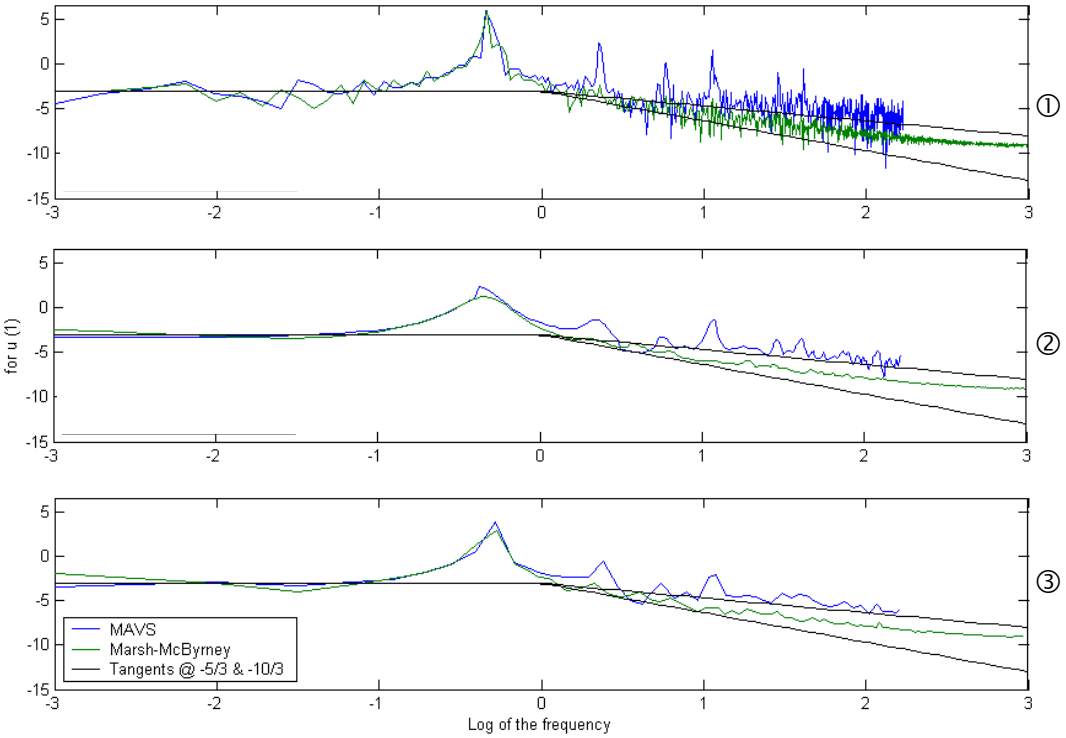

Figure 4.9: Difference between ① regular, ② smoothed and ③ box-car averaged spectra

This segmentation of the frequency domain into parcels is illustrated in Figure 4.10 and as it is represented in the zoomed box, the dashed line represents the original spectrum and the dotted one represents the average values obtained from application of the box car average.

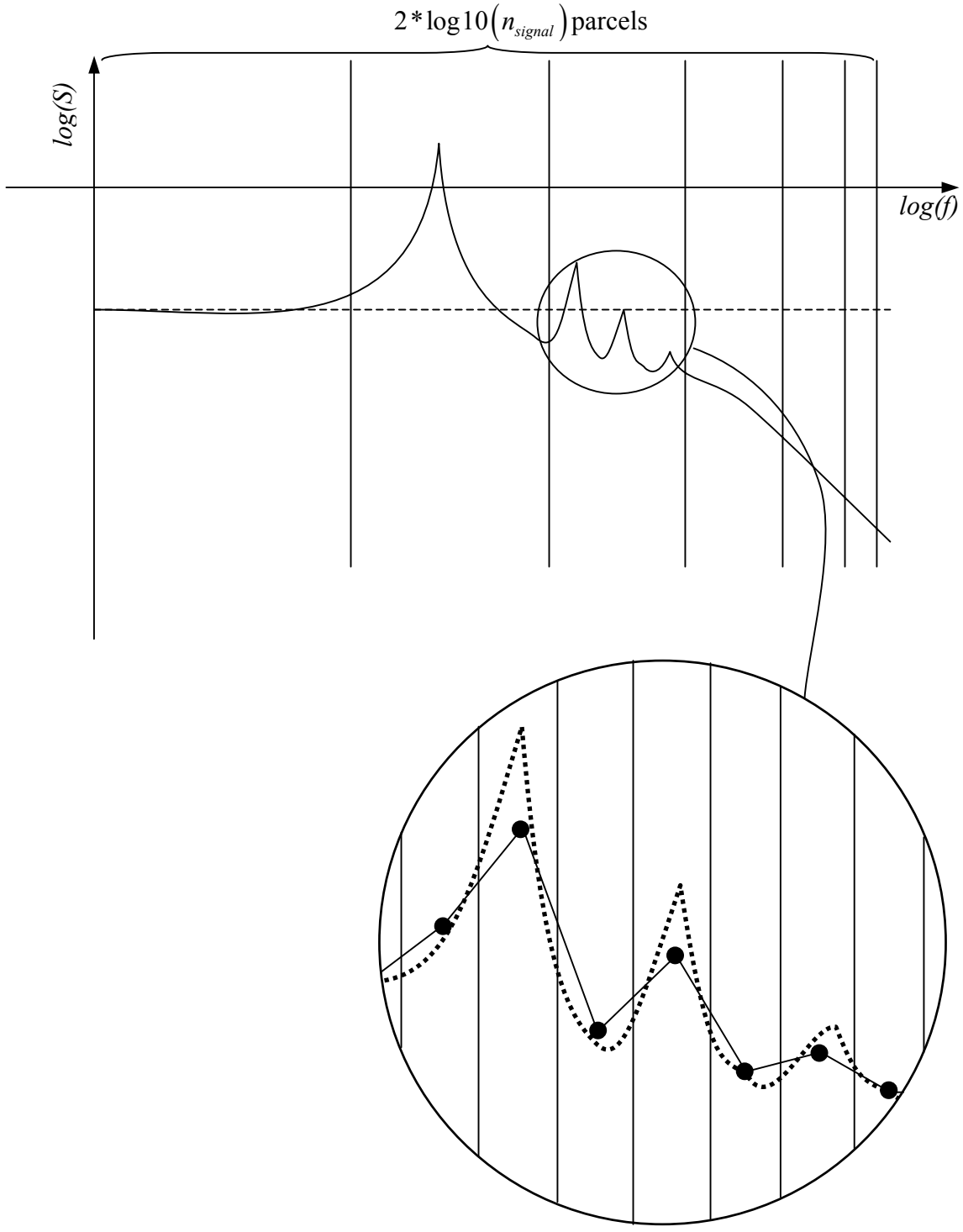

Figure 4.10: Spectral smoothing by frequency averaging

4.4 Calculation of Velocity from Measured Wave Elevation

For the wave tests, in addition to velocity measurements, the wave elevation above the current meter was measured. It is possible using wave theory to compute the velocity at any depth knowing the free surface wave elevation. Having the right phase information is very important in order to generate a correct velocity signal from the wave elevation signal in order to compare with the velocity measured by the MAVS and the Marsh-McByrney sensors. Several ways of extracting the phase to have the best representation of the signal were attempted, however we were confronted by several issues. In a first attempt, we extracted the phase directly from the linear wave elevation assuming that the amplitude was the envelope of the signal (Figure 4.11).

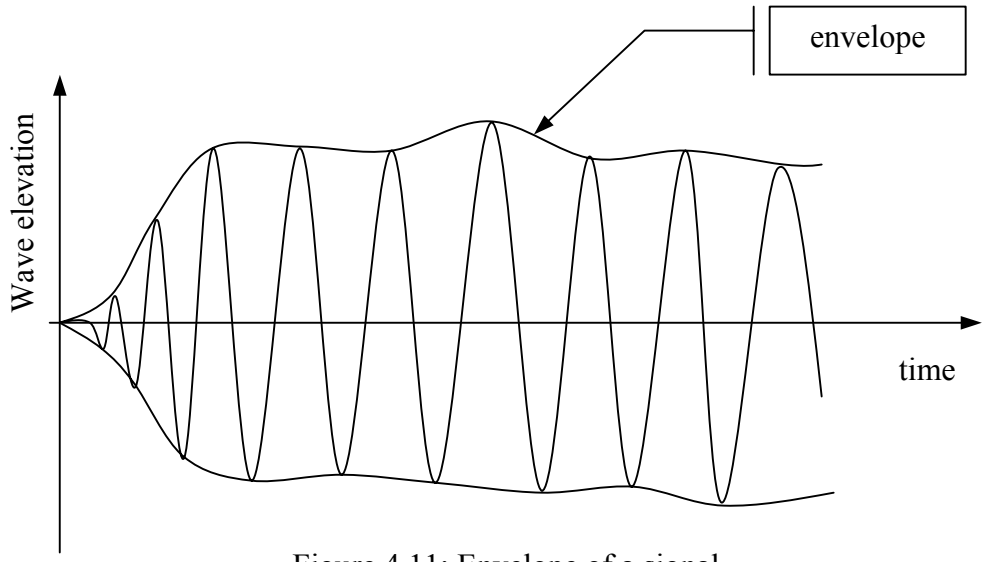

Figure 4.11: Envelope of a signal

The main advantage of such a method is that we can generate the wave elevation perfectly from our amplitude and phase for the whole signal. However, that phase estimate wasn't sufficiently accurate when using it to calculate the vertical velocity field. We therefore considered applying the same method but based on the nonlinear Stokes

theory. However, we could no longer have the assumption that the envelope of the signal is our amplitude as we don't have a simple relationship between the elevation and the amplitude. Indeed, the equation of the wave elevation based on the second-order Stokes theory is:

$$\eta(x;t) = A\cos(kx-\sigma t) + \frac{A^2 k}{4}\frac{\cosh(kh)}{\sinh^3(kh)}\left[2+\cosh(2kh)\right]\cos\left[2(kx-\sigma t)\right] \qquad (4.16)$$

We still can find the amplitude by solving this quadratic equation. But, we also have to notice that *kh* is not that much bigger than one. Indeed, for a wave period of 1.4s, we have a frequency of 45rad/s which give us a wave number of 2.05m^{-1}.As the maximum depth of the OTRC wave basin is 5.79m (19ft), we have *kh*=11.89, which is not so big. We shall therefore use the intermediate depth water formulas instead of the deep water ones. Then, when the quadratic equation is solved, we have the amplitude but the problem is that we based the calculation on the linear phase and now if we regenerate the signal, we will have a distorted trough. Using recurrence switching between the phase and amplitude can solve this problem but it will be very time consuming so we will use a different method.

The next approach is to use the Maximum Likelihood Method. As we are using several sensors in different locations, we can estimate the wave direction spreading with both Maximum Likelihood Method (MLM) and Maximum Entropy Method (MEM). These two methods have been improved into respectively the Extended Maximum Likelihood Method (EMLM) (Isobe et al. 1984) and the Extended Maximum Entropy Method (EMEM) (Hashimoto et al. 1994) in order to use several various properties. Although the EMEM can be more accurate, we adopted the EMLM because it is known to be less consuming in computations while still having good accuracy in the case of a uni-modal field. A uni-modal field is characterized by having each discrete frequency free waves spread around one main direction but the main directions of the free waves at different frequencies are usually different. An example of a multi-modal field is when

the waves are reflected like in a wave basin or on a coastline. Also, this method is known to give better results than the Longuet-Higgins method (1963).

However, the EMLM is used to derive a directional wave spectrum. For this experimental study, only uni-directional waves were generated. Nevertheless, we can still try to apply the Maximum Likelihood Method by Brillinger (1975) in order to find the phase lag of our signal. This method has some limitations that will be discussed later.

In the MLM, the wave elevation η_i at the discrete time t_i is described as the sum of a random noise e_i and the model terms $X_{ij}a_j$ according to the following equation:

$$\eta_i = X_{ij}a_j + e_i \tag{4.17}$$

This signal can be represented up to the third order as:

$$\eta_i - e_i = \sum_{m=1}^{3} A^{(m)} \cos\left(m\sigma t_i + \phi^{(m)}\right) \tag{4.18}$$

which can be expanded with the help of trigonometric formulas according to:

$$\begin{aligned}\eta_i - e_i &= A^{(1)}\cos\left(\phi^{(1)}\right)\cos\left(\sigma t_i\right) - A^{(1)}\sin\left(\phi^{(1)}\right)\sin\left(\sigma t_i\right)\\ &+A^{(2)}\cos\left(\phi^{(2)}\right)\cos\left(2\sigma t_i\right) - A^{(2)}\sin\left(\phi^{(2)}\right)\sin\left(2\sigma t_i\right)\\ &+A^{(3)}\cos\left(\phi^{(3)}\right)\cos\left(3\sigma t_i\right) - A^{(3)}\sin\left(\phi^{(3)}\right)\sin\left(3\sigma t_i\right)\\ &=\sum_{j=1}^{6} X_{ij}a_j\end{aligned} \tag{4.19}$$

with $a_j = A^{(n)}\cos\left[\phi^{(n)} + \left(1+\left(-1\right)^j\right)\frac{\pi}{4}\right]$ and n related to j by $\begin{cases} j = 2\left(n-1\right)+1 \\ j = 2n \end{cases}$, which means that while we have $n \in [\![1;3]\!]$, we have $j \in [\![1;6]\!]$ (Mercier and Niedzwecki, 1994).

This set of equations can be written in matrix form as:

$$\underline{Y} = \underline{\underline{X}}\underline{a} + \underline{e} \tag{4.20}$$

The coefficients may be estimated through the MLM by computing:

$$\underline{a} = \left(\underline{\underline{X}}^T \underline{\underline{X}}\right)^{-1} \underline{\underline{X}}^T \underline{Y} \tag{4.21}$$

Finally, the amplitude and phase can be given by again using trigonometric formulas:

$$\begin{cases} A^{(n)} = \sqrt{a_{2(n-1)+1}^2 + a_{2n}^2} & (4.22) \\ \phi^{(n)} = \tan^{-1}\left(-\dfrac{a_{2(n-1)+1}}{a_{2n}}\right) & (4.23) \end{cases}$$

The most important limitation of this method is to make sure that the input frequency σ is known accurately. If we use a zerocrossing or extrema method to find the period, we can have a slight error. In our example, we had a wave of period of 1.4s (Figure 4.12) while our method of identifying maxima of the sampled time series detected a period of 1.407s, which represents an error of 0.5% (Figure 4.13). However, when examining the result of regenerating the signal from the coefficients from the MLM, though the elevation from the linear or nonlinear theory using those coefficients appear similar in the two cases, the signal generated using the formula from the Maximum Likelihood method has an error up to 14% in this case.

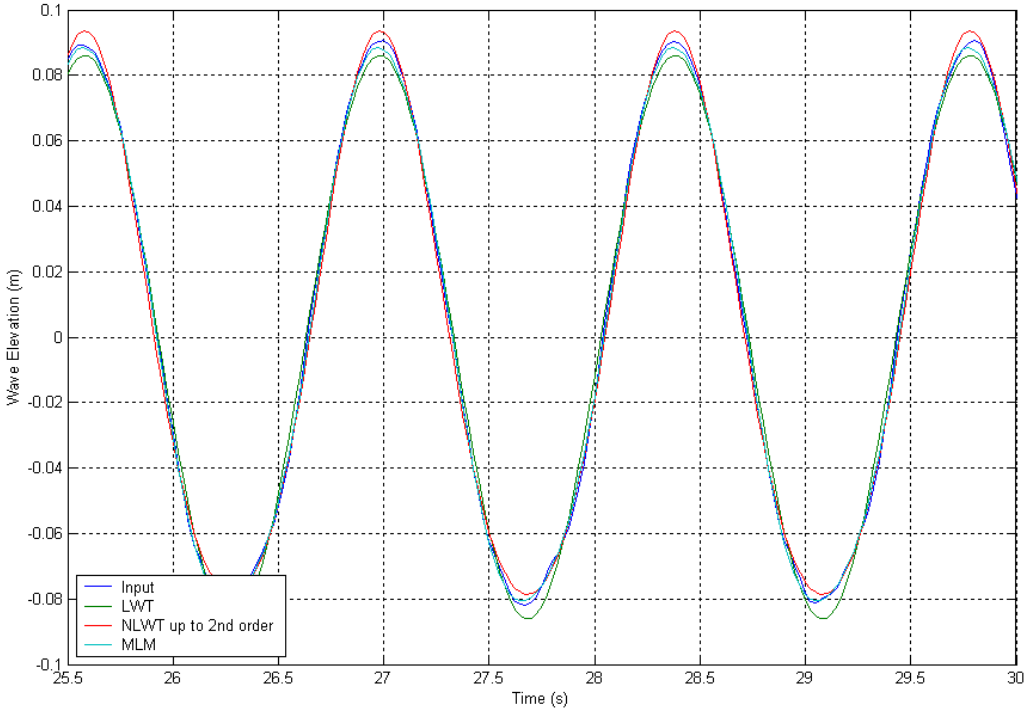

Figure 4.12: MLM with the correctly specified frequency

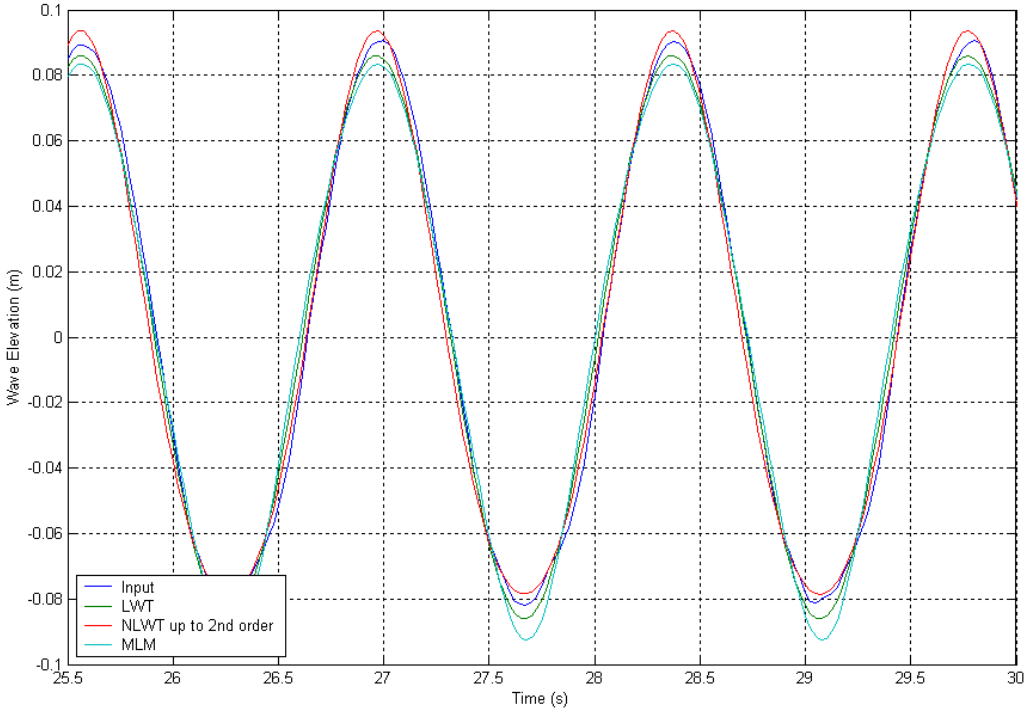

Figure 4.13: MLM with a specified frequency with 0.5% error

This is due to the fact that a small mistake in the input period makes the elevation from the MLM harder to fit to the real free surface wave elevation. As we can see in the Figure 4.14, if we set an input period at 1.5Hz, the signal from the MLM coefficients is completely wrong. In applying this method, it is therefore necessary to make sure that we log correctly the frequency of the wave. Fortunately, the frequency of the wave is known quite precisely since it is specified as an input in generating the drive signal for the wavemaker. This method can only work in the case of a narrow-band spectrum. In other cases, the EMLM should be used.

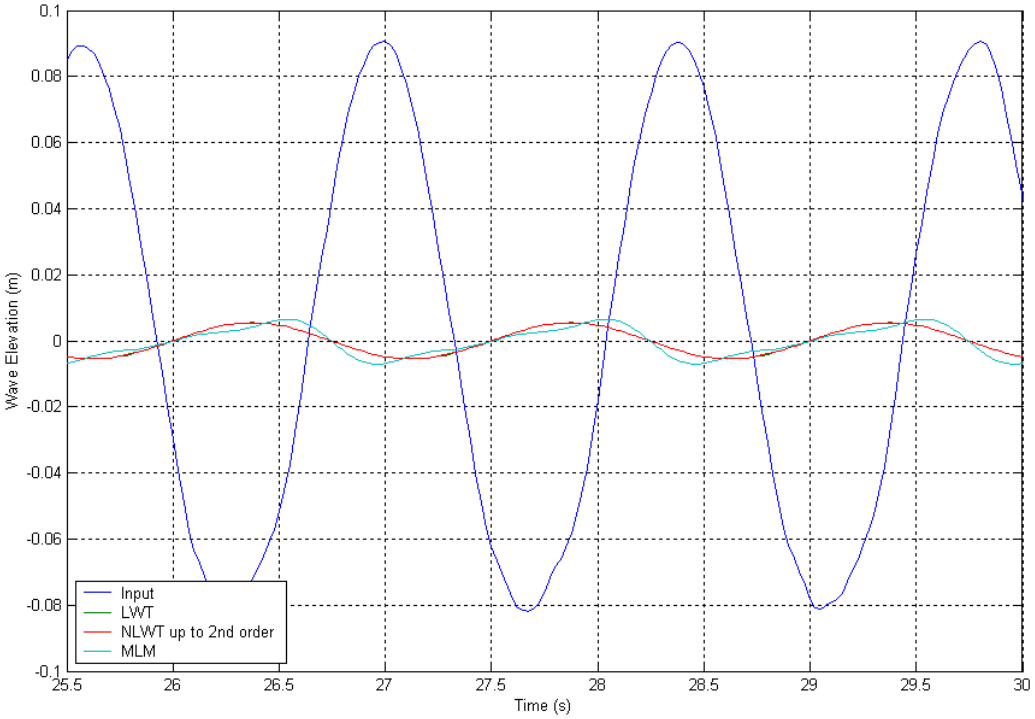

Figure 4.14: MLM with a specified frequency with 7% error

A final drawback of the maximum likelihood method is that the transient part of the signal cannot be generated. Indeed, we are only generating a third order wave, we don't generate a wave with a whole spectrum but only 3 frequencies corresponding to the main wave frequency and its two first harmonics (Figure 4.15).

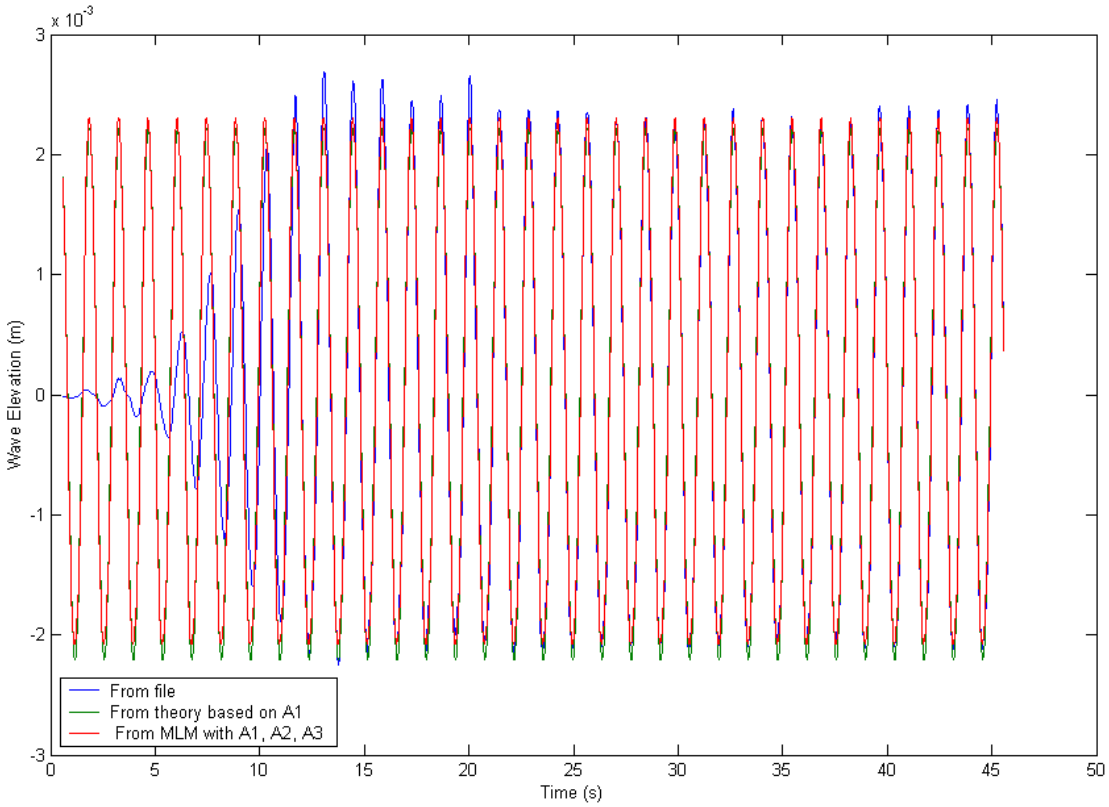

Figure 4.15: Generated signal from the MLM (no transient response)

5. RESULTS OF THE MAVS CALIBRATION TESTS

The previous sections being introductory sections of the analysis that was done, we are now looking at the results that will lead ultimately to a calibration procedure for the MAVS. In this section, we will examine the coherence of the sensor in the time and frequency domain. Then, an analysis will be done for every type of verification test: where are the peaks in the power spectrum, what are those peaks corresponding to, how is the sensor behaving depending on the array mounting, the sensor orientation, etc.

5.1 Resampling of the Time Series

In the first phase of the project (demo mode), the digital data was sampled and recorded internally by the MAVS sensor. However, in the second phase, the MAVS was re-configured with an analog output and data acquisition was performed by the NEFF. Whereas the internal data acquisition by the MAVS was found to have timing problems, the NEFF data acquisition provided a "perfect" sampling rate of 40Hz. Also, we have to notice that in the first phase, we only have a current measurement precision up to 1mm/s while the other phases have a precision of 5 digits.

At first sight, the time signal recorded by the MAVS in the demo mode looked quite coherent. The sampling frequency was set at 20Hz and the sampling interval appeared to be 0.05s. However, upon further examination, it was determined that the mean Δt was not quite right but always greater than expected (0.0537s). Knowing that, we wanted to resample our time series as it may induce errors in the later computations or at least check if resampling was needed or even possible.

Figure 5.1 illustrates the principle of aliasing. As the sensor is taking samples at a given frequency, the acquired discrete signal is not the real signal but only a close

representation. Thus, except if the frequency of sampling is very high, the measurement will never be a perfect representation of the actual signal.

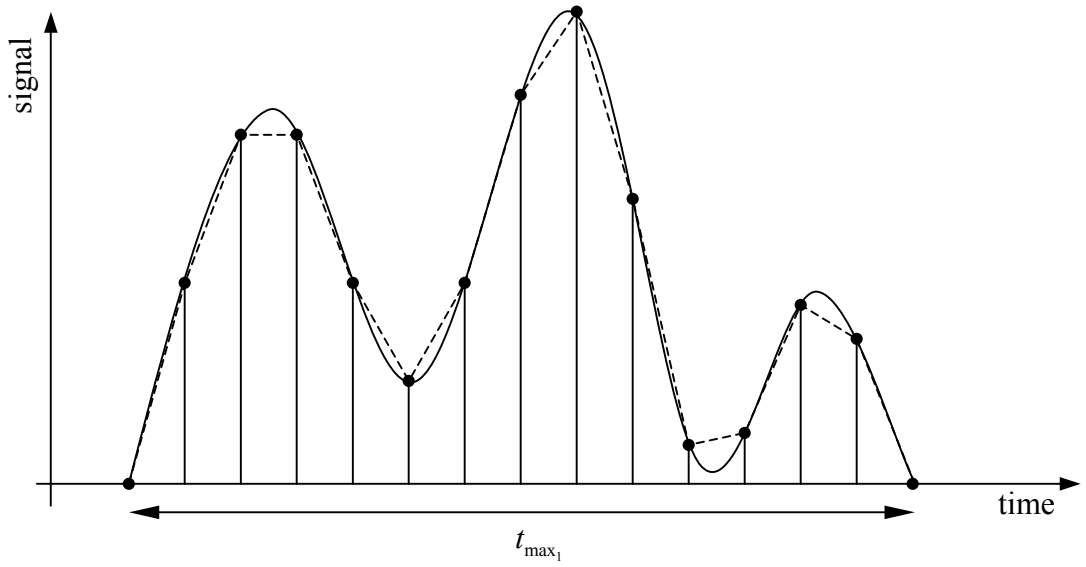

Figure 5.1: Aliasing

The resampling of the MAVS velocity time series can be based on many assumptions as to the nature of the problem. The first one is that the internal clock of the sensor may be wrong and so we have the wrong time logged but the sensor is nevertheless sampling at the right frequency. In that case, we can assume that we have the right sample rate of 20Hz which is equivalent to a Δt of 0.05s (instead of 0.0537s) that will lead us to a smaller t_{max} record length as illustrated in Figure 5.2.

Another method is to consider that we still have the correct sample rate of 20Hz but the sensor may have skipped a few points. In this case, we have to regenerate the signal based on the existing one by using a spline or a polynomial chip. However, due to the sampling error inherent to every measurement, the resampled signal can be very

different from the original one especially in the case of a noisy signal. This case is illustrated in Figure 5.3.

The last method is to make the samples fit to the right time base. Indeed, as we have seen before, our Δt is an average over the whole signal and at every time step, we can have a higher or smaller Δt. However, this will require the theoretical sample and the actual sample to be not too far away in time. To verify this, we plotted the difference of time between the resampled time and the real time. As shown in Figure 5.4, we don't have a regular time difference that varies around zero as we were expecting but we have a time difference that increases during the early part of the record and then decreases in the later part of the record (Figure 5.4), leading to an important error. It basically means that at the beginning of the record, the sensor takes samples slower and slower compared to what should be expected and then accelerates the sampling rate at the end of the record.

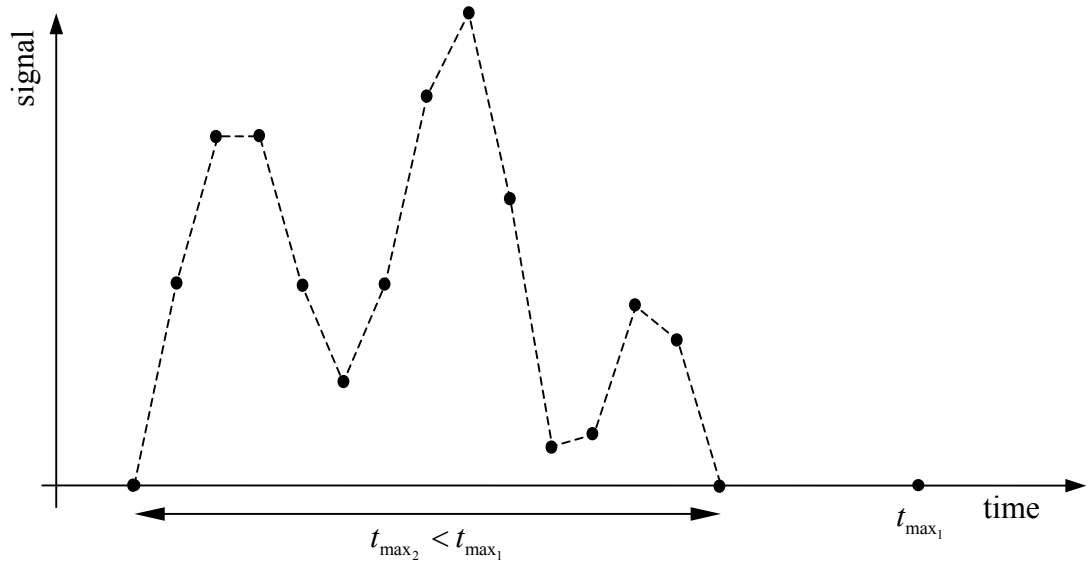

Figure 5.2: Resampling $t_{max_2} < t_{max_1}$

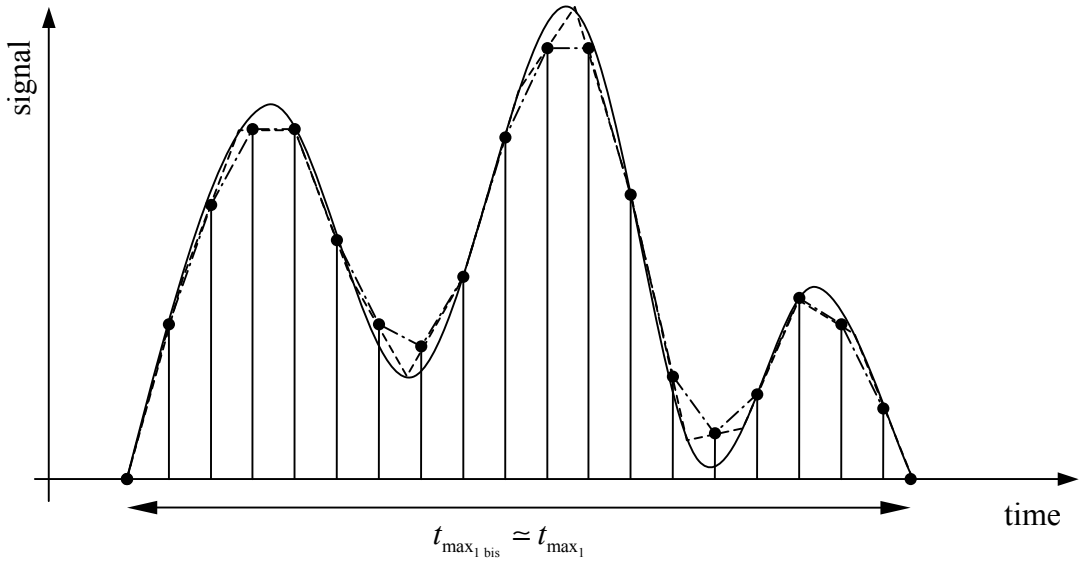

Figure 5.3: Resampling after aliasing

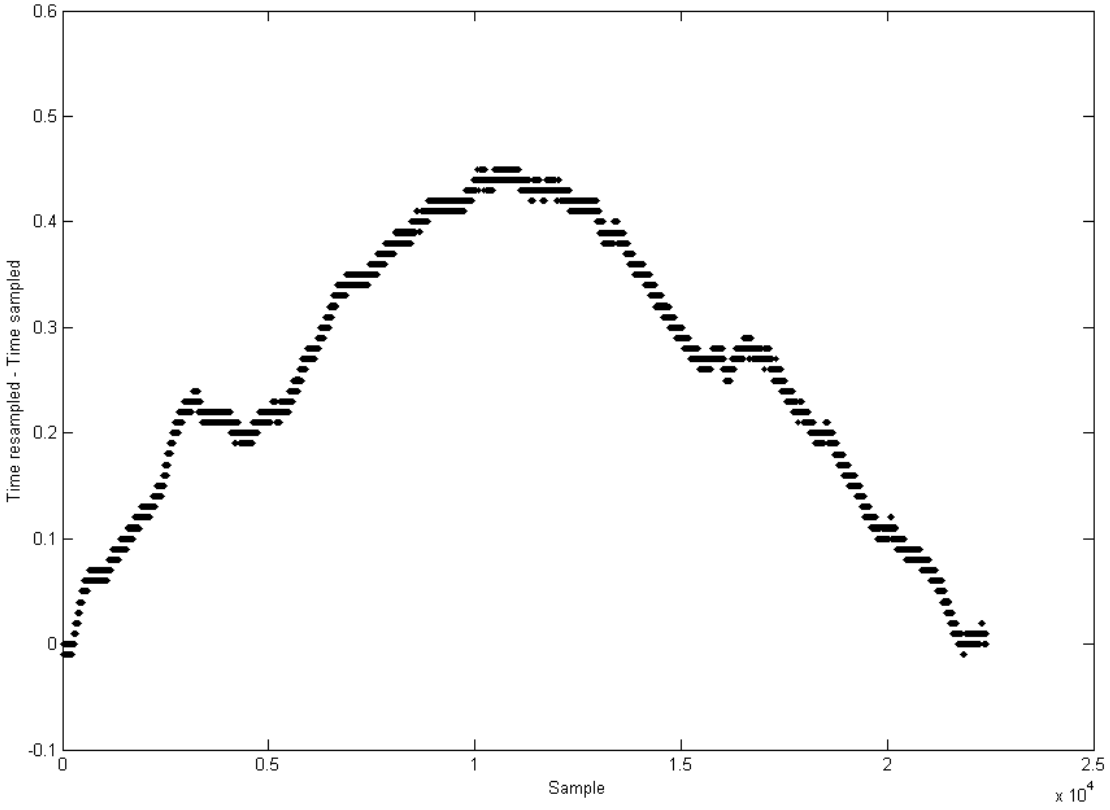

Figure 5.4: Accumulation of the sampling error along the test in Phase I

Finally, some tests were made with the new MAVS units simultaneously recording a digital time series internally sampled at 20Hz and outputting the analog signal to the NEFF, where it was sampled at 40Hz. Unfortunately, the time stamps for the internally recorded time series were not logged. Therefore, we aligned the signals at the beginning and at the end of the time series. This lead us to Figure 5.5 where we can see that generally speaking, the sampling frequency in the analog mode (40Hz) is twice the one in the demo mode (20Hz). However, if we examine a longer time window between 2 and 24 seconds, we find that 881 samples were done in the analog signal whereas only 384 were taken in the internally recorded signal. We therefore have an average sampling frequency of 17.46Hz in the internal record. This study clearly shows us that the sensor's internal data logging is unable to keep up at the 20Hz sampling frequency setting but is still able to record the signal right, which is why the third resampling method should be used.

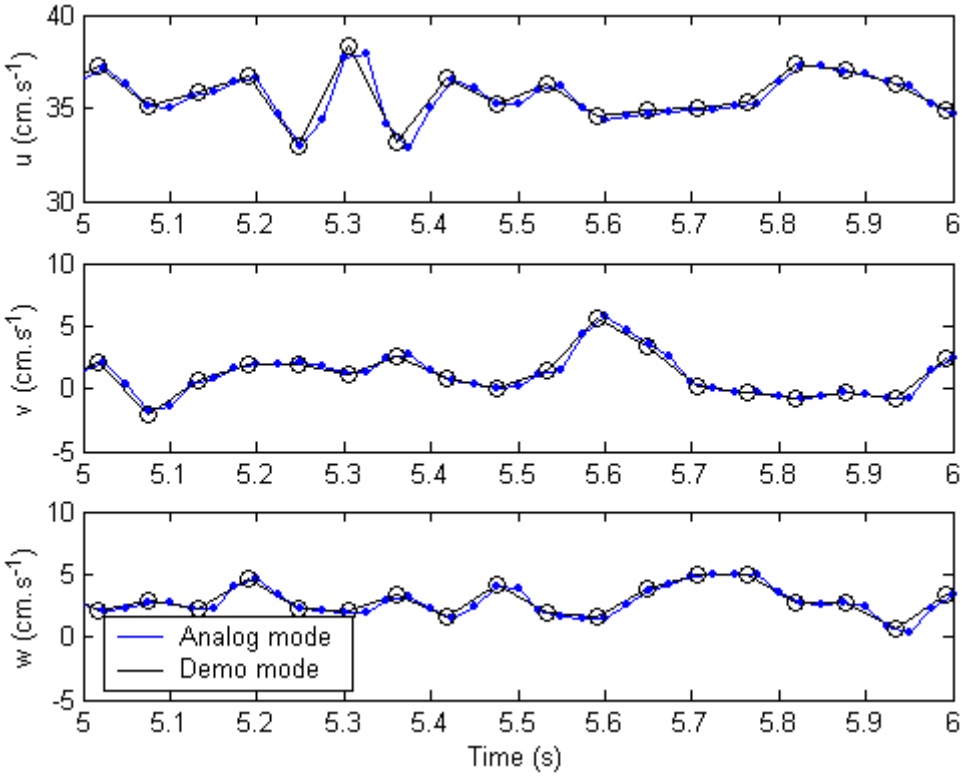

Figure 5.5: Comparison between analog and demo mode for a time series in a tow test

5.2 Coherence of the Sensor in the Frequency Domain

The first phase of the study provided interesting results regarding the sensitivity of the MAVS to the orientation relative to the current. For example, at 100% current (one pump operating at full capacity) Figure 5.6 shows that the turbulent velocity spectra are quite similar regardless of the orientation of the MAVS.

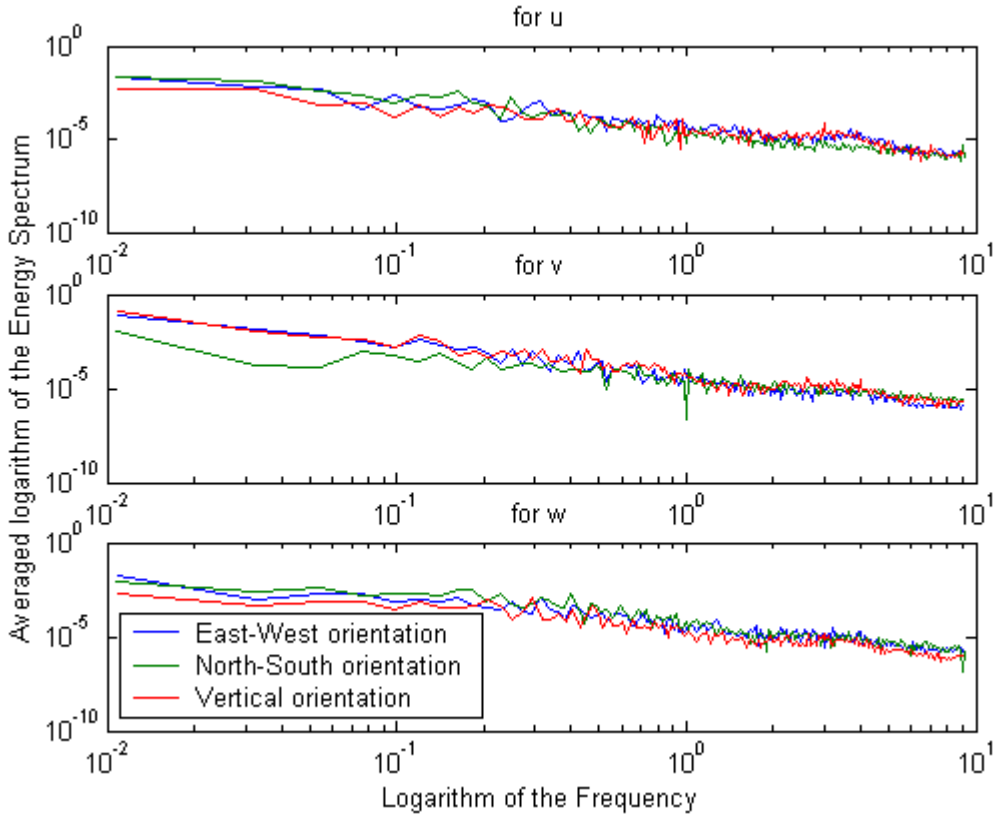

Figure 5.6: Power spectrum for the 3 sensor orientations in the 3 directions

It is also interesting to note that when we are smoothing the energy spectrum (according to the procedure described in Section 4.3), as we are taking more points with the frequency increasing, the difference tends to zero (compare Figures 5.7 and 5.8). Evidently, the orientation of the MAVS does not affect the measurement of the high frequency turbulence, although there may be some sensitivity to orientation in the measurement of the low frequency turbulence.

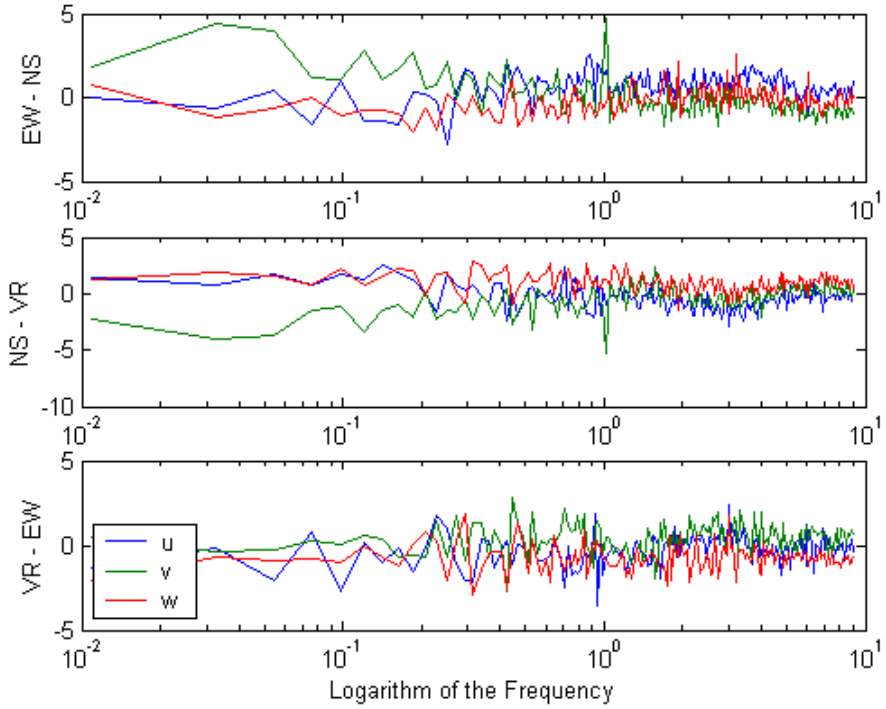

Figure 5.7: Difference for the spectrum under 3 different orientations

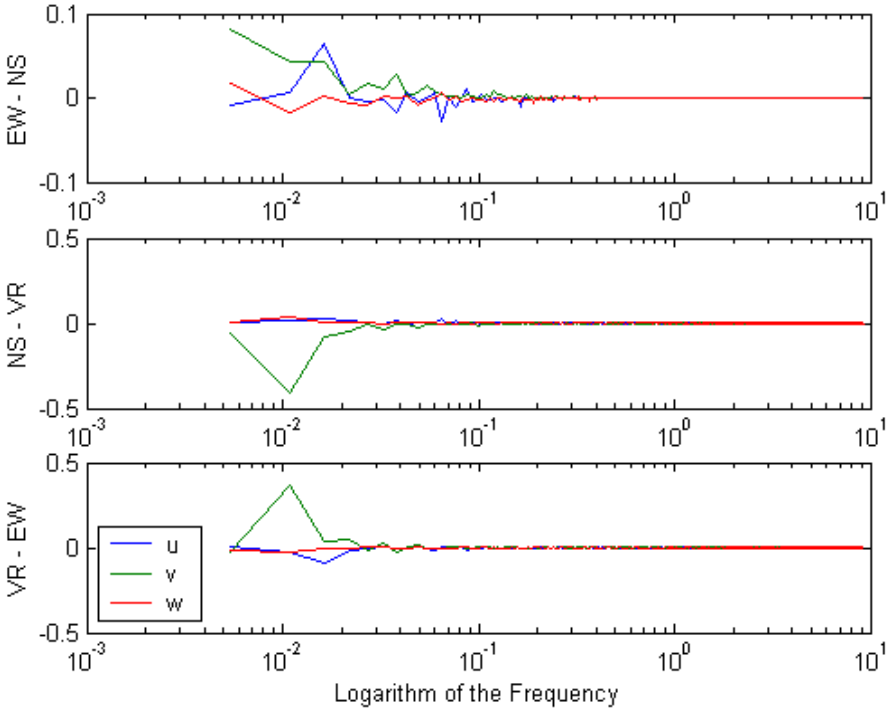

Figure 5.8: Difference for the averaged spectrum under 3 different orientations

5.3 Calm Tests

Calm tests are used to record the response of the sensors in "calm water", primarily to identify any zero offset bias. For example, in a regular wave test, the mean of the wave elevation as recorded in a wave probe should be zero. A mean value recorded in a calm test may be removed from subsequent test records to achieve the desired zero average.

In calm water, both MAVS and Marsh-McByrney sensors have a pretty much constant mean but MAVS is more "stable" in the sense that the velocity measurements vary by ± 0.3 cm/s. On the other hand, the Marsh-McByrney has larger calm water variations of about ± 1 cm/s.

5.3.1 First Phase

As we have seen before, the first phase tests are useful for comparing the MAVS and the Marsh-McByrney sensors. However, we cannot put too much confidence in the MAVS results as the demo model was found to have a sampling problem as discussed in Section 5.1. Nevertheless, examining the spectra from a calm test (Figure 5.9), we can see that the Marsh-McByrney sensor behaves like it is in a turbulent environment while the MAVS shows the same level of energy for all the frequencies. We believe the high frequency roll-off in the spectrum for the Marsh-McByrney sensor is due to a loss of high frequency response sensitivity.

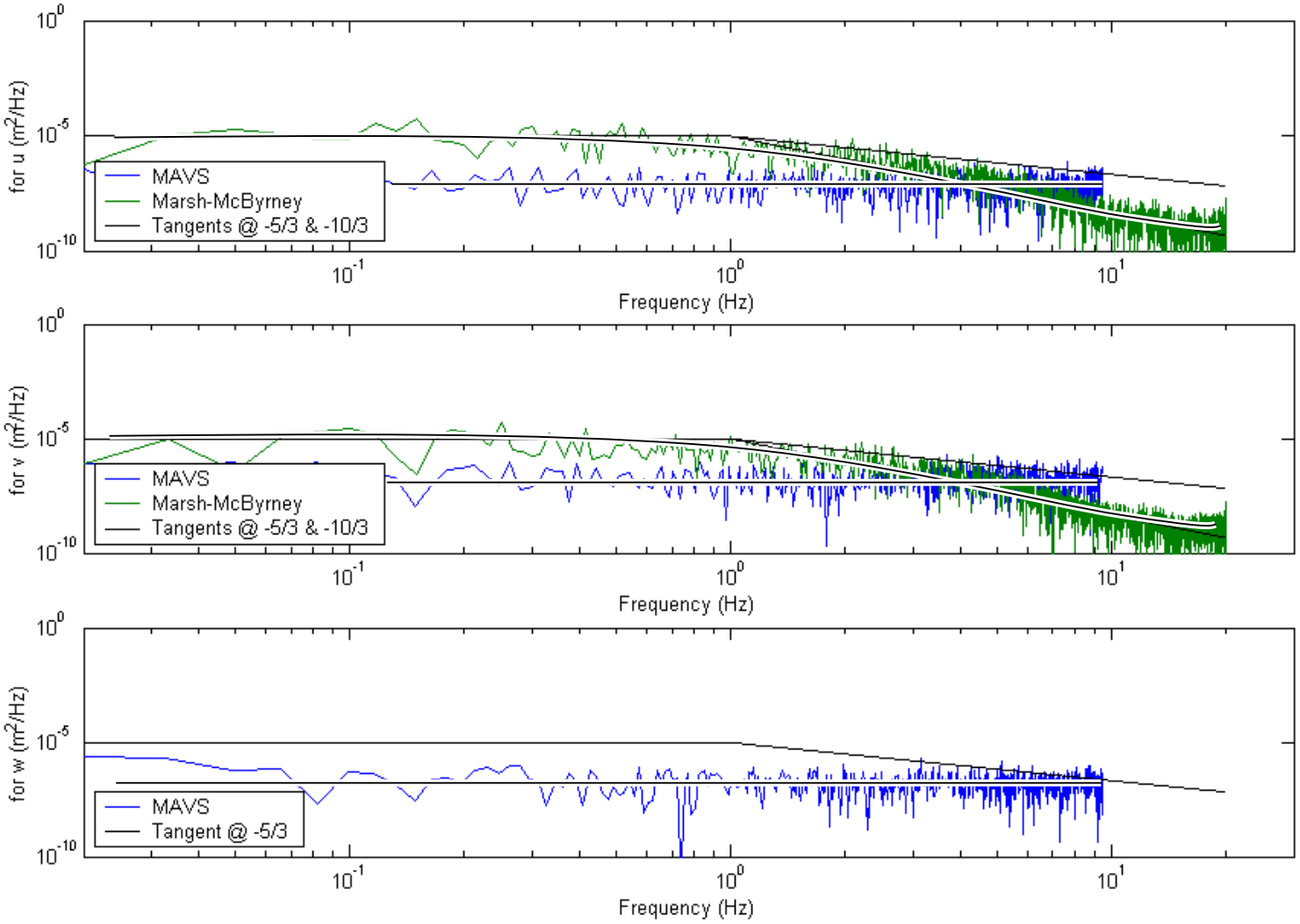

Figure 5.9: Power spectrum of a calm test in Phase I

5.3.2 Other Phases

In the subsequent test phases, nine MAVS sensors were deployed, each configured to output analog signals. Each sensor was zeroed by placing it in a water bucket and performing a calm test, as recommended by the manufacturer. Calm tests were also performed with the sensors deployed in the wave basin. Figure 5.10 compares the mean velocity recorded by each sensor for all the calm tests. Although all of the nine sensors generally behaved the same way, it was noted before Test #15 that air bubbles tended to collect on the transducer heads, leading to important variations in the velocity measured. Following Test #15, efforts were made to flush away the air bubbles prior to each test. Note that sensor #8 cable was bad and therefore omitted thorough Phase II but was replaced in Phase III.

If we examine the spectrum for the *u*-velocity of a calm test (Figure 5.11), we can see that we have much less energy than before (compare with top window in Figure 5.9). This is presumably due to the sampling error for the MAVS noted in the first phase, which appeared as spurious energy across all the frequencies.

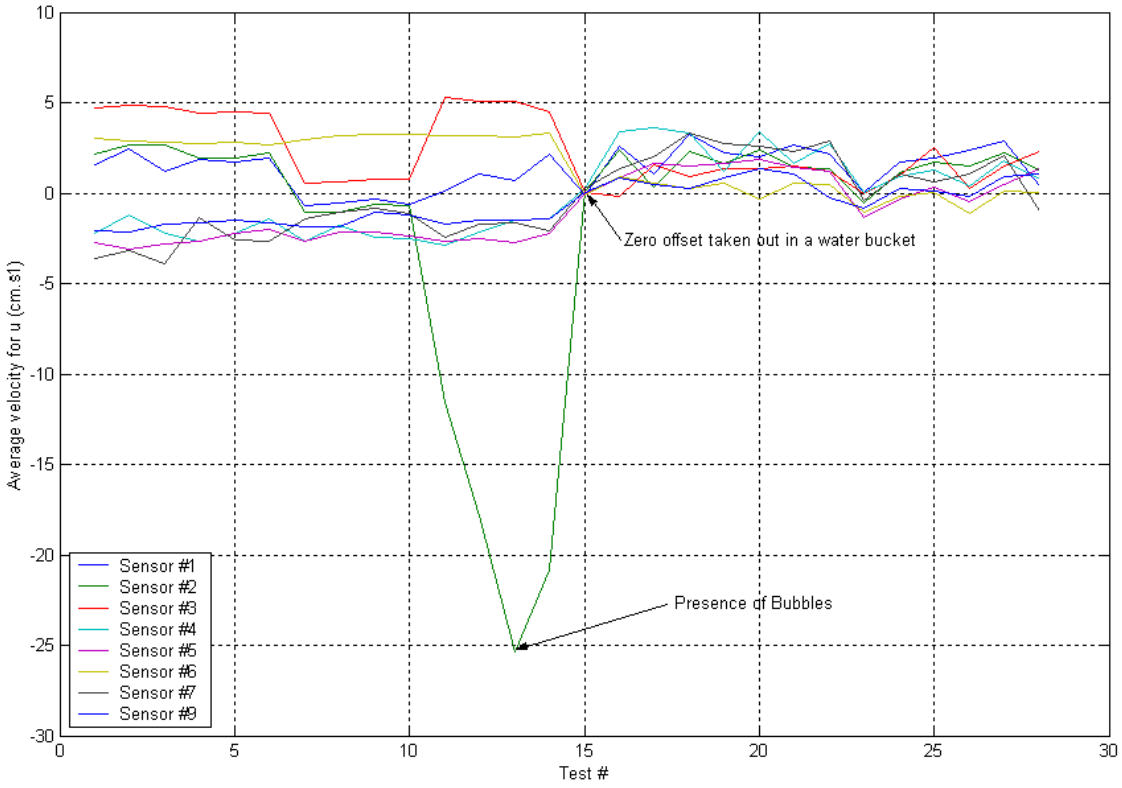

Figure 5.10: Average velocity for the calm tests in Phase II

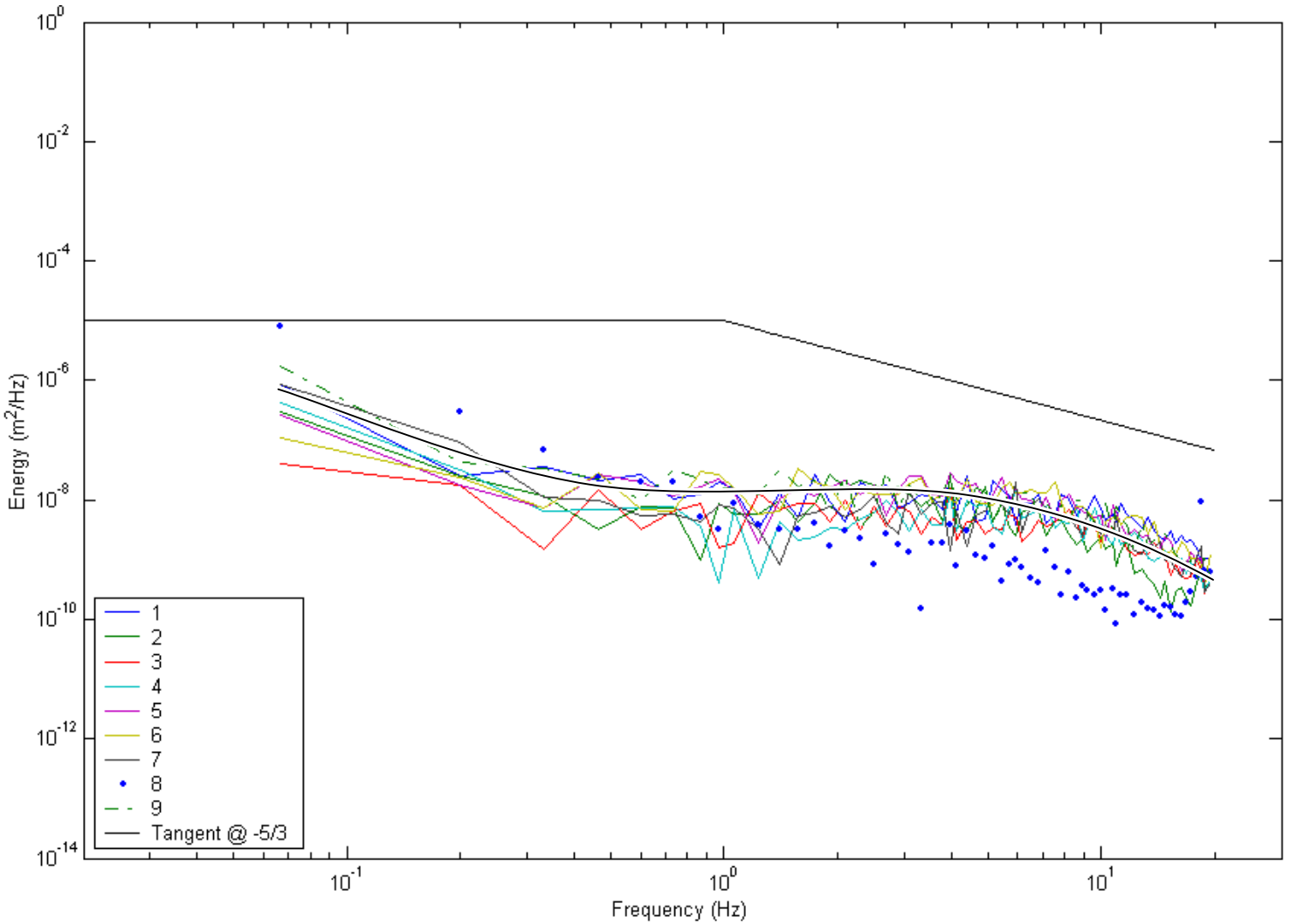

Figure 5.11: Power spectrum for *u* for a calm test in Phase II

5.4 Tow Tests

It is of interest to check the behavior of the current meters in a tow test situation where the sensor is towed at a known constant speed in calm water and experiences a non-turbulent relative flow. The purpose of these tests is to verify the measurement of the mean speed, identify the peaks in response associated with vortex shedding from the transducer rings, identify the peaks in response associated with bridge vibrations and verify the high frequency roll-off.

In the case of the MAVS, there is a possibility of wake flow from the transducer rings and support rod contaminating the measurement. There is also a possibility of flow blockage by the sensor contaminating the measurement. Finally, there is a possibility that dynamic forces associated with vortex shedding from the sensor will cause resonant vibrations of the mounting assembly, which will show up as speed variations.

Some frequency peaks in the MAVS spectrum may be induced by the wake flow from the transducer rings entering the measurement volume (Figure 5.12). We recall that the Strouhal number is

$$S_t = \frac{fD}{U} \tag{5.1}$$

with f being the frequency of vortex shedding, U being the flow velocity and D being the body dimension (diameter of a transducer mounting ring in our case).

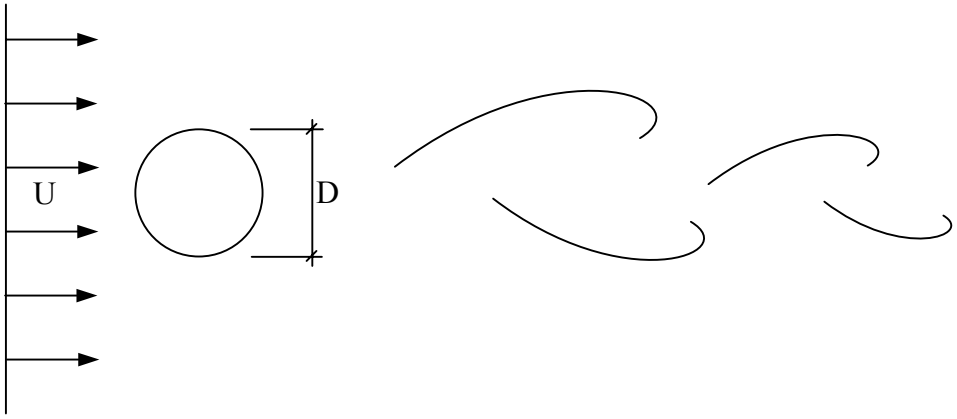

5.12: Vortex shedding

Previous studies have shown that in a case of a circular cylinder, the Strouhal cylinder is $S_t \simeq 0.2$ while in the case of a rectangular cylinder, $S_t \simeq 0.13$. Thus, in our case with a range of tow speeds from 15cm/s to 60cm/s and a cylinder diameter of approximately 1cm, the frequency of vortex shedding is:

$$f = \frac{S_t U}{D} \Rightarrow \frac{0.2*15\times10^{-2}}{1\times10^{-2}} \le f \le \frac{0.2*60\times10^{-2}}{1\times10^{-2}} \Rightarrow f \in [\![3;12]\!]\text{Hz} \qquad (5.2)$$

Since for the 40Hz sampling rate used in this study, the Nyquist frequency is 20Hz, in order to have the vortex shedding captured by the sensor, we need a speed of $U = \frac{fD}{S_t} = \frac{20\text{Hz}*1\text{cm}}{0.2} \le 100\text{cm.s}^{-1}$. Thus, all of our measurements will have vortex shedding captured by the MAVS. However, a precise study of the Strouhal number will be done using the Phase II results as the diameter of the ring is not precisely 1cm and the rings themselves are not circular cylinders.

The towing carriage at the OTRC basin is equipped with a variable frequency drive motor. Table 5.1 provides the approximate carriage speed for various frequency settings. The more precise speed at each test setting was determined with a stopwatch measurement knowing the distance traveled. Also indicated in Table 5.1 is the expected vortex shedding frequency from the MAVS transducer mount, assuming a Strouhal number of $S_t = 0.18$ and a diameter D = 1cm.

Table 5.1: Tow carriage motor drive frequency vs. tow speed

Drive Frequency (Hz)	Tow Speed (cm/s)	Vortex shedding frequency (Hz)
15	≃ 15	2.7
20	≃ 20	3.6
30	≃ 30	5.4
45	≃ 45	8.1
60	≃ 60	10.8

5.4.1 First Phase

If as before we examine the time series (Figure 5.13), we clearly see again that the Marsh-McByrney sensor is varying significantly in time and exhibits maxima of about 50cm/s, which is very important and should not be taken into account. Generally speaking, we can see in the other tests that the Marsh-McByrney sensor often has some fast variations in the time series even if it keeps a pretty accurate average. On the other hand, the signal from the MAVS is much more stable and just has some small variations that we can attribute to regular noise or just to a lack of sensitivity of the sensor.

Figure 5.14 shows typical velocity spectra for *u*, *v* and *w*. Several peaks are noticeable and have been indicated in the figure. Moreover, Table 5.2 shows that the MAVS sensor is indicating on almost every spectrum for the Vertical and North-South orientations under 45cm/s tow speed a vibration at 4Hz that may be attributed to the vibration caused by the bridge. It is strange that the Marsh-McByrney sensor can't capture what we attribute to bridge vibration in some configurations where MAVS can and vice versa. Generally speaking, we have both sensors indicating different peak response frequencies and they are often not consistent during the same tests. One of the causes of this effect is the geometries of the Marsh-McByrney and MAVS sensors. Only the MAVS will have peaks related to vortex shedding. If such peaks exist for the MAVS, the corresponding frequencies can be found in Table 5.1. However, as it is summarized in Table 5.2, we can't see any peaks corresponding to the vortex shedding in Phase I or these peaks are not significant.

For example, from Table 5.2, we see in the test at 15cm/s in the East-West orientation that both sensors indicate vibrations at 4Hz and that peak responses at 7Hz and 12Hz are indicated by the Marsh-McByrney only. Also, we notice that at the same tow speed, the MAVS results are completely different depending on the orientation. Indeed, we can't just rotate the results and find the same behavior. On the other hand, we find some identical features for the same orientation but at different tow speed (which is true for both sensors). That leads us to recognize the importance of the orientation of the sensor relative to the mean flow direction. To have an idea of the difference of behavior of both sensors, we summarized the frequencies of the peak responses in Table 5.2.

Table 5.2: Frequency of spectral peaks for the tow tests in Phase I

Signal			15cm/s	20cm/s	30cm/s	15cm/s
Vertical orient.	MAVS	*u*	5Hz	5Hz	5Hz	
		v		Small 4Hz		
		w		Small 4Hz		
	MMB	*u*		9 & 12Hz	12Hz	10Hz
		v		9 & 12Hz	12Hz	10Hz
North-South orient.	MAVS	*u*	Small 4Hz	3Hz	3Hz	Small 8Hz
		v	Small 4Hz	Start at 9Hz	4Hz	
		w	4 & 6Hz	6Hz	4 & 6Hz	
	MMB	*u*		12Hz	11Hz	Small 12Hz
		v		12Hz	11Hz	Small 12Hz
East-West orient.	MAVS	*u*	4 & 12Hz	8 Hz	9Hz & small at 4&5Hz	Small at 6&9Hz
		v	4 & 7Hz	6Hz		
		w	4Hz			
	MMB	*u*	4Hz	5 & 9Hz	11Hz	9Hz
		v	4Hz	5 & 9Hz	11Hz	9Hz

Table 5.3: Comparison of the average speed for the tow tests in Phase I

Sensor	Orientation	Speed	Avg. speed for u		Avg. speed for *v*	Avg. Speed for *w*
			speed	error		
MAVS	Vertical	15cm/s	13.57	-10.5 %	-0.07	0.9
MMB			15.24	1.6 %	-7.17	
MAVS	East-West		13.15	-14 %	-0.85	0.39
MMB			16.17	7.3 %	0.56	
MAVS	North-South		11.36	-32 %	-0.21	0.11
MMB			17	11.7 %	-0.7	
MAVS	Vertical	20cm/s	17.8	-12.4 %	0.26	1.11
MMB			21.25	5.9 %	-0.28	
MAVS	East-West		18.07	-10.7 %	-0.78	0.58
MMB			20.873	4.2 %	0.04	
MAVS	North-South		15.25	-31.2 %	-0.22	0.02
MMB			20.88	4.2 %	0.4	
MAVS	Vertical	30cm/s	27.65	-8.5 %	0.4	1.18
MMB			31.96	6.1 %	9.86	
MAVS	East-West		27.52	-9 %	-0.78	0.86
MMB			31.02	3.3 %	-0.9	
MAVS	North-South		23.8	-26.1 %	-0.49	0.5
MMB			30.77	2.5 %	-0.29	
MAVS	Vertical	45cm/s	41.81	-7.6 %	0.54	1.46
MMB			44.57	-1 %	-0.58	
MAVS	East-West		41.31	-8.9 %	-1.25	0.66
MMB			45.12	0.3 %	-0.22	
MAVS	North-South		36.98	-21.7 %	-0.68	0.87
MMB			46.31	2.8 %	-0.32	

Table 5.4: Code of the colors

: Over estimates
: Under estimates
: Over estimates of over 10% or 1cm/s
: Under estimates of over 10% or 1cm/s

We also can compare the average speed measured by the current meters with the mean tow speed of the bridge. The results are summarized in Table 5.3 with an explanation of the colors in Table 5.4. As we can see, in the North-South orientation the MAVS measurement error for the mean velocity is 25% on average while for the other two orientations, the mean velocity error is about 9%. These rather large measurement errors are probably due to flow blockage from the housing of the sensor.

As we can also see in Table 5.3, the Marsh-McByrney sensor has some high mean velocities. This is mostly due to the fact that the Marsh-McByrney sensor has some fast variations in the time series as illustrated in the v signal in Figure 5.13.

In examining the spectrum (Figure 5.14), we can't see any general behavior except that the Marsh-McByrney sensor has a –10/3 slope high frequency roll-off while the MAVS is generally constant up to the Nyquist frequency. This indicates that the high frequency response of the MAVS is superior to the Marsh-McByrney.

Note that in all cases, the mean value was removed prior to computing the spectrum.

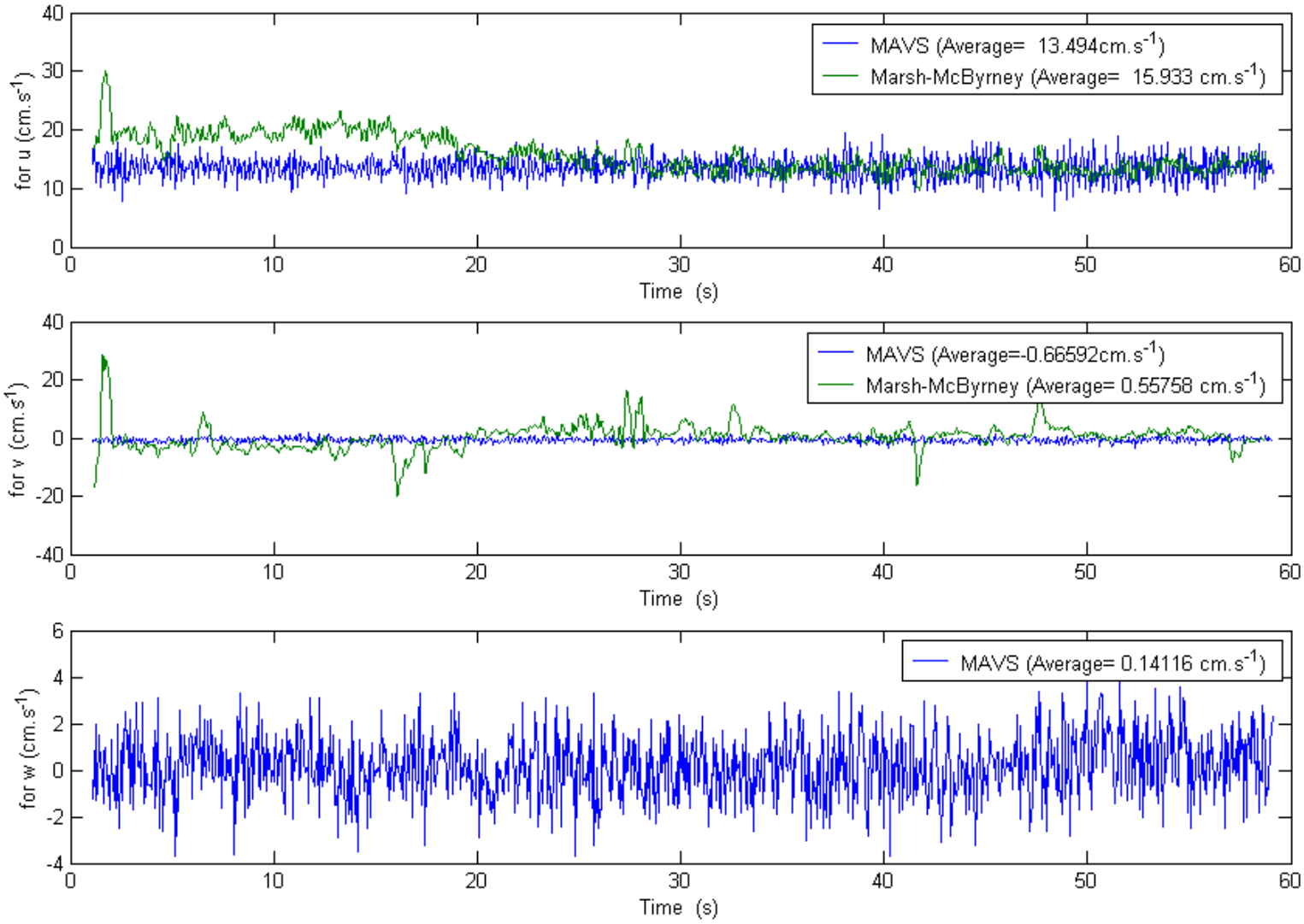

Figure 5.13: Time series for a tow test at 15cm/s under an East-West orientation in Phase I

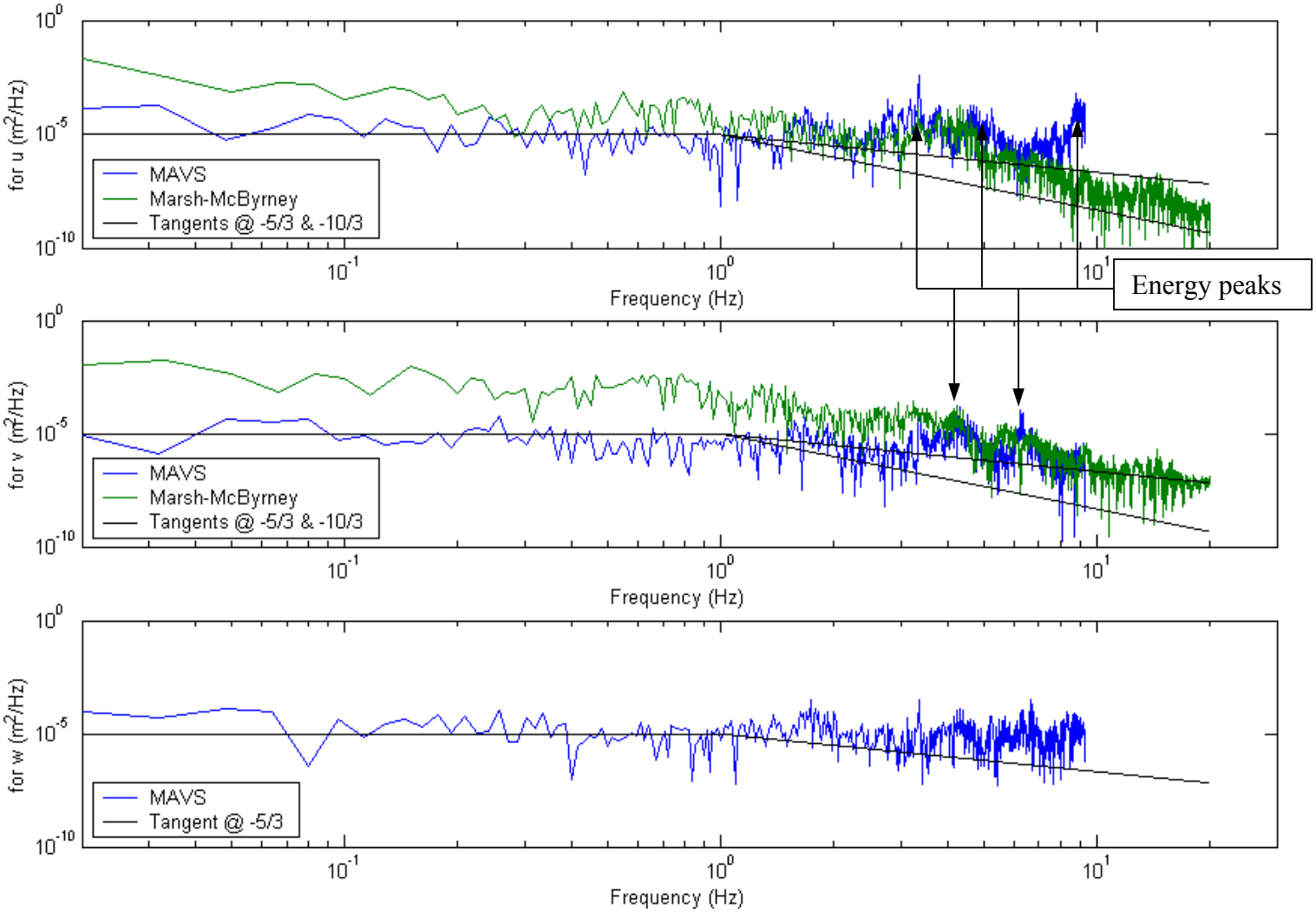

Figure 5.14: Power spectrum for a tow test at 15cm/s under an East-West orientation in Phase I

5.4.2 Other Phases

We saw in the first set of calm tests (Figure 5.10) what the consequences of air bubbles on the transducer heads are. Figure 5.15 shows a regular time series of a tow test while Figure 5.16 shows the effect of air bubbles where we have shifts in the velocity of about 100cm/s. After the bubbles have been flushed away, we can have good measurements but still the zero offset error is important for every sensor, as was already shown by the study of the calm tests. We will simply take out the zero offset from the calm tests from the average of the tow test to be more accurate.

In the tests from Phase II and later, there weren't many tests done under different orientations. For example, the East-West orientation was only used for three sensors in only one of the six sets of tests with the North-South orientation. Also, the Vertical orientation was only tested in the third phase.

When we average all the results (without including the tests with an East-West orientation and without the tests with the bubbles), we see that the accuracy of the mean velocity measurement is not generally dependent on the speed (Figures 5.17 to 5.20 for a North-South orientation). Also, it appears that the faster the tow speed is, the less the standard deviation of the mean velocity error (Figure 5.18).

Also, we can see an important feature that we can attribute to blockage from the array mount (Figures 5.21 to 5.24). The tests corresponding to Figures 5.21 and 5.22 were executed with a 3*3 array. Referring to Figure 3.8 for the numbering of the sensors in the array, we have to compare the error of sensors 1, 4 and 7 or sensors 2 and 5 or sensors 3, 6 and 9 (that is, compare sensors mounted at the same depth). Figures 5.23 and 5.24 show a similar behavior for the horizontal array. As we can see, we have the same profile of the error for different tow speed. However, we can see now that the standard deviation is higher in the case of an East-West orientation or higher tow speeds.

In Figures 5.25 and 5.26, contrarily to the other figures where the results were averaged for all the tests and showed per sensor, the results are shown for sensor #1 only and illustrated per test. All the tests were effectuated with sensors in the North-South orientation. Only the test #6 will have a rotation of the sensors 1 to 3 from North-South to East-West, this is giving us a better accuracy. Figures 5.27 to 5.29 on the other hand show the linear behavior of the measured velocity as a function of tow speed (the actual velocity) and validate the idea of the use of correction factors to correct the measured mean flow velocity for blockage effects.

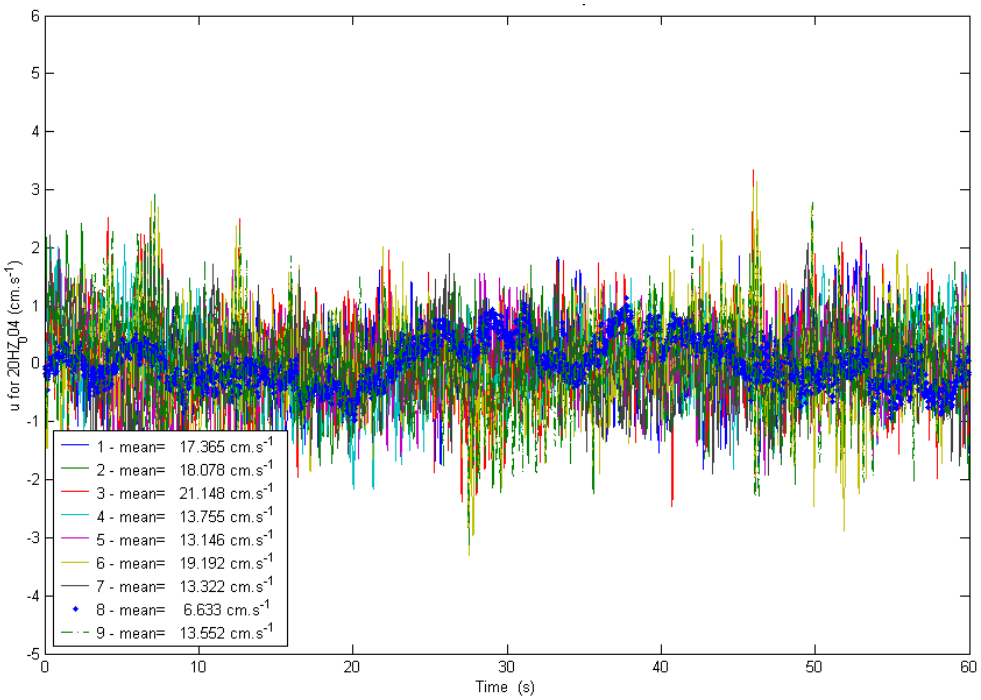

Figure 5.15: Time series for a tow test in Phase II

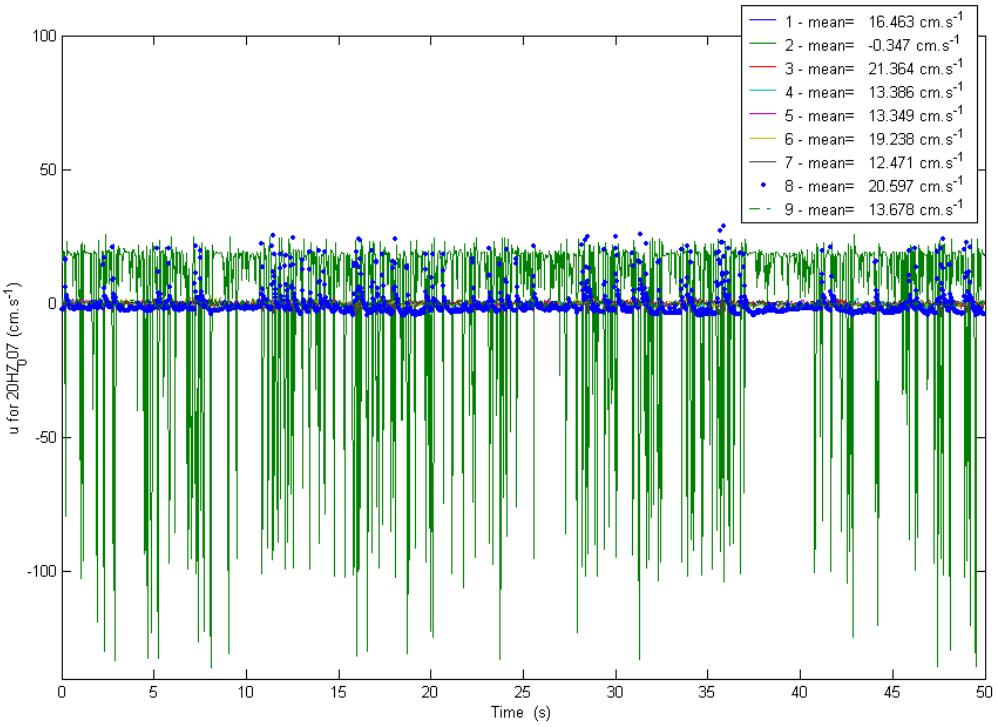

Figure 5.16: Time series for a tow test with air bubbles in Phase II

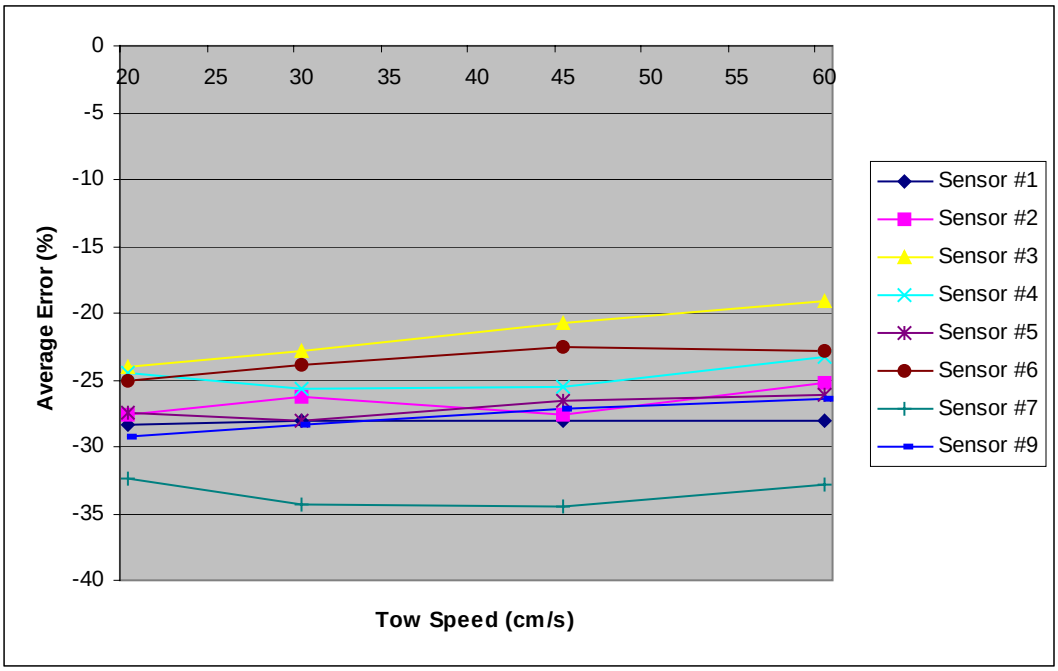

Figure 5.17: Average error of the mean velocity from the Phase II tow tests (North-South orientation.)

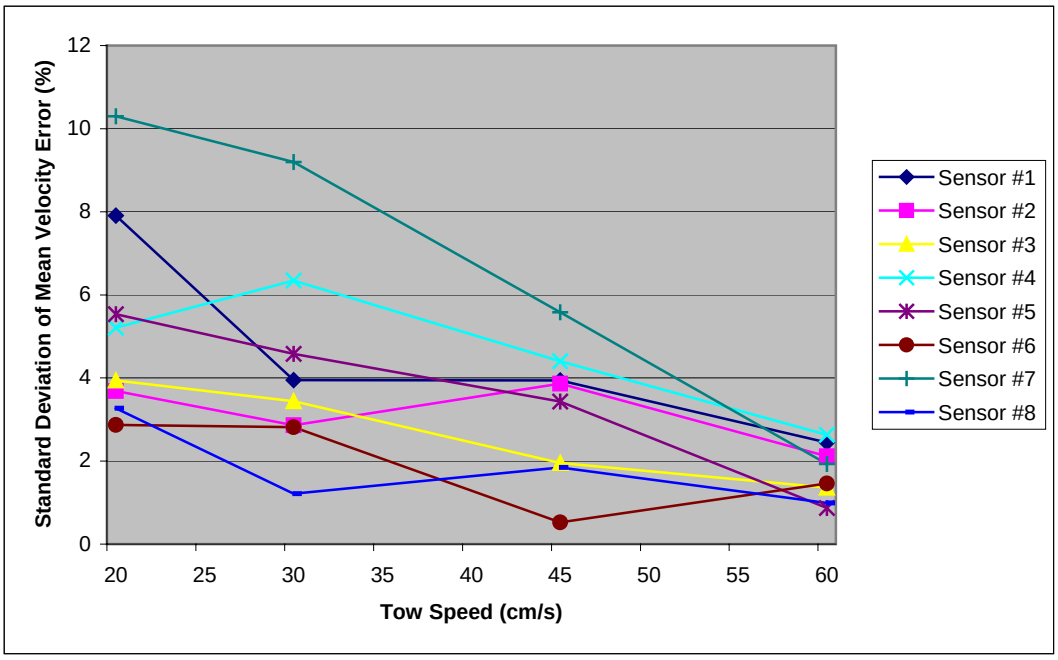

Figure 5.18: Standard deviation of the mean velocity from the Phase II tow tests (North-South orientation)

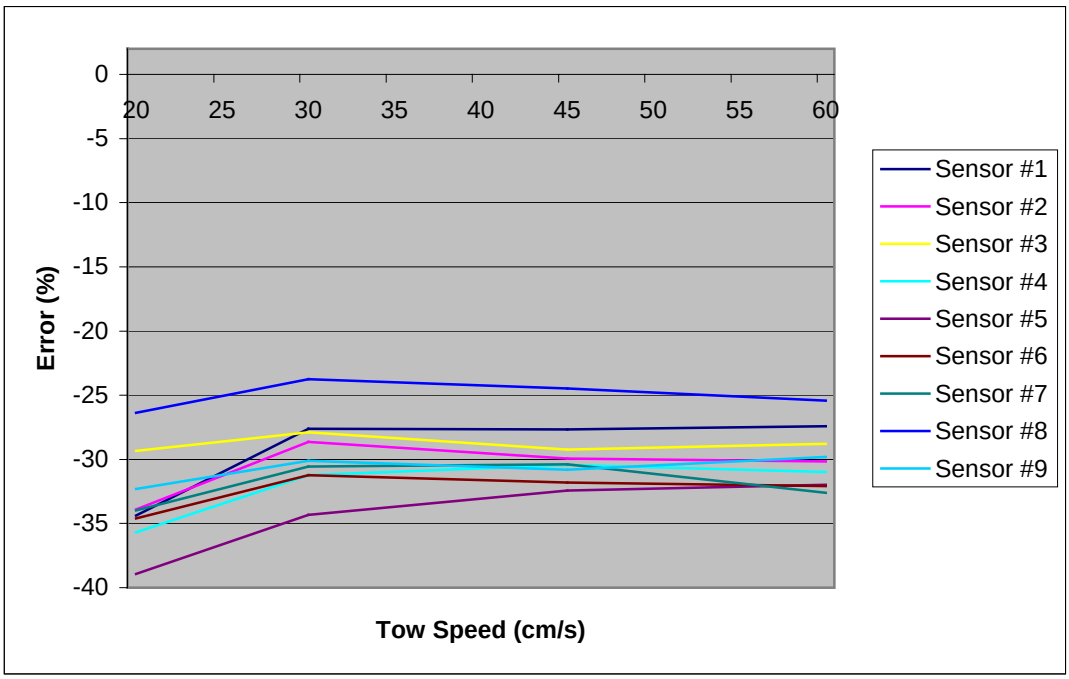

Figure 5.19: Average error of the mean velocity from Phase III tow tests (North-South orientation)

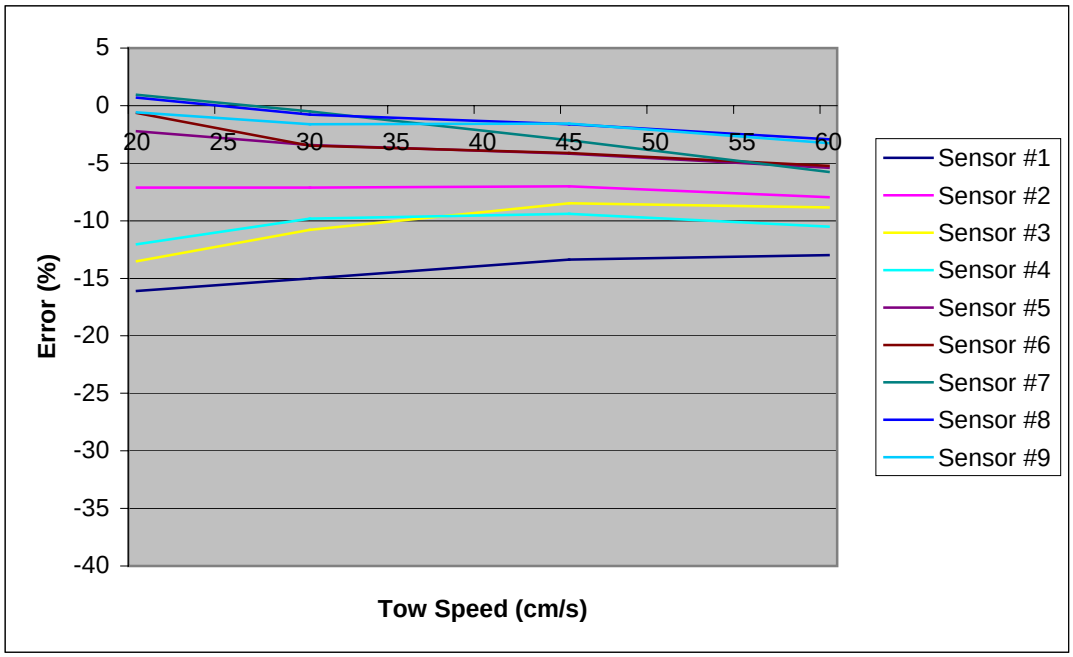

Figure 5.20: Average error of the mean velocity from Phase III tow tests (Vertical orientation)

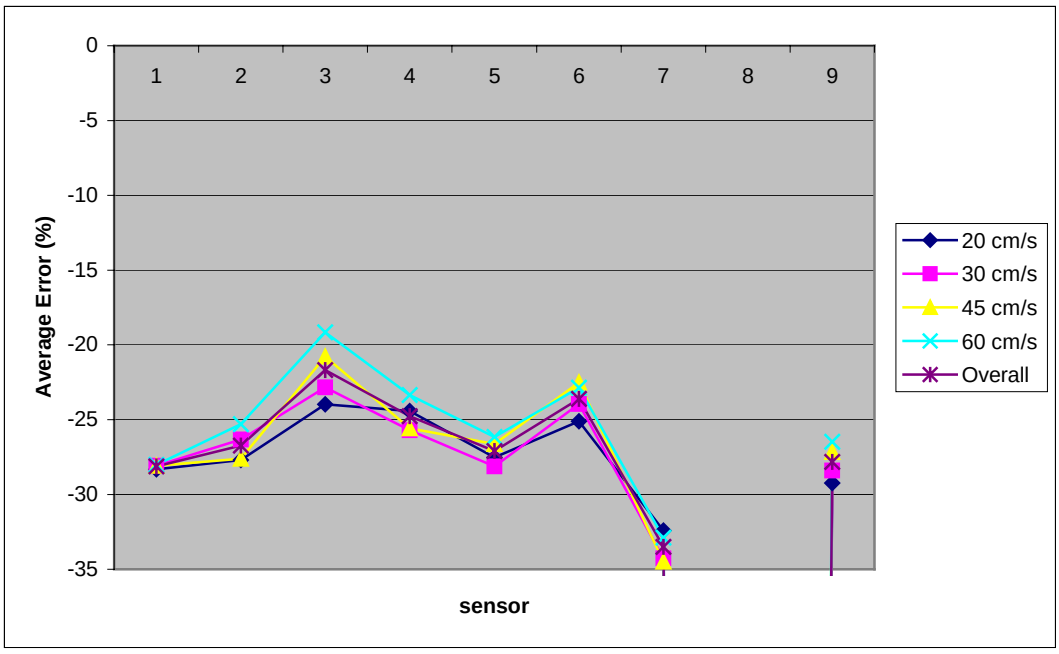

Figure 5.21: Average error according to the sensor in Phase II

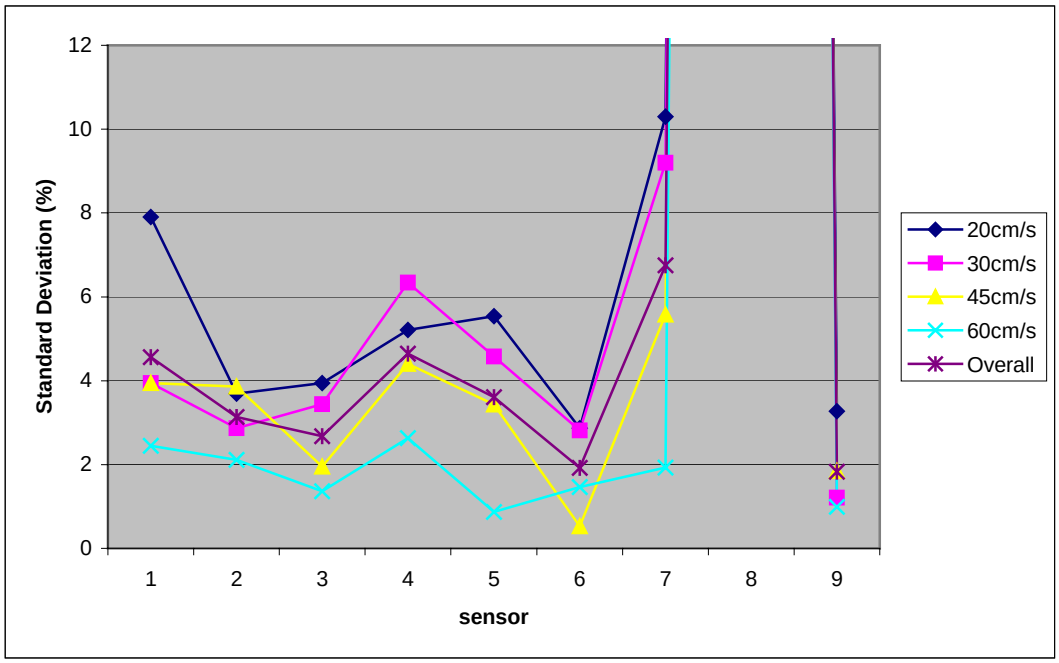

Figure 5.22: Standard deviation of the error according to the sensor in Phase II

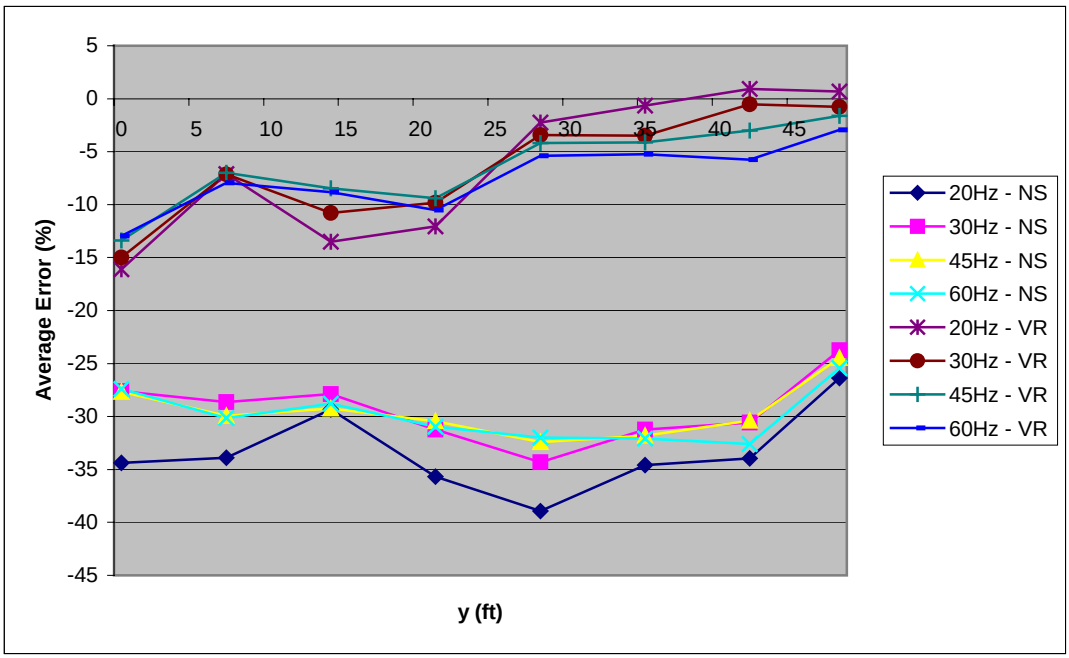

Figure 5.23: Average error according to the sensor in Phase III

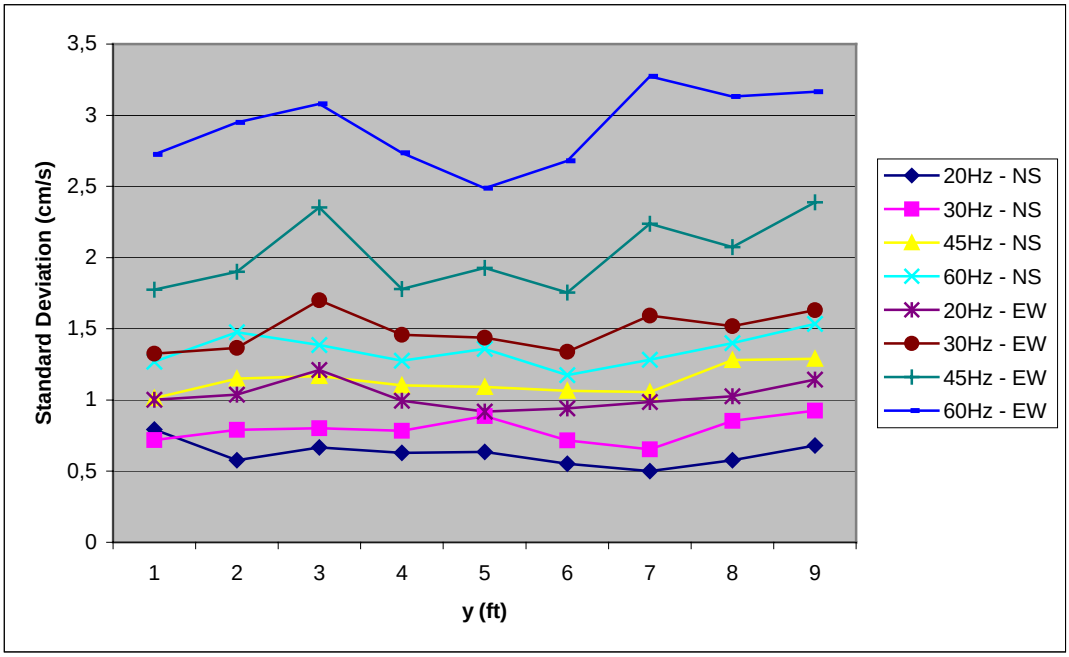

Figure 5.24: Standard deviation of the mean velocity according to the sensor in Phase III

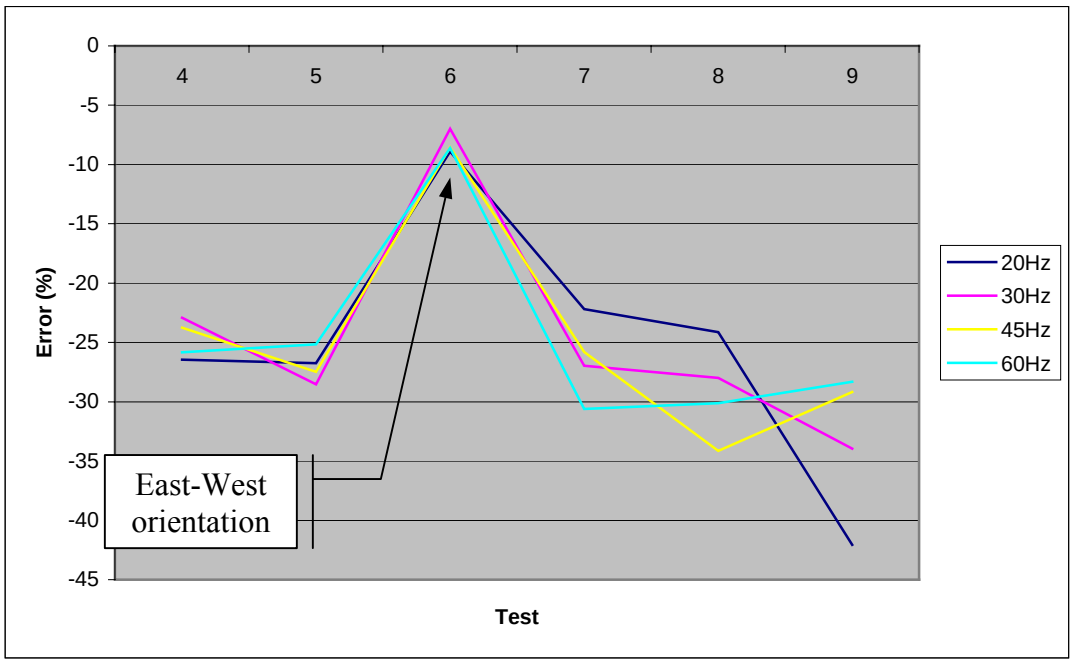

Figure 5.25: Average error according to the test for sensor 1 in Phase II

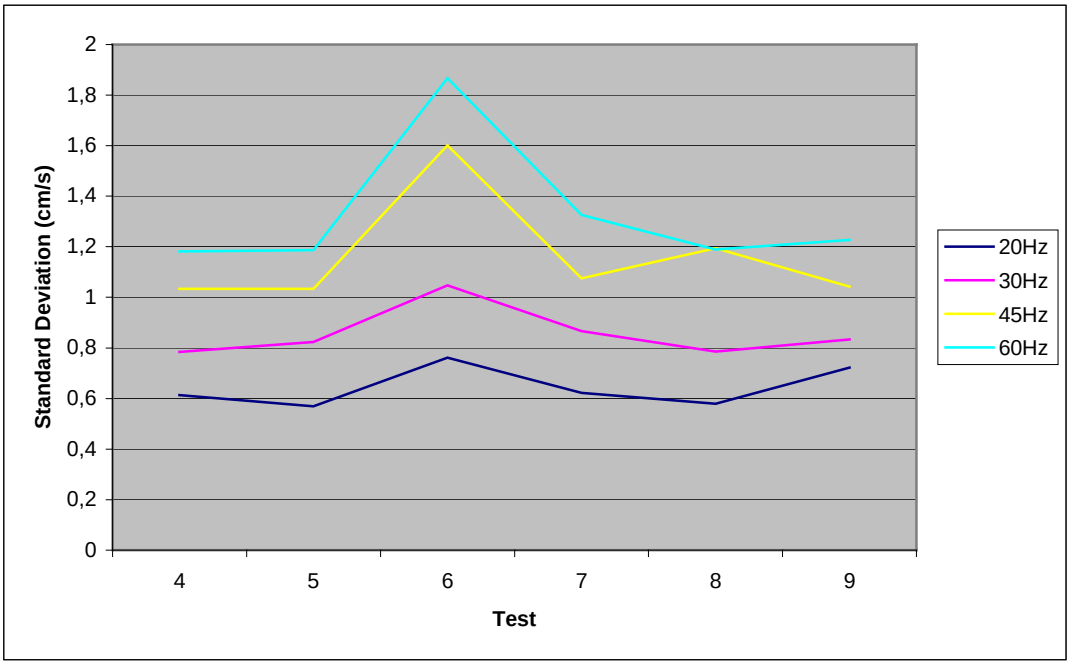

Figure 5.26: Standard deviation of the mean velocity according to the test for sensor 1 in Phase II

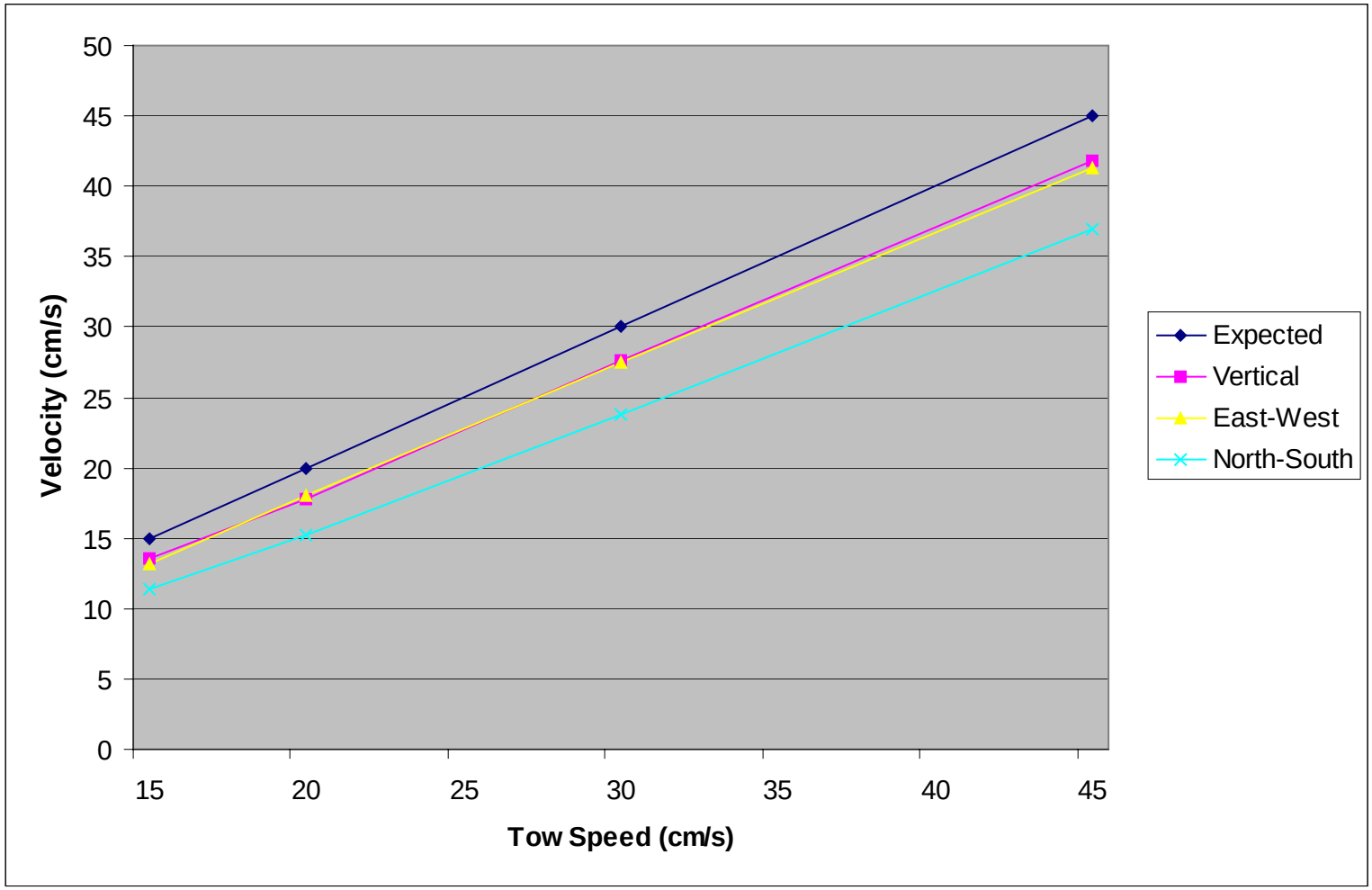

Figure 5.27: Comparison between measured velocity and tow speed for Phase I

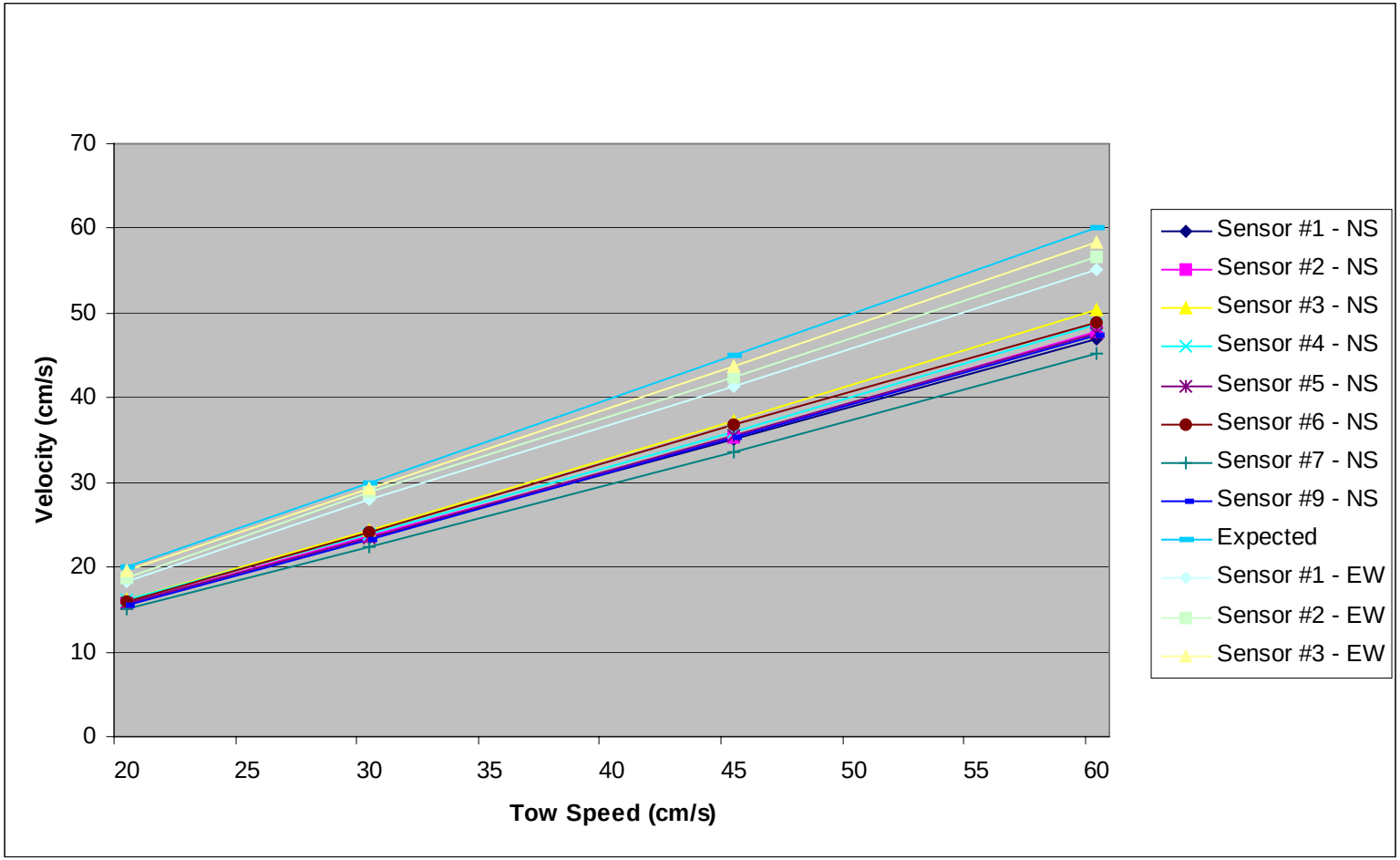

Figure 5.28: Comparison between measured velocity and tow speed for Phase II

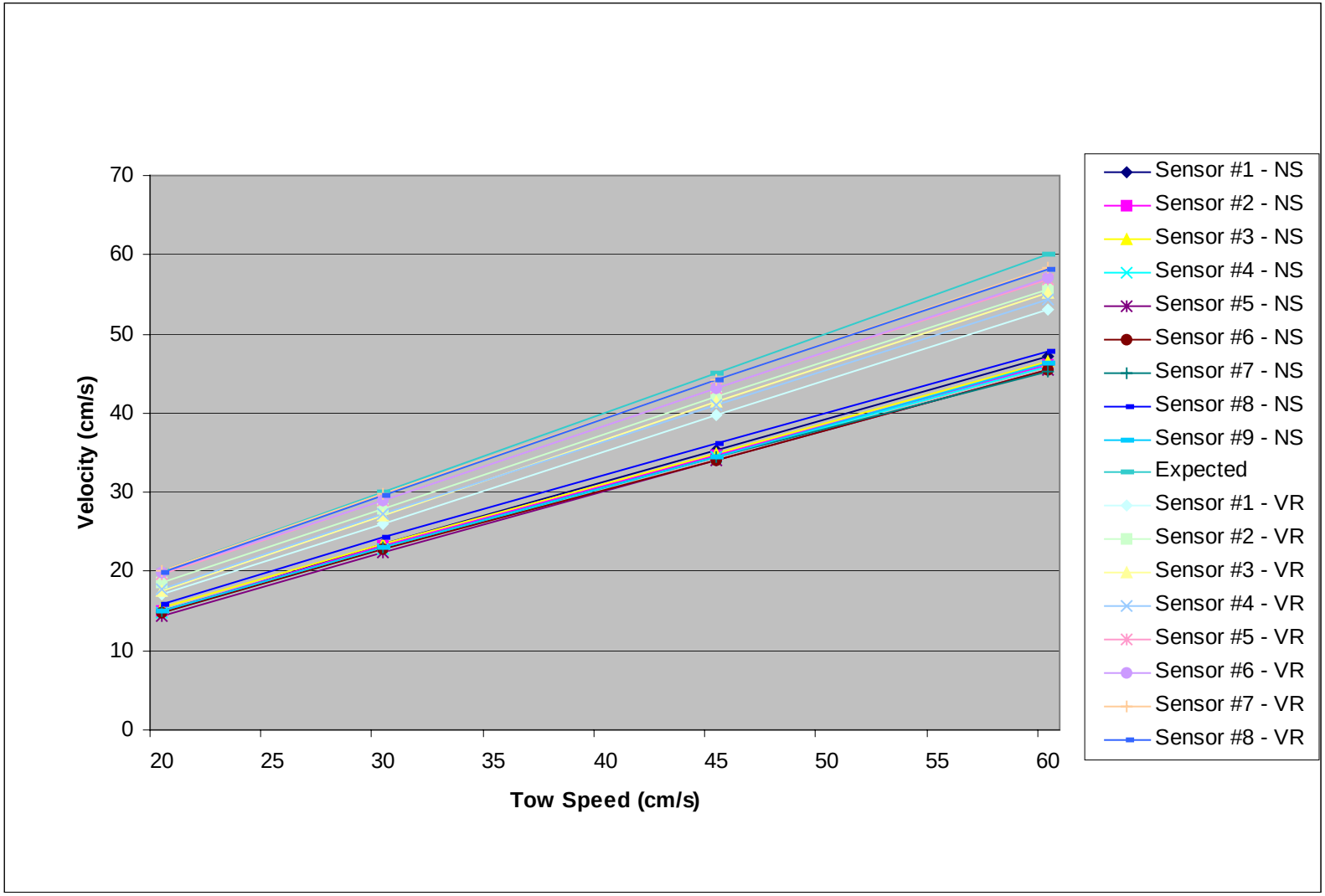

Figure 5.29: Comparison between measured velocity and tow speed for Phase III

We will now examine the behavior of the sensor in the frequency domain and only look at the *u*-component signal summarized in Figure 5.30 for increasing tow speeds. Generally speaking for a 20cm/s tow speed (Figure 5.31), we have a peak at 3.5Hz for all the sensors, one at 4.5Hz for sensors 3, 6 and 9, one at 13Hz for 1, 3, 7 and 9, two at 15Hz and 17Hz for all the sensors but for sensors 7 and 9, these two appear merged. In the case of a tow test at 30cm/s, that we have the same behavior as before but the peak at 3.5Hz is now around 5Hz, which cause the peaks at 4.5Hz to be absorbed.

If we continue to increase the tow speed to 45cm/s, we notice that the behavior is still identical except for the first peak that has moved from 5Hz to 8Hz now (Figure 5.32). Also, the two peaks at high frequency have almost disappeared and we notice a drop-off of the energy at high frequency for sensor #9. Finally, for a test at a 60cm/s tow speed, the moving peak reaches the frequency of 11Hz. We can see in Figure 5.32 the behavior of the *u*-velocity spectra for an increasing speed.

We consider the peaks at a frequency higher than 12Hz to be due to bridge vibration because they are present for all tow speeds and do not appear in other types of tests (calm, wave, current).

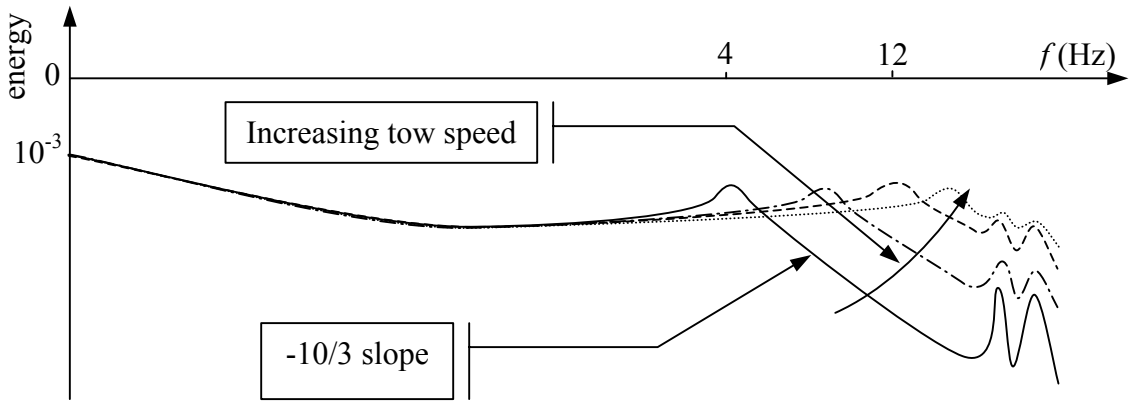

Figure 5.30: Power spectrum for increasing tow speed

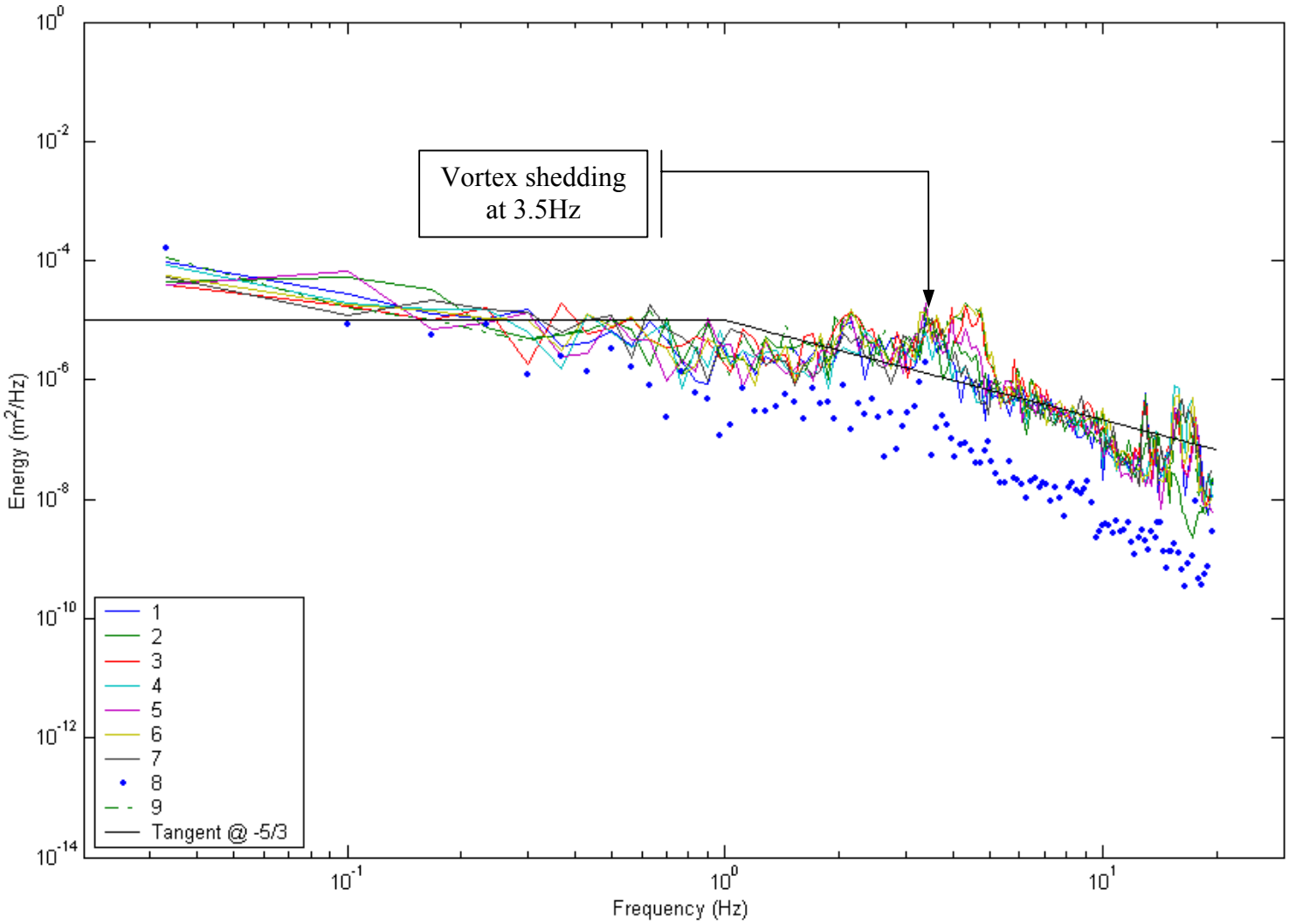

Figure 5.31: Power spectrum for a tow test at 20cm/s in Phase II

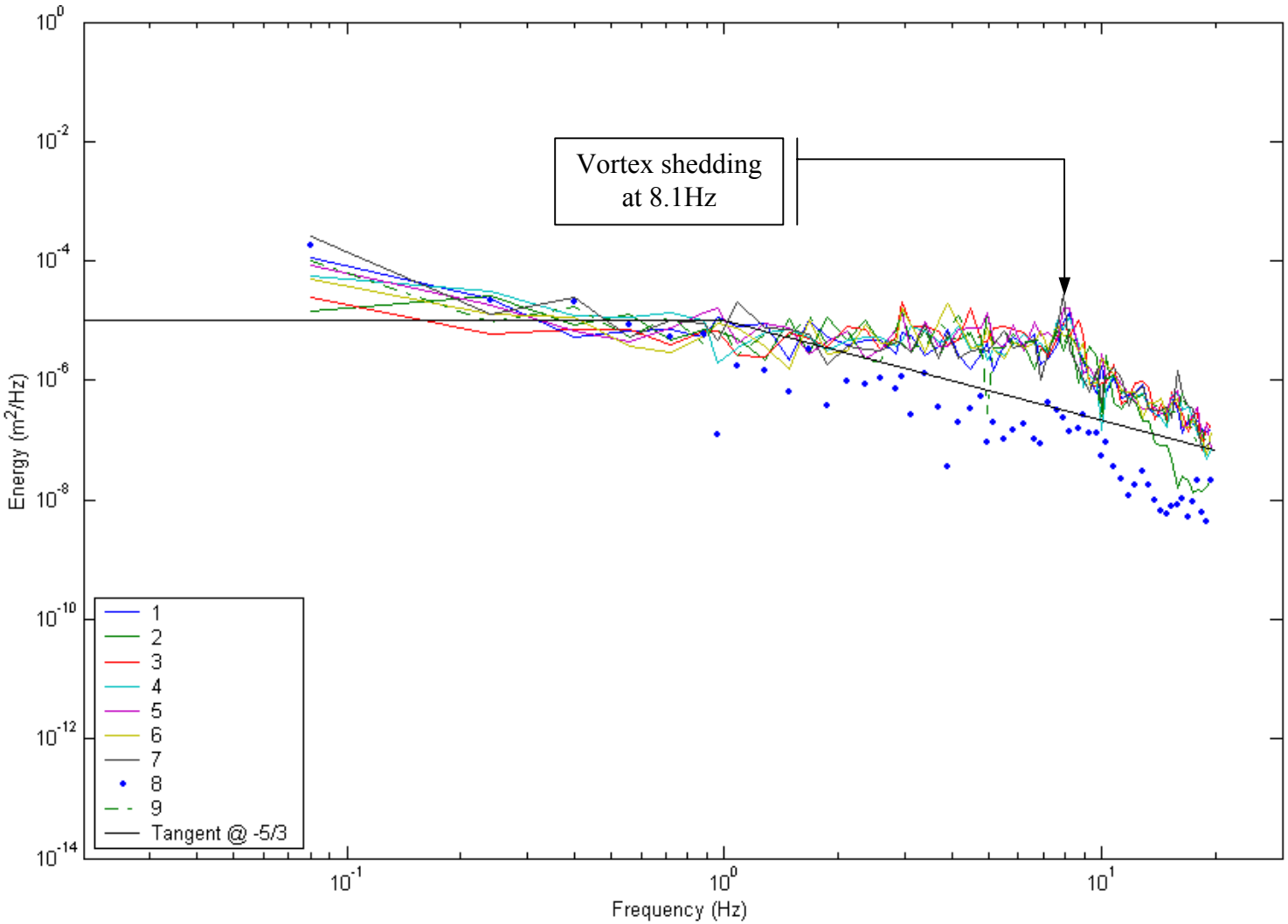

Figure 5.32: Power spectrum for a tow test at 45cm/s in Phase II

As described in section 5.4, the peak that is moving as the tow speed changes is due to vortex shedding. A Strouhal number of 0.2 is characteristic for a circular cylinder. However, the rings of the MAVS are not perfectly circular. As can be seen in Figure 5.33, we found that a Strouhal number of 0.18 provided a better fit. Also, we can note the standard deviation of the Strouhal number over all the tests of only 0.00069, which implies an excellent correlation.

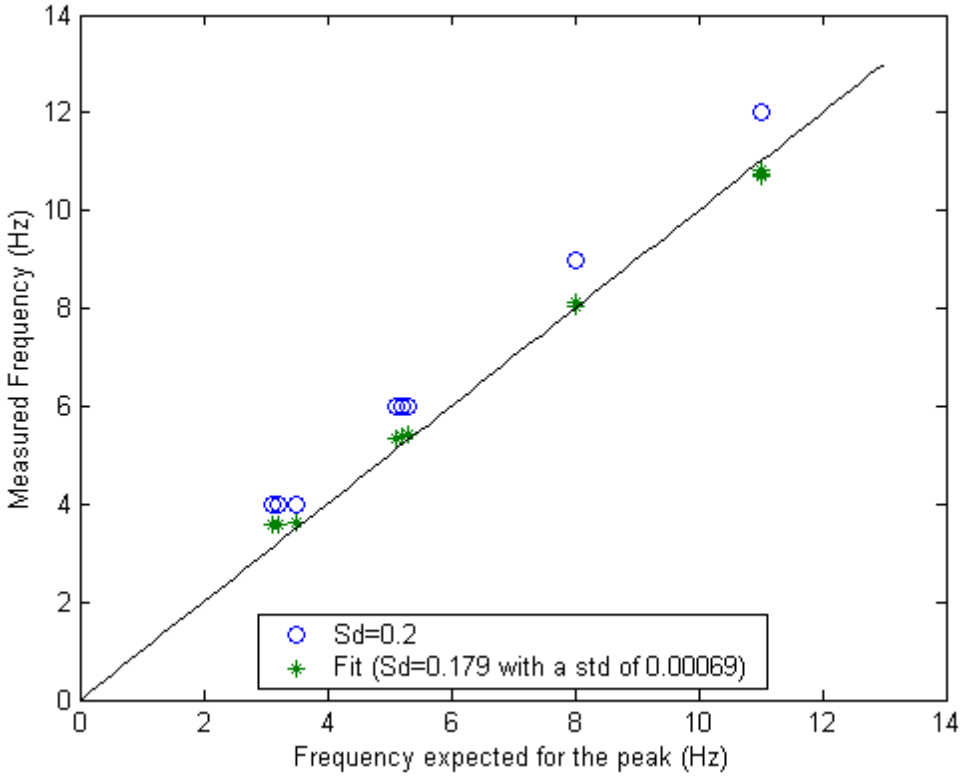

Figure 5.33: Scatter plot of the expected versus the measured frequency of the vortex shedding

Finally, this vortex shedding is present on the spectra for the *u*, *v* and *w* measurement, which makes us think that the turbulence generated by the vortex shedding is somewhat isotropic.

5.5 Wave Tests

As a last benchmark, the behavior of the sensor in a wave flow was tested. For the wave tests, the current meter was mounted at some depth and the wave elevation directly above the meter was measured using a capacitance type wave gauge. From the measured wave elevation, it was possible to calculate the orbital velocity at the current meter for comparison measurements. For Phase I tests, both the MAVS and the Marsh-McByrney sensors were deployed, while for Phase II tests, only the MAVS was deployed. Note that while the MAVS measures the three velocity components, the Marsh-McByrney measures only two velocity components and it was mounted so as to measure the two horizontal velocity components.

5.5.1 First Phase

For the first set of tests, the current meters were mounted at a depth of one foot only. In all cases, the signal was captured on both *x* and *z* components for MAVS and only on the *x* component for the Marsh-McByrney sensor. It is interesting to see that we have a very noisy transverse *v*-velocity signal (Figure 5.34). Indeed, even if we are supposed to have no transverse component at all (or at least, only the reflections from the walls of the wave basin and some refraction by the rings of the MAVS sensor), we see that we still have a signal with an average maximum of 3cm/s for MAVS and 2cm/s for Marsh-McByrney. It is also interesting to see that the wave signals (*u* and *w* components) are pretty clear and we don't see any noise in them.

On the other hand, when we take examine the energy spectrum of our wave test (Figure 5.35), we often find a small trace of the wave frequency on the *y* component. That shows us that the spectrum helps us to see things that are seemingly invisible by looking at the time series. Moreover, we can see for the East-West orientation of the MAVS that *v* has an important periodic signal corresponding to the frequency of the

wave. This can also be seen in the time series. Thus, we can say that in that test, the MAVS sensor was not mounted perfectly on its support and that it was rotated slightly on the *z*-axis.

Figure 5.36 shows that the measured velocities compare reasonably well with the theoretical velocities computed from the measured wave elevation, though there are discrepancies near the extreme values. By forming the average of the maxima, we can see (with a code of colors referenced in Table 5.4) that in Tables 5.5 and 5.6, the results are not that accurate still. In the case of sensors at a depth of –1ft, we can see that the Marsh-McByrney sensor is very accurate while the MAVS is only accurate in the East-West orientation and has an error between 15 and 20% in the North-South and Vertical orientations. On the other hand, in the case of sensors at a –3ft depth, we can see now that for every sensor and in every orientation, the theoretical velocity is underestimated by 10% for the Marsh-McByrney and between 20 and 25% for the MAVS.

Finally, it is also interesting to see that for every signal that we worked on in Phase I, we had to shift the time of the theoretical velocity so that it adapts to the signal from the MAVS. Often, that phase lag was the same as the one that we used to match the velocities from Marsh-McByrney to the one from MAVS with an extra lag of 0.2s.

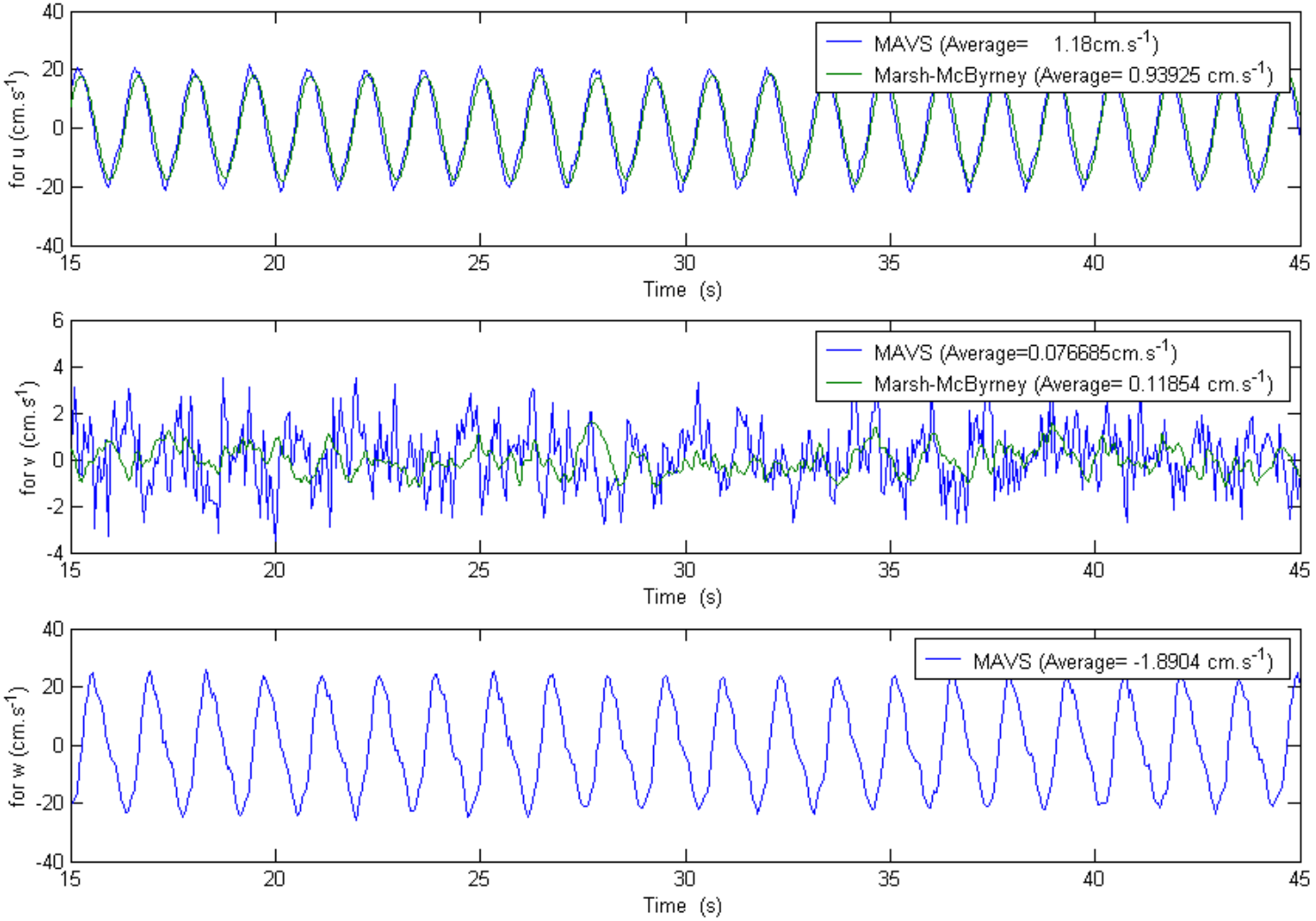

Figure 5.34: Time series for a wave test in Phase I at *z*=-1ft and for a North-South orientation

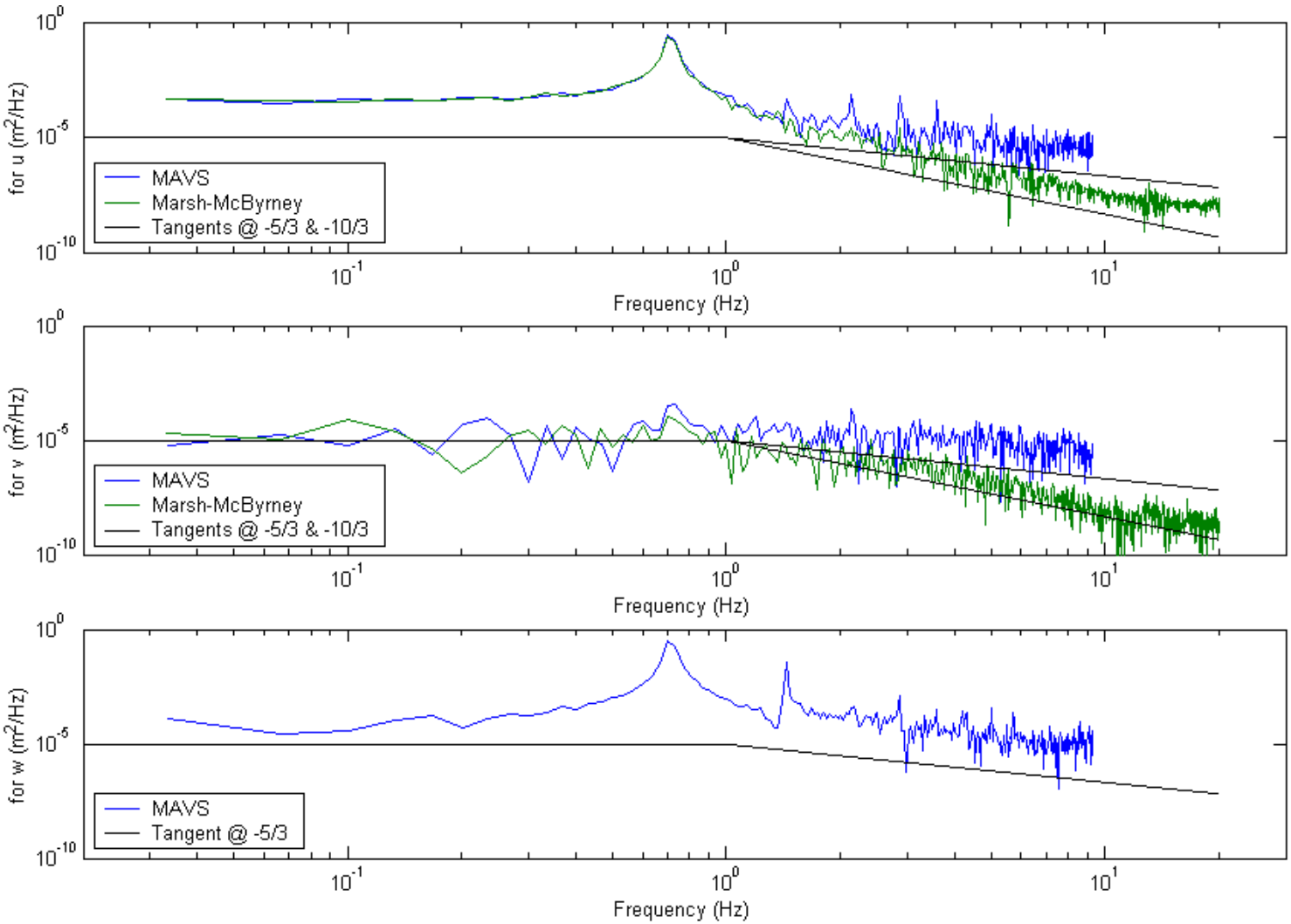

Figure 5.35: Power spectrum for a wave test with a North-South orientation at *z*=-1ft in Phase I

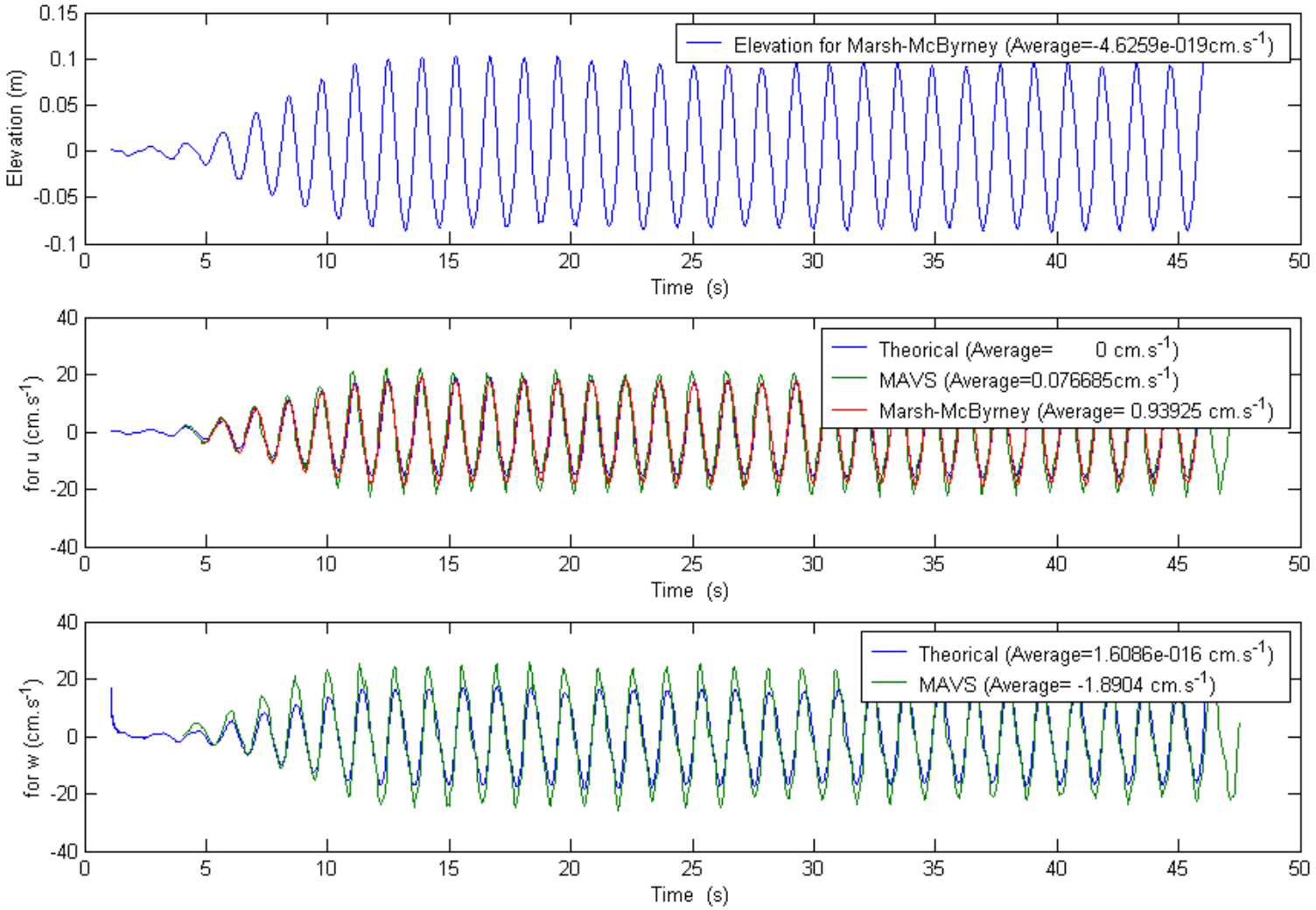

Figure 5.36: Comparison of *u* and *w* for Phase I at *z*=-1ft and for a North-South orientation

Table 5.5: Average maxima at z=-1ft

Sensor	Orientation	Max		Min		Height	
		Speed (cm/s)	% difference	Speed (cm/s)	% difference	Speed (cm/s)	% difference
MAVS	North-South	21.61	19.3	-20.03	10.5	20.82	14.9
MMB		18.79	3.7	-17.12	-5.5	17.96	-0.9
MAVS	East-West	17.6	-2.9	-19.19	5.9	18.4	1.5
MMB		18.4	1.6	-18.18	0.3	18.29	0.9
MAVS	Vertical	21.15	16.7	-22.28	22.9	21.71	19.8
MMB		18.78	3.6	-17.23	-4.9	18.01	-0.6
Theory	All	18.12		-18.12		18.12	

Table 5.6: Average maxima at z=-3ft

Sensor	Orientation	Max		Min		Height	
		Speed (cm/s)	% difference	Speed (cm/s)	% difference	Speed (cm/s)	% difference
MAVS	North-South	7.04	35.8	-5.86	13.1	6.45	24.5
MMB		5.31	2.6	-6.15	18.6	5.73	10.6
MAVS	East-West	6.16	18.9	-6.12	18.1	6.14	18.5
MMB		5.52	6.5	-5.69	9.8	5.6	8.2
MAVS	Vertical	6.72	29.8	-6.66	28.6	6.69	29.2
MMB		5.68	9.6	-6.09	17.5	5.88	13.5
Theory	All	5.18		-5.18		5.18	

5.5.2 Second Phase

In the second phase, as the depths of the sensors were not logged, two methods were used to estimate the sensor depths. A first analysis of the times series (Figure 5.37) shows three clearly different types of signals (as expected) so we tried to find the depth of the sensors by applying the linear wave theory. This analysis gave us three different depths of 4, 5.9 and 7.89ft (1.22, 1.8 and 2.4m) for the RG2 tests and 5.37, 7.35 and 10.35ft (1.64, 2.24 and 3.16m) for the RE5 tests. However, the two sets of depths should be identical. We therefore estimated the depths of the sensors from the pictures taken during the tests. This method indicated depths of 1, 3.5 and 7ft (0.3, -1.07 and –2.13m), which we felt were more accurate.

Looking at the spectrum (Figure 5.38), we find the same behavior as in the first phase of a spectrum without bumps. Moreover, this time we clearly see the higher harmonics of the wave. The spectra from the RN tests (Figures 5.39 & 5.40) are different from the other two types of tests in that we have a random wave signal so the spectrum is broader. Also, some peaks are found for sensors at the intermediate and deeper depth of the 3*3 array. For the u-component, these peaks are located at 2, 3.5 and 4.5Hz (Figure 5.39). In the case of the v-component, they are located at 2.5 and 3.1Hz (Figure 5.40). Finally, for the v-component (Figure 5.41), there is only one peak at 2Hz. As the peaks at 2Hz appear only on the u and w components, we could speculate that they are residuals from the wave generation. However, we don’t have any explanation about the cause of the generation of these modes.

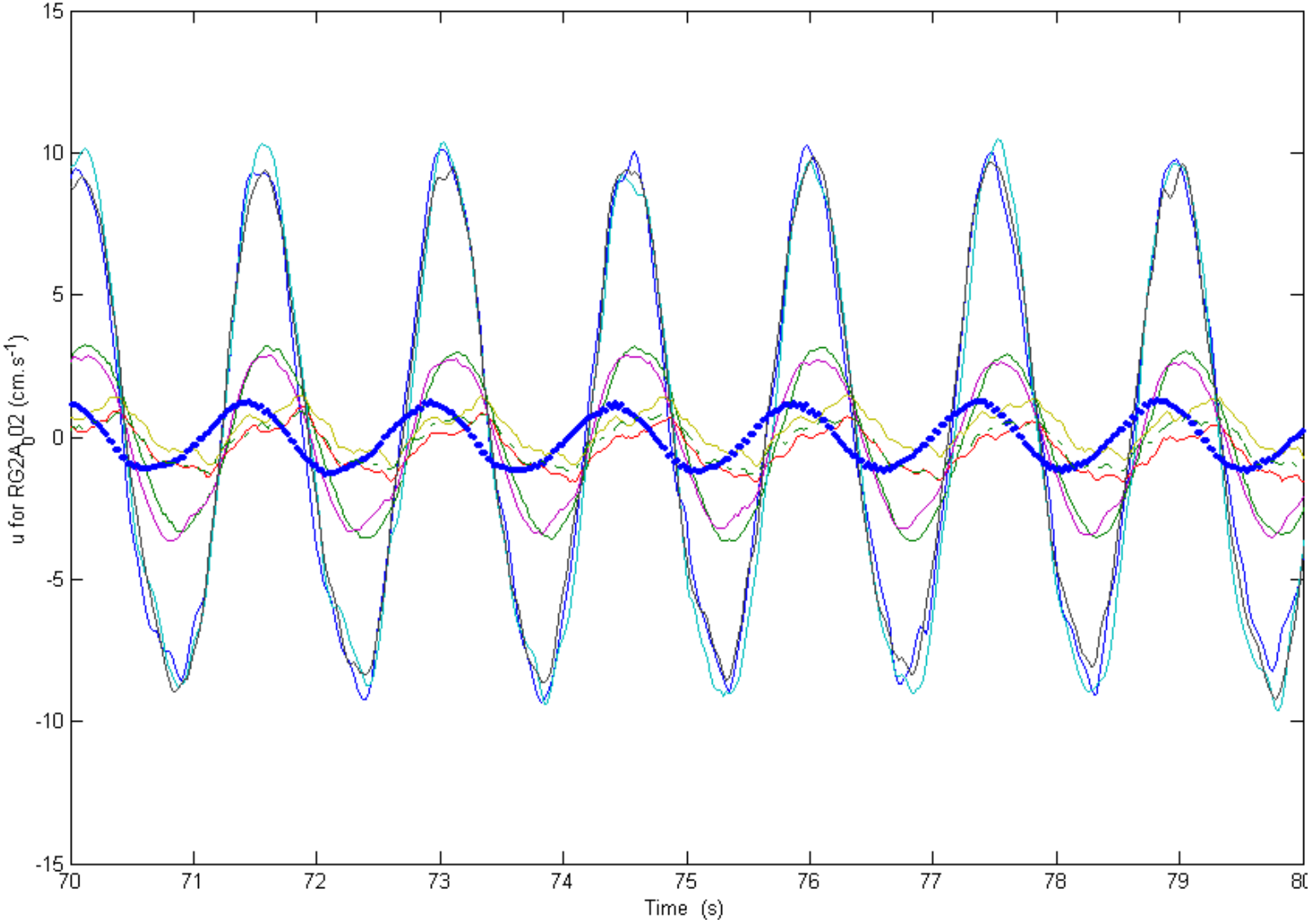

Figure 5.37: Time series of *u*-velocity for regular wave test in Phase II

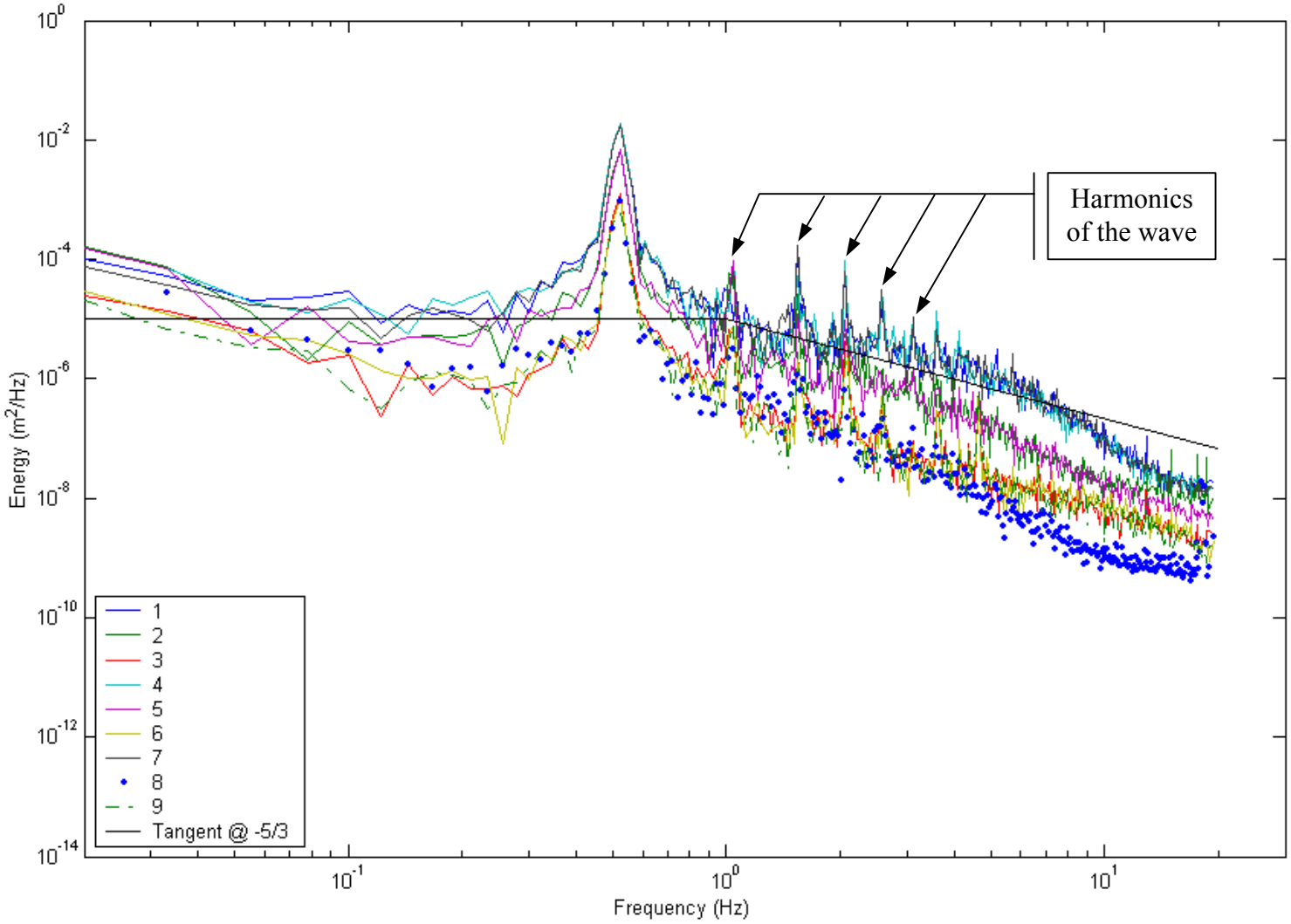

Figure 5.38: Velocity spectrum for *u* in a regular wave test in Phase II

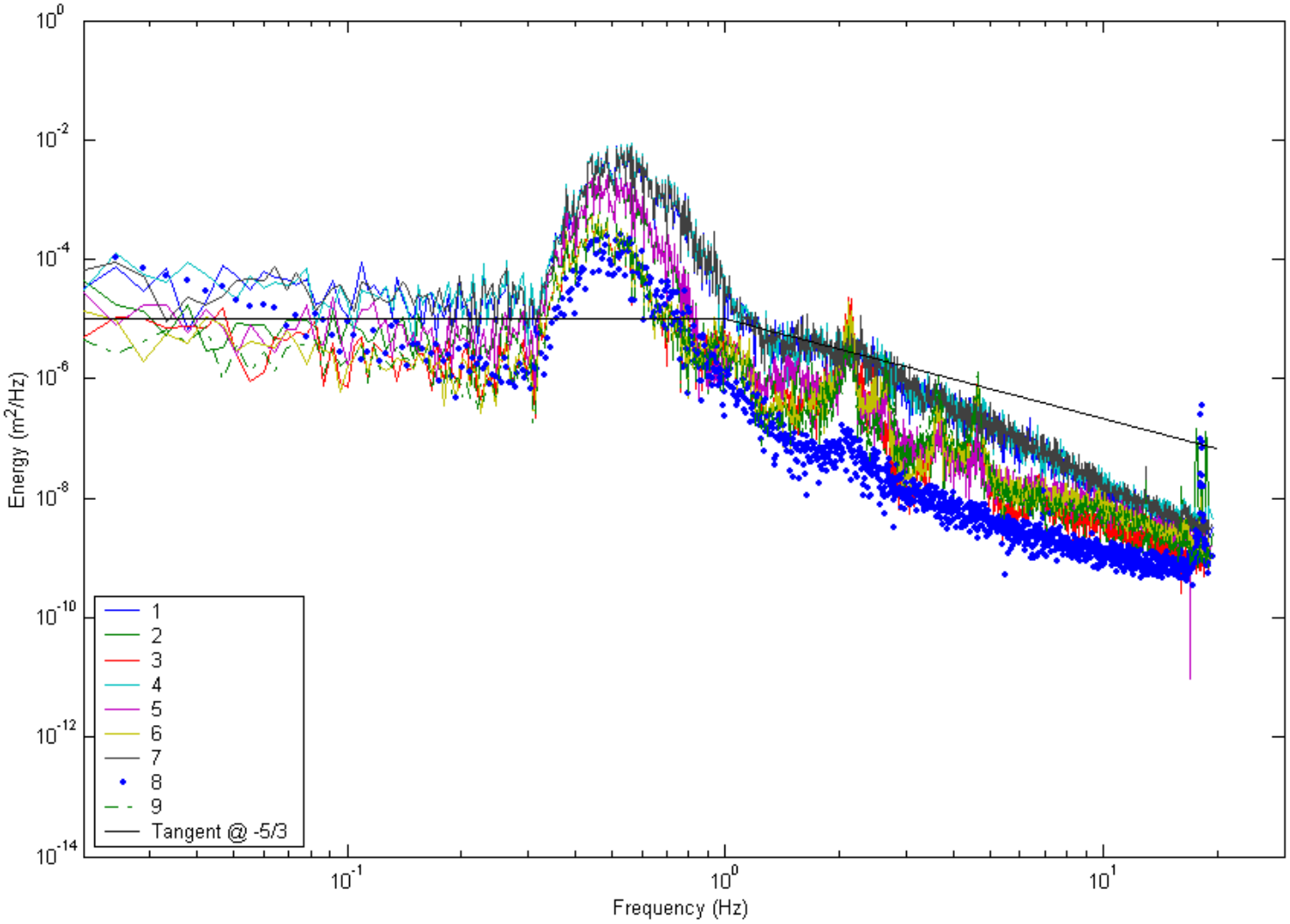

Figure 5.39: Velocity spectrum for *u* in a random wave test in Phase II

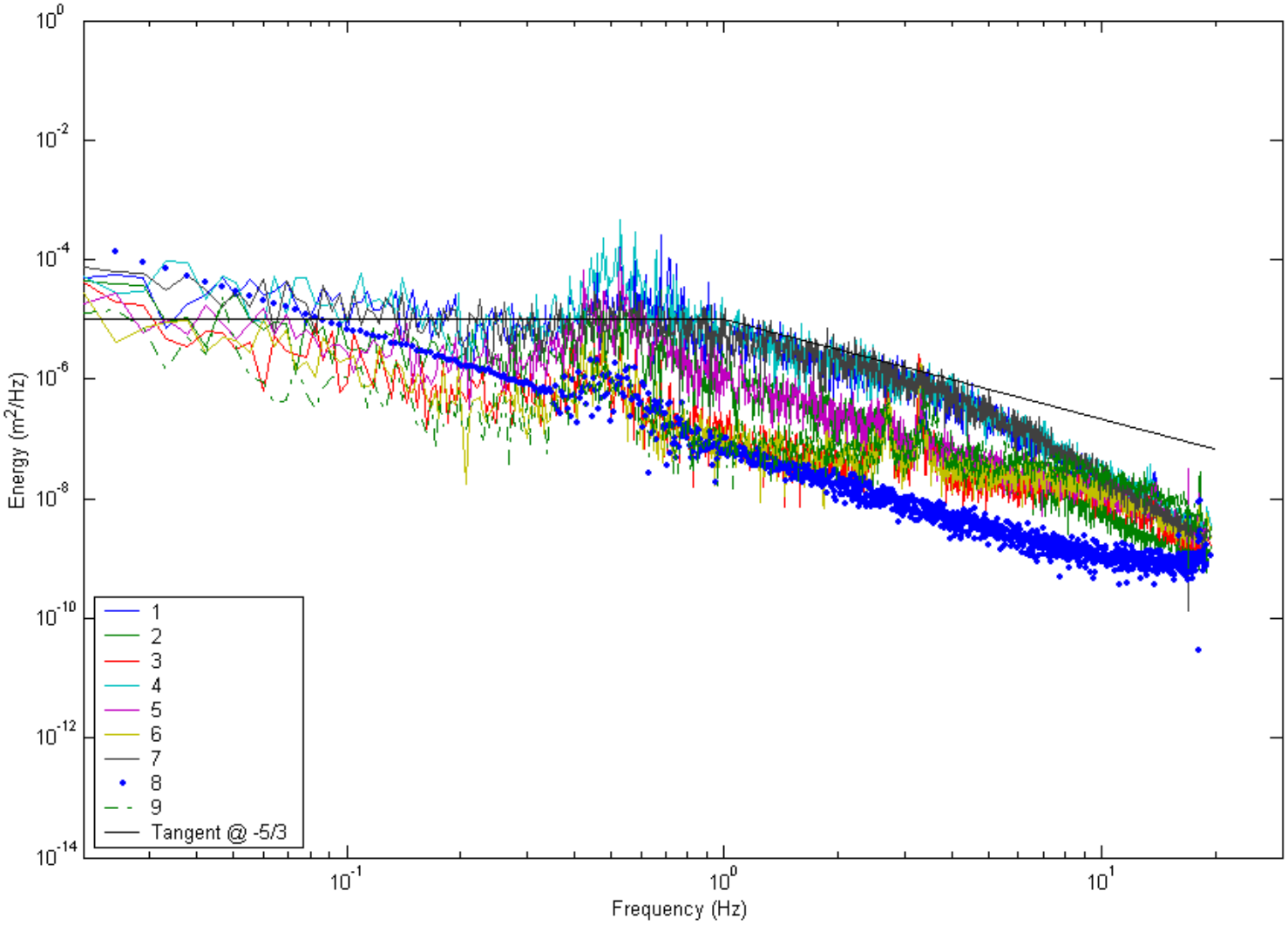

Figure 5.40: Velocity spectrum for *v* in a random wave test in Phase II

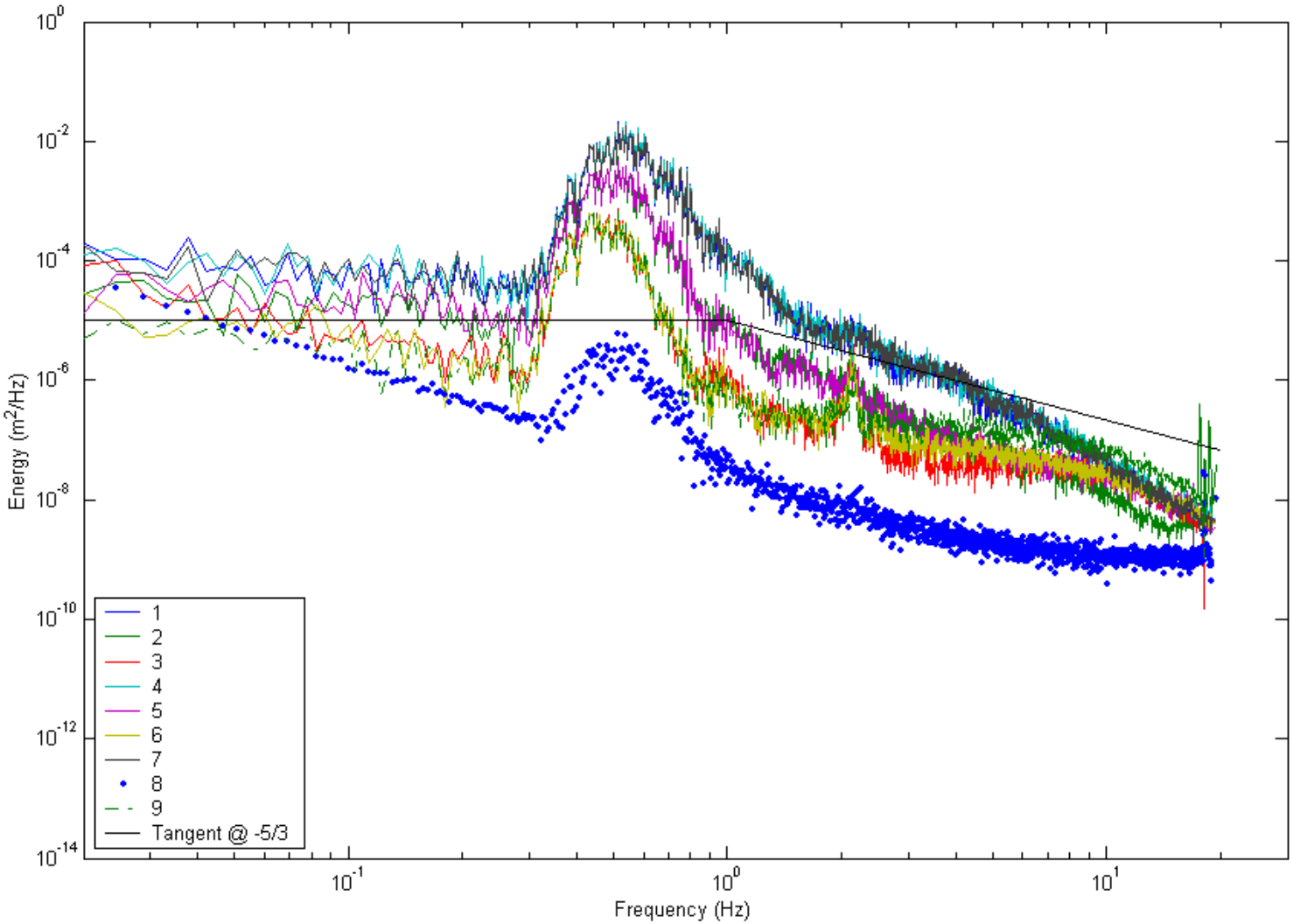

Figure 5.41: Velocity spectrum for *w* in a random wave test in Phase II

The deeper we are going, the more the spectra look like the ones of a calm test and also, the spectra for sensors at the same water depth are nearly identical. This may be due to the displacement of the fluid particles that will be too small to be detected by the MAVS (we estimate that an order of 1cm should be the minimum water displacement). Moreover, because of the vortex shedding from the transducer rings, the volume between the rings is perpetually turbulent. We recall that the displacement of a water particle in a two-dimensional propagating wave is defined by Equations 5.3 and 5.4 and illustrated in Figures 5.42, 5.43 and 5.44 for the different type of waves used in the tests.

$$\begin{cases} \varsigma = -A\dfrac{\cosh\left[k\left(z+h\right)\right]}{\sinh\left(kh\right)}\sin\left(kx-\sigma t\right) & (5.3) \\ \xi = A\dfrac{\sinh\left[k\left(z+h\right)\right]}{\sinh\left(kh\right)}\cos\left(kx-\sigma t\right) & (5.4) \end{cases}$$

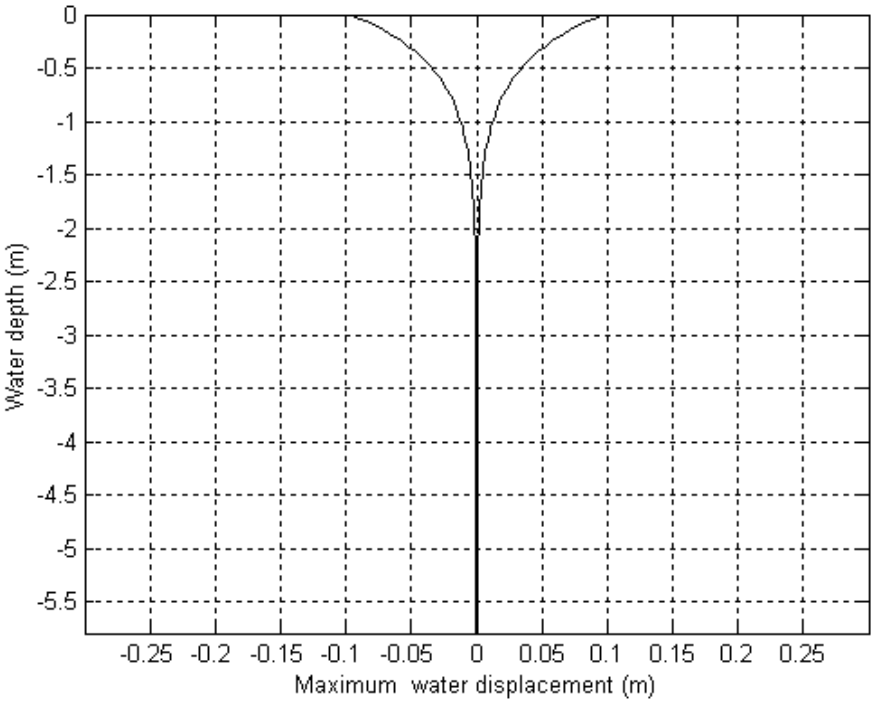

Figure 5.42: Water displacement for a wave test in Phase I

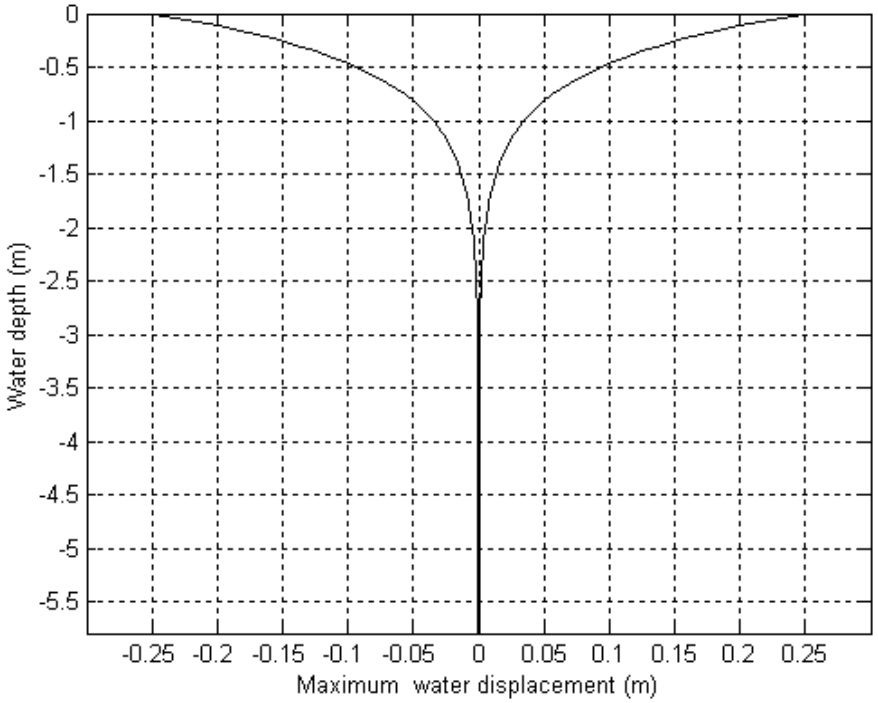

Figure 5.43: Water displacement for a RG2 wave in Phase II

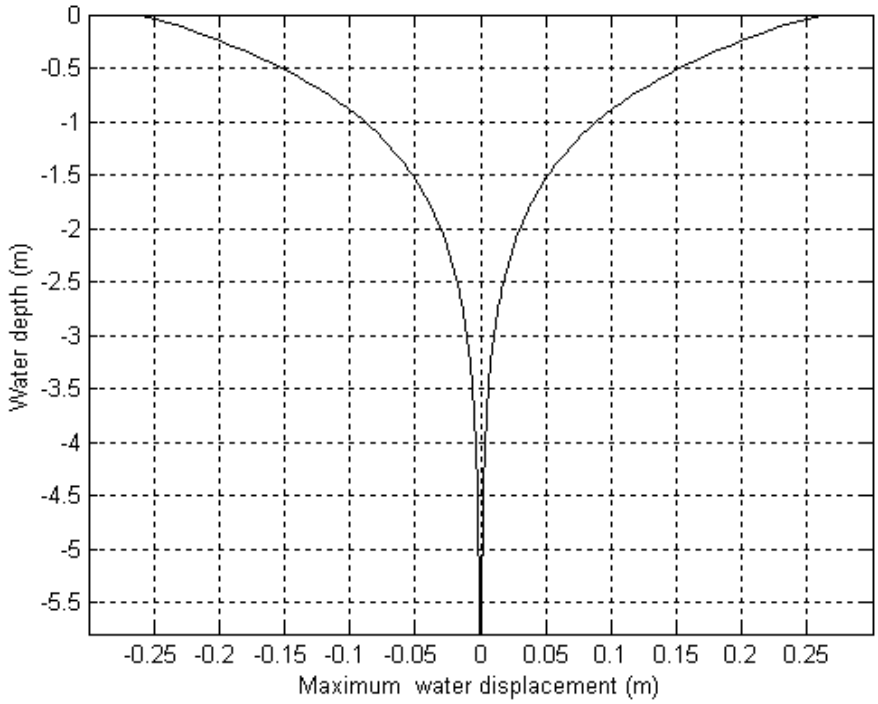

Figure 5.44: Water displacement for a RE5 wave in Phase II

5.6 Current Tests

Finally, we are studying the case that will lead us to the mapping of the wave basin and we will see if the conditions of the tow tests can be applied to the current tests.

5.6.1 First Phase

Figure 5.45 shows a typical time series of velocity measured in a current. We can see that the current is much more variant than the relative flow in a towing situation and that the signal looks much more noisy. Moreover, not only are the variations much bigger than before (order of 10cm/s instead of 4cm/s in the towing tests), but we also have a lot of low frequency variation and both sensors barely match.

Because we have longer time series measurements for the current tests than for the tow tests, we have more resolution in the frequency domain as we have a smaller Δf. However, we have to look at the averaged or smoothed spectrum for a clearer view on what is really happening (Figure 5.46). The first thing that we see, opposed to the results of the tow tests, is that the MAVS sensor has a turbulent spectrum for the whole range of frequencies. The Marsh-McByrney sensor on the other hand has the same kind of behavior as in the tow test but show us much less peaks in the power spectrum. Generally, we have a –10/3 slope until a frequency of 12Hz where the spectrum flattens. It looks like the only similarity between the two sensors is in the low frequency behavior. This is to be expected since the poor high frequency response of the Marsh-McByrney was already noted in the results for the tow tests (Section 5.2.1).

Interestingly, in the case of the Variable Frequency Drive (VFD) pump set up at 30Hz (50% of its capacity), the spectrum for the Marsh-McByrney sensor shows a broad energy peak at a frequency of 0.25Hz. On the other hand, the MAVS shows a similar behavior at a frequency of 4Hz in the North-South orientation. However, this wave

signal is not only not present in the other MAVS results (except in the North-South orientation as illustrated in Figure 5.47) but also in none of the results with the regular current pumps. We don't have an explanation for this curious result which appears to be associated with the use of the VFD pump.

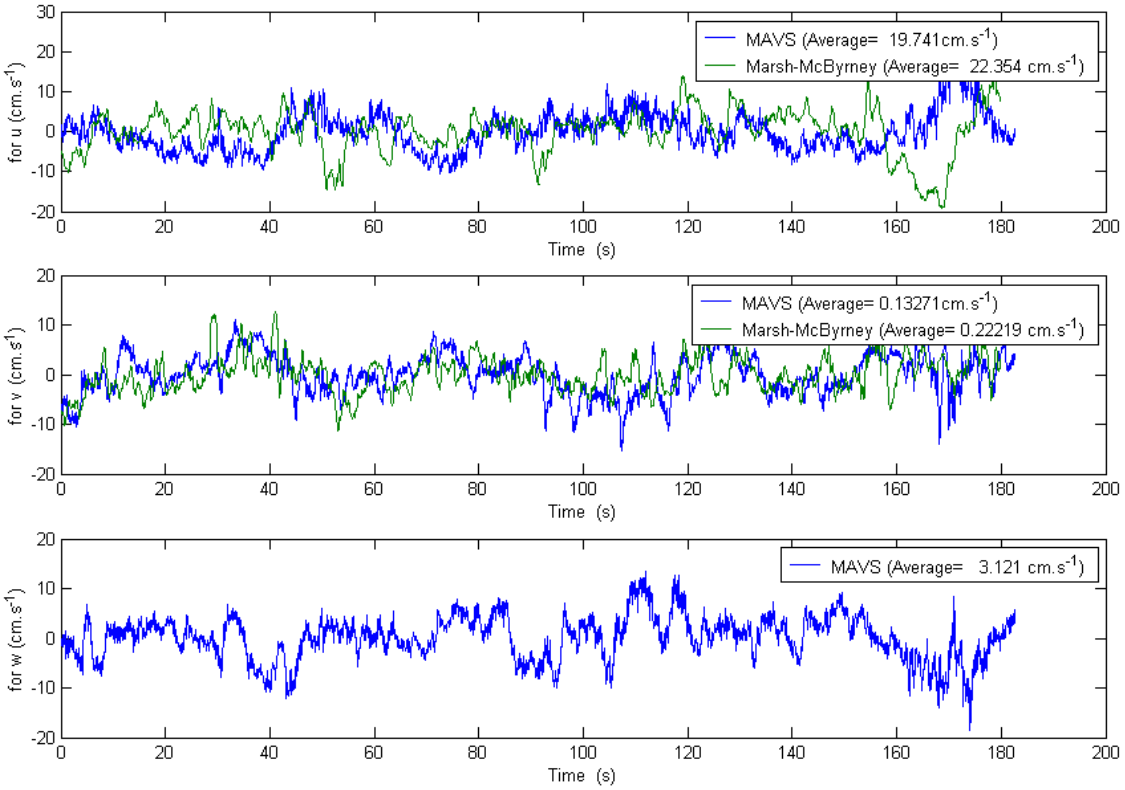

Figure 5.45: Time series for a current measured at 6ft depth in Phase I

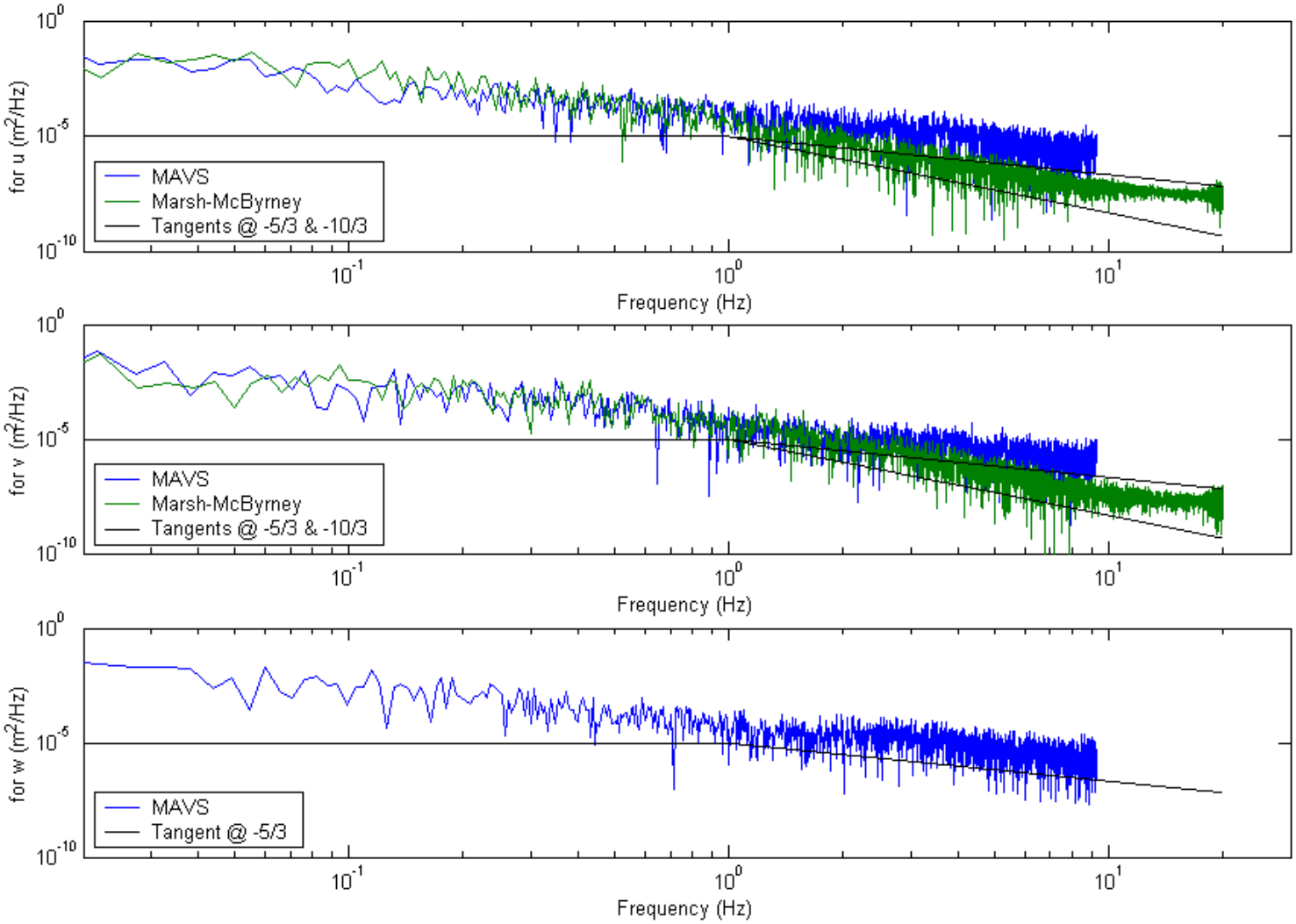

Figure 5.46: Power spectrum of a current measured at 6ft with an East-West orientation in Phase I

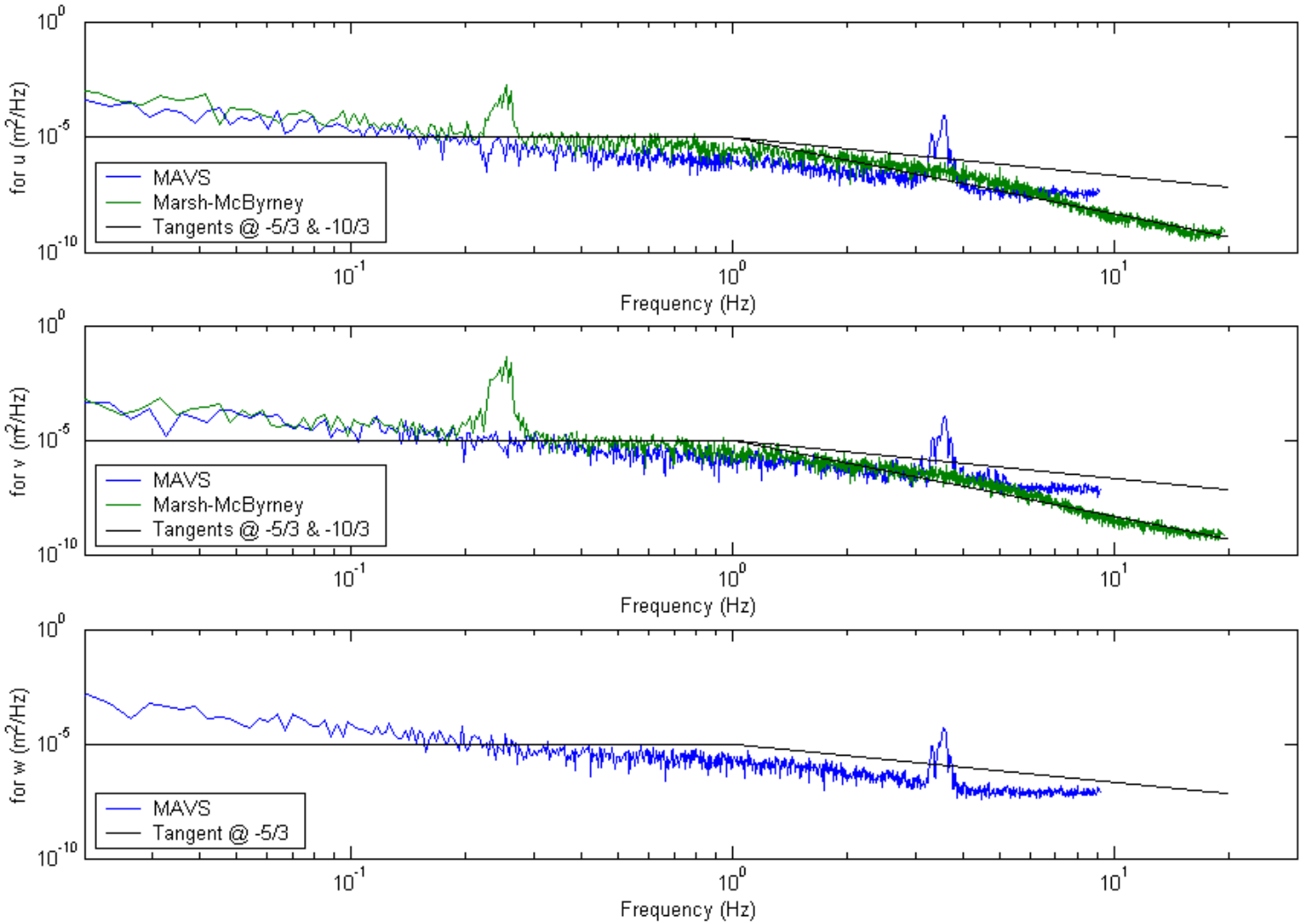

Figure 5.47: Power spectrum of a current measured at 6ft with a North-South orientation and the VFD on in Phase I

5.6.2 Second Phase

In the second phase, we had tests using the vertical, horizontal and 3*3 arrays at capacities of the current generators of 100, 200 and 225%. However, not all tests were for every type of setting available.

For Phase II, we have a 40Hz sampling rate which provides access to higher frequencies. We can see that we have a perfect -5/3 slope until a frequency of around 5Hz where the curve turns into a -10/3 slope (drop-off), which can be seen in Figures 5.48 to 5.51 for different configurations of current and location.

Moreover, we can see that all the sensors are in a range of 2dB from each other and from one test to another will move in that range (meaning more or less energy). As expected, it looks like the closer we are to the current generator, the more energy we have in the whole spectrum.

The main thing that we can see in the current tests is the presence of energy at high frequencies that we will refer to as a "bump" (Figure 5.48). What we can see from all the spectra is that the deeper we are going, the more the bump tends to flatten as it joins the -10/3 curve. As we go further in the *x* direction, the spectrum from the shallower sensors join those from the deeper ones at a median position, keeping still a bump but a little bit flattened. However, this phenomenon is very subtle and we can find some exceptions. On the other hand, as we approach the basin wall (*y* increasing), the bump becomes less important and this, contrary to the previous phenomenon, is always occurring.

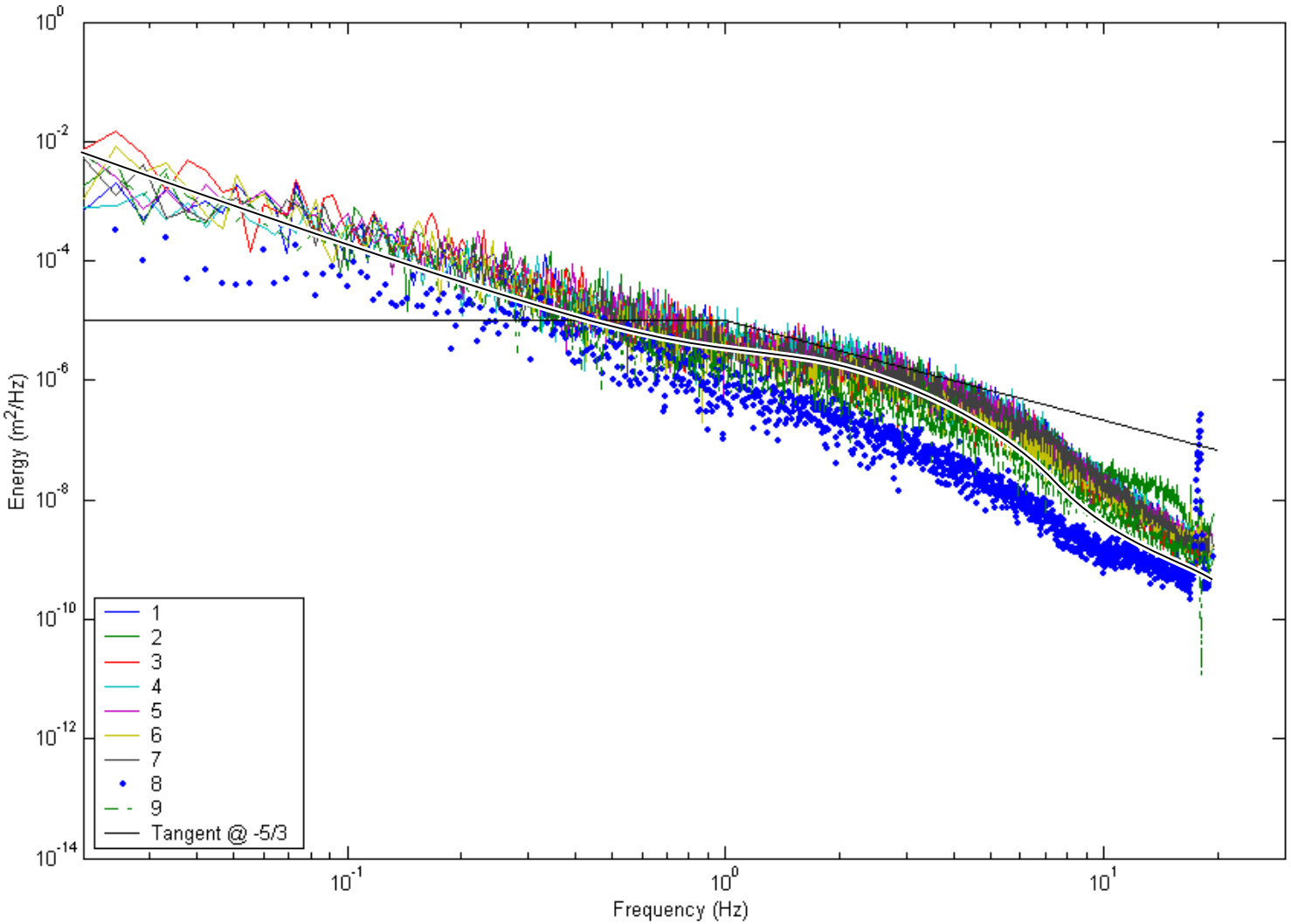

Figure 5.48: Power spectrum of a current at 100% with a 3*3 array in Phase II

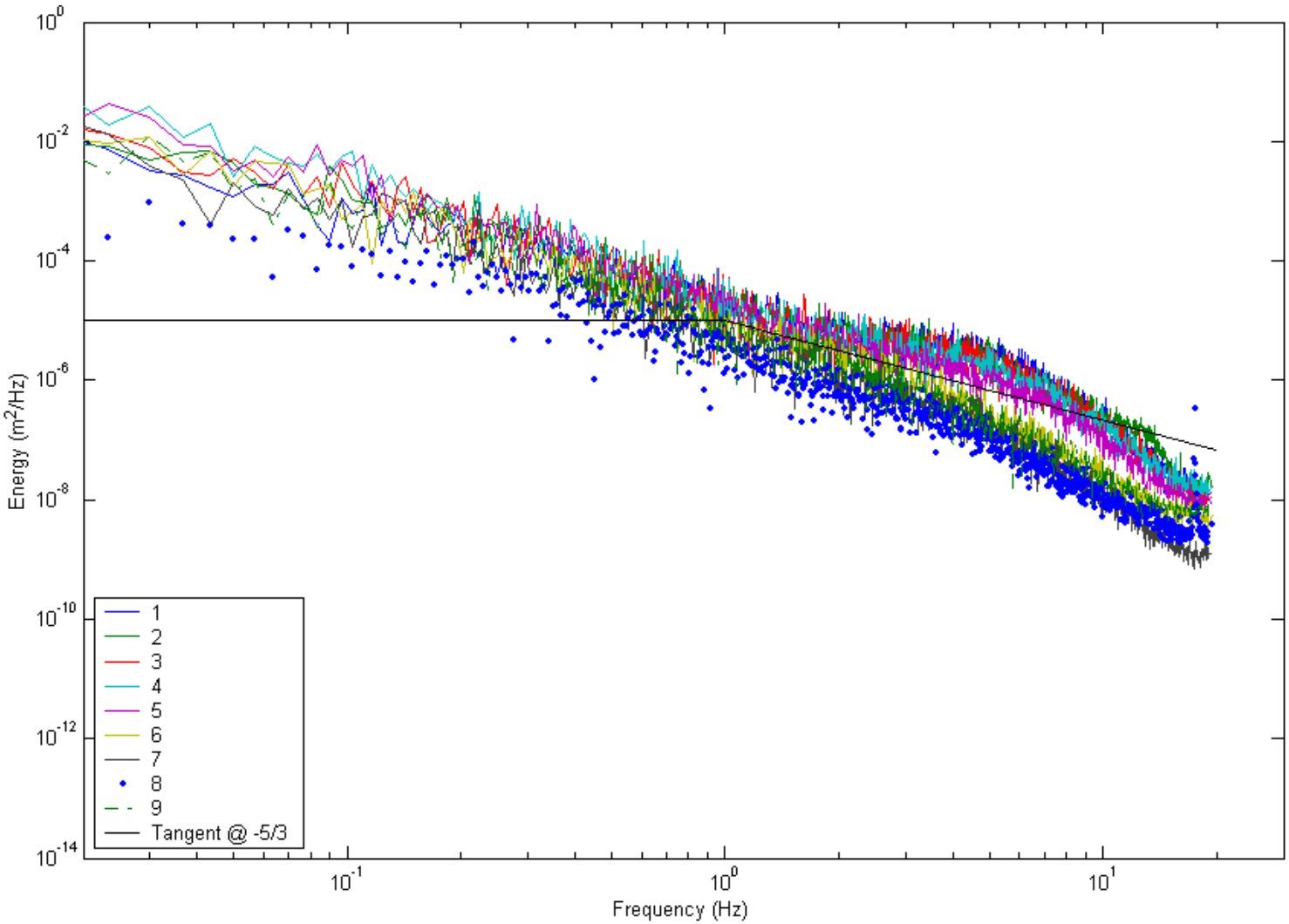

Figure 5.49: Power spectrum for a vertical array with at x=0m & y=7m for a current at 200% in Phase II

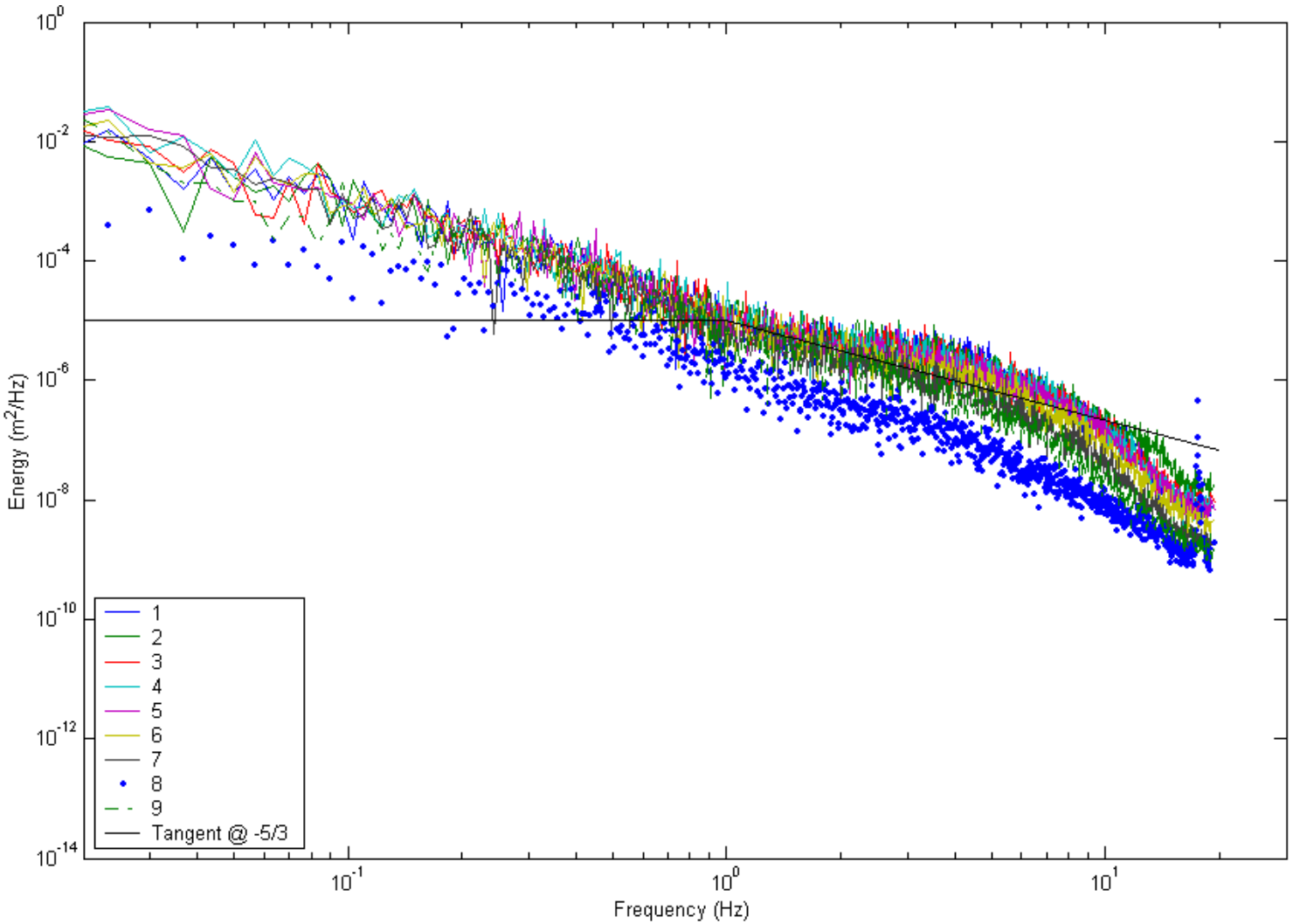

Figure 5.50: Power spectrum for a vertical array with at *x*=-24m & *y*=7m for a current at 200% in Phase II

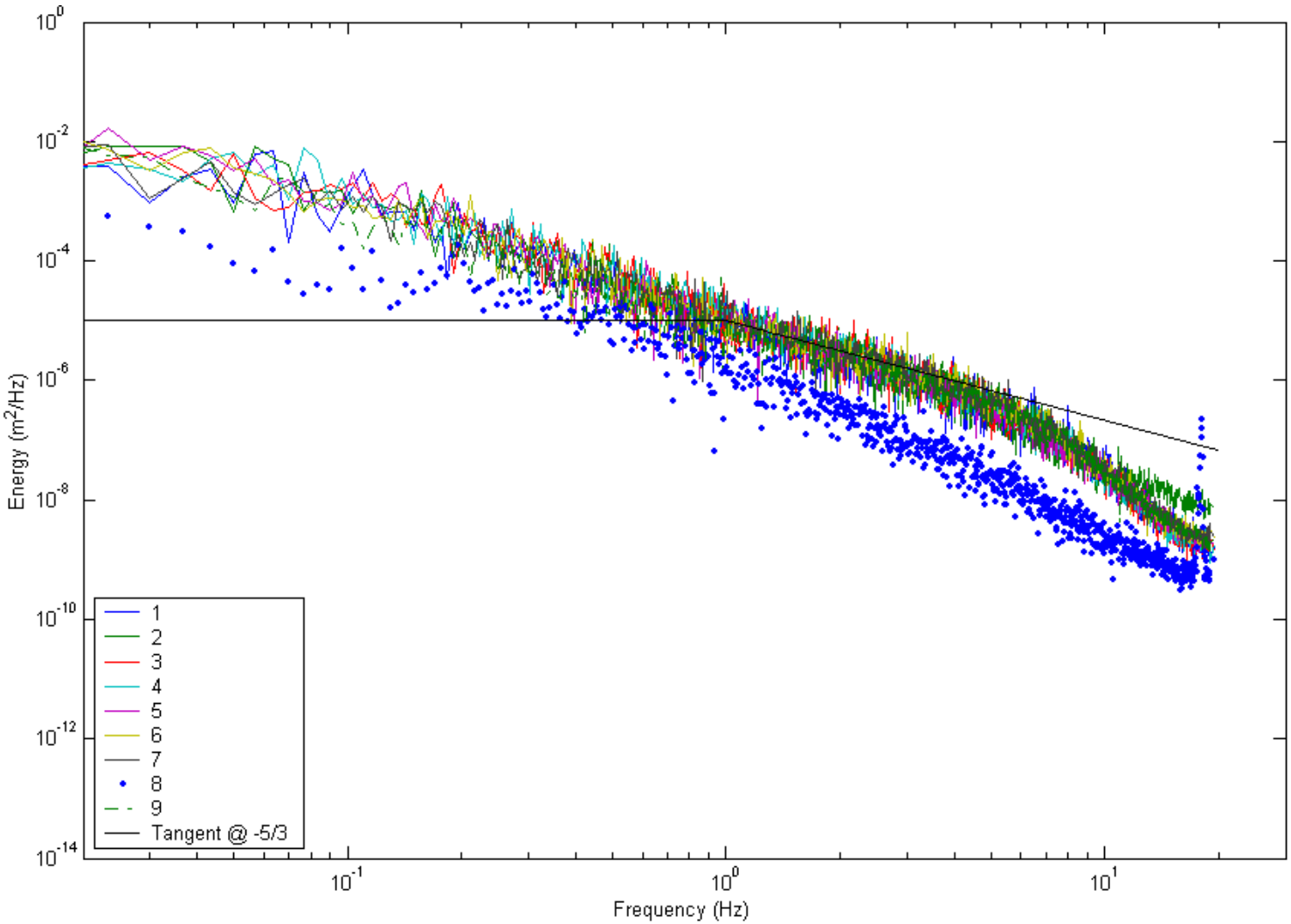

Figure 5.51: Power spectrum for a vertical array with at *x*=0m & *y*=42m for a current at 200% in Phase II

5.7 Wave + Current Tests

Now that we have examined the principal types of tests, we need to make sure that what we have seen earlier can still be applied in the case of a test where waves and current are combined. When a model is tested in the wave basin, it is more commonly tested in combined waves and current than in current alone. It is interesting to investigate whether, according to the theorem of superposition, our result is a linear combination of a current test and a wave test, as illustrated in Figure 5.52.

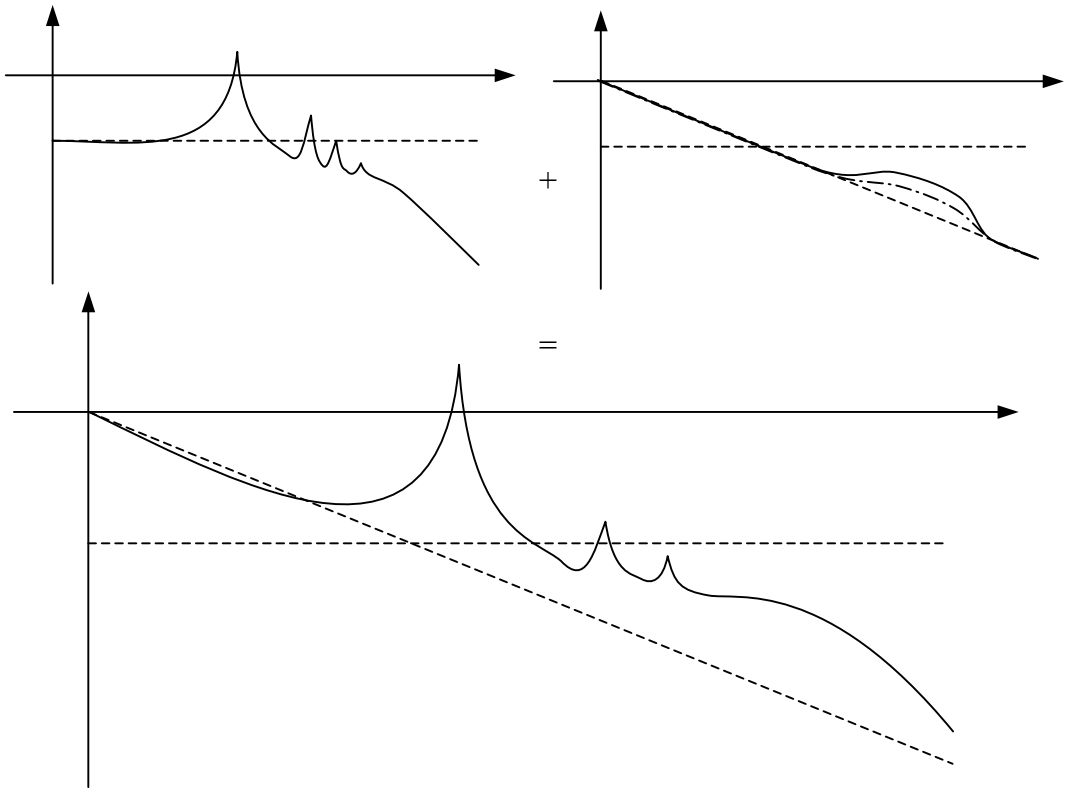

Figure 5.52: Expected process of superposition

Regarding the time series (Figure 5.53), we note that the signal is a superposition of a wave and a current: periodic signal modulated by a low frequency signal and some noise (Figure 5.54). We also have the same wave signal for each of the three depths.

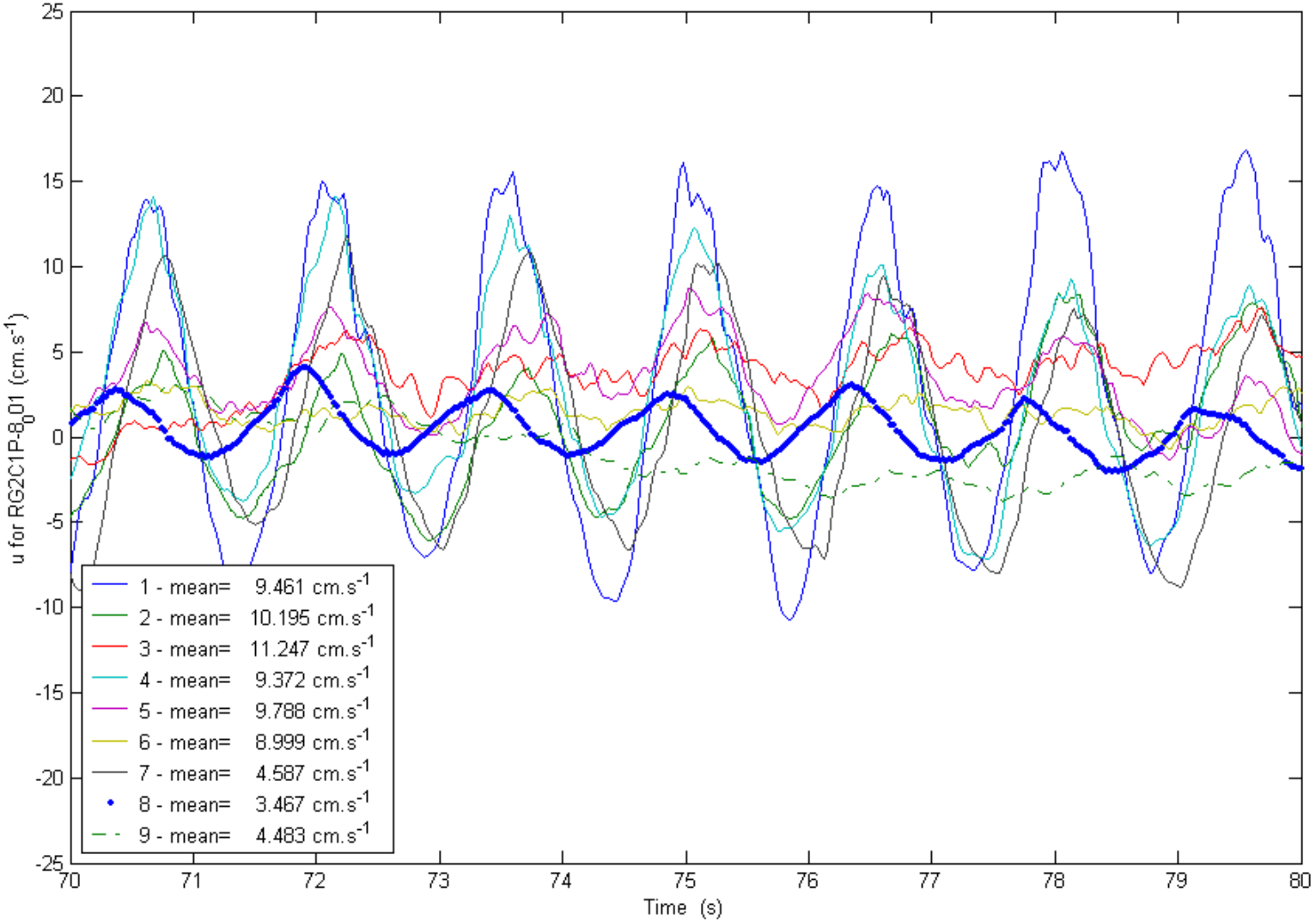

Figure 5.53: Time series for a regular wave + current test

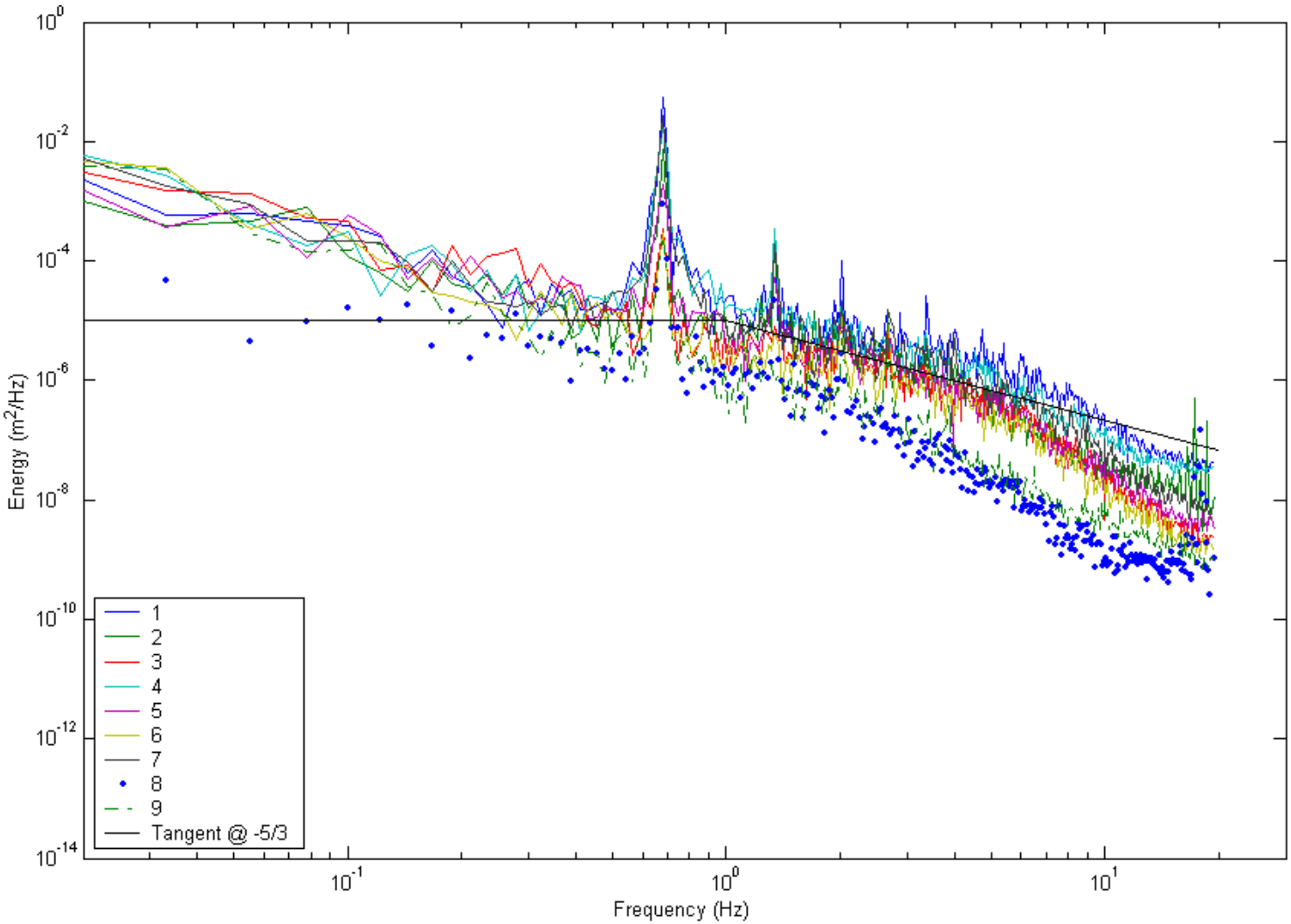

Figure 5.54: Power spectrum of the vertical velocity of a regular wave + current test

5.8 Blockage Correction Factors for Mean Velocity Measurements

5.8.1 Method

The results of the tow tests presented in Section 5.2 showed a linear relationship between the measured and actual velocity. We therefore applied a linear regression to the results in order to find the best approximation of the error under any circumstances and to find a good way to correct those errors measured. We tried to make the results fit the curve $V = a_0 + a_1 V_r + a_2 V_r^2$ where V_r is the measured velocity from the sensor and V is the actual velocity. We also tried to make the results fit to $V = a_1 V_r + a_2 V_r^2$ or $V = a_1 V_r$ in order to find the most robust relationship with the least number of coefficients. The coefficients are easily found by applying the following equations:

$$\begin{cases} \underline{a} = \underline{V} / \left[\underline{1} \quad \underline{V_r} \quad \underline{V_r^2} \right] \\ \underline{a} = \underline{V} / \left[\underline{V_r} \quad \underline{V_r^2} \right] \\ \underline{a} = \underline{V} / \left[\underline{V_r} \right] \end{cases} \tag{5.5}$$

All the coefficients were plotted in Appendix A. In this appendix, we plotted a_0, a_1 and a_2, for every orientation (North-South, East-West and Vertical), and finally for every method (3, 2 and 1 coefficient).

5.8.2 *Quadratic Model with Non-Zero Bias:* $V=a_0+a_1v+a_2v^2$

This method is the one that should provide the most accurate result and will serve as a basis for the next comparisons. As we can see in Appendix A, the coefficient a_0 is varying significantly. However, the absolute value of that coefficient is always under 3cm/s, which is relatively small. We can notice that though there are fewer tests, the a_0 results for the East-West orientation are less variable than for the other two orientations.

The next step is then to look at a_1. For the North-South orientation, a_1 is varying around 1.2m and it is varying from sensor to sensor. On the other hand, for the two other orientations, the coefficient is very close to 1, which means that the measured value is almost the actual value.

Finally, looking at the coefficient a_2, we can see that it is really small (4.10^{-3} s/cm maximum) so that it is just an adjustment to optimize the model. The small values of a_2 indicate that the quadratic term is possibly unnecessary.

Now that we have our coefficients, we can have a look at the error according to the tow speed. We used two different methods for computing the error. The first one was to calibrate one set of coefficients per phase and the other one was to calibrate only one set of coefficients for all phases combined together. As we can see in Appendix A, the behavior of the error according to the tow speed is the same in both cases but in the case of only one set of coefficients, the errors are amplified while still staying under 5%. Also, an interesting feature is that the error is getting lower as the tow speed is increased.

Finally, examining the standard deviation of the error, we note that whether we are using a coefficient for each phase or just an overall coefficient for the North-South and East-West orientation, the standard deviation is not changing and stays below 3%. However in the Vertical orientation, the values are twice as high: from 6% to 3%

5.8.3 *Quadratic Model with Zero Bias:* $V= a_1v+a_2v^2$

We will now compare the results to the first model with the three coefficients. We note that a_1 is now varying less according to the sensor and it stays around the value of 1.3 for the three phases with the North-South orientation. We have the same behavior for the Vertical and East-West orientations where the coefficient is pretty close to 1. We can see that a_2 is closer to 0 now and that it is getting negligible for the North-South

orientation (maximum of 1.5×10^{-3}) but is pretty much the same for the Vertical and East-West orientations.

We have the exact same behavior in the error as in the first model except for the East-West case where we have a bigger error for the low tow speeds. Finally, the profile of the standard deviation is also the same as in the previous model.

5.8.4 Linear Model with Zero Bias: V= a_1v

For the linear model, we see that a_1 is very close to the previous values associated with the quadratic models. However, without a quadratic term, we expect to have a bigger error. Except for Phase I, the error is almost the same as in the case of the two coefficients and we find the same profile when we take only one set of coefficients. Finally, the standard deviation is the same as for the two previous models.

5.8.5 Conclusions on the Regression Model

The coefficients for the three blockage correction models are all summarized in Table 5.7. It appears from the results that the coefficient a_0 is not significantly different than zero, which is to be expected since the zero offset has already been removed using the calm tests. The linear term is by far the most important. For the North-South orientation, a_1 is in the range of 1.2 to 1.3, indicating a 20%-30% error correction. For the Vertical and East-West orientations, a_1 is in the range of 1.0 to 1.1.

The coefficients for the quadratic term are pretty small. The quadratic term does provide a small improvement. Its use is a matter of choice. Note that blockage correction factors cannot be applied to the velocity components that are transverse to the mean flow direction.

Table 5.7: Coefficients from the regression

Summary of the coefficients			$V = a_0 + a_1 V_r + a_2 V_r^2$			$V = a_1 V_r + a_2 V_r^2$			$V = a_1 V_r$		
			NS	EW	V	NS	EW	V	NS	EW	V
a0	Average	1	0.6052	1.8477	0.506						
		2	-0.4187	0.4298							
		3	1.77218		0.63433						
		all	0.73363	0.7843	0.6215						
	St Dev	2	1.07665	0.3033							
		3	1.00834		1.09007						
		all	1.46718	0.7509	1.02853						
a1	Average	1	1.3069	0.9771	1.0896	1.363	1.1272	1.1303	1.2431	1.0944	1.0853
		2	1.3143	1.0222		1.2849	1.0472		1.26078	1.05693	
		3	1.1855		1.00458	1.3121		1.0429	1.29964		1.06402
		all	1.24949	1.0109	1.01308	1.3028	1.0672	1.0517	1.27923	1.0663	1.06615
	St Dev	2	0.0946	0.0089		0.0281	0.0246		0.03837	0.02806	
		3	0.07378		0.06021	0.0385		0.0751	0.02428		0.03931
		all	0.10288	0.0237	0.06281	0.0379	0.0448	0.076	0.03663	0.02959	0.03766
a2	Average	1	-0.0029	0.0016	-0.0006	-0.004	-0.001	-0.001			
		2	-0.0011	0.0006		-0.0006	0.0002				
		3	0.00163		0.00094	-0.0003		0.0004			
		all	0.00019	0.0008	0.00079	-0.0006	-0.0001	0.0003			
	St Dev	2	0.00115	0.0003		0.0004	1E-04				
		3	0.0012		0.00074	0.0006		0.0009			
		all	0.0019	0.0006	0.00085	0.001	0.0006	0.001			

6. MAPPING OF THE CURRENT STRUCTURE

6.1 Mapping of the Average Current in the Wave Basin

All of the measurements for the mapping of the current in the wave basin were done using a North-South orientation of the MAVS sensors. However, we also have seen that, due to blockage effects, this orientation is giving us the least accurate results. But as demonstrated in Section 5.6, we are now able to correct most of that error, leaving a small residual error for the mean velocity up to 5%.

The mapping of the current in the wave basin will be done with the corrected values of the mean velocity and also for all x, y and z velocity components u, v and w. Although views with arrows representing the flow field are more natural, the 3-dimensional representation is not clear. Therefore, separate maps for the three velocity components will be presented.

The velocity maps for all the currents investigated are provided in Appendix B. The plots have been grouped so that we can see the effect of an increase in the current generated (100%, 200% and finally 225% pump capacity). Finally, the plots are grouped according to the type of array used for a current only condition (3*3 array with x<0, 3*3 array with x>0, Vertical array and Horizontal array) and for a Wave + Current condition (always in a 3*3 array but with different types of waves, whether regular (RG2 and RE5) or random (RN)).

Appendix C on the other hand contains one-dimensional velocity profiles along the x, y or z-axis. The plots are organized to facilitate comparisons of profiles at different current speeds (100% *vs*. 200% or 100% *vs*. 225%). The order in which the arrays are presented is the same as in Appendix B.

*6.1.1 3*3 Array*

The first series of tests for the mapping of the current in the wave basin was done with a 3 by 3 array. This type of array covers the center of the wave basin well and provides some information about the symmetry of the current. The main interest will be directed toward the *u* signal but we will also look at the *v* and *w* components to determine the circulation pattern in the wave basin.

Referring to Figures B.13 and B.17, we can see that close to the current generator nozzles ($x \simeq 10\text{m}$), the surface currents are really strong. The *u*-velocity map (Figures B.14 and B.18) shows a bulge that dissipates with increasing distance from the current nozzles. On the other hand, for the vertical *w*-velocities, the profile is constant over *y* for x=0, but as *x* decreases and the measurements are made further away from the current generator, the downward velocities move from the center to the extremities of the area of interest (Figures B.4 and B.8). For the transverse horizontal *v*-velocity, we notice that there is a rotation of the current at the bottom east side and at the top west side of the area of study (Figures B.3 and B.11) but these *v*-velocities are of the order of 10% of the horizontal *u*-velocity.

Given the 3D mapping of the average current in the basin, it is interesting to see what the profile of the current is, as it will lead us later to an assessment of the uniformity of the current in the basin. First of all, there is clearly a decrease of the velocity in the *x* direction as we are going toward the wave absorber. However, the rate of decrease is relatively low. The velocity also decreases with the depth. There is an interesting feature when we superpose waves on a current, it seems that the current profile deepens and the surface current reduces (see velocity profiles in Appendix C).

Finally, we notice from the 3*3 array measurements that in the transverse *y* direction, the profile is not perfectly symmetric. It seems that the velocities measured on

the west side of the basin are larger than the ones measured on the east side ($y<0$). This seems to be confirmed from the tests with a current set up at 225%.

6.1.2 Vertical Array

The measurements made with the Vertical array provide the maximum area coverage with the best grid resolution. Figures B.22 and B.26 clearly show the characteristic bulge in the *u*-velocity map at the center of the wave basin associated with the primary jet flow. This bulge is decaying with distance from the current generator as expected. For the test at a 200% current (Figure B.26), the bulge is much more noticeable but also there is a more noticeable counter current on the sides of the wave basin. As *u* is getting bigger, this counter current is getting stronger and the width of the bulge is getting narrower.

The horizontal *v*-velocity appears stratified in the 100% current case (Figure B.23). On the other hand, in the 200% current case (Figure B.27), those areas of stratification narrow to create bulges above the area where there is the shear of the horizontal current *u*. Moreover, in the same areas, we have the presence of an upward current (Figure B.28).

The profiles with a vertical array show the same behavior as for the 3 by 3 array. However, because the area covered by the measurements is larger, there is more information on the extremities. For example, we see better the bulge in the center, but it is interesting to notice that the bulge does not maintain a perfect straight profile of the *u* velocity along the *y*-axis. That is, the shear and return current near the basin wall are now clearly visible. For the profile along the *z*-axis, we have confirmation that the velocity is linearly decaying with the depth. This vertical decay is more noticeable for the 200% current case.

6.1.3 Horizontal Array

Contrary to the previous types of arrays, measurements with the horizontal array were not done at different water depths. The horizontal array was use to develop a more detailed map of the surface current. In particular, the measurements provide more detail on the return current at the surface.

The velocity profile of *u* along the *y*-axis, for 100% and 200% current are very similar (Figures B.29 and B.30). The only difference is on the extremities as this time the return current displays a negative velocity. We can see too that the bulge is decaying along the *x*-axis pretty fast with a current set up at 200%, while it stays almost constant with the current tests at 100%.

6.1.4 Spatial Uniformity of the Mean Current

It is of great interest to assess the spatial uniformity of the current in the OTRC basin. Ideally, one would like to be able to generate a current that is uniform through the length and width of the basin. Obviously, this is not possible with the set-up in the OTRC basin. We therefore need to quantify the degree of uniformity achievable.

The degree of uniformity will be assessed by defining the boundary within which the difference between the *u*-velocity component and a reference value is within a specified threshold ε (10% or 20% difference). In the following Figures 6.1 through 6.4, the blue circles correspond to the location of the reference current profile, which is $x = 0$, $y = -7\text{ft}$. The reference profile was not chosen at $x = 0$ & $y = 0$ because of an anomalously high velocity measured at that location, which would have distorted the subsequent results.

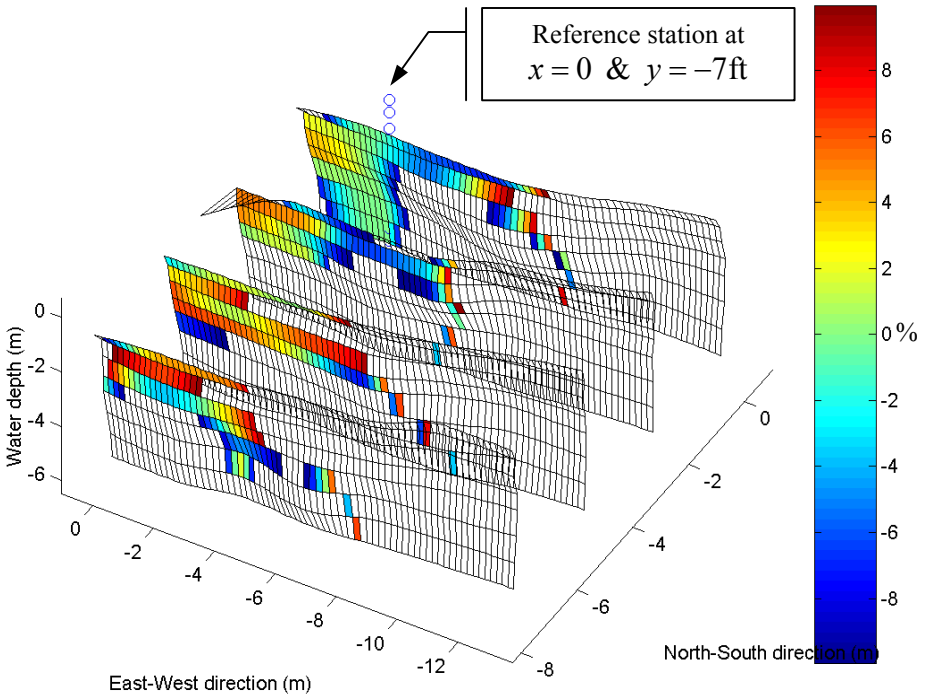

Figure 6.1: Variability for a vertical array with a current at 100% and ε=10%

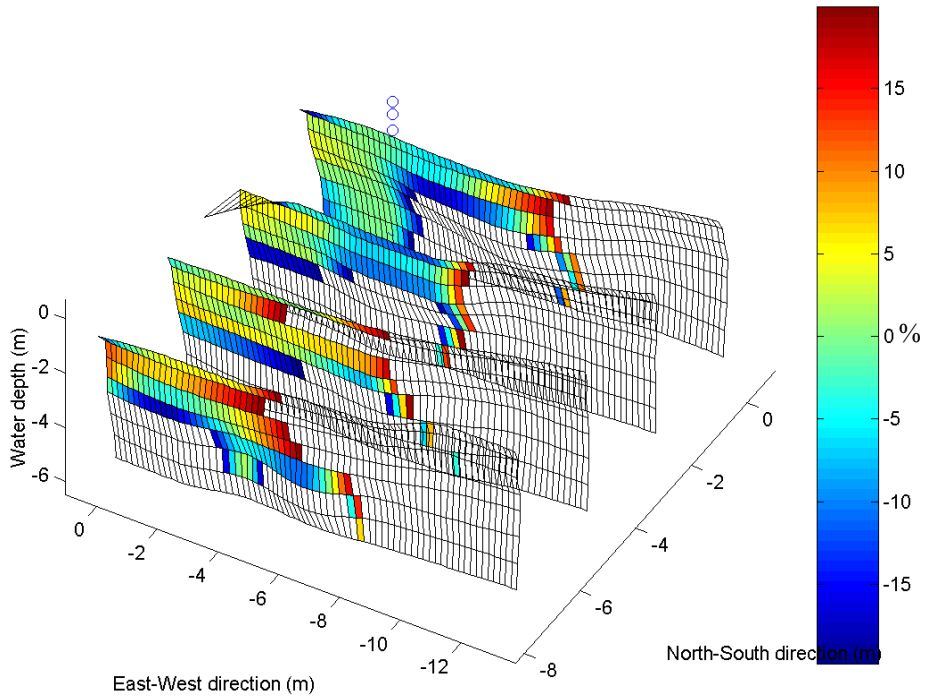

Figure 6.2: Variability for a vertical array with a current at 100% and ε=20%

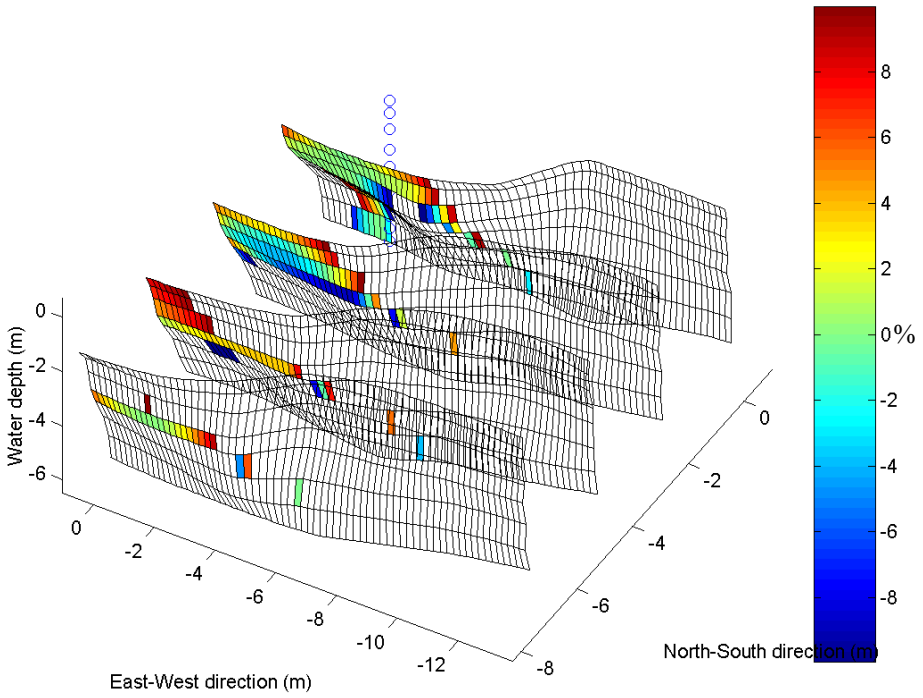

Figure 6.3: Variability for a vertical array with a current at 200% and ε=10%

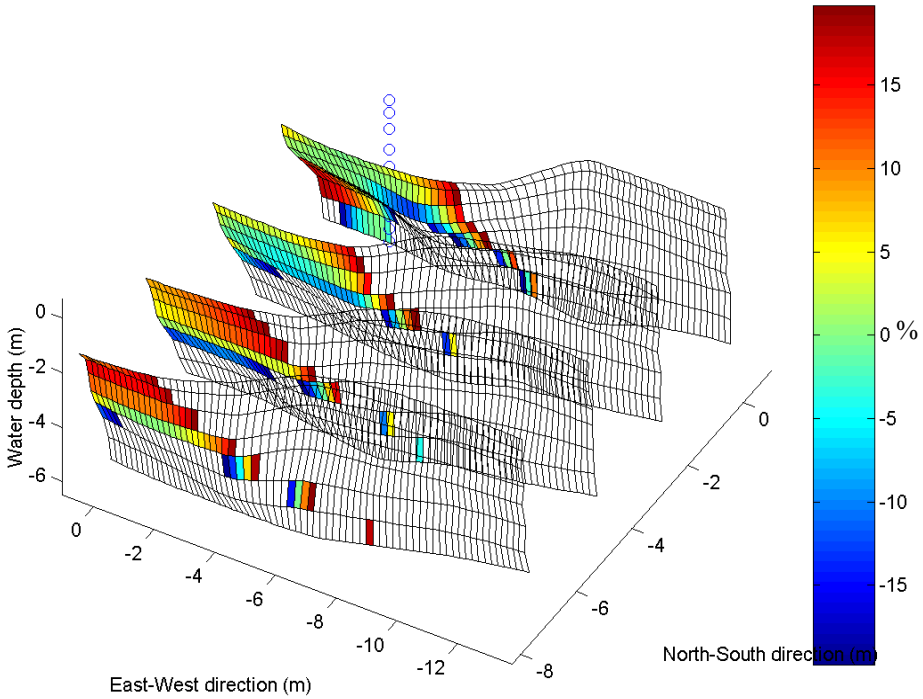

Figure 6.4: Variability for a vertical array with a current at 200% and ε=20%

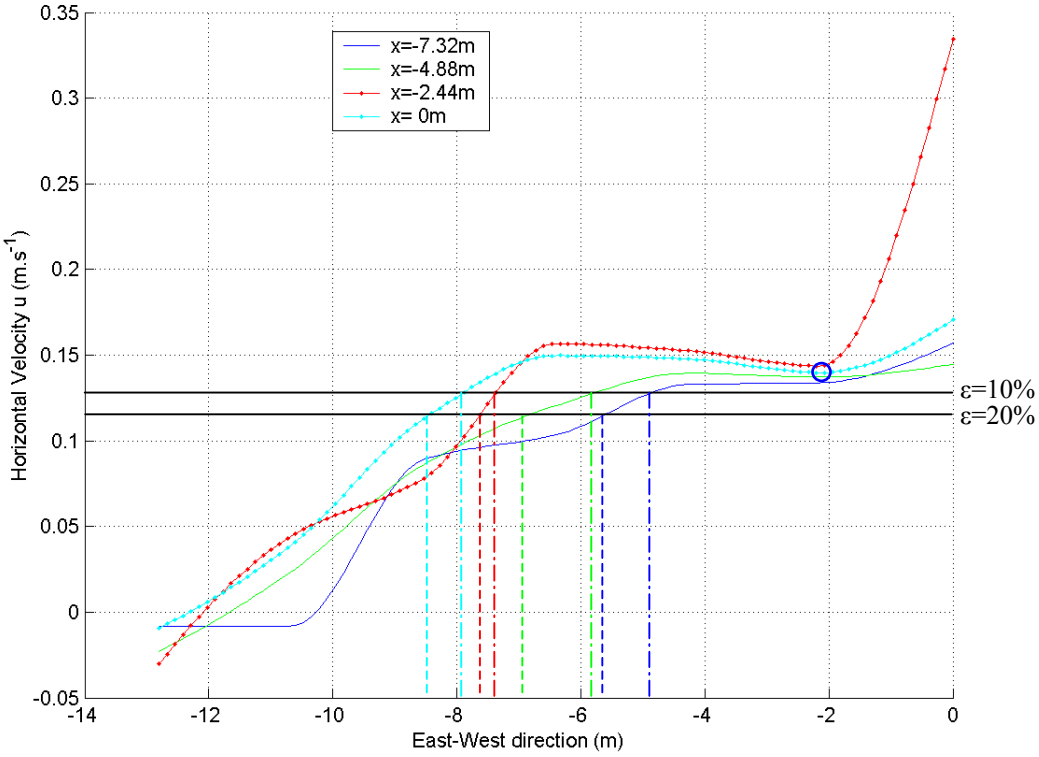

Figure 6.5: Surface velocity profile for a current at 100%

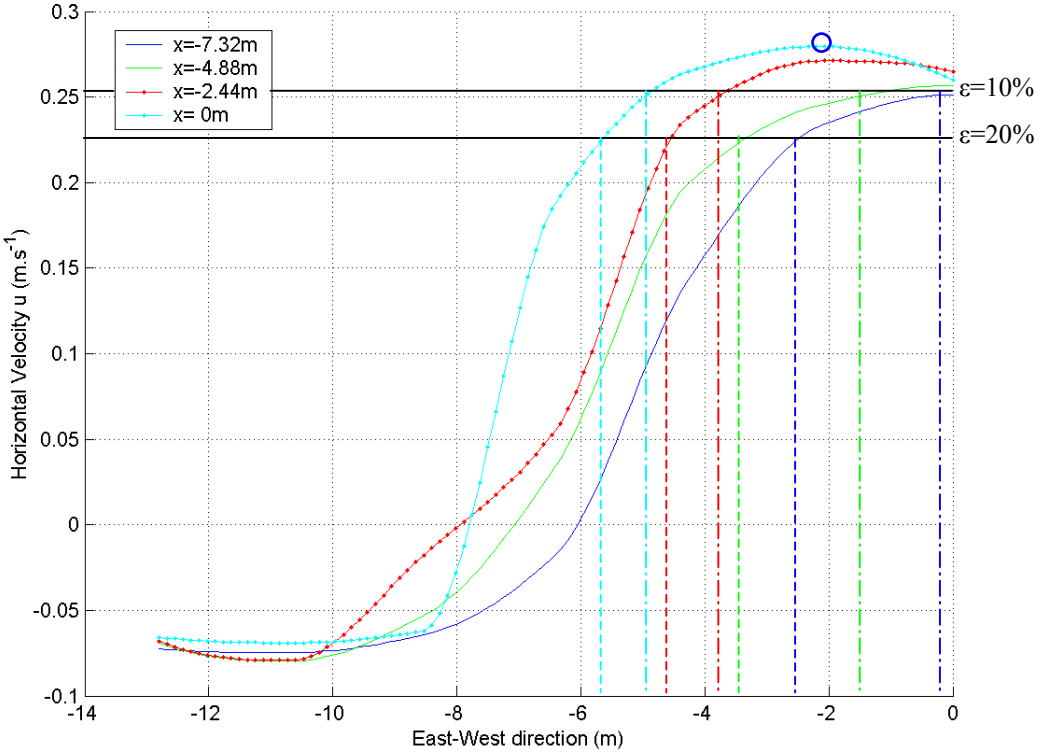

Figure 6.6: Surface velocity profile for a current at 200%

Figures 6.1 through 6.4 clearly show the domain in which the specified threshold difference is not exceeded. The colored panels define the domain. As expected, an increase of the threshold will increase the domain size. However with a stronger current at 200%, the strong return current narrows the domain size. In order to illustrate the concept of a domain of uniform current, Figures 6.5 and 6.6 represent the surface velocity profiles for current at respectively 100% and 200% measured using the vertical array. In these figures, the dotted lines represent the measurements taken for $x \in [-5\text{m}; 5\text{m}]$. The blue circle represents in every case the location of the reference station. To illustrate the domain of uniformity, the dash-dotted line represents the threshold of 10% while the dashed line represents the threshold of 20%. A summary of all the threshold values can be found in Table 6.1.

The results show that in the region where $x \in [-7.32\text{m}; 0\text{m}]$, the surface velocity of the 100% current is reasonably uniform over a 10m width (5m on either side of the centerline). For the 200% current, the surface velocity is reasonably uniform in the region where $x \in [-4.88\text{m}; 0\text{m}]$ over a 3m width (1.5m on either side of the centerline).

Table 6.1: Limits of the volume corresponding to a 10% or 20% difference to a reference value with 10 interpolation values

		y minimum (m)				*y* maximum (m)			
		100% Pump		200% Pump		100% Pump		200% Pump	
x (m)	*z* (m)	10% threshold	20% threshold	10% threshold	20% threshold	10% threshold	20% threshold	10% threshold	20% threshold
0	-0.3	-7.98	-8.53	-4.82	-5.75	-0.74	0	0	0
	-0.76	-6.87	-8.16	-5.01	-5.57	0	0	0	0
	-1.37	-7.61	-7.98	-5.38	-5.57	0	0	0	0
	-2.13	-7.98	-8.16	-5.57	-5.75	0	0	-0.93	0
	-2.74	-8.35	-8.53	-5.75	-5.94	0	0	-1.3	0
	-3.66	-8.35	-8.53	-6.31	-6.49	0	0	-1.48	0
	-4.57	-7.98	-8.16	-7.24	-7.61	0	0	-0.74	-0.37
	-5.49	-5.94	-6.12	-9.28	-9.28	-1.48	-1.3	0	0
-2.4384	-0.3	-7.42	-7.61	-3.71	-4.45	-1.86	-1.48	0	0
	-0.76	-7.05	-7.42	-4.08	-4.64	0	0	0	0
	-1.37	-7.052	-7.24	-4.45	-4.82	0	0	0	0
	-2.13	-7.24	-7.24	-5.01	-5.38	0	0	0	0
	-2.74	-7.05	-7.24	-5.57	-5.75	-7.05	-7.98	0	0
	-3.66	N.A.	N.A.	N.A.	N.A.	N.A.	N.A.	N.A.	N.A.
	-4.57	N.A.	N.A.	N.A.	N.A.	N.A.	N.A.	N.A.	N.A.
	-5.49	N.A.	N.A.	-0.74	-0.93	N.A.	N.A.	-0.56	-0.37

Table 6.1: Continued

		y minimum (m)				*y* maximum (m)			
		100% Pump		200% Pump		100% Pump		200% Pump	
x (m)	*z* (m)	10% threshold	20% threshold	10% threshold	20% threshold	10% threshold	20% threshold	10% threshold	20% threshold
-4.8768	-0.3	-5.94	-7.24	-1.48	-3.53	0	0	0	0
	-0.76	-2.78	-3.9	-1.48	-3.71	0	0	0	0
	-1.37	-6.49	-7.05	-1.86	-4.27	0	0	0	0
	-2.13	-7.05	-7.24	-4.64	-5.01	0	0	0	0
	-2.74	-7.42	-7.42	N.A.	-5.57	0	0	N.A.	0
	-3.66	N.A.	N.A.	N.A.	N.A.	N.A.	N.A.	N.A.	N.A.
	-4.57	N.A.	N.A.	N.A.	N.A.	N.A.	N.A.	N.A.	N.A.
	-5.49	N.A.	N.A.	-0.56	-2.78	N.A.	N.A.	-0.56	-0.56
-7.3152	-0.3	-5.01	-5.94	-0.37	-2.6	-0.19	0	0	0
	-0.76	-3.34	5.38	N.A.	-2.78	-0.56	0	N.A.	0
	-1.37	-5.01	-5.94	N.A.	-3.34	-0.37	0	N.A.	0
	-2.13	-5.19	-6.31	N.A.	-4.64	0	0	0	0
	-2.74	N.A.	N.A.	-4.08	-5.19	N.A.	N.A.	N.A.	0
	-3.66	N.A.	N.A.	N.A.	N.A.	N.A.	N.A.	N.A.	N.A.
	-4.57	N.A.	N.A.	N.A.	N.A.	N.A.	N.A.	N.A.	N.A.
	-5.49	N.A.	N.A.	N.A.	N.A.	N.A.	N.A.	N.A.	N.A.

6.2 Mapping of the Turbulence in the Wave Basin

The mapping of the turbulence in the OTRC basin will be done on the basis of the simple isotropic turbulence model presented in Section 2.4. We will use that model to determine the integral length scale and energy dissipation rate at each point by fitting the model for the one-dimensional velocity spectrum to the data. The fitting procedure finds the integral length scale that minimizes the summation of the square of the error between the spectral ordinates while preserving the total variance. The fitting procedure is robust and yields consistent values for the dissipation rate. However, because of insufficient low frequency / wavenumber resolution, the indicated values of the integral length scale are highly variable. This deficiency could be improved by taking longer data records that would lead to a smaller frequency increment and thus, a better resolution in the lower frequencies.

Appendix D contains maps of the turbulent energy dissipation rate ε, the integral length scale l and the turbulence intensity S_D/U obtained from the u-velocity spectrum for all the current conditions tested. The plots are organized so that we see the outcome of a change in velocity for each type of sensor array. The integral length scale is the only variable that has a meaning in terms of length while plotted. The dissipation rate can be related to the integral length scale through the relationship:

$$\varepsilon \sim \frac{u'^3}{l} \tag{6.1}$$

We are using the local mean velocity U as the average velocity transporting the turbulence in order to apply the frozen turbulence approximation and to find the integral length scale at the same point. Indeed, there is no way to find the integral length scale at $y \neq 0$ using the velocity at $y = 0$. As they are too close to zero, the average velocities v and w can't be used to derive wavenumber spectra for the transverse velocities. The

frozen turbulence approximation cannot be applied in the case of a transverse velocity as the eddy velocity is not much smaller than the mean velocity (Taylor's hypothesis) in the transverse direction. For the same reason, for the inline velocity *u*, there will be locations where S_D/U is not sufficiently small and the frozen turbulence approximation is not valid. We will consider that the frozen turbulence approximation is not valid in the areas where $S_D/U > 0.25$ or $U < 0.1$. These areas are marked with a superposed mesh in the maps provided in Appendix D.

The results in Appendix D show that, in general, the greater the integral length scale, the smaller the dissipation rate. The measurements from the vertical array show that the dissipation rate is higher in the regions where the shear stress is greater, *i.e*. in the region where the counter-current and the currents are meeting. However, the validity of this observation is diminished by the fact that S_D/U is often greater than 25% in the region of counter-current shear, which indicates that the basis for application of the frozen turbulence approximation was not satisfied in the first place.

Another interesting observation is that the superposition of waves with current generates a much higher dissipation rate and a smaller integral length scale. This is partially due to the fact that the wave train is providing more energy to the spectrum, which in turn increases the dissipation and reduces the integral length scale. The fitting procedure for the turbulence model has been adjusted to take that into account by removing the wave part of the spectrum and replacing it by a -5/3 slope (as illustrated in Figure 6.7). But this is also changing the spectrum and it results in some loss of accuracy (we recall that a small shift in the fit of the turbulence model may result in a non negligible difference in the integral length scale).

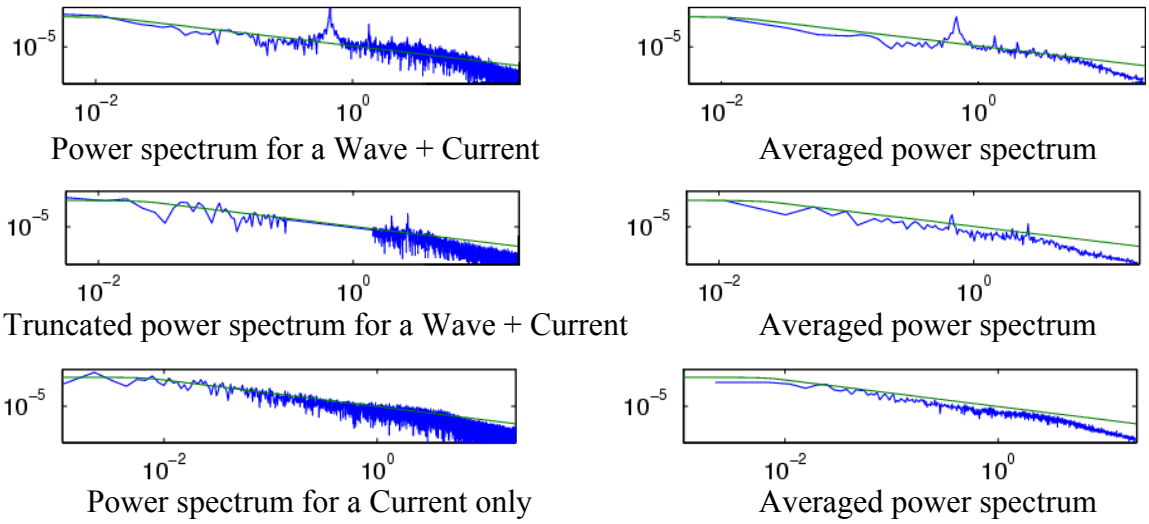

Figure 6.7: Turbulence model

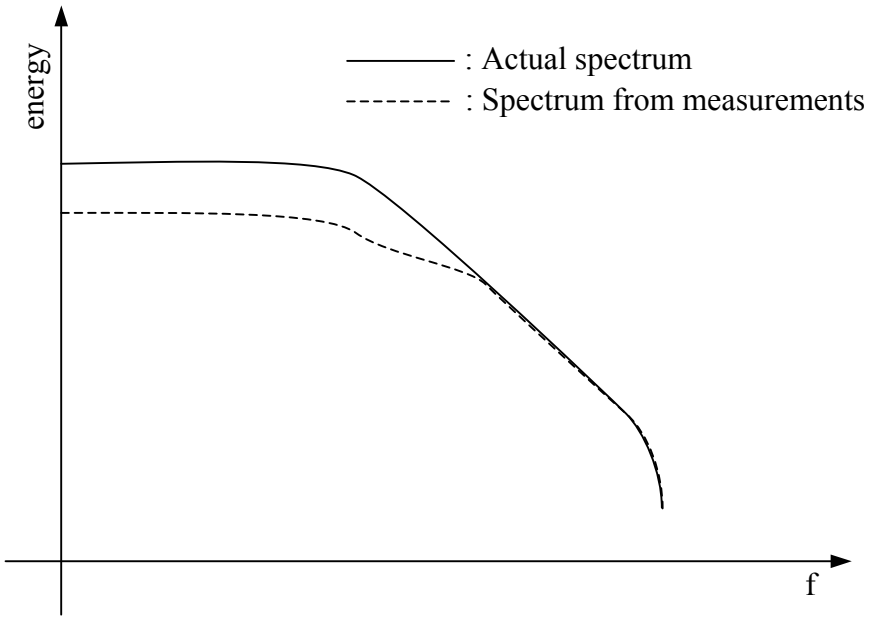

Figure 6.8: Possible consequence of low frequency distortion of MAVS due to blockage effects

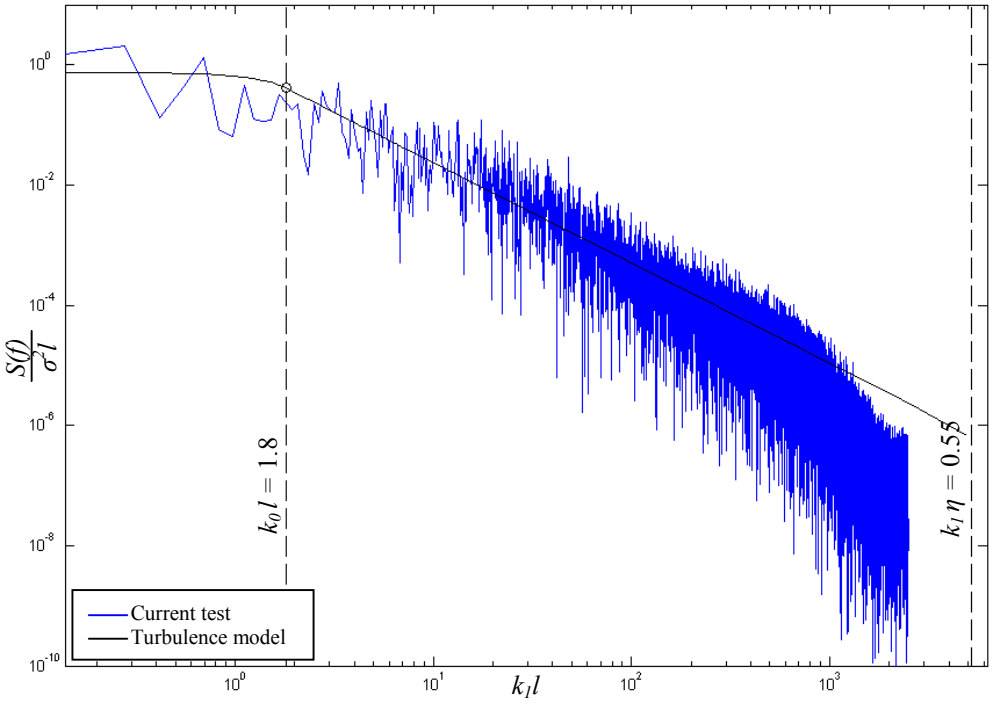

Figure 6.9: Turbulence model with a wavenumber scale

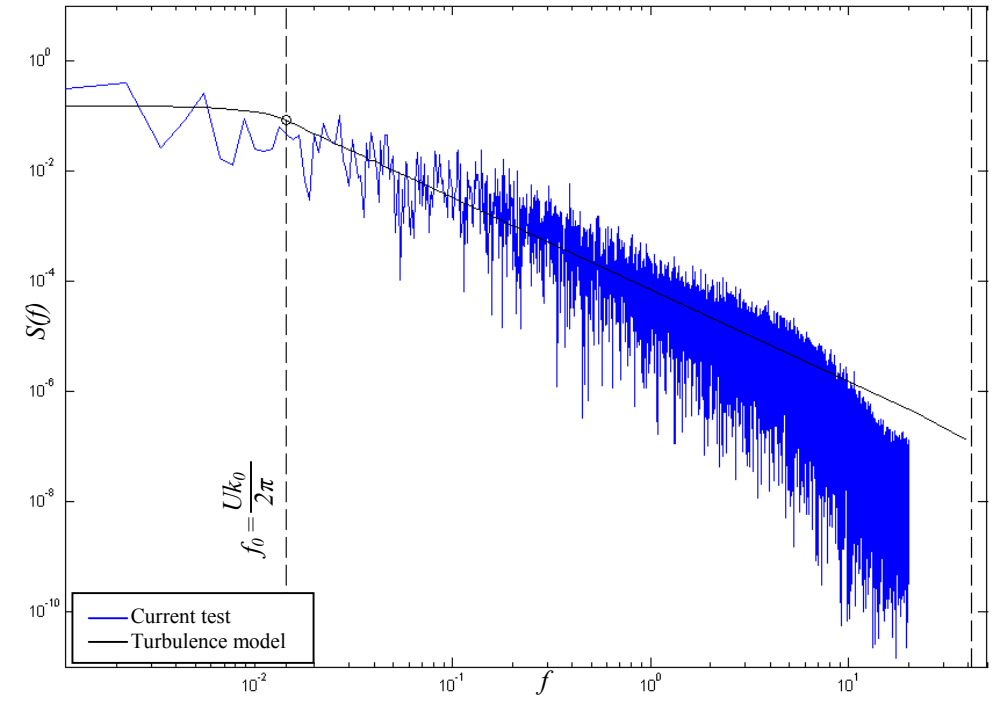

Figure 6.10: Turbulence model with a frequency scale

In Figure 6.7, the *x*-axis corresponds to the frequency and the *y*-axis is the power spectral density, both axes using a logarithmic scale. Figure 6.8 on the other hand shows the possible consequence of the low frequency distortion on the power spectrum, as it would be discussed later. The difference of scales between the frequency domain and the wavenumber domain is represented in Figures 6.9 and 6.10. We clearly see in these figures the fit of the model spectrum to the data measured. On these figures, the circle represents the wavenumber found by the model as the boundary between the production subrange and the inertial subrange. For this example, we had an average *u*-velocity of $U = 16.72\text{cm/s}$ and a standard deviation of $S_D = \sigma_u = 6.02\text{cm/s}$, which lead to an integral length scale of $l = 3.31\text{m}$, a dissipation rate of $\varepsilon = 7.1\times10^{-5}\text{m}^2.\text{s}^{-3}$ and a microscale of $\eta = 3.5\times10^{-4}\text{m}$.

There is a possible important limitation of the turbulence measurements due to the fact that in the North-South orientation in particular, the MAVS may not have a good response for low frequencies due to the blockage effect. Indeed, as shown in Figure 6.8, if the sensor measures less energy in the low frequencies than is actually present in the flow, this may be the cause of what has been called the bump in Section 5.6, after which the sensor starts to measure correctly the energy in the higher frequencies. If this is the case, it would lead to a difference of the area under the spectrum that cannot be corrected by the previously calibrated correction factors which apply to the average velocity only, and it would lead to a smaller integral length scale.

Finally, it is of some interest to determine whether the far field structure of the current jet in the OTRC basin exhibits the characteristics of a self-similar flow. For example, in a plane jet flow, we know that the integral length scale along the centerline of the jet should increase as x^1. Figure 6.11 shows the centerline values of the integral length scale determined from the surface velocity measurements in both the 100% and 225% current. Unfortunately, there is too much scatter in the results to be conclusive. The integral lengths scale values for the 225% current show much less scatter than for the 100% current. However, it does appear that the rate of increase of the integral length scale is less than in a plane jet: somewhere in the range of $x^{0.3}$ for the 100% current to $x^{0.05}$ for the 225% current. It is not possible to conclude that the rate of growth of the integral length scale is independent of the flow rate.

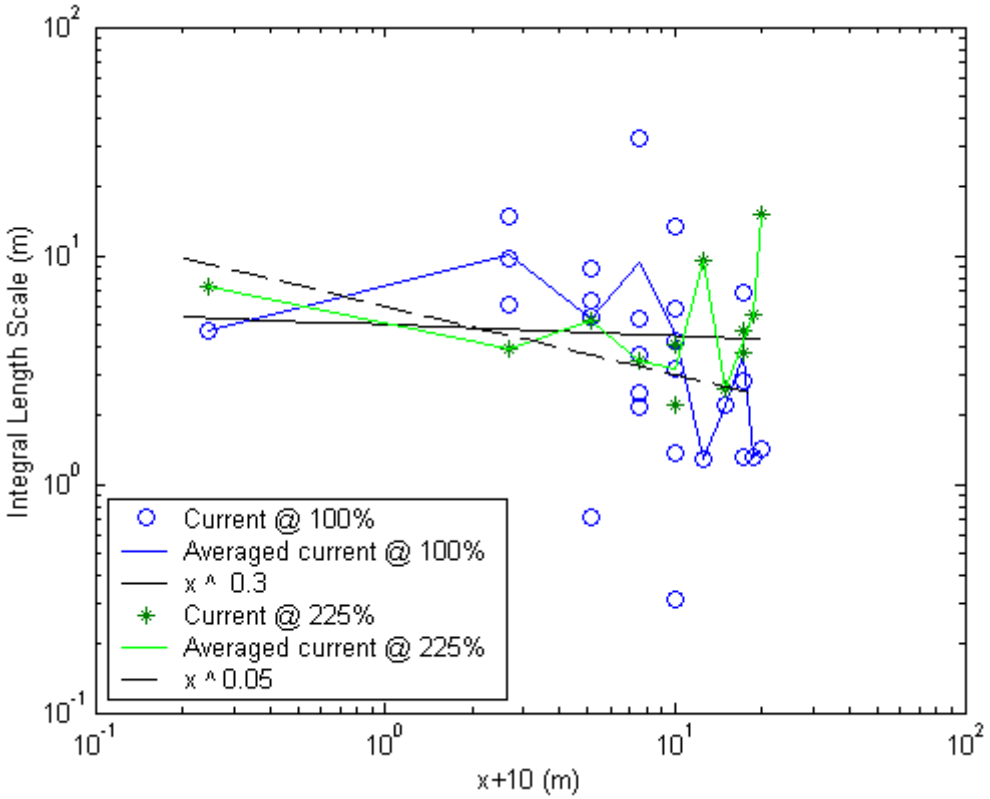

Figure 6.11: Integral length scale along the *x*-axis

7. CONCLUSIONS AND RECOMMENDATIONS

7.1 Summary and Conclusions

A thorough analysis of the performance of the MAVS current meter in different flow environments relevant to the OTRC wave basin has been performed. All of the features identified at the outset were identified in the MAVS time series measurement, namely:

- vortex shedding from transducer mounting rings and support rod;
- the effect of bridge vibrations in situations where the MAVS is towed;
- flow blockage by the main housing and by other sensors in close proximity and by the array mounting.

Figure 7.1 illustrates the velocity spectra for all the different types of flow conditions and all the features identified. The calm tests don't have a lot of energy over the whole range of frequencies (as expected). The spectrum for the tow tests on the other hand has more energy but is still relatively flat until the vortex shedding frequency is reached, beyond which the curve turns into a -5/3 slope until the Nyquist frequency of 20Hz is reached (with some high frequency peaks corresponding to bridge vibrations embedded). The spectrum for the regular wave flow is globally following the spectrum of the tow test with the addition of some peaks corresponding to the primary wave frequency and its harmonics. Since the waves generated in this study were of relatively small amplitude, the current-wave interaction was not very strong and so the spectrum for the wave + current flow appears to be a simple superposition of the associated wave spectrum and current spectrum. Also represented in Figure 7.1 is the turbulence model corresponding to the current spectrum.

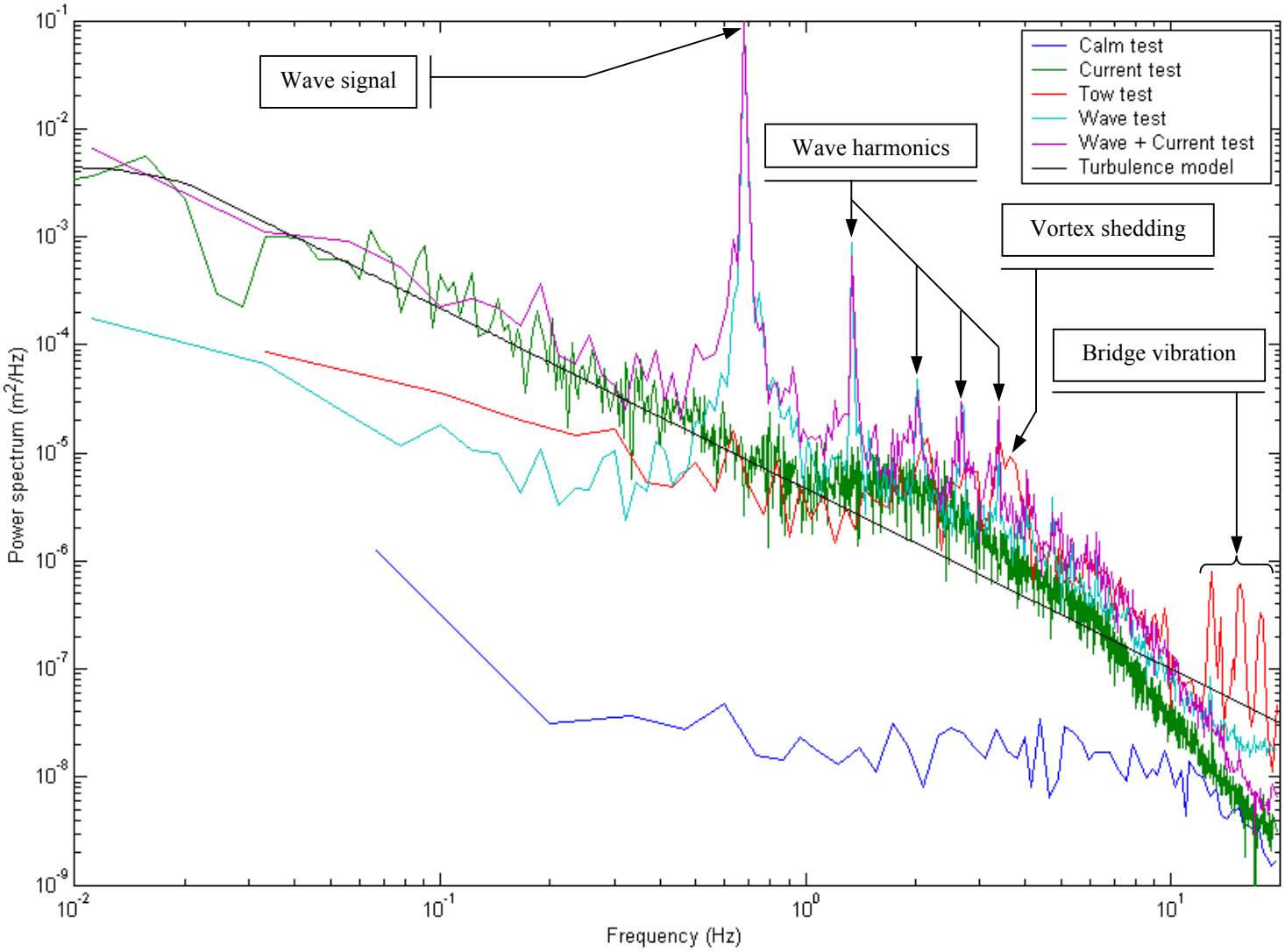

Figure 7.1: Comparison of the characteristic velocity spectra from various types of tests

A detailed analysis of the tow test results demonstrated that the measurement of mean velocity by the MAVS is sensitive to the orientation of the sensor relative to the mean flow, apparently due to flow blockage effects by the sensor housing, by the mounting device, and by other sensors mounted in close proximity. Fortunately, for any given sensor orientation and mounting scheme, it is possible using tow tests to calibrate simple linear and quadratic equations to correct the measured mean velocity for the blockage effect. The feasibility of applying the mean flow correction equations was demonstrated for three different sensor orientations (North-South, East-West and Vertical) and three different types of arrays (3*3, Vertical and Horizontal). It was observed that the mean flow blockage effect was significantly more severe for the North-South orientation (20-30% error) than for the other orientations (<10% error).

The experimental program was not specifically designed to investigate flow blockage for arbitrary sensor orientations or blockage effects on the measurement of low frequency/low wavenumber turbulence. This is left for subsequent studies. For example, one could study the low frequency response of the sensor with a forced oscillation mounting.

Using the knowledge gained on the performance of the MAVS, the measurements from the current tests (with and without waves) were used to map the three dimensional mean flow and turbulence structure of the current in the OTRC wave basin for the given set-up of the current generator. The measurements showed a jet-like flow that decays with distance from the current generator with weak return currents on the edges and floor of the basin. The higher the flow rate from the generator is, the narrower the jet and the stronger the return current are.

The turbulence structure in the jet was shown to be well-modeled using a simple isotropic turbulence model presented by Tennekes and Lumley (1972), By fitting the model to the MAVS measurements, it was possible to map the three-dimensional

structure of the turbulence energy dissipation rate and the integral length scale for regions where the mean flow was sufficiently strong to allow application of the frozen turbulence approximation.

The maps of the current flow allow one to determine the domain where the flow is reasonably uniform (within 10% or 20% variation). This knowledge is important for planning and interpreting model tests with current, where one wants to ensure that the scale model is located in the basin in a region of uniform flow.

7.2 Limitations of the Study

The analysis of the experimental measurements uncovered a number of limitations that should be addressed in subsequent studies.

An important limitation is the fact that nowhere in the study was the exact location of the sensors for the 3*3 array logged precisely. Indeed, this lack of information compromised the study of the wave tests where no correction factors could have been calculated and only a study of Phase I tests results was done. Although an attempt was made to estimate the sensor depths by an analysis of the pictures taken during the tests, a small error in the depth can generate a significant error in the theoretical velocity calculated using the measured wave elevation above the current meter.

Work should be done to find the distribution of the velocity correction factors according to the frequency and to the Keulegan-Carpenter number of the flow (measuring the amplitude of the oscillatory fluid motion relative to the sensor size). Once established, this distribution of correction factors can be applied to the power spectrum and then, by reversing the FFT, would generate the corrected velocity time

series. Such a capability would allow correction of the velocity measurements in both wave flows and turbulent flows.

The biggest limitation of the sensor is its use outside a wave basin test program. Indeed, as the correction factors to apply to the results during the post-processing are different depending on the relative sensor orientation, it is difficult to apply the right correction factors in the case of a measurement in the ocean where the orientation of the current is unknown, and thus, the correct results can't be found. However, if an accuracy of 15% is good enough, the MAVS satisfies most of our requirements.

A limitation of the turbulence model that we applied is that the Kolmogorov inertial subrange only exists for a Reynolds number $R_e > 10^5$. In the OTRC wave basin, if we have $L = 1\text{m}$ and $U = 0.1\text{m/s}$, then $Re = \frac{UL}{\nu} = \frac{0.1*1}{1\times10^{-6}} = 10^5$. Since in practical applications we are interested in flow velocities $U > 0.1\text{m/s}$, we can expect the inertial subrange to be visible and the turbulence model to be valid.

On the other hand, application of the turbulence model does require that the mean flow is sufficiently strong to permit use of the frozen turbulence approximation. For this reason, only the spectra of the *u*-velocity component were developed in this study. Without a mean velocity in the *v* and *w* directions, it was not possible to develop wavenumber spectra for these velocity components. As we know, eddies are not perfect spheres, so the integral length scales in the *x*, *y* and *z* directions are different. In many cases, the vertical length scale will be smaller than the horizontal ones.

7.3 General Recommendations for Tests Programs Using MAVS Current Meters

Before each test program, a correct log file should be completed logging the depth and orientation of each sensor. Indeed, it is easier to record the local velocities of the sensor and then rotate them during the post-processing. The format for the MAVS log should be such as in Table 7.1, where the type of arrays is a plot of the way the sensors are mounted.

Table 7.1: Sample of MAVS log sheet

Sensor	*x*	*y*	*z*	Orientation	Type of array	Comments
1						
2						
…						

The first thing to do is to run a test in calm water to establish the zero offset bias. This has to be done for every sensor. Monitoring the time series and the spectrum from the calm test provides information on the idling performance for the subsequent tests: persistent vibrations and their frequencies, mean current, etc.

As we have seen earlier, the measurement error is different depending on the orientation of the sensor. In order to have the best accuracy possible, one should run several tow tests in order to calibrate the velocity correction regression equations. The number of tow tests and range of tow speeds should be sufficient to determine the regression coefficients without loss of accuracy. We also should use one set of coefficients for each sensor.

In the case where preliminary calibration tow tests can't be done, we can use the coefficients given in Table 5.10. However, we should only use the method with two

coefficients as a_0 is varying a lot while a_1 and a_2 are pretty much constant for all the sensors.

Procedures have yet to be developed for correcting the orbital velocities measured under wave conditions. Indeed, in a wave, there is a positive and negative velocity in the x and z directions. We also have to be very careful to take free surface elevation measurement above the sensors and to log the exact location of all the sensors.

REFERENCES

Anikouchine, W. A., Sternberg R. W., 1973. The World Ocean, an Introduction to Oceanography. Prentice-Hall, Englewood Cliffs, NJ.

Bretschneider, C. L., 1959. Wave variability and wave spectra for wind-generated gravity waves. Beach Erosion Board, U.S. Army Corps of Engineers. Technical Memorandum 118.

Brillinger, D. R., 1975. Time Series: Data Analysis and Theory. Holt, Rinehart and Winston, Inc, New York.

Chakrabarti, S. K., 1993. Dynamics of Offshore Structures. 2nd edition. Computational Mechanics Publications, Southampton, U.K. 102-124.

Cohen, I. M., Kundu, P. K., 2002. Fluid Mechanics. Academic Press, San Diego, CA.

Cokelet, E. D., 1977. Steep gravity waves in water of arbitrary uniform depth. Philosophical Trans. Royal Society of London, Series A. 286, 183-230

Cooley, J. W., Turkey, J. W., 1965. An algorithm for the machine computation of complex Fourier series. Mathematics of Computation, 19, 297-301

Dean, R. G, Dalrymple, R. A., 1984. Water Wave Mechanics for Engineering and Scientists. Prentice-Hall, Englewood Cliffs, NJ.

Forristall, G. Z., Ward, E. G., Cardone, V. J., Borgman, L. E., 1978. The directional spectra kinematics of surface gravity waves in tropical storm Delia. Journal of Physical Oceanography, 8, 888-909.

Forristall, G. Z., 1981 Kinematics of directionally spread waves. Proceedings of Directional Wave Spectra Applications. University of California, Berkeley, CA, 129-146.

Goda, Y., 1978. The observed joint distribution of periods and heights of sea waves. Proceedings of the 16th Coastal Engineering Conference, 2, 227-246.

Goda, Y., 1985. Random Seas and Design of Maritime Structures. University of Tokyo Press, Tokyo.

Hashimoto, N., Nagai T., Asai T., 1994. Extension of the maximum entropy principle method for directional wave spectrum estimation. Proceedings of the 24th Conference on Coastal Engineering, 1, 232-246.

Hasselmann, D. E., Dunkel M., Ewing J. A., 1980. Directional wave spectra observed during JONSWAP. Journal of Physical Oceanography, 10, 1264-1280.

Hasselmann, K., Barnett, T. P., Bouws, E., Carlson, H., Cartwright, D. E., et al., 1973. Measurements of wind-wave growth and swell decay during Joint North Sea Wave Project (JONSWAP). German Hydrographic Institute, Hamburg, German Fed. Republic.

Isobe, M., Kondo, K., Horikawa, K., 1984. Extension of MLM for estimating directional wave spectrum. Symposium on Description and Modeling of Directional Seas. Danish Hydraulic Institute and Danish Maritime Institute, Copenhagen, Paper A-6, 1-15.

Kinsman, B., 1965. Wind Waves, Their Generation and Propagation on the Ocean Surface. Prentice-Hall, Englewood Cliffs, NJ.

Kolmogorov, A. N., 1941. The local structure of turbulence in incompressible viscous fluids for very large Reynolds numbers, Doklady Akademii nauk SSSR, 30, 301-305.

Kraus, E. B., 1977. Modeling and Prediction of the Upper Layers of the Ocean. Pergamon Press, New York.

Liagre, P. F., 1999. Generation and analysis of multi-directional waves. M.S. Thesis. Texas A&M University, College Station, TX.

Longuet-Higgins, M. S., Cartwright, D.E., Smith, N.D., 1963. Observations of the directional spectrum of sea waves using the motion of a floating buoy. Ocean Wave Spectra, Prentice Hall, Englewood Cliffs, NJ. 111-136.

Mellor, G. L., Durbin, P. A., 1975. The structure of the ocean surface mixed layer. Journal of Physical Oceanography, 5, 718-728.

Mercier, R. S., Niedzwecki, J. M., 1994. Experimental measurement of second-order diffraction by a truncated vertical cylinder in monochromatic waves. Behavior of Offshore Structures, BOSS'94, 2, 265-288. Cambridge, MA.

Mitsuyasu, H., Tasai, F., Suhara, S., Mizuno, M., Ohkusu, T., Honda, T., Rikiishi, K., 1975. Observation of the directional spectra of ocean waves using a clover-leaf buoy. Journal of Physical Oceanography, 5, 750-760.

Monin, A. S., Kamenkovitch, V. M., Kort, V. G., 1977. Variability of the Ocean. John Wiley & Sons, Inc., New York.

Niedzwecki, J. M., Whatley C. P., 1991. A parametric study of directional modeling. Journal of Ocean Engineering, 18, 118-128.

Ochi, M. K., Hubble E. N., 1976. Six parameter wave spectra. Proceedings of the 15th Coastal Engineering Conference, 1, 301-328.

Ochi, M. K., 1998. Ocean Waves - The Stochastic Approach (Cambridge Ocean Technology Series). Cambridge University Press, Cambridge, United Kingdom.

Pierson, W. J., Moskowitz L., 1964. A proposed spectral form for fully-developed wind sea based on the similarity law of S. A. Kitaigorodoskii. Journal of Geophysical Research, 69, 5181-5203.

Tennekes, H., Lumley, J. L., 1972. A First Course in Turbulence. The MIT Press, Cambridge, MA.

Thwaites, F. T., Williams, A. J. 3rd, 1996. Development of a modular acoustic velocity sensor, Oceans 96, 607-612.

Torsethaugen, K., 2004. Simplified double peak spectral model for ocean waves, http://www.fargisinfo.com/DPWS/TorsethaugenDPWS/index.html.

Williams, A. J. 3rd, Thwaites, F. T., Morrison III A. T., 1996. Transducer supports for acoustic travel-time current meters - flow sampling, wake, and potential flow distortion considerations, Proceedings of Microstructure Workshop, Mt. Hood, OR.

Williams, A. J. 3rd, Thwaites, F. T., 1998. Earth coordinate 3-D currents from a modular acoustic velocity sensor, Oceans 98, 244-247.

Zhang J., Chen, L., 1999. General third-order solutions for irregular waves in deep water. Journal of Engineering Mechanics, 7, 768-779.

APPENDIX A

BLOCKAGE CORRECTION FOR MEAN FLOW MEASUREMENTS

$a_0\left(cm.s^{-1}\right) vs.$ sensor

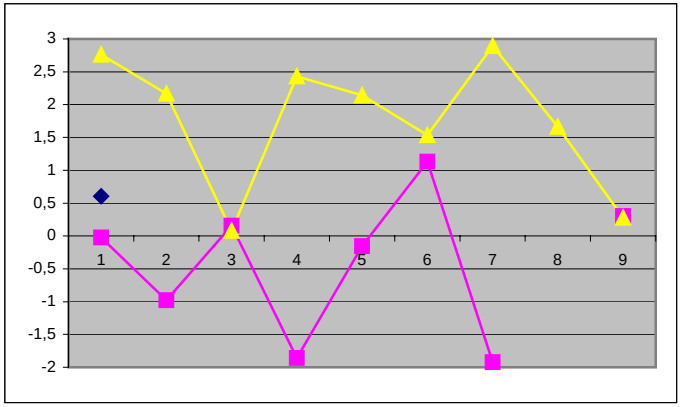

Figure A.1: 3 coefficients in North-South orientation

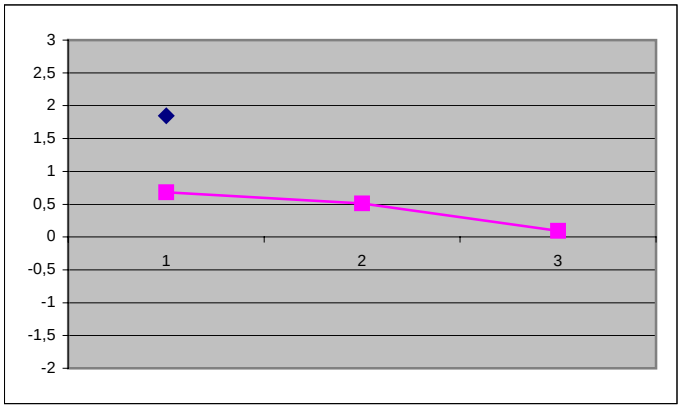

Figure A.2: 3 coefficients in East West orientation

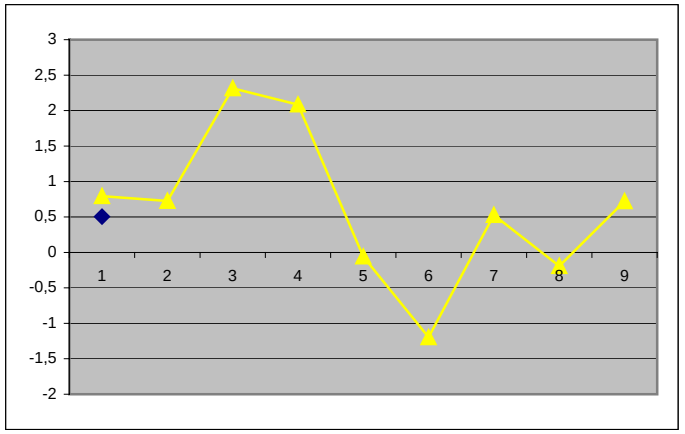

Figure A.3: 3 coefficients in Vertical orientation

$a_1(1) vs.$ sensor

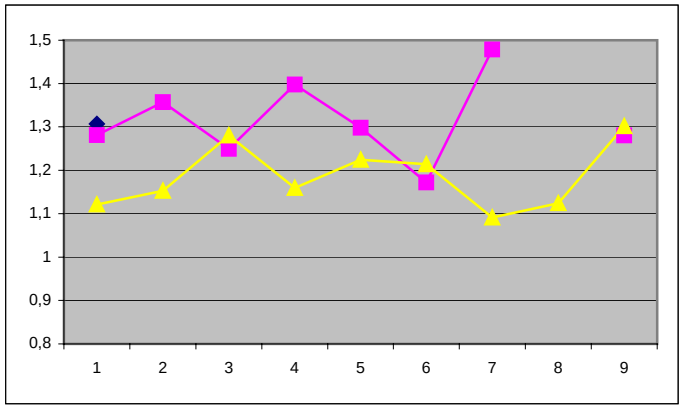

Figure A.4: 3 coefficients in North-South orientation

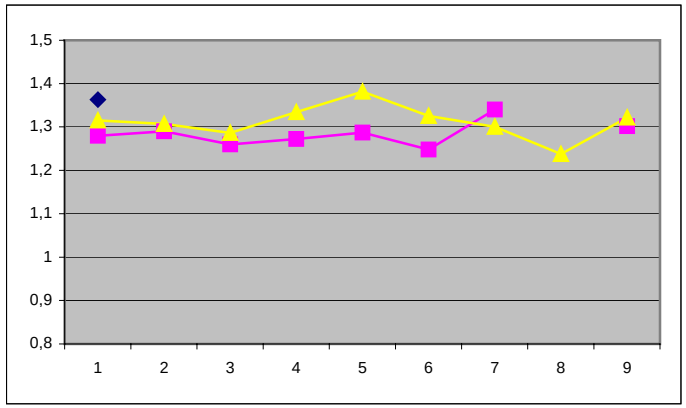

Figure A.5: 2 coefficients in North-South orientation

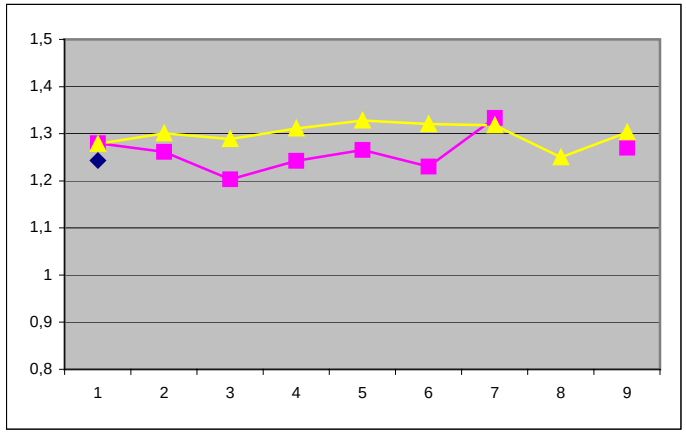

Figure A.6: 1 coefficient in North-South orientation

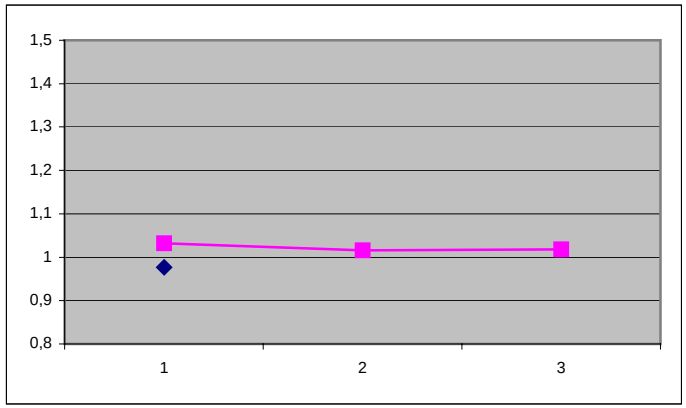

Figure A.7: 3 coefficients in East-West orientation

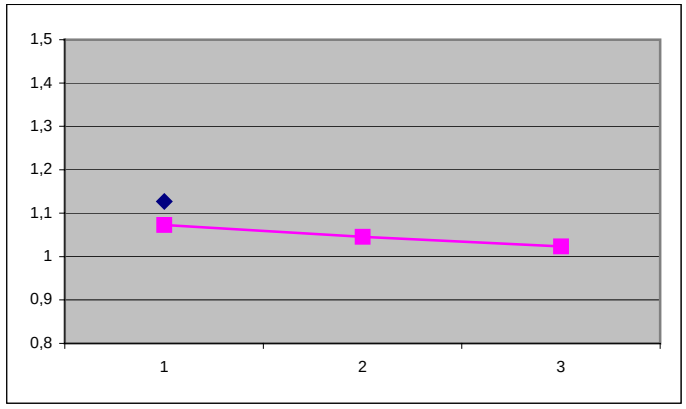

Figure A.8: 2 coefficients in East-West orientation

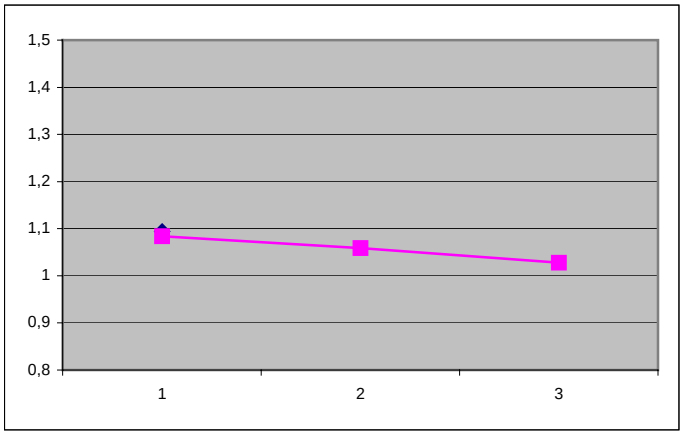

Figure A.9: 1 coefficient in East-West orientation

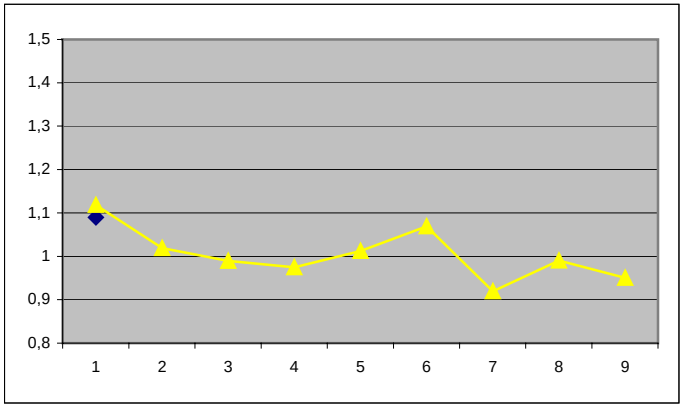

Figure A.10: 3 coefficients in Vertical orientation

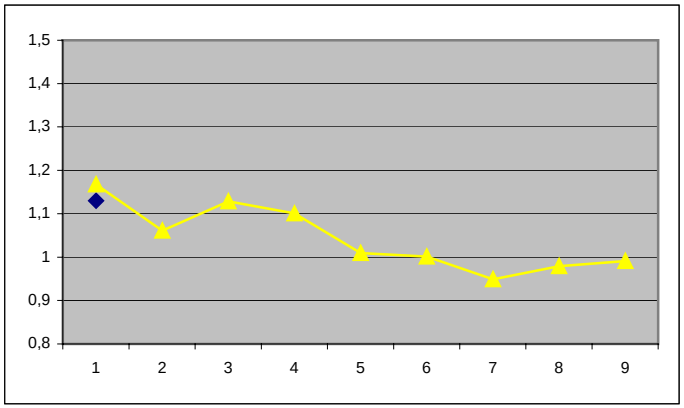

Figure A.11: 2 coefficients in Vertical orientation

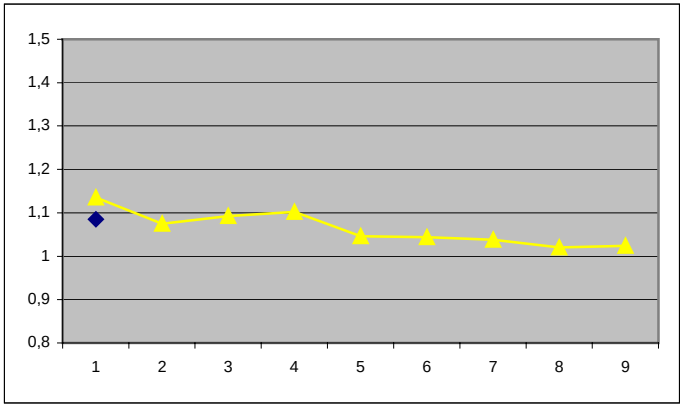

Figure A.12: 1 coefficient in Vertical orientation

$a_2\left(s.cm^{-1}\right)vs.$ sensor

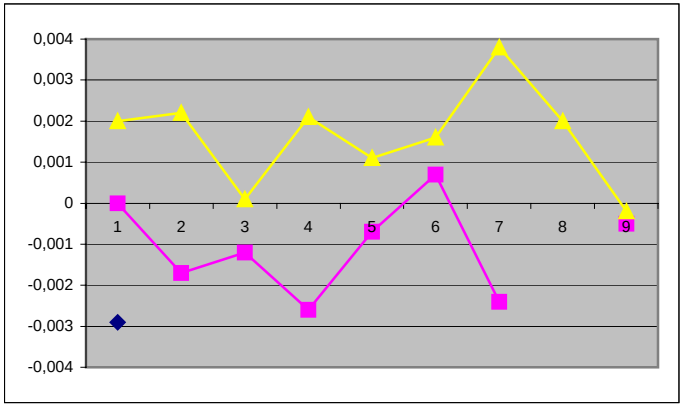

Figure A.13: 3 coefficients in North-South orientation

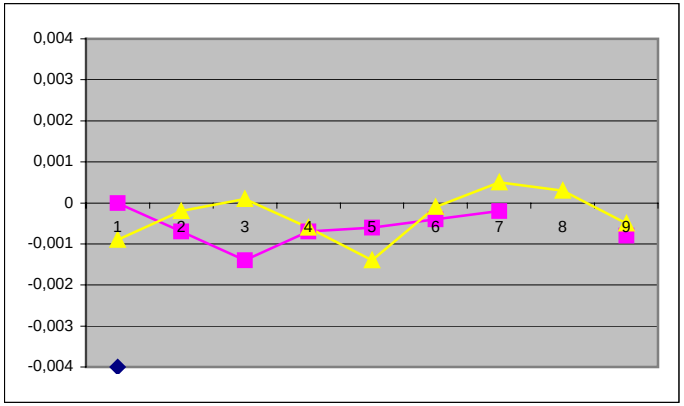

Figure A.14: 2 coefficients in North-South orientation

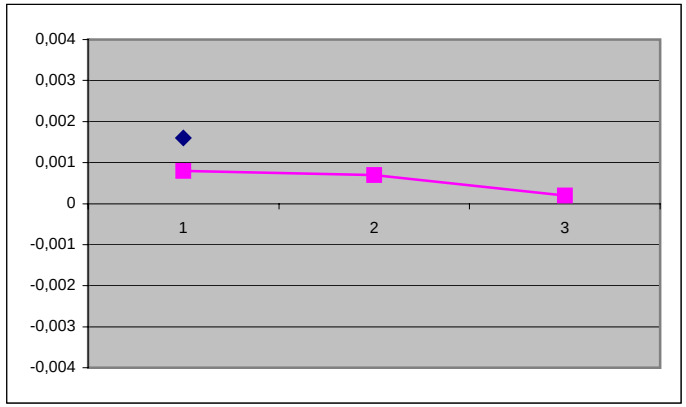

Figure A.15: 3 coefficients in East-West orientation

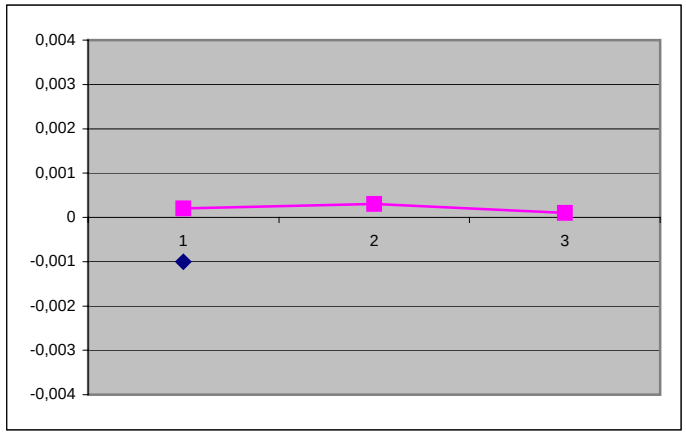

Figure A.16: 2 coefficients in East-West orientation

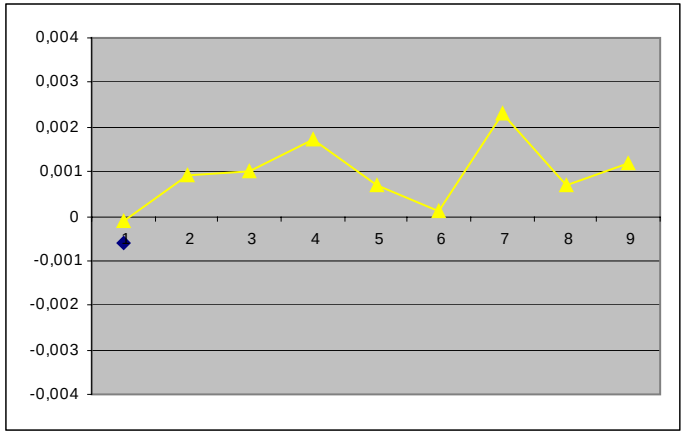

Figure A.17: 3 coefficients in Vertical orientation

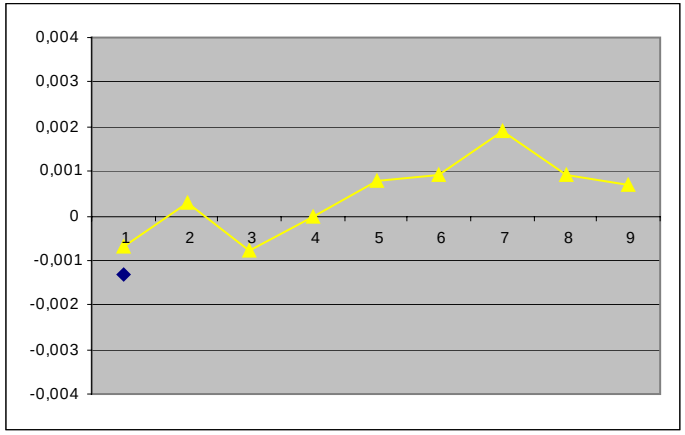

Figure A.18: 2 coefficients in Vertical orientation

$$\text{Error}\,(\%)\,vs.\ \text{Tow speed}\left(cm.s^{-1}\right)$$

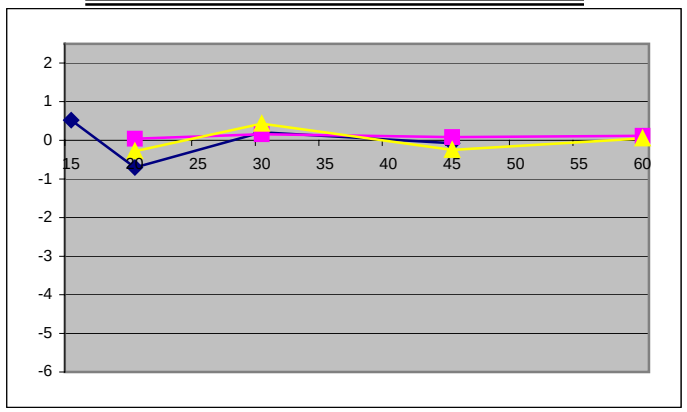

Figure A.19: Error with 3 coefficients in North-South orientation

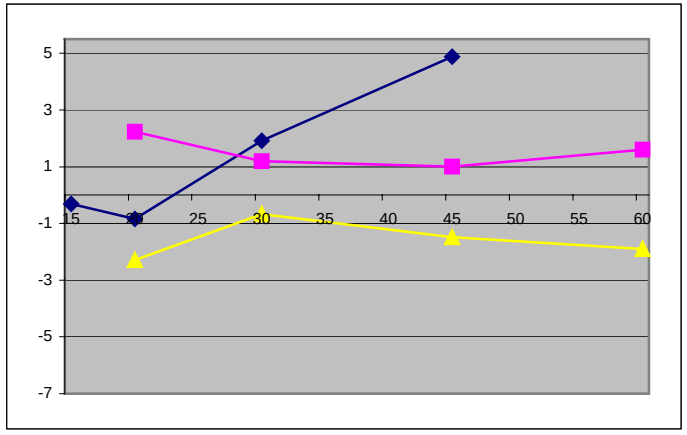

Figure A.20: Error with 3 coefficients in North-South orientation with one set of coefficients

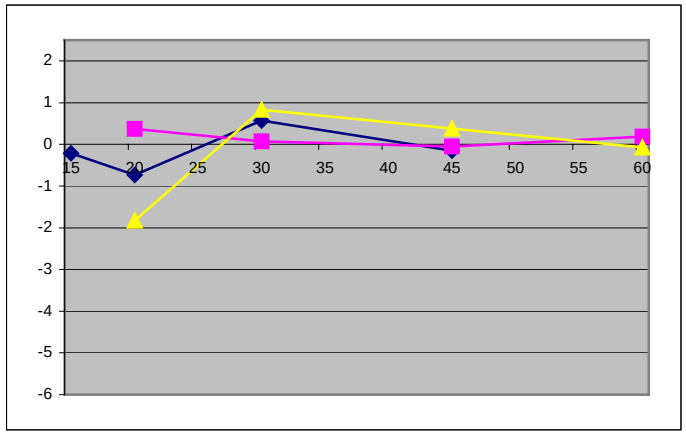

Figure A.21: Error with 2 coefficients in North-South orientation

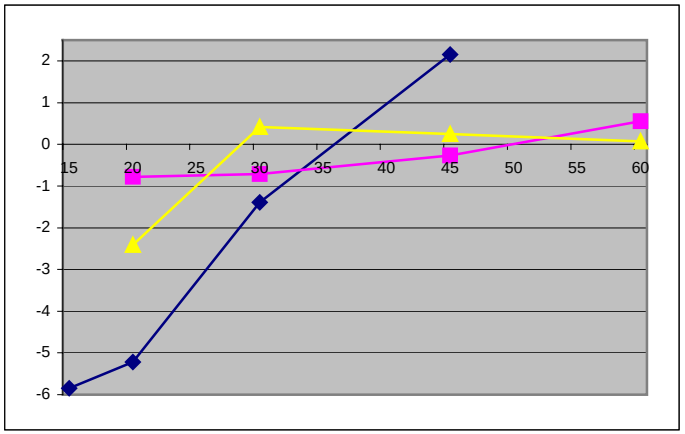

Figure A.23: Error with 1 coefficient in North-South orientation

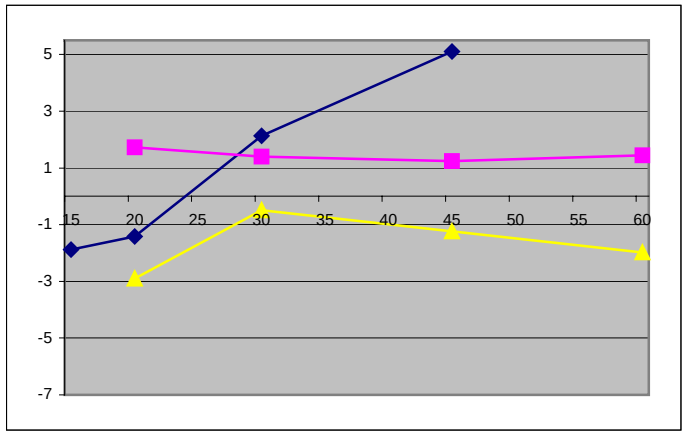

Figure A.22: Error with 2 coefficients in North-South orientation with one set of coefficients

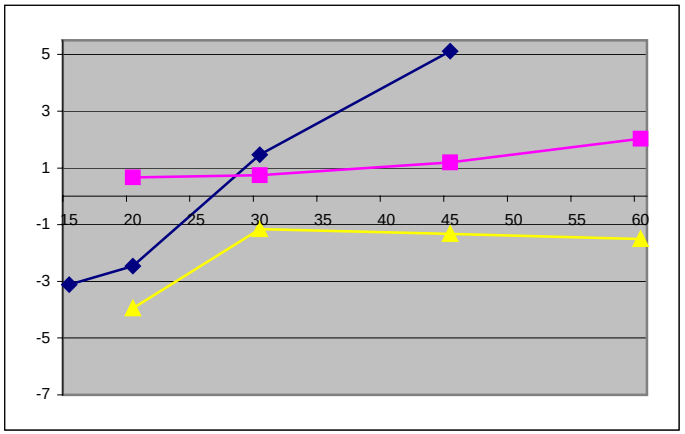

Figure A.24: Error with 1 coefficient in North-South orientation with one set of coefficients

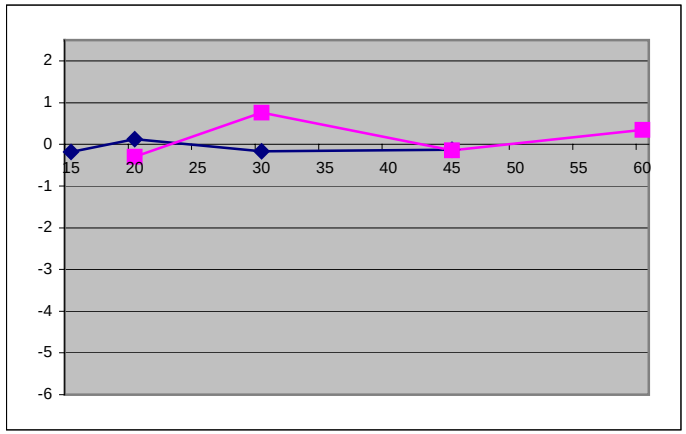

Figure A.25: Error with 3 coefficients in East-West orientation

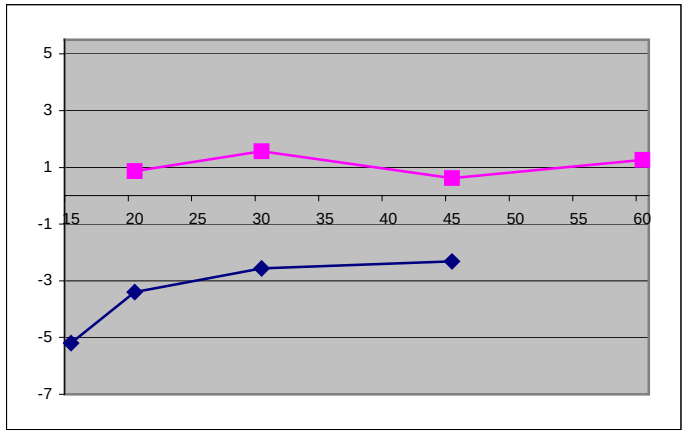

Figure A.26: Error with 3 coefficients in East-West orientation with one set of coefficients

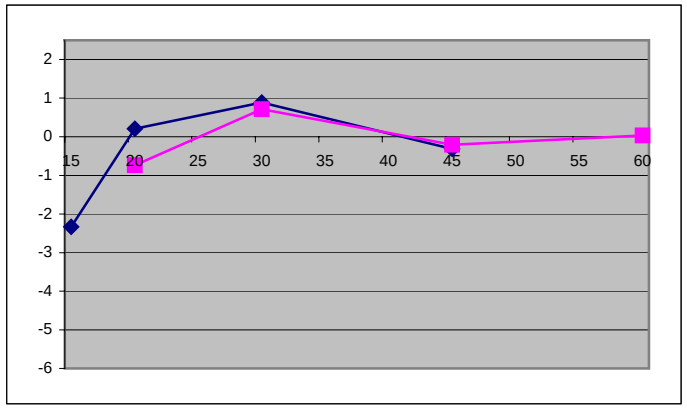

Figure A.27: Error with 2 coefficients in East-West orientation

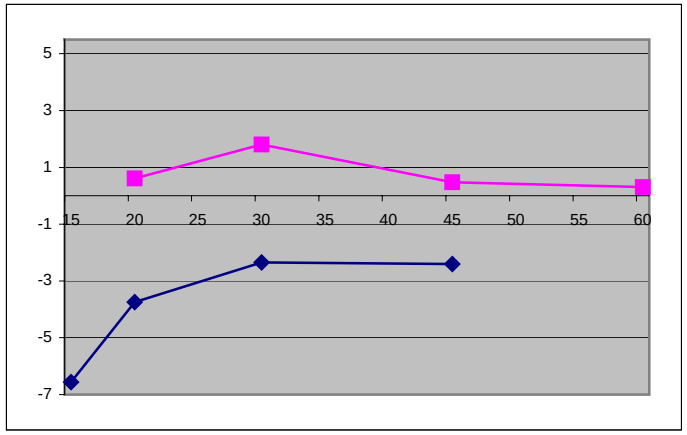

Figure A.28: Error with 2 coefficients in East-West orientation with one set of coefficients

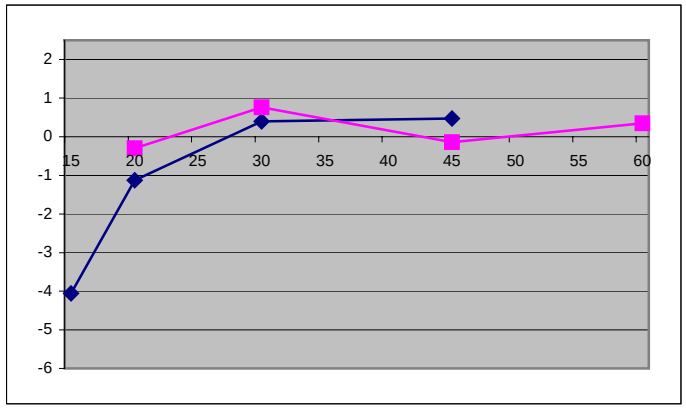

Figure A.29: Error with 1 coefficient in East-West orientation

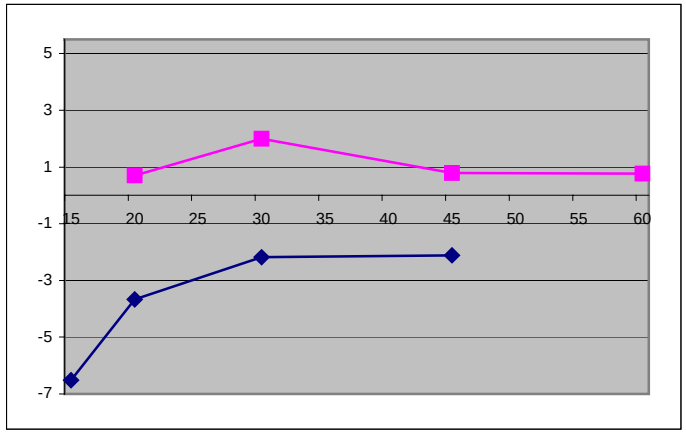

Figure A.30: Error with 1 coefficient in East-West orientation with one set of coefficients

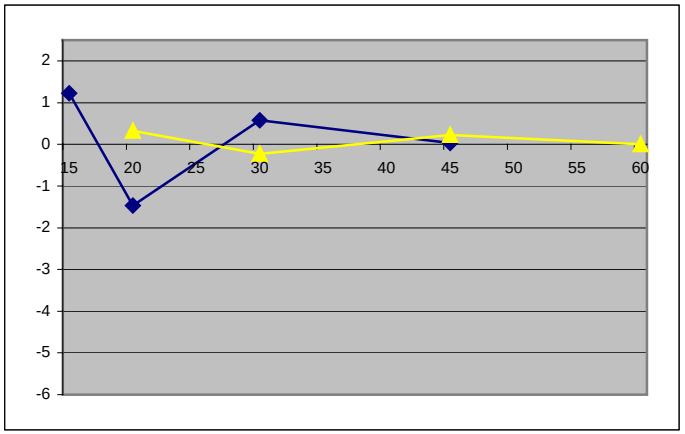

Figure A.31: Error with 3 coefficients in Vertical orientation

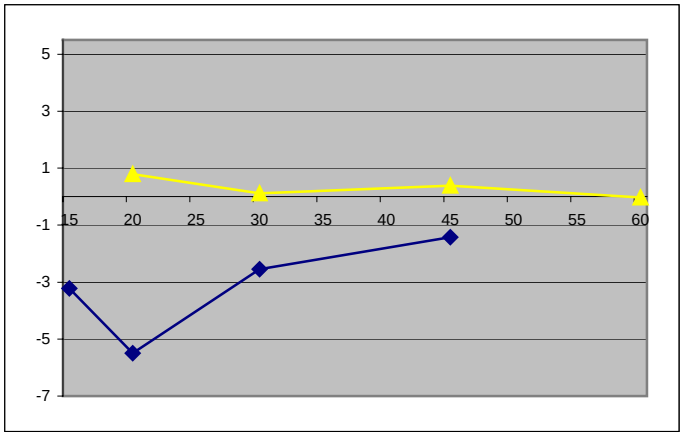

Figure A.32: Error with 3 coefficients in Vertical orientation with one set of coefficients

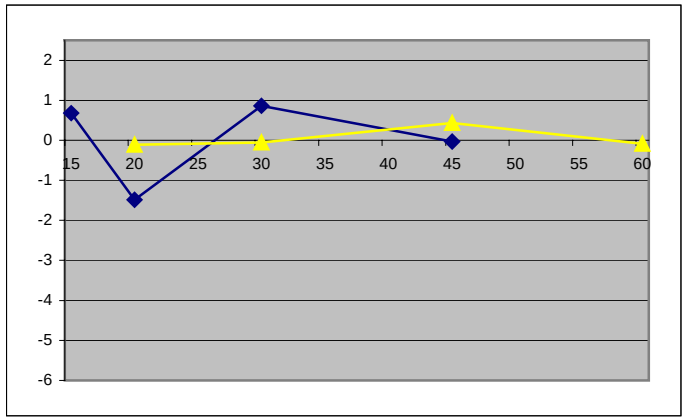

Figure A.33: Error with 2 coefficients in Vertical orientation

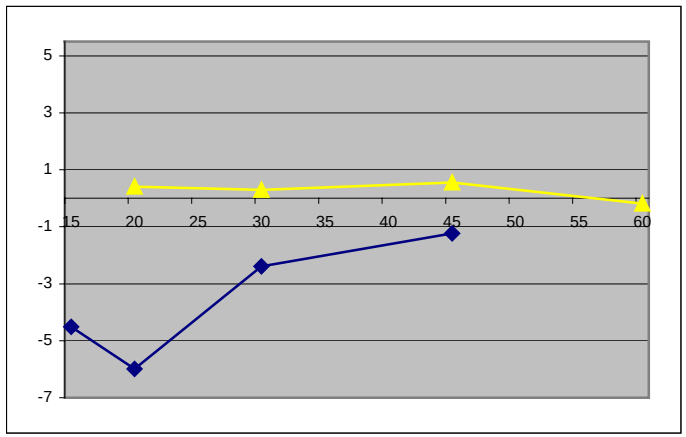

Figure A.34: Error with 2 coefficients in Vertical orientation with one set of coefficients

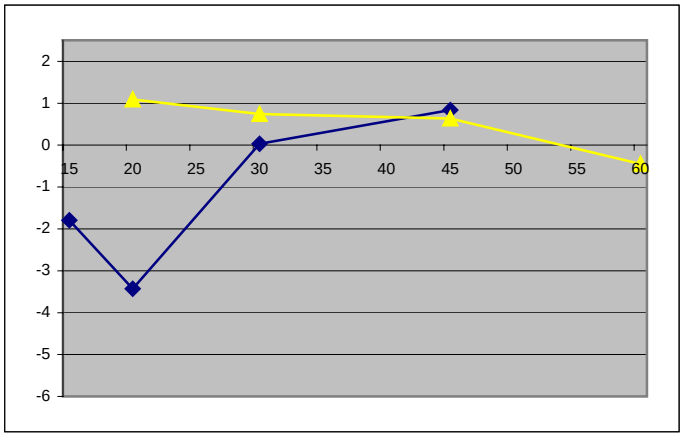

Figure A.35: Error with 1 coefficient in Vertical orientation

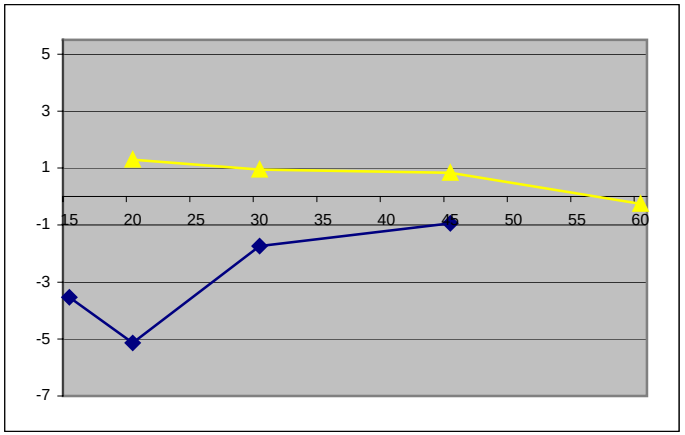

Figure A.36: Error with 1 coefficient in Vertical orientation with one set of coefficients

Standard Deviation of the Error *vs.* Tow speed $\left(cm.s^{-1}\right)$

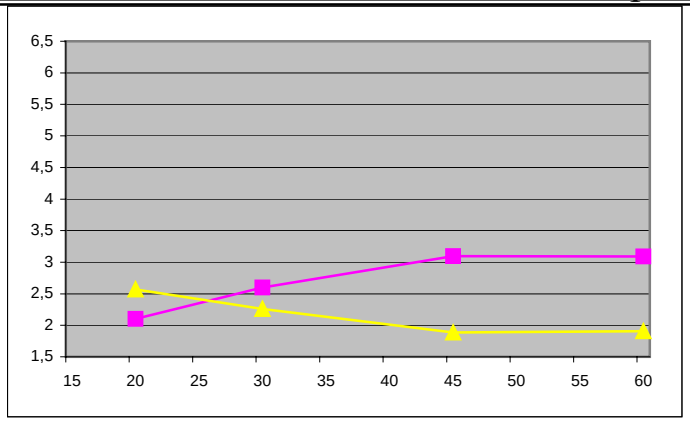

Figure A.37: Standard Deviation of the Error with 3 coefficients in North-South orientation

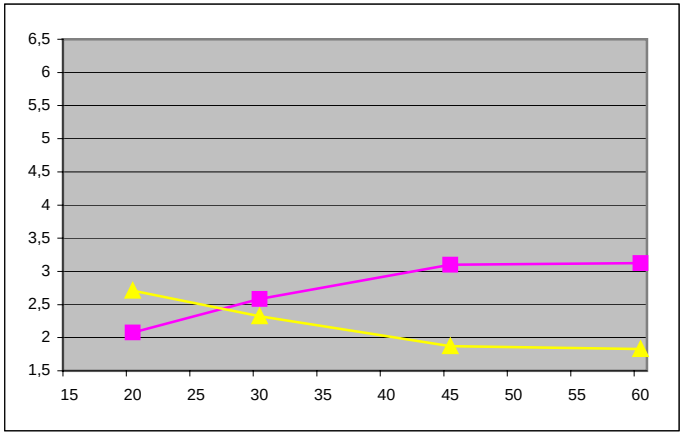

Figure A.39: Standard Deviation of the Error with 2 coefficients in North-South orientation

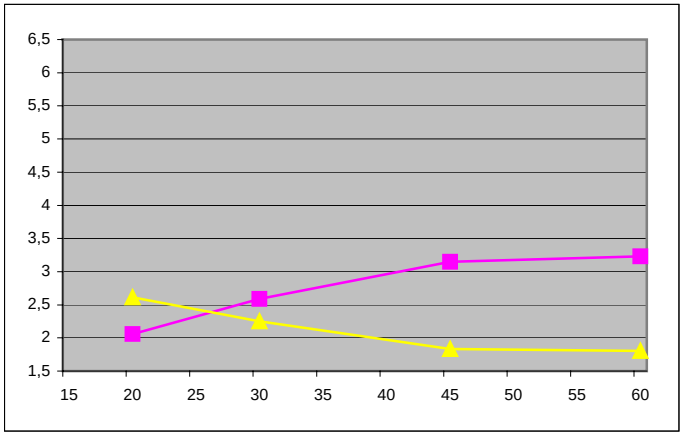

Figure A.38: Std of the Error with 3 coefficients in North-South orientation with one set of coefficients

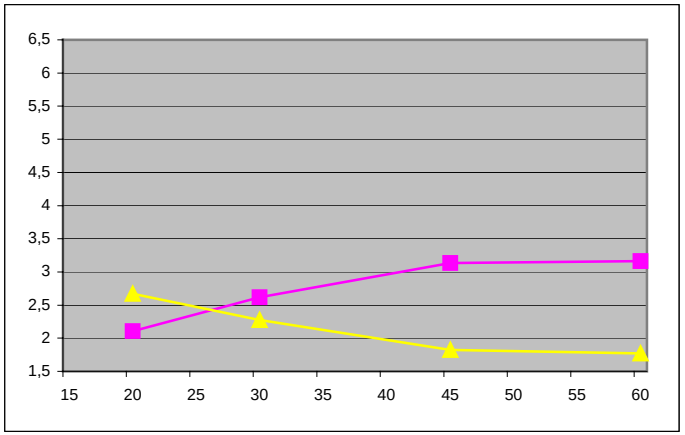

Figure A.40: Std of the Error with 2 coefficients in North-South orientation with one set of coefficients

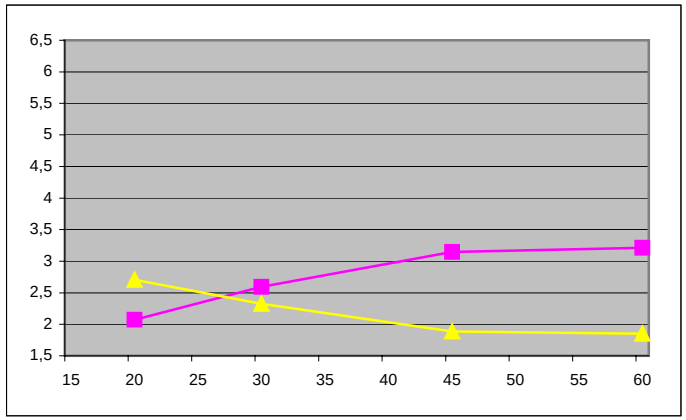

Figure A.41: Standard Deviation of the Error with 1 coefficient in North-South orientation

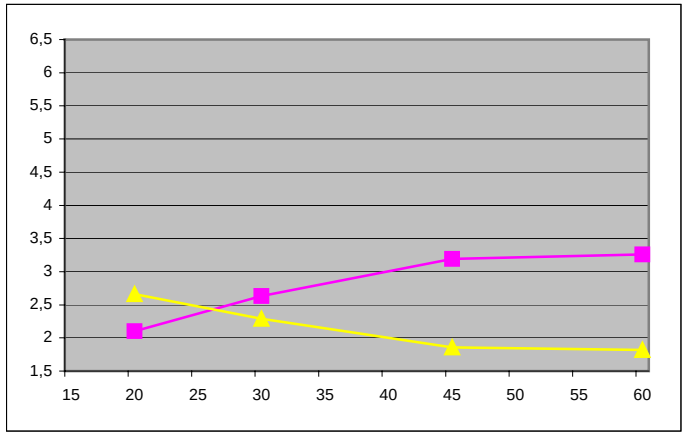

Figure A.42: Std of the Error with 1 coefficient in North-South orientation with one set of coefficients

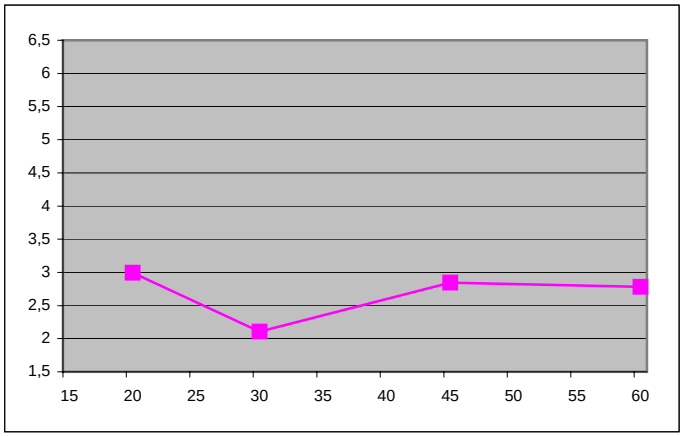

Figure A.43: Standard Deviation of the Error with 3 coefficients in East-West orientation

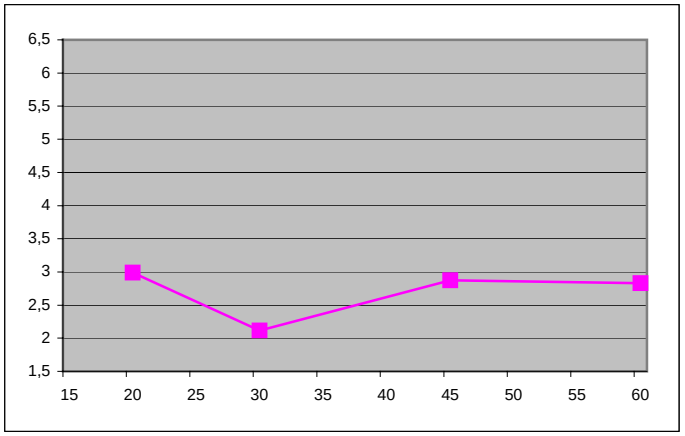

Figure A.44: Std of the Error with 3 coefficients in East-West orientation with one set of coefficients

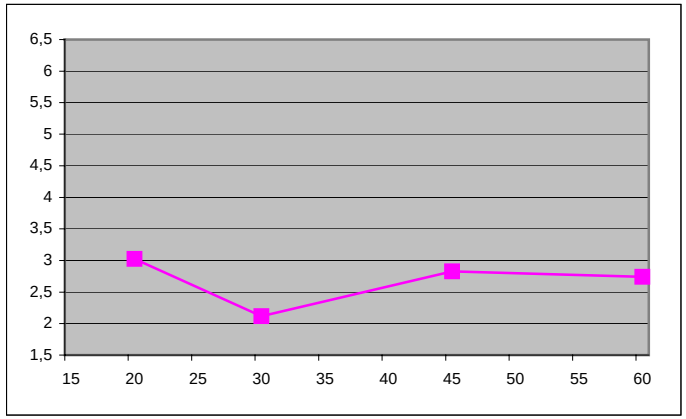

Figure A.45: Standard Deviation of the Error with 2 coefficients in East-West orientation

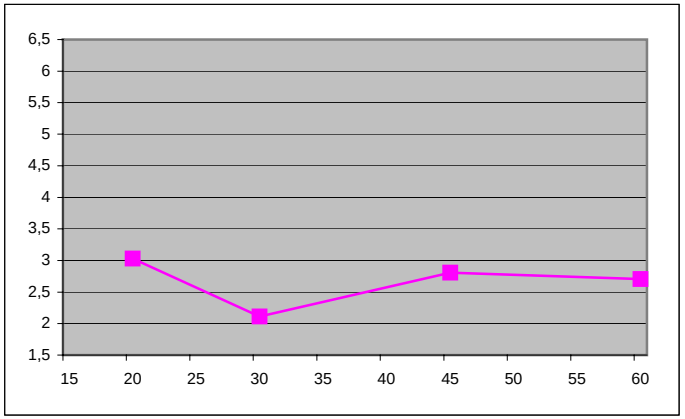

Figure A.47: Standard Deviation of the Error with 1 coefficient in East-West orientation

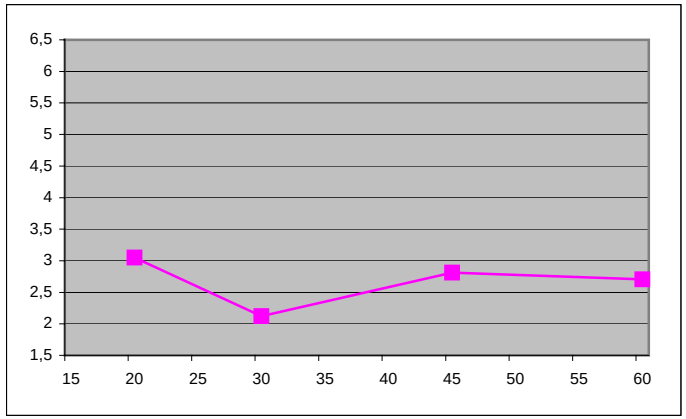

Figure A.46: Std of the Error with 2 coefficients in East-West orientation with one set of coefficients

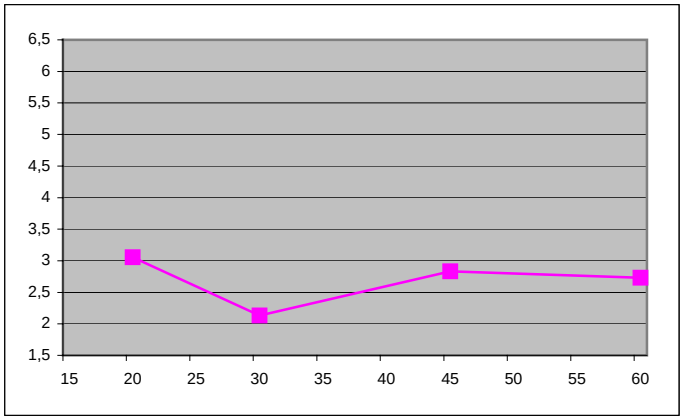

Figure A.48: Std of the Error with 1 coefficient in East-West orientation with one set of coefficients

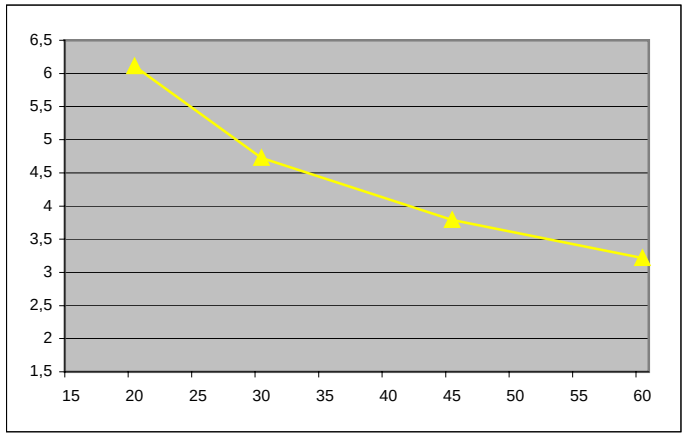

Figure A.49: Standard Deviation of the Error with 3 coefficients in Vertical orientation

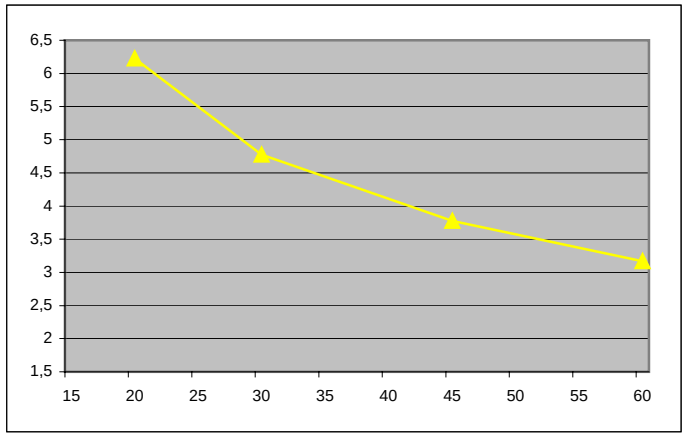

Figure A.51: Standard Deviation of the Error with 2 coefficients in Vertical orientation

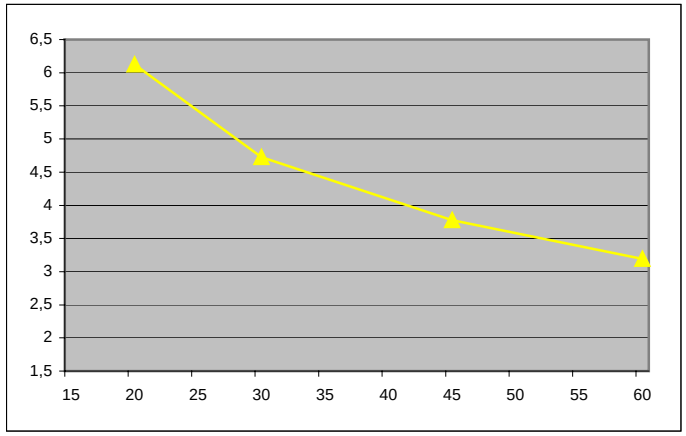

Figure A.50: Std of the Error with 3 coefficients in Vertical orientation with one set of coefficients

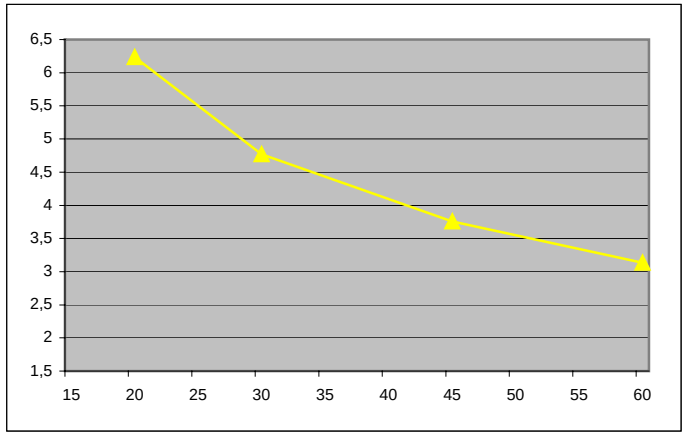

Figure A.52: Std of the Error with 2 coefficients in Vertical orientation with one set of coefficients

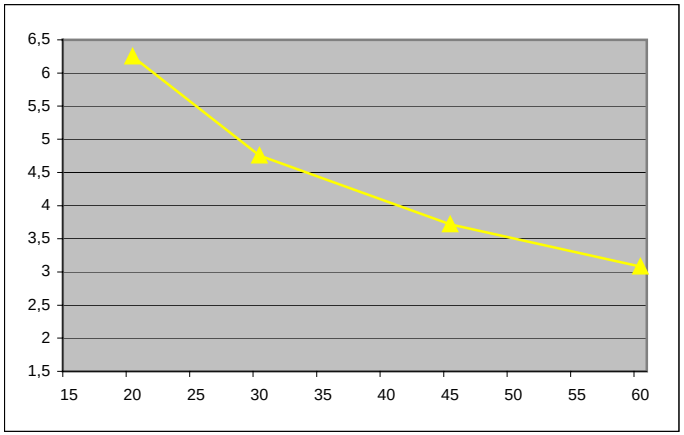

Figure A.53: Standard Deviation of the Error with 1 coefficient in Vertical orientation

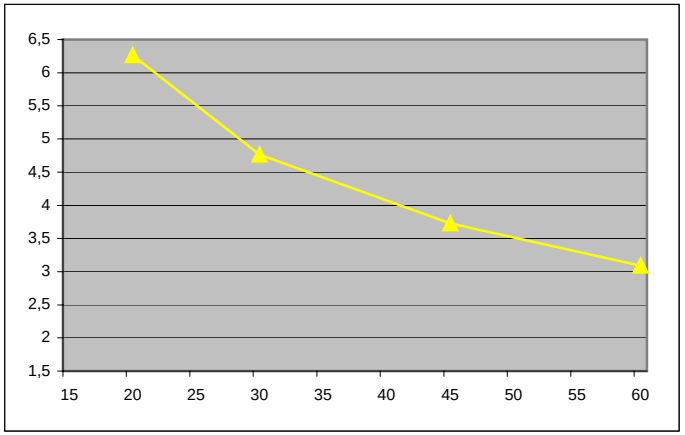

Figure A.54: Std of the Error with 1 coefficient in Vertical orientation with one set of coefficients

Figure A.55: Legend of the previous figures

APPENDIX B

MAPPING OF THE AVERAGE CURRENT

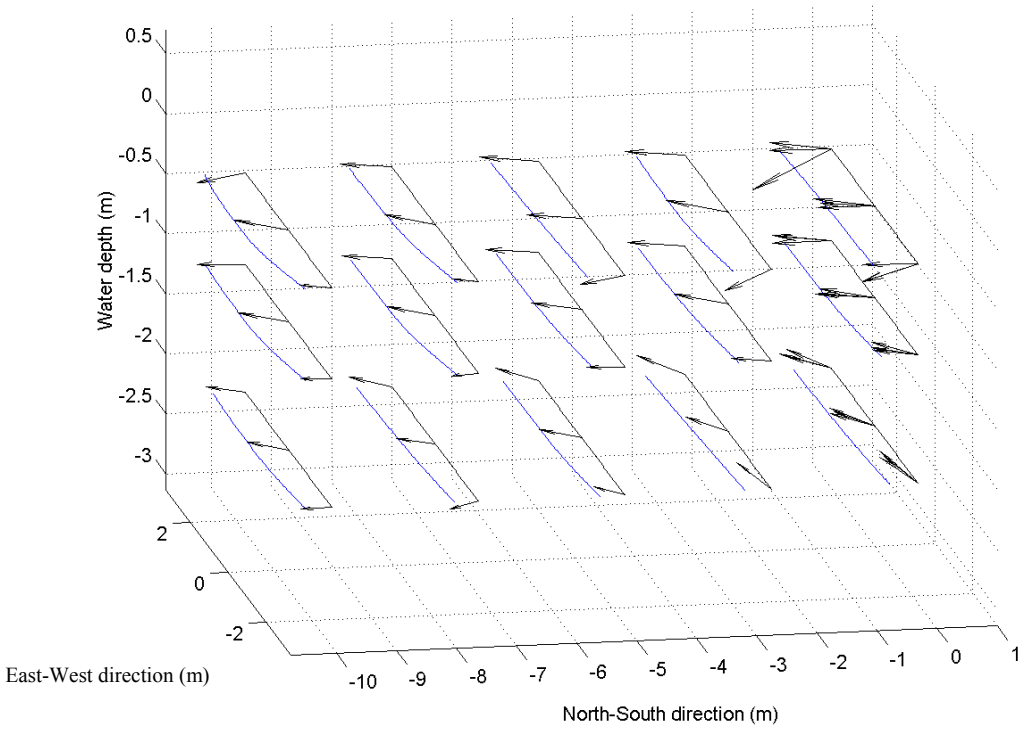

Figure B.1: Average Velocity for a 3*3 array current test at 100% for *x*-

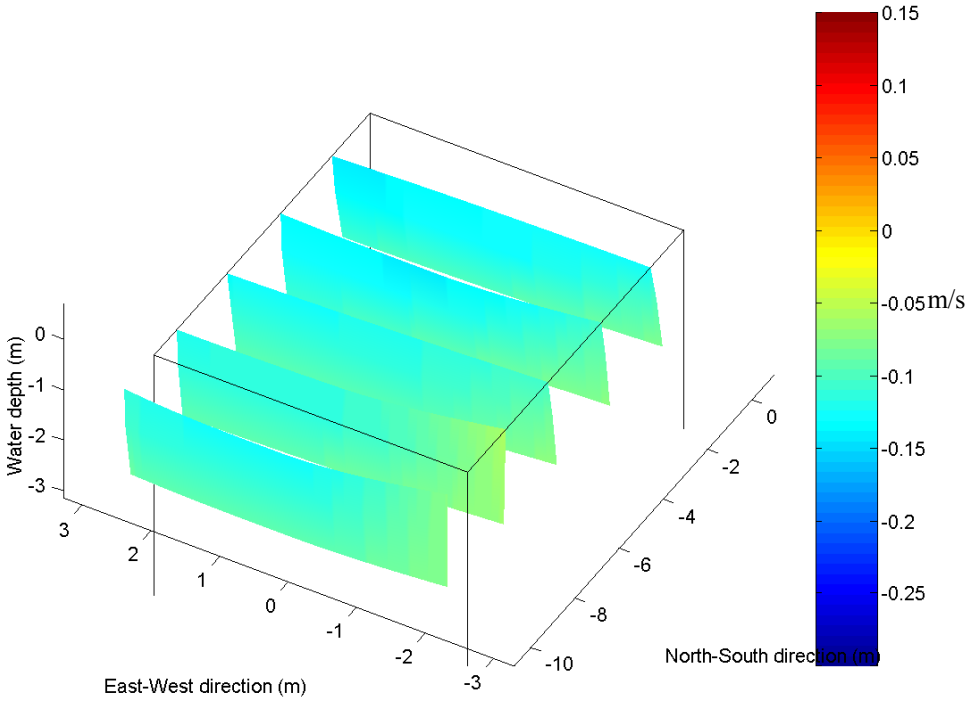

Figure B.2: Contours for *u* for a 3*3 array current test at 100% for *x*-

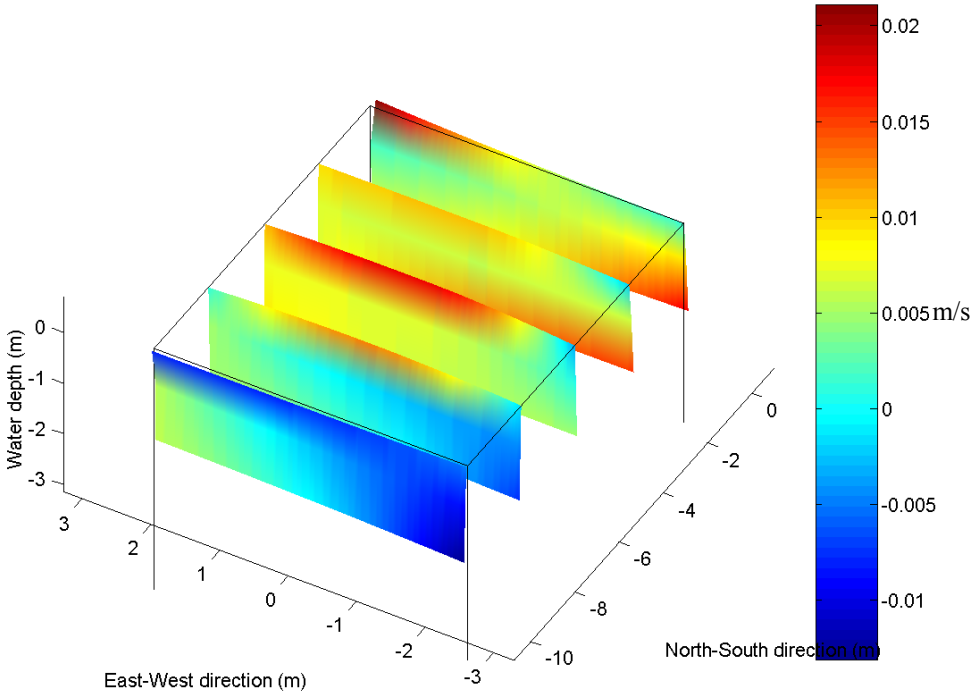

Figure B.3: Contours for *v* for a 3*3 array current test at 100% for *x*-

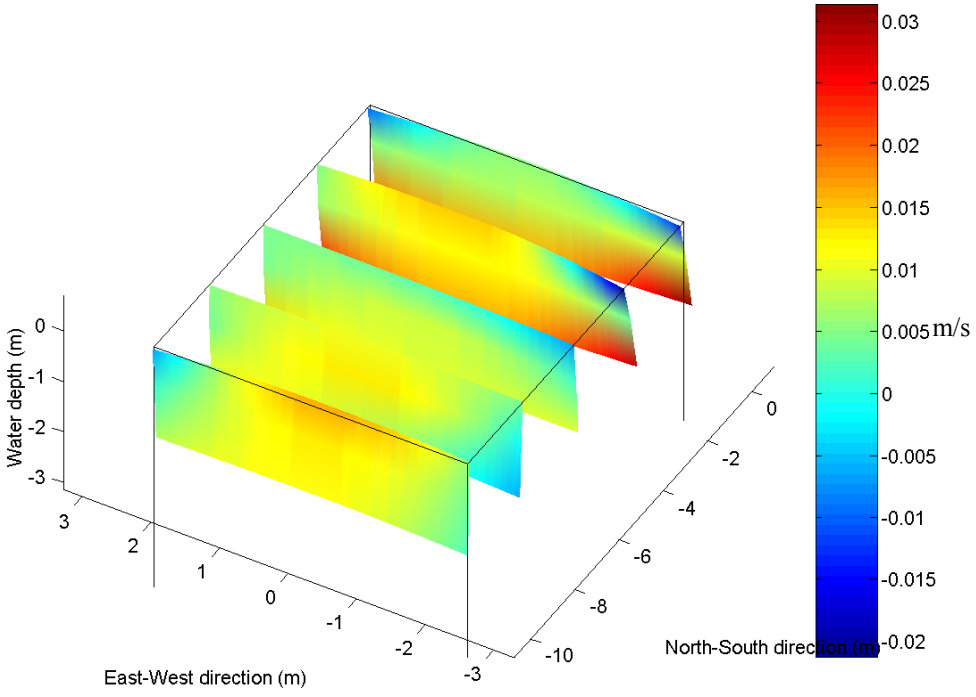

Figure B.4: Contours for *w* for a 3*3 array current test at 100% for *x*-

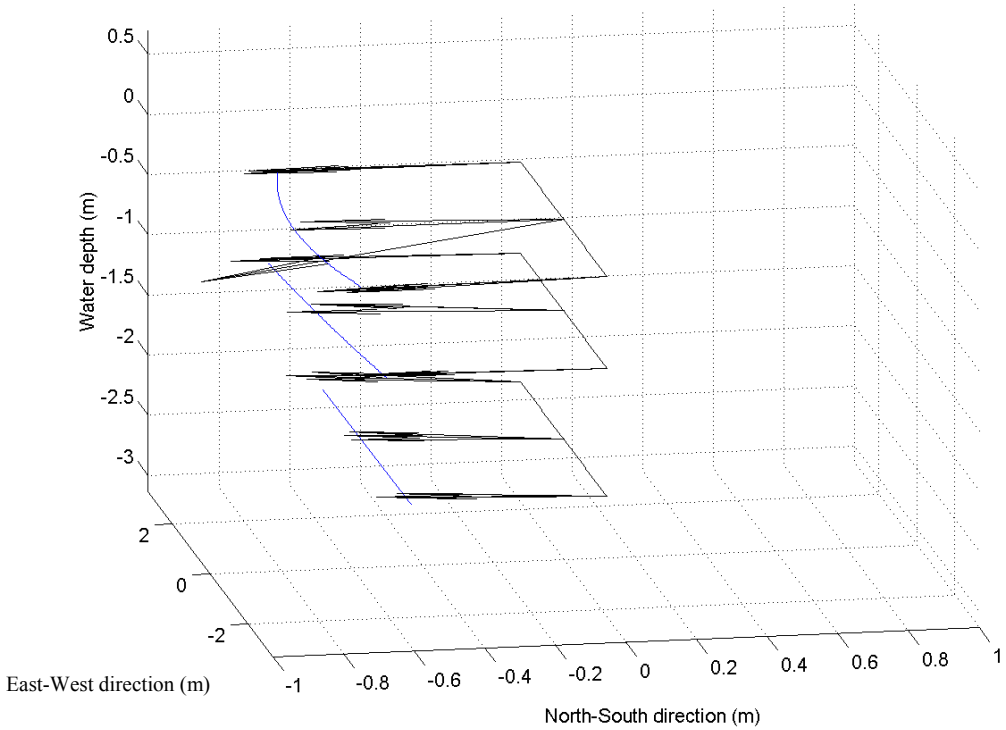

Figure B.5: Average Velocity for a 3*3 array current test at 200%

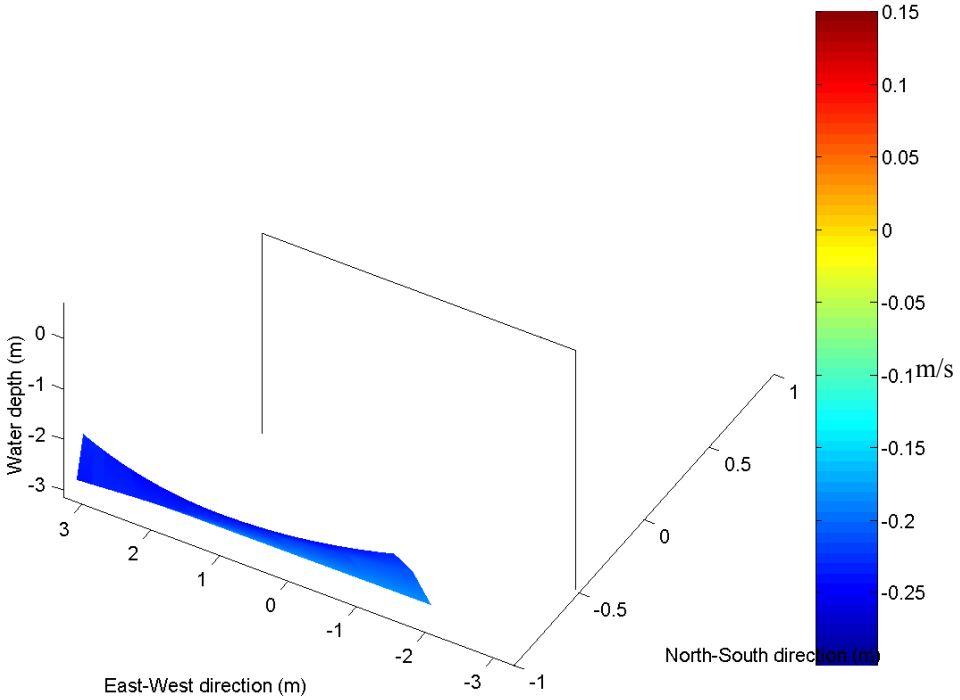

Figure B.6: Contours for *u* for a 3*3 array current test at 200%

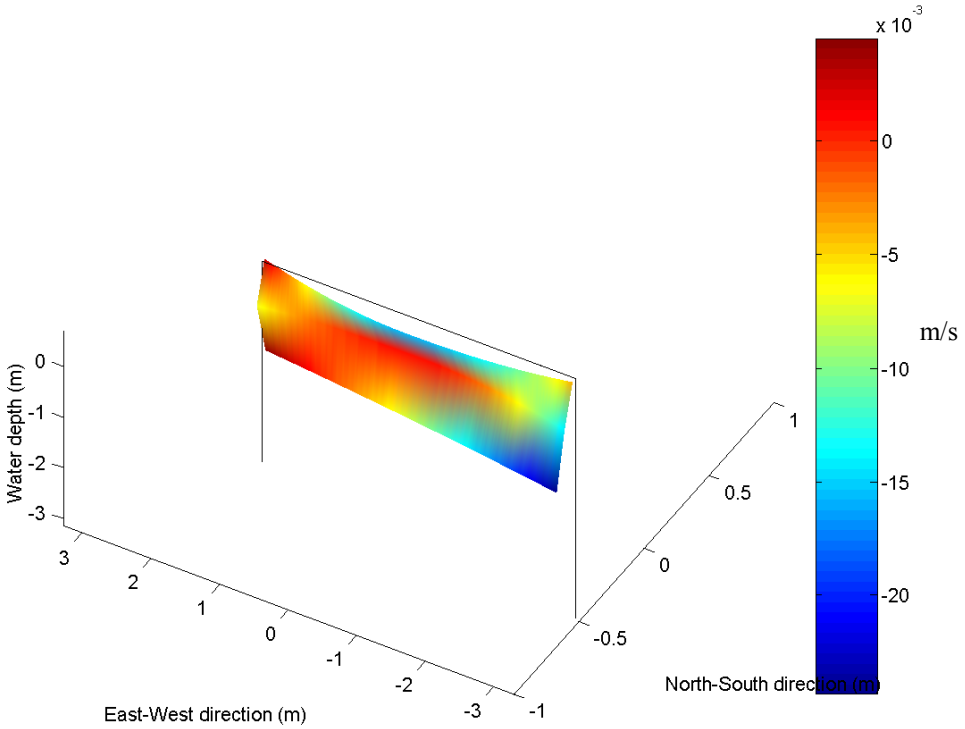

Figure B.7: Contours for *v* for a 3*3 array current test at 200%

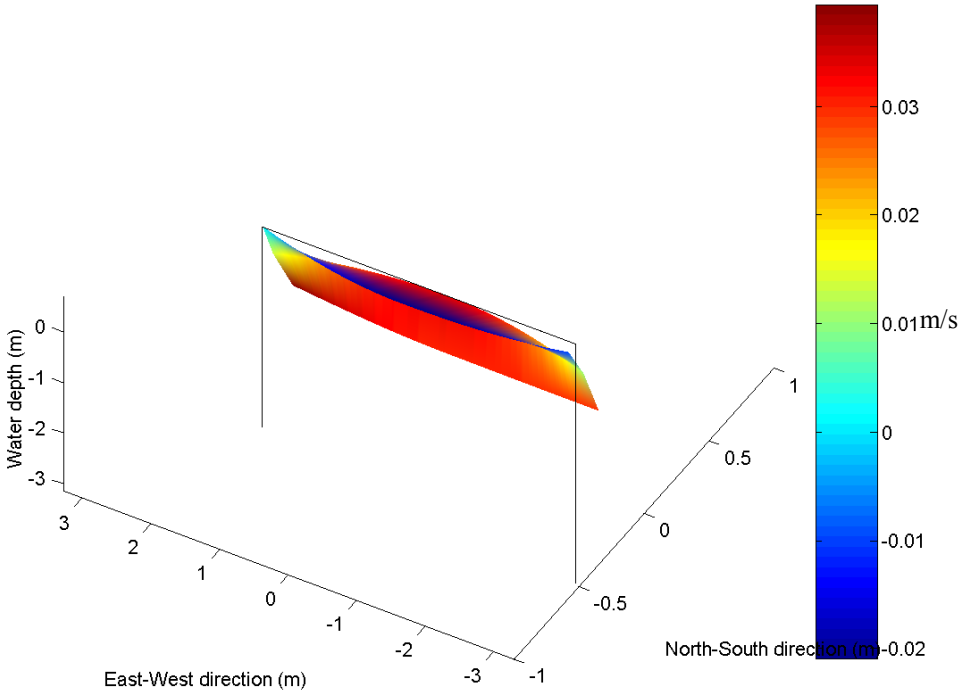

Figure B.8: Contours for *w* for a 3*3 array current test at 200%

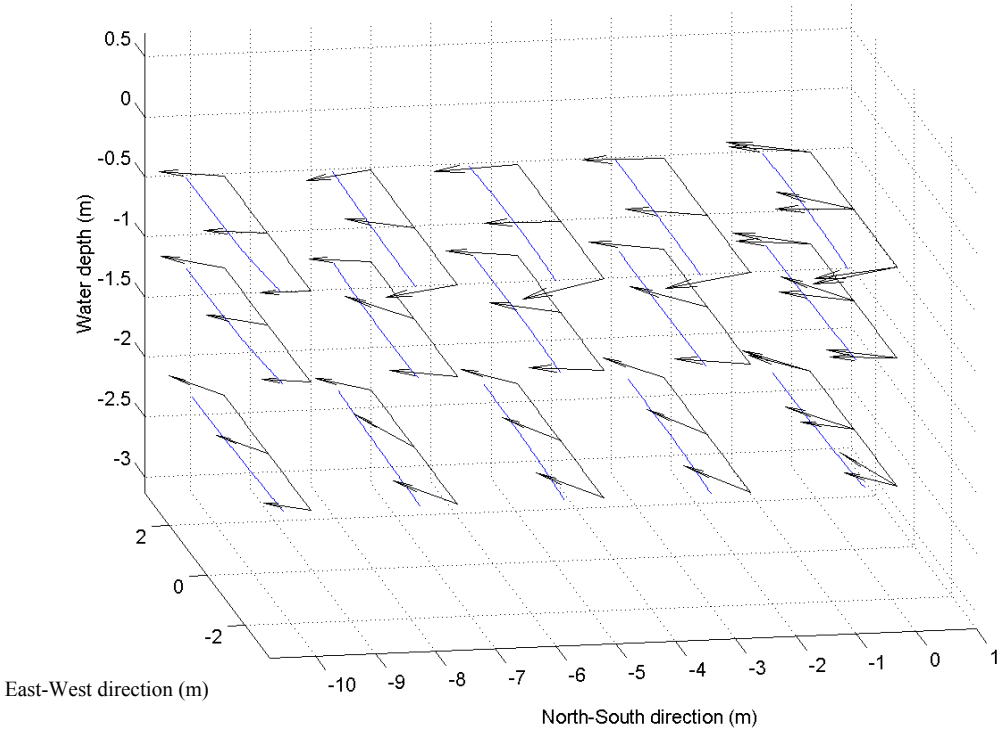

Figure B.9: Average Velocity for a 3*3 array current test at 225% for *x*-

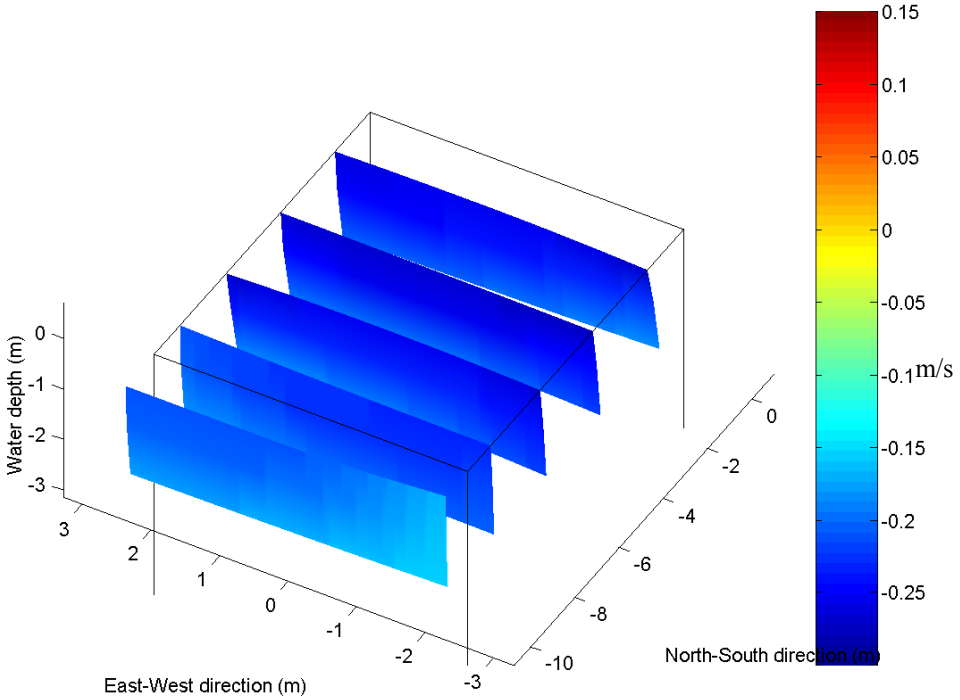

Figure B.10: Contours for *u* for a 3*3 array current test at 225% for *x*-

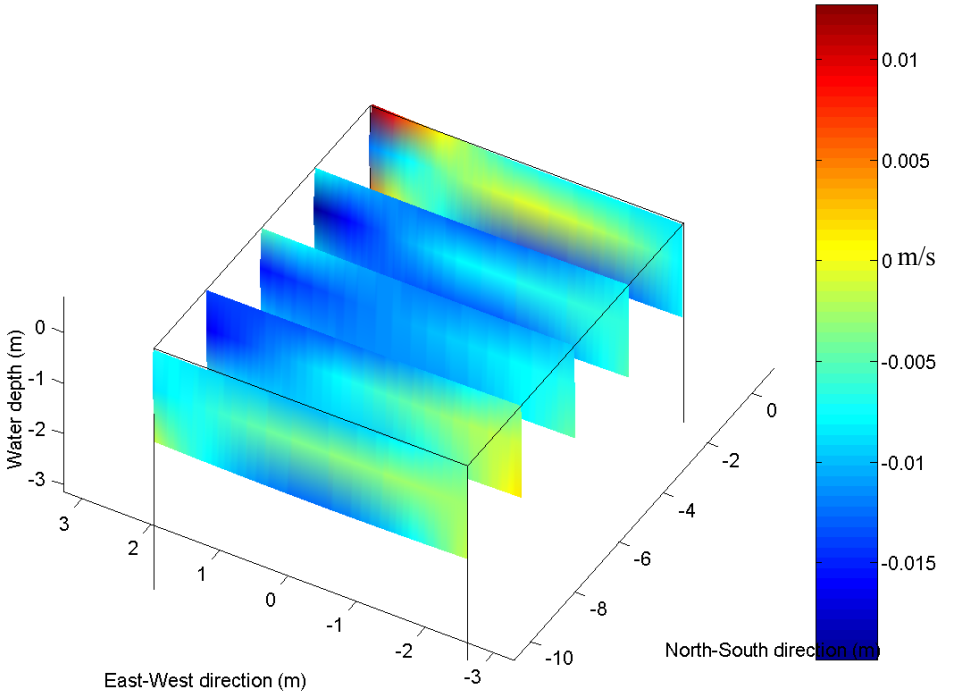

Figure B.11: Contours for *v* for a 3*3 array current test at 225% for *x*-

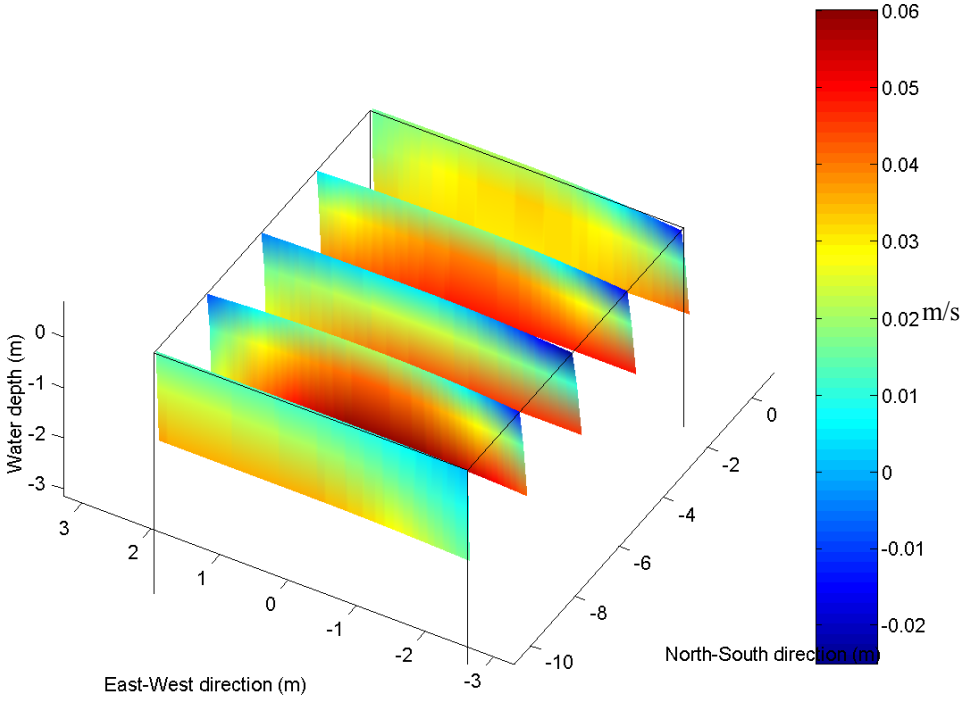

Figure B.12: Contours for *w* for a 3*3 array current test at 225% for *x*-

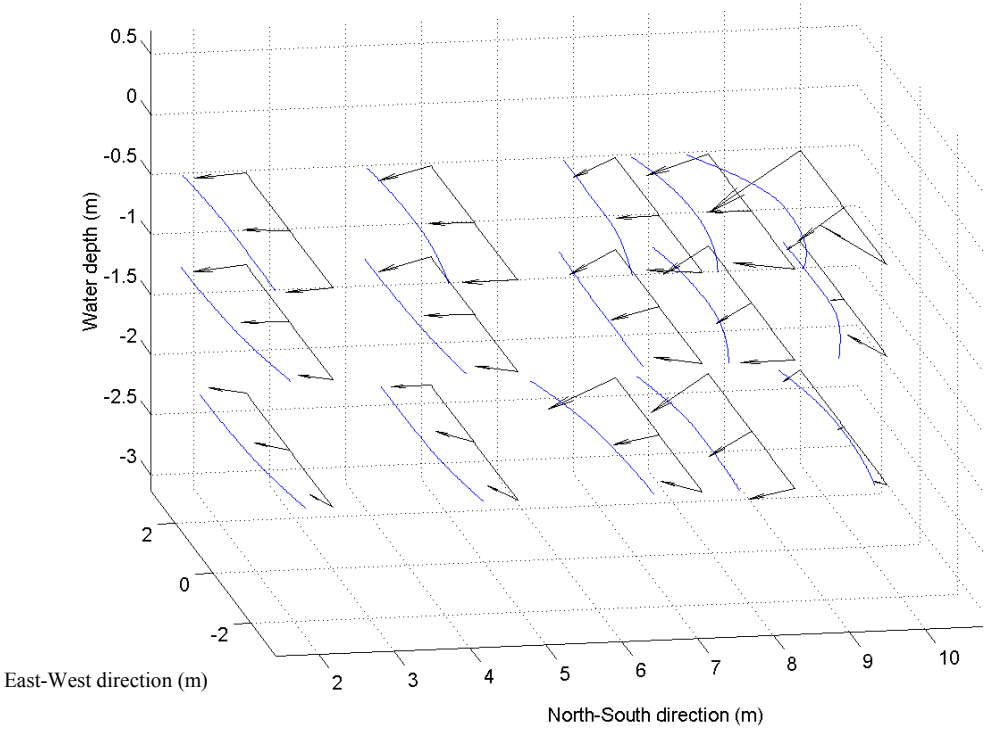

Figure B.13: Average Velocity for a 3*3 array current test at 100% for *x*+

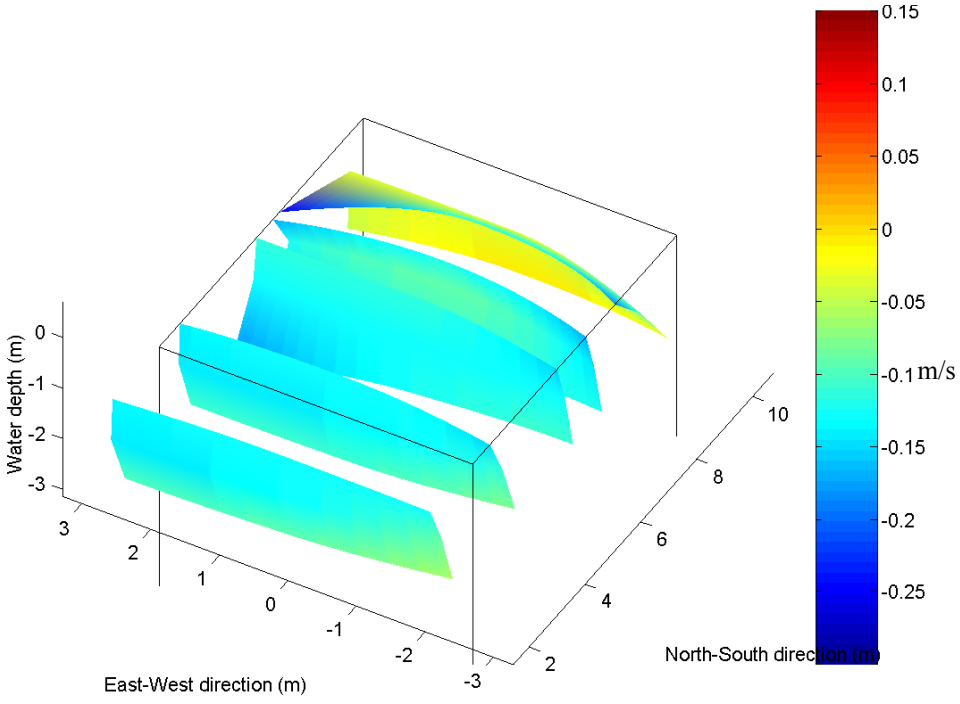

Figure B.14: Contours for *u* for a 3*3 array current test at 100% for *x*+

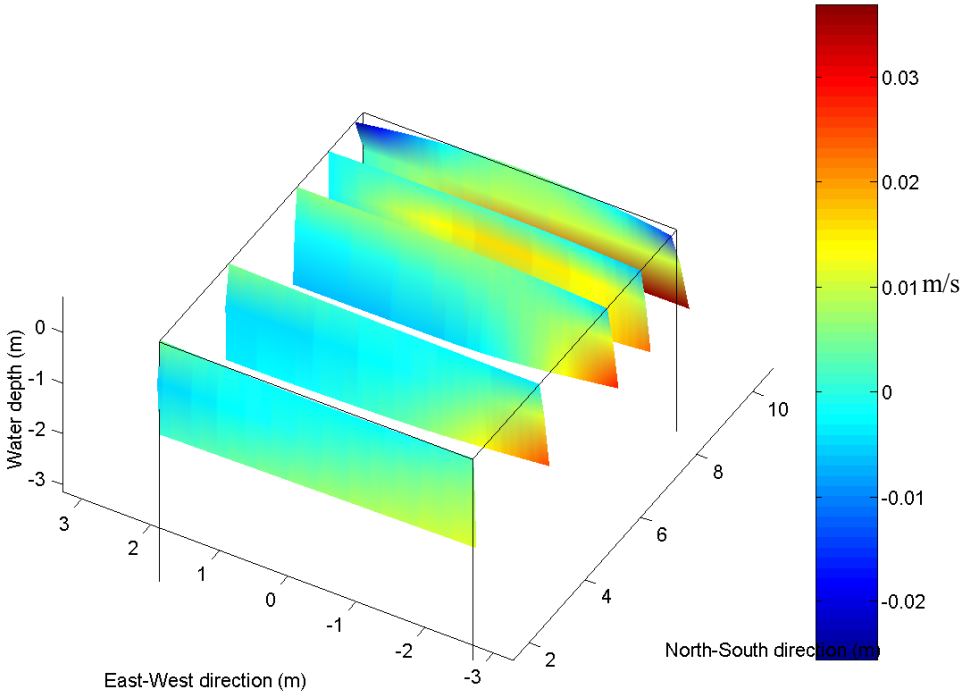

Figure B.15: Contours for *v* for a 3*3 array current test at 100% for *x*+

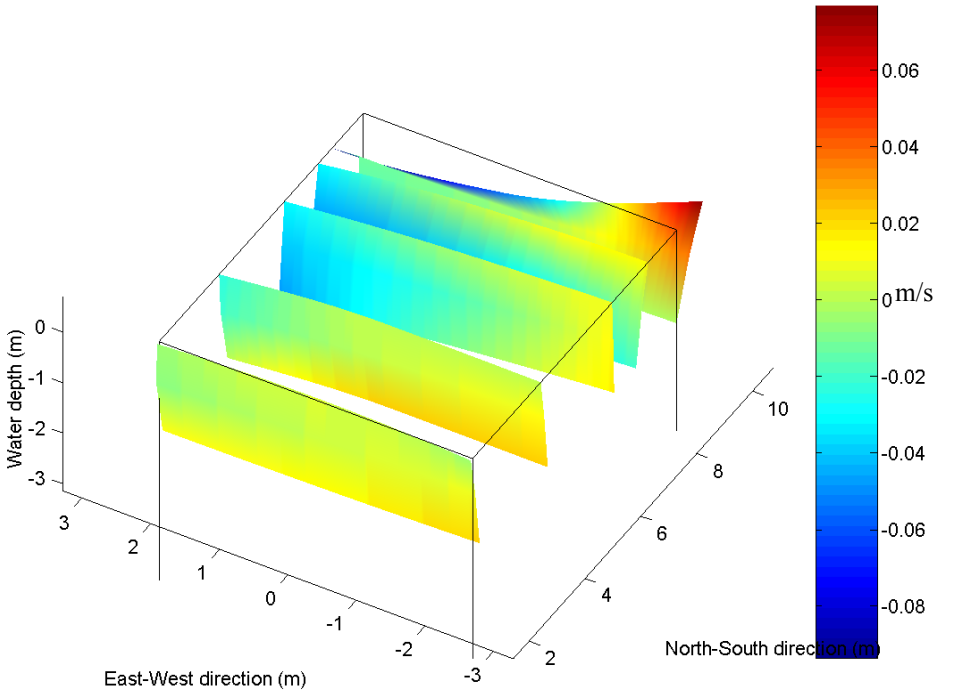

Figure B.16: Contours for *w* for a 3*3 array current test at 100% for *x*+

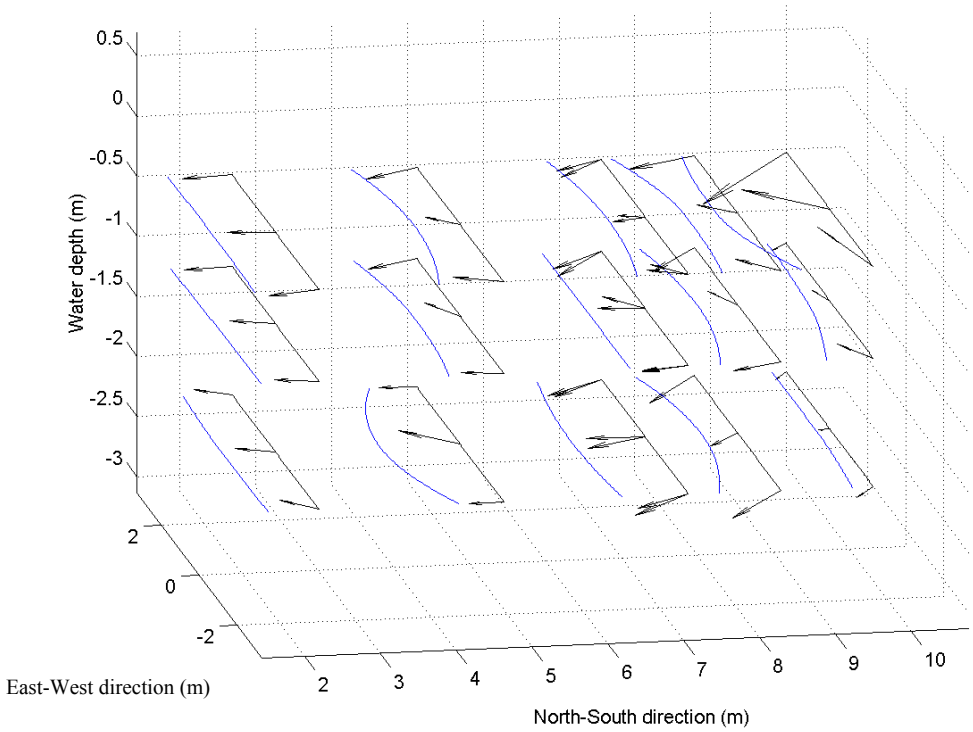

Figure B.17: Average Velocity for a 3*3 array current test at 225% for *x*+

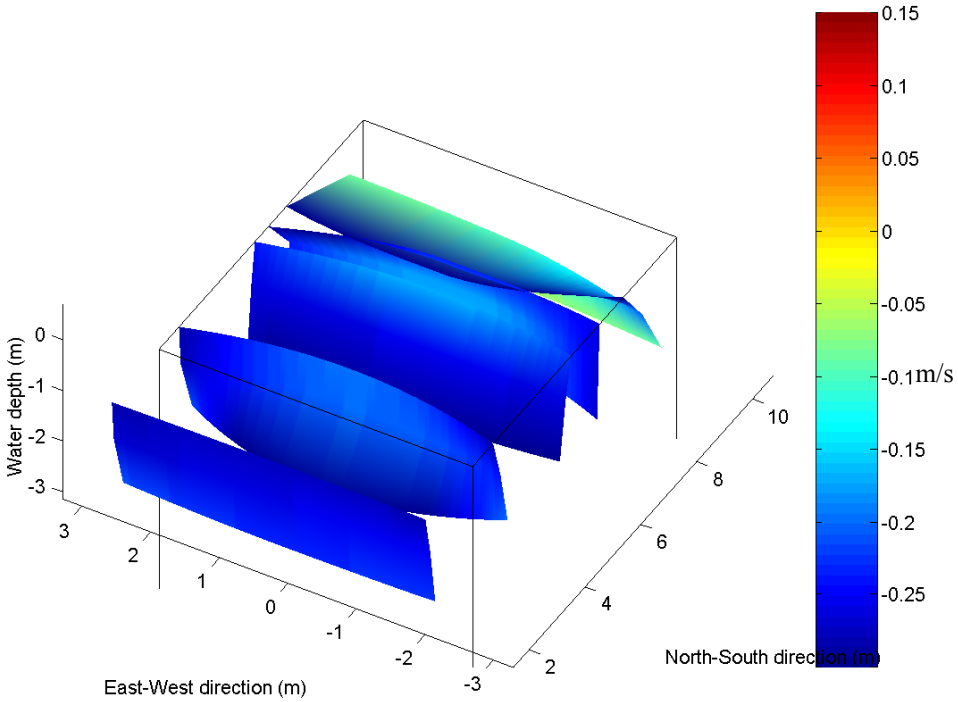

Figure B.18: Contours for *u* for a 3*3 array current test at 225% for *x*+

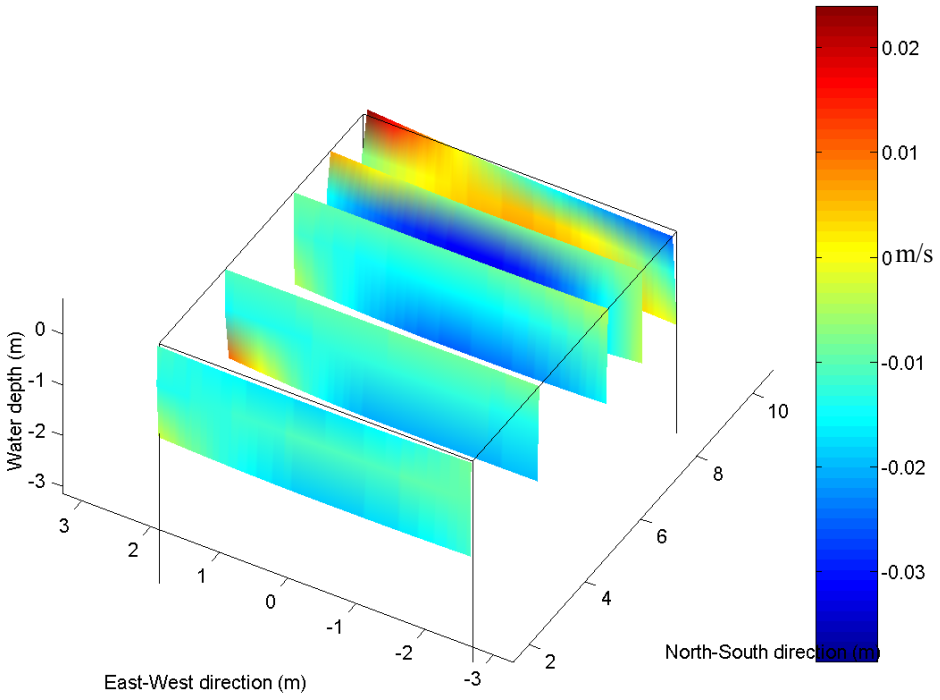

Figure B.19: Contours for *v* for a 3*3 array current test at 225% for *x*+

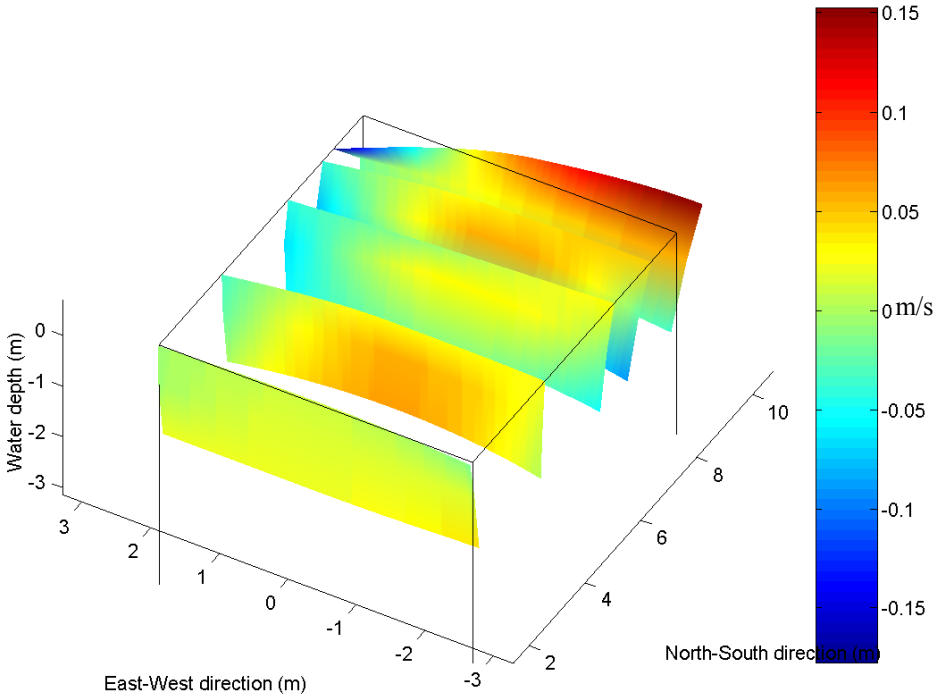

Figure B.20: Contours for *w* for a 3*3 array current test at 225% for *x*+

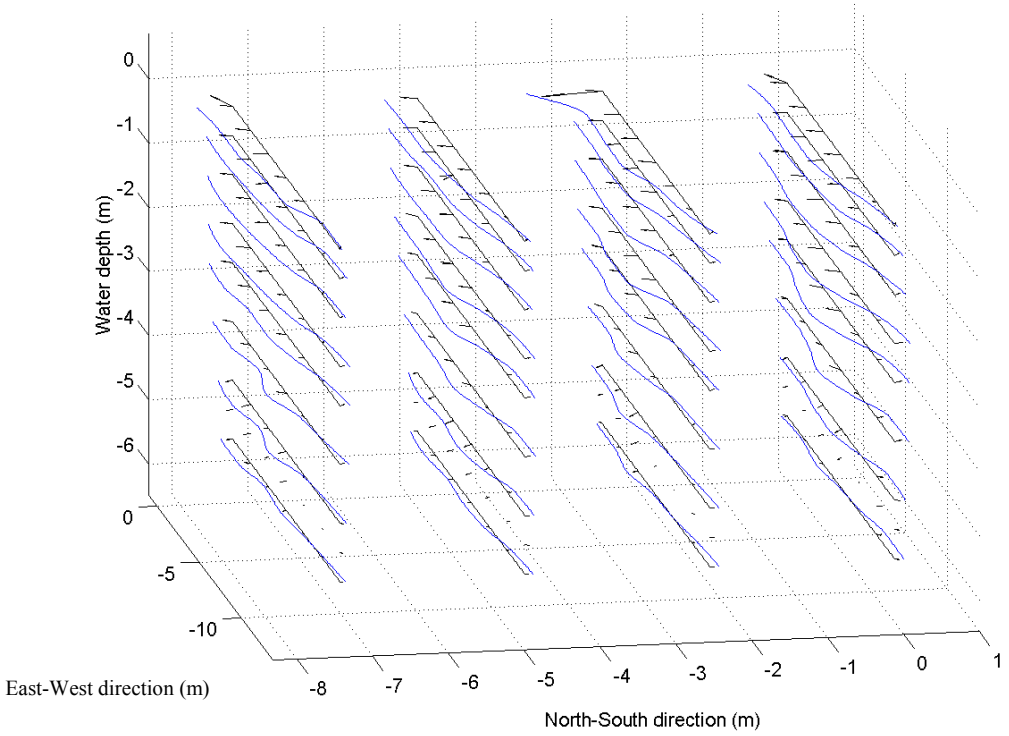

Figure B.21: Average Velocity for a Vertical array current test at 100%

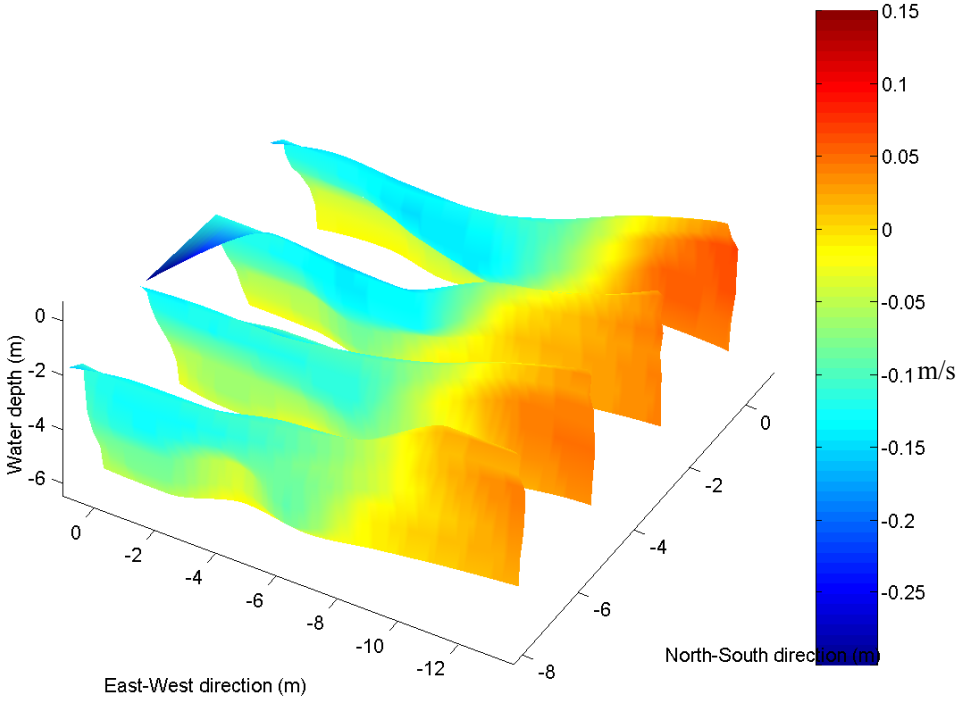

Figure B.22: Contours for *u* for a Vertical array current test at 100%

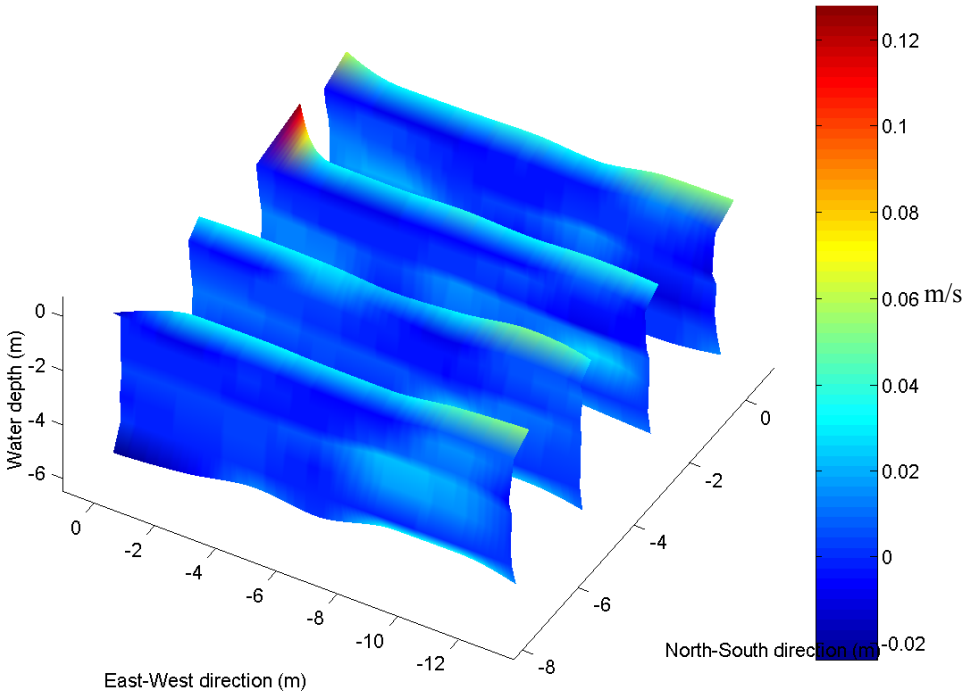

Figure B.23: Contours for *v* for a Vertical array current test at 100%

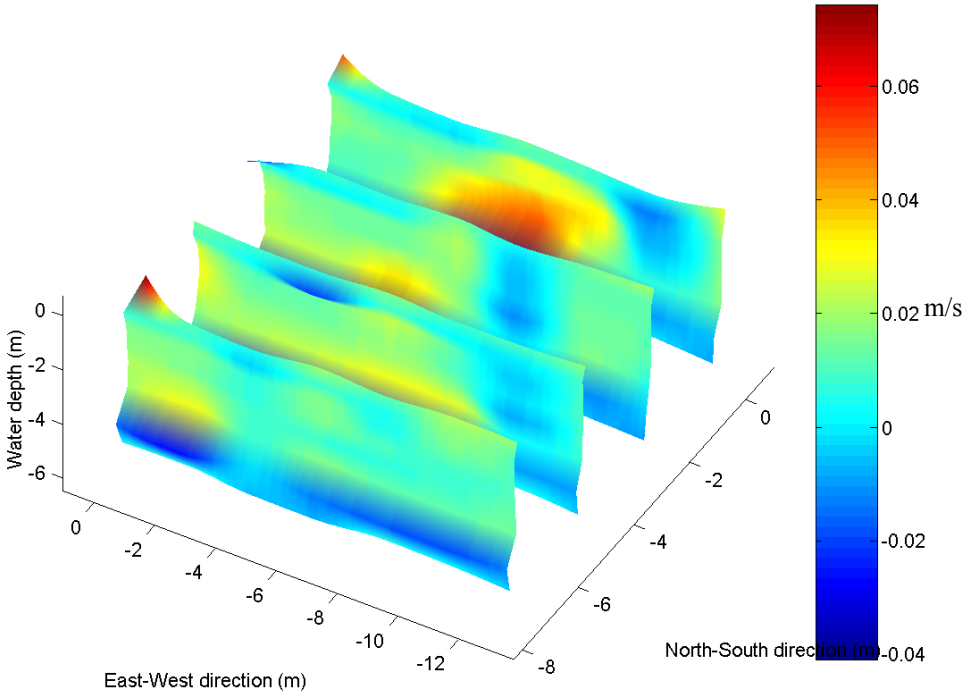

Figure B.24: Contours for *w* for a Vertical array current test at 100%

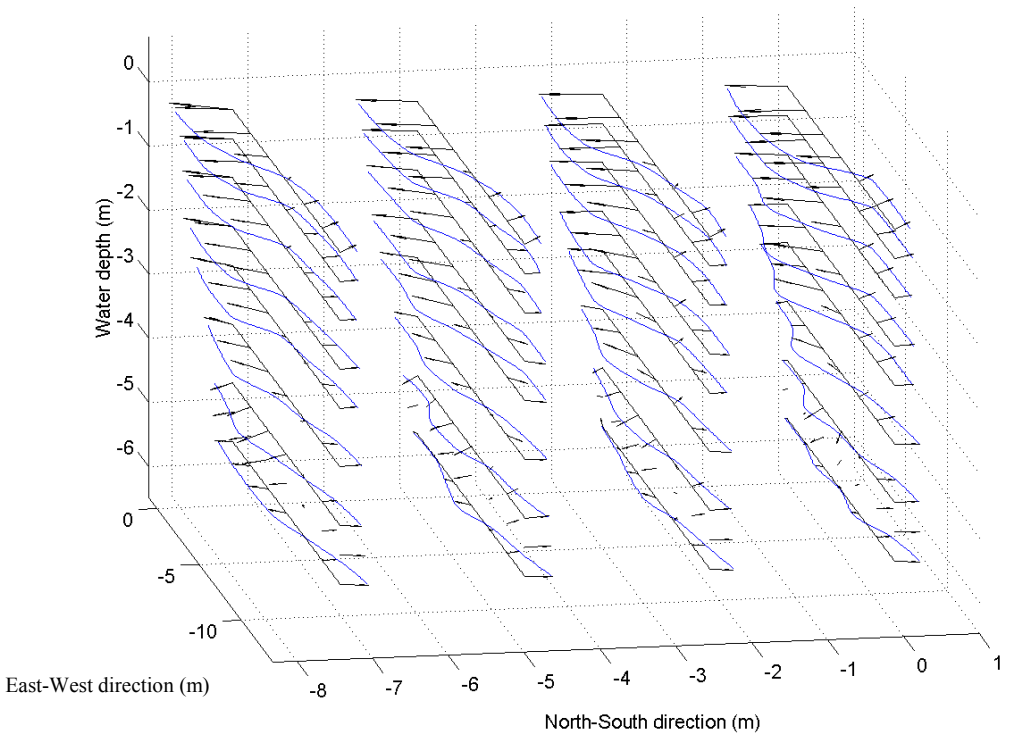

Figure B.25: Average Velocity for a Vertical array current test at 200%

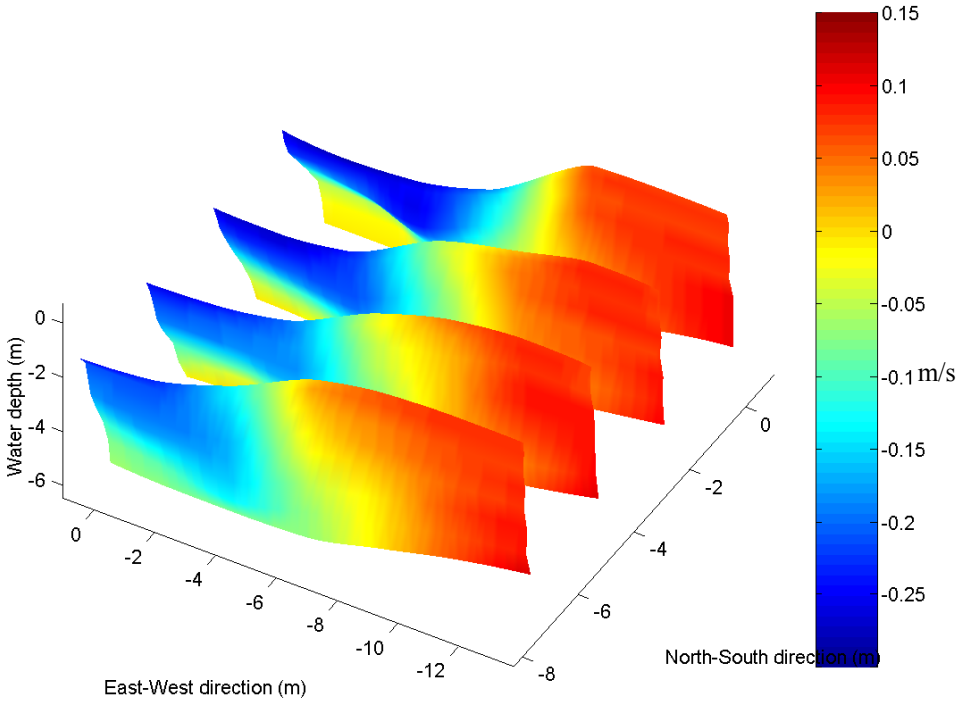

Figure B.26: Contours for *u* for a Vertical array current test at 200%

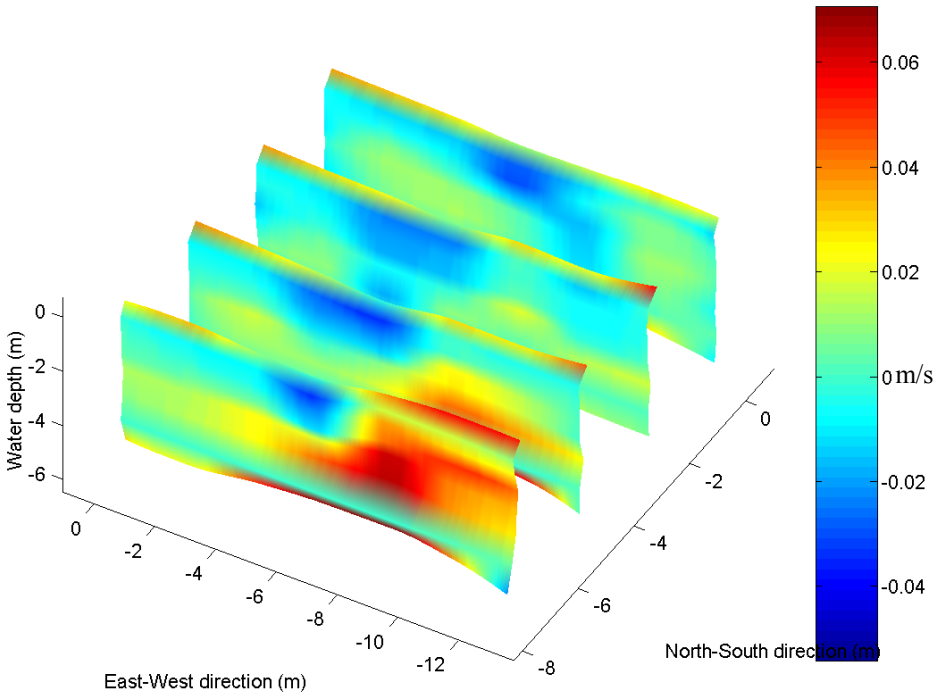

Figure B.27: Contours for *v* for a Vertical array current test at 200%

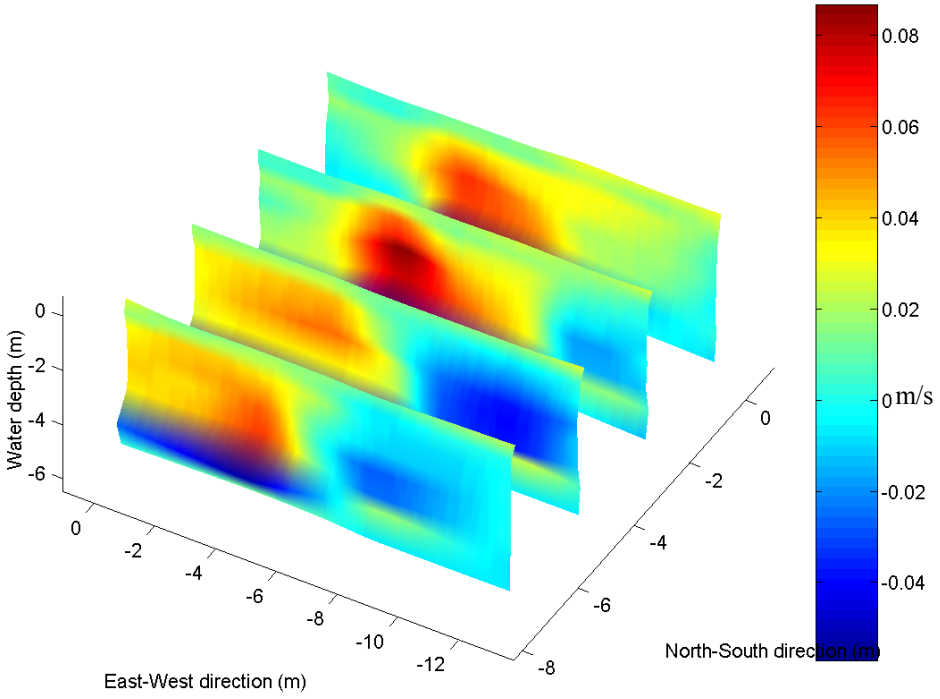

Figure B.28: Contours for *w* for a Vertical array current test at 200%

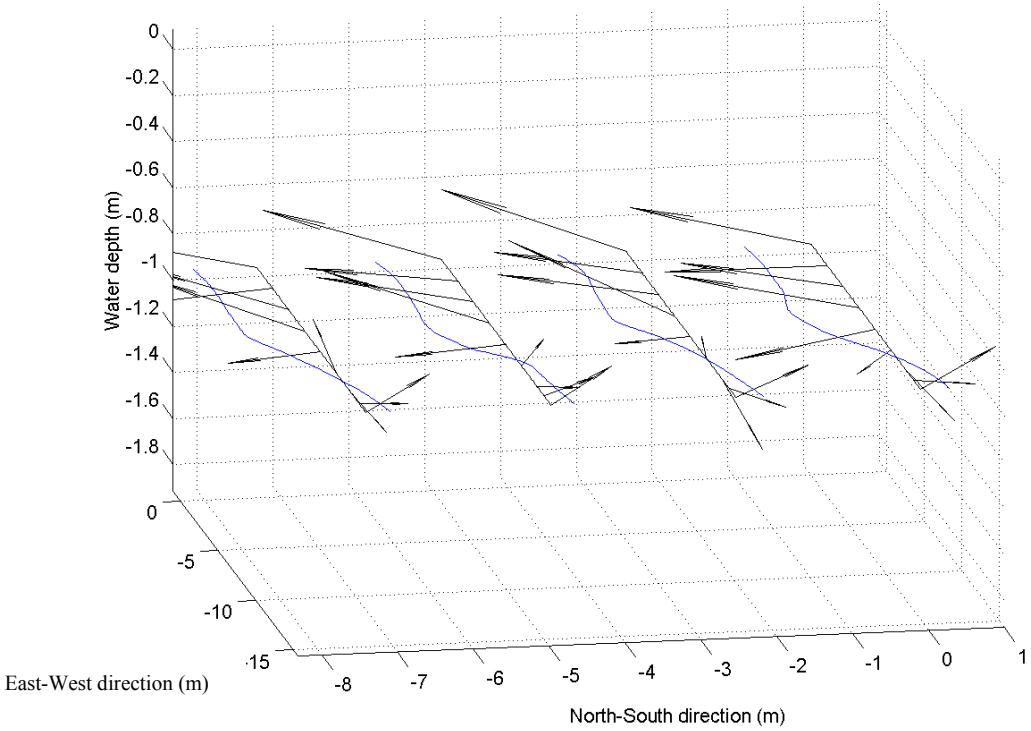

Figure B.29: Average Velocity for a Horizontal array current test at 100%

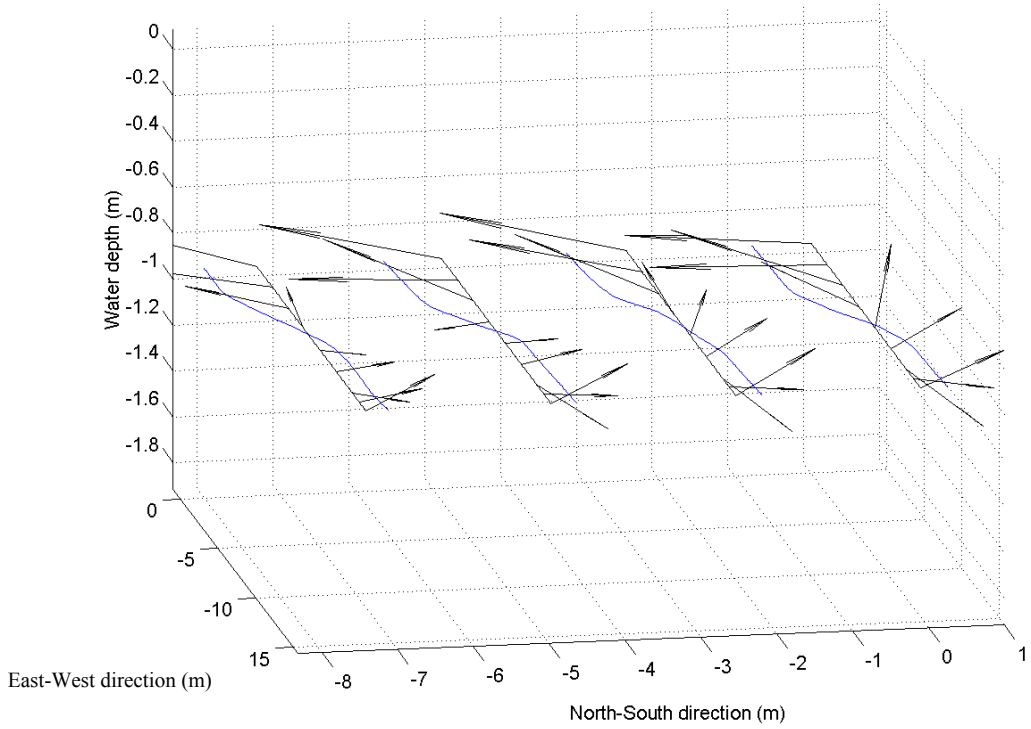

Figure B.30: Average Velocity for a Horizontal array current test at 200%

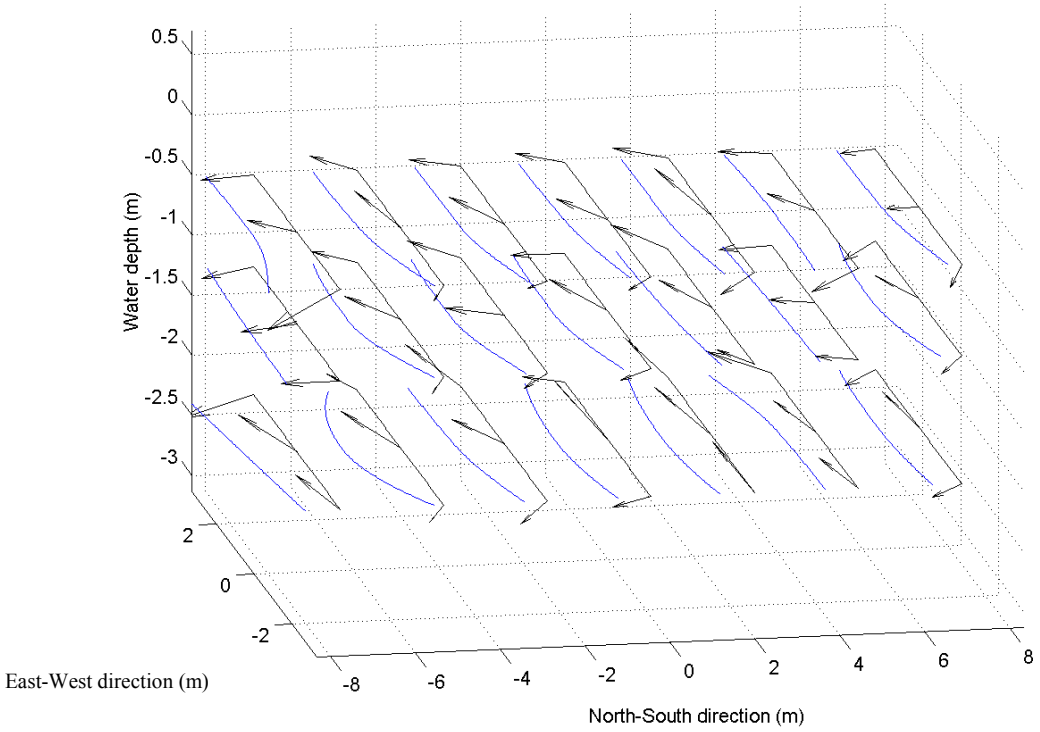

Figure B.31: Average Velocity for a 3*3 array with a RG2 wave + current test at 100%

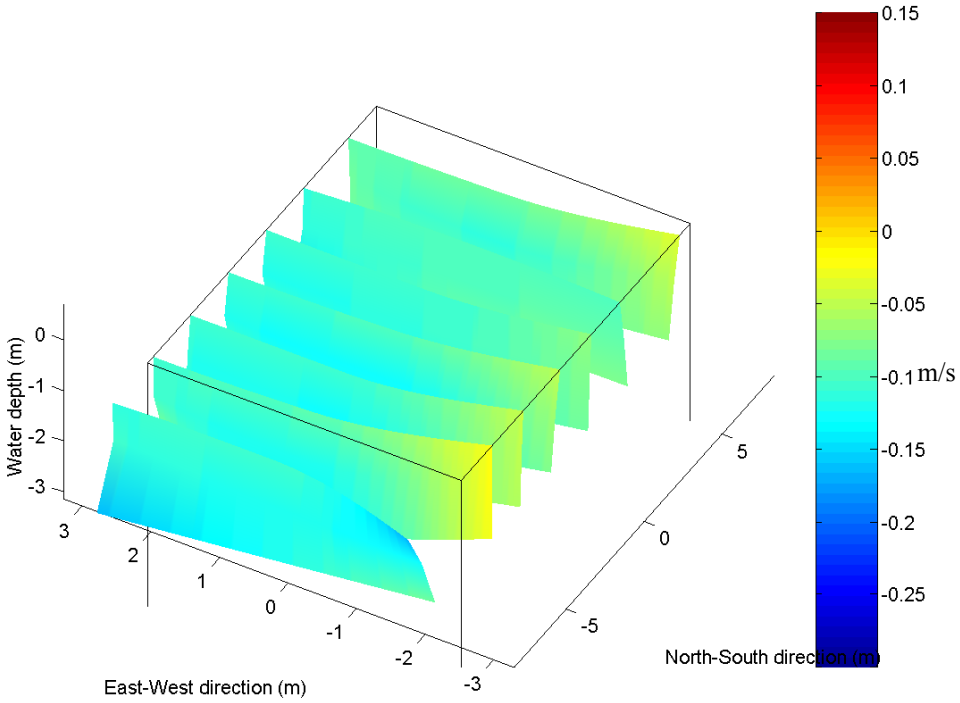

Figure B.32: Contours for *u* for a 3*3 array with a RG2 wave + current test at 100%

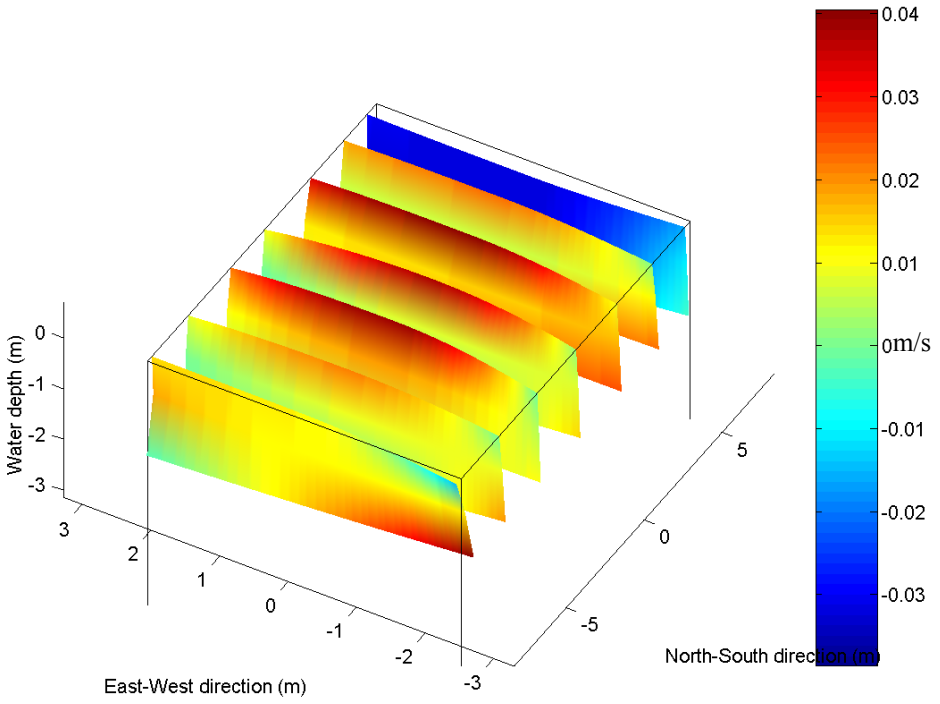

Figure B.33: Contours for *v* for a 3*3 array with a RG2 wave + current test at 100%

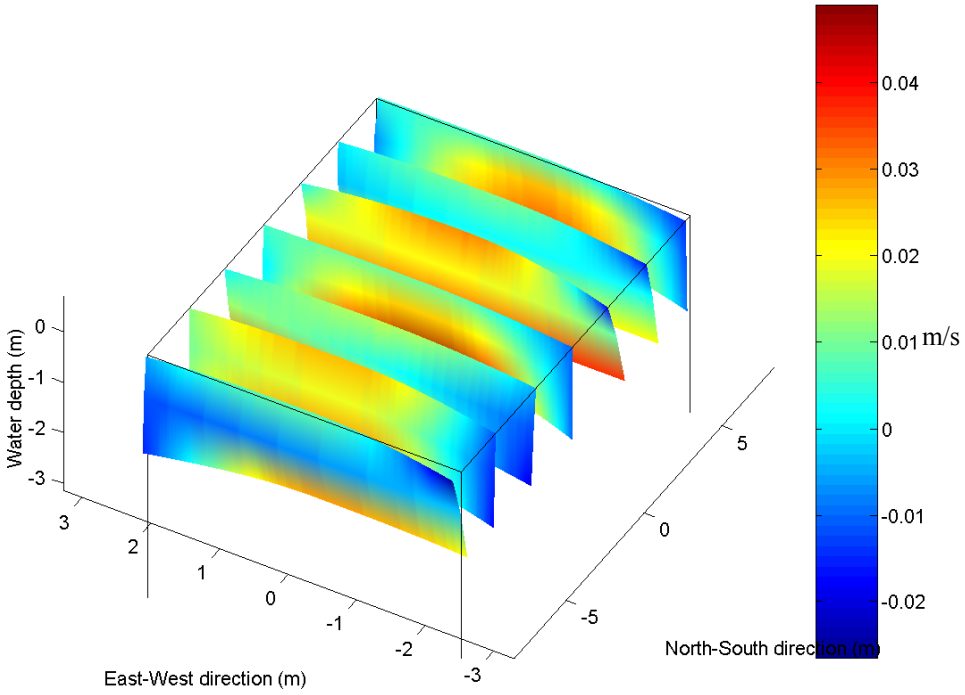

Figure B.34: Contours for *w* for a 3*3 array with a RG2 wave + current test at 100%

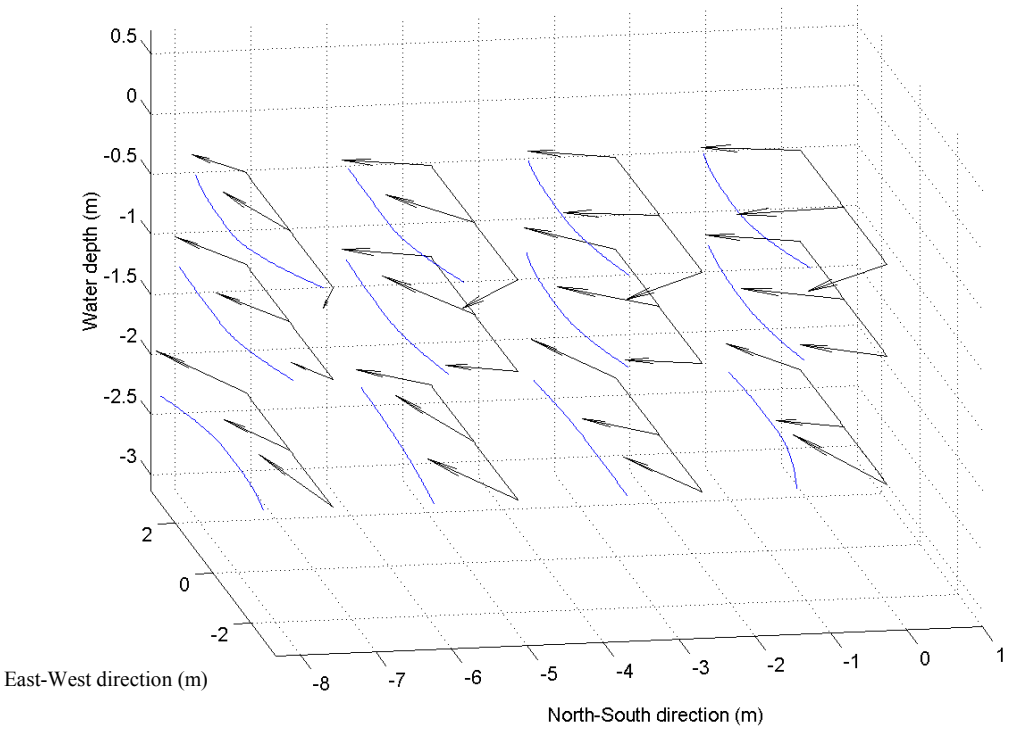

Figure B.35: Average Velocity for a 3*3 array with a RG2 wave + current test at 200%

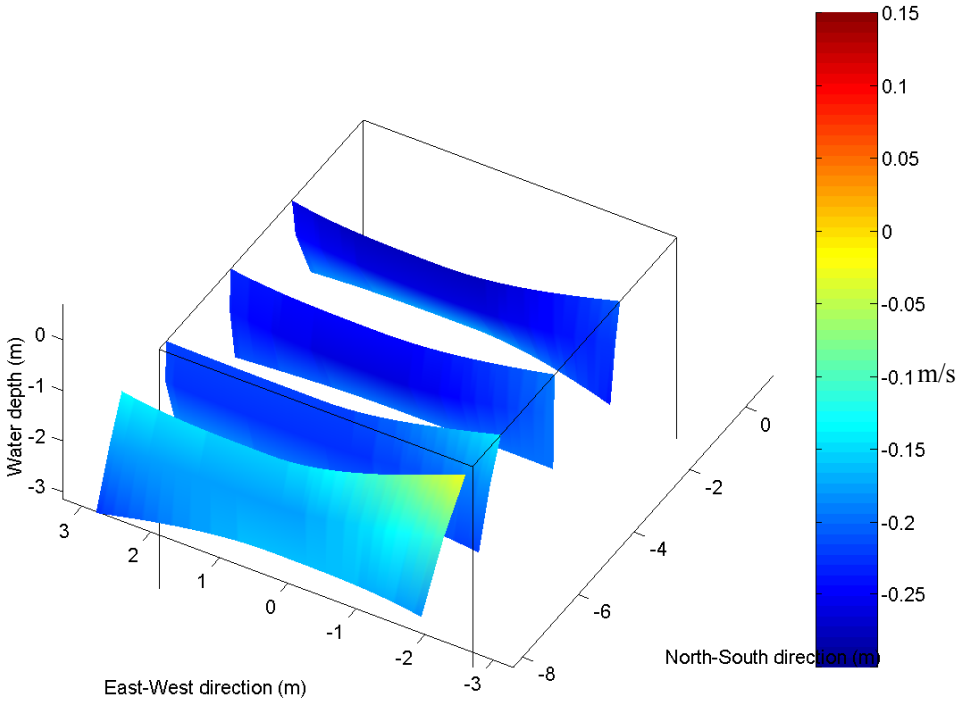

Figure B.36: Contours for *u* for a 3*3 array with a RG2 wave + current test at 200%

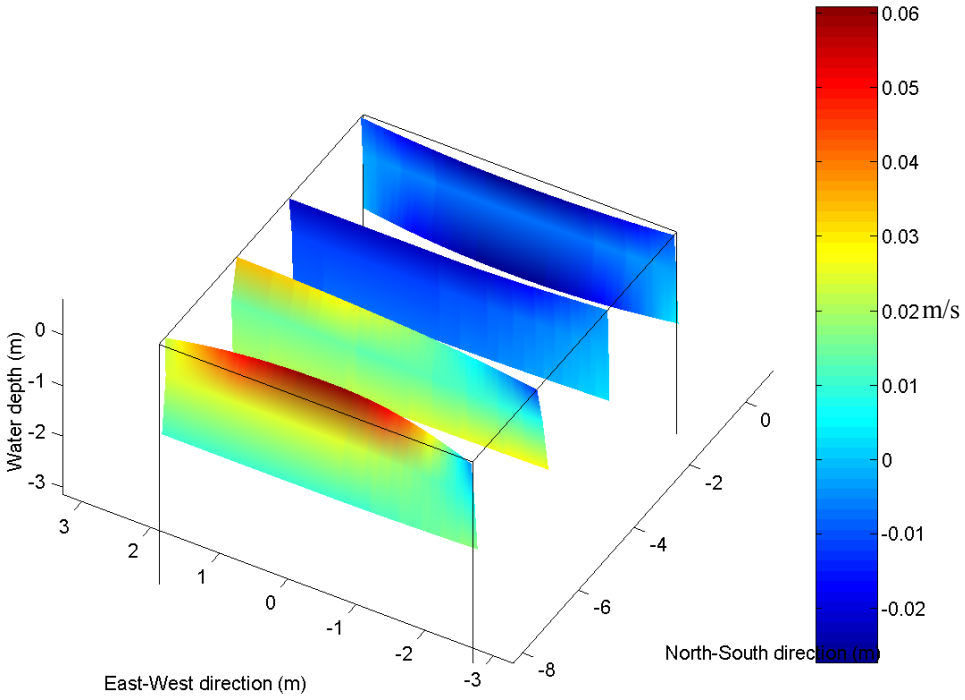

Figure B.37: Contours for *v* for a 3*3 array with a RG2 wave + current test at 200%

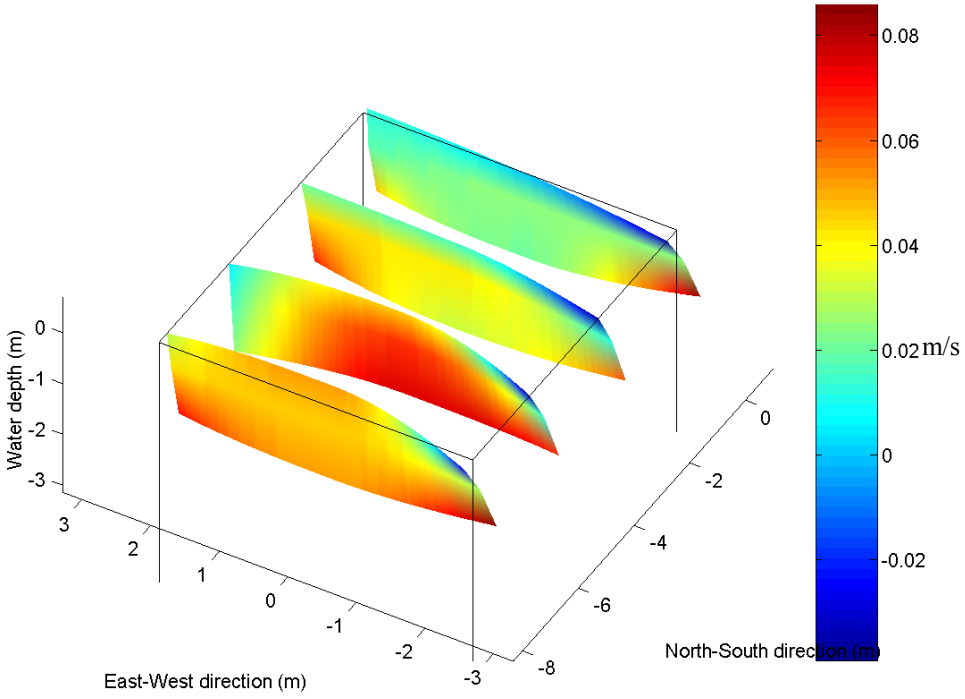

Figure B.38: Contours for *w* for a 3*3 array with a RG2 wave + current test at 200%

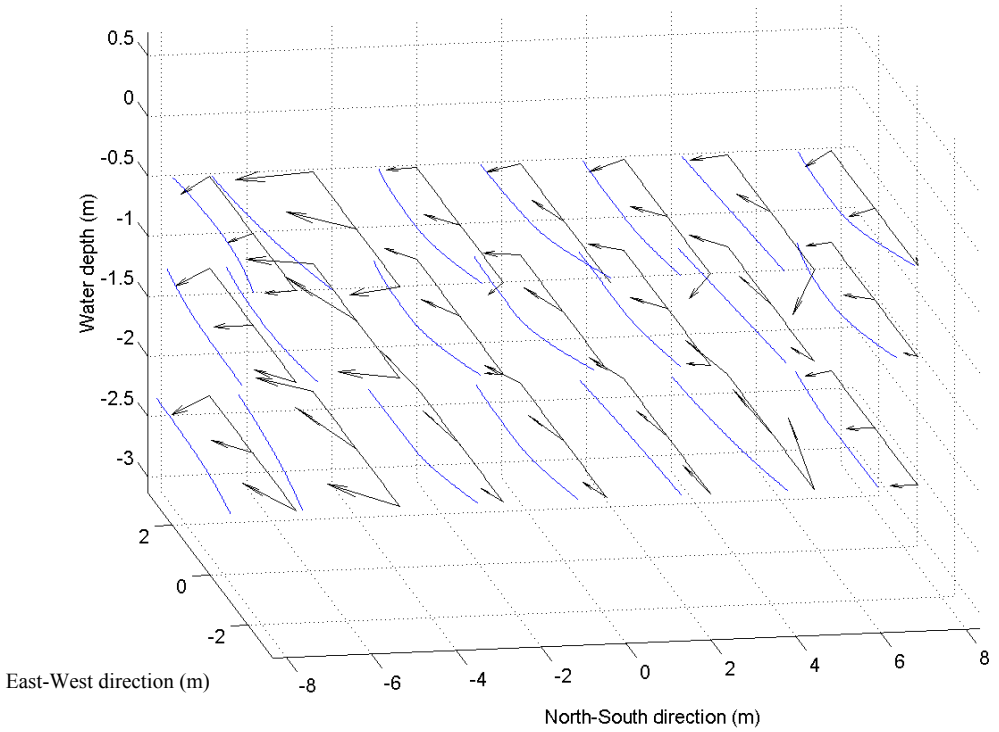

Figure B.39: Average Velocity for a 3*3 array with a RG5 wave + current test at 100%

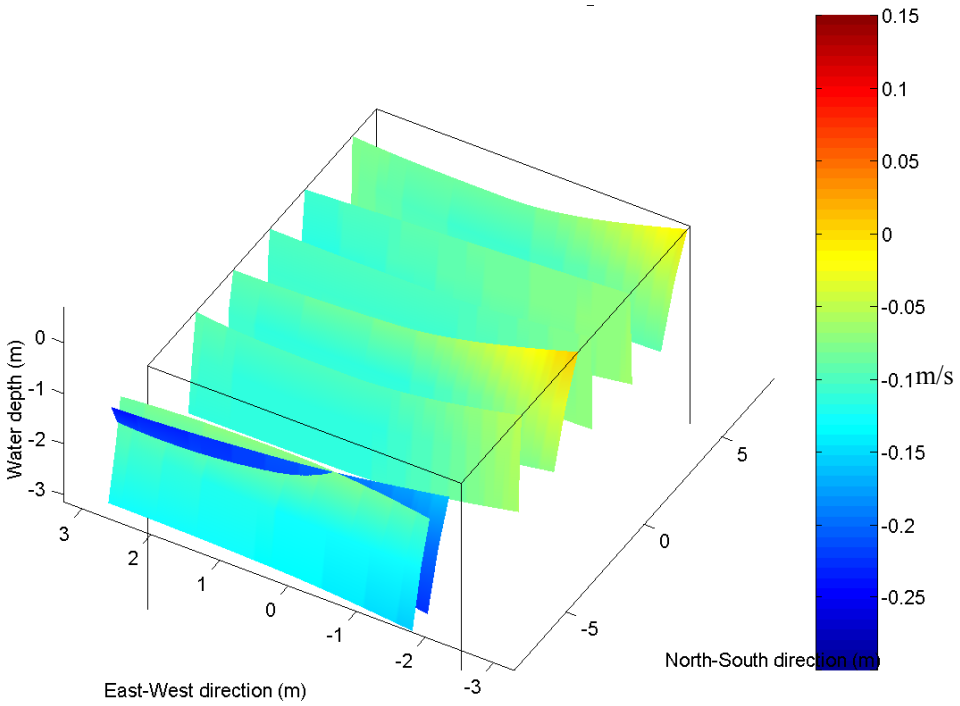

Figure B.40: Contours for *u* for a 3*3 array with a RG5 wave + current test at 100%

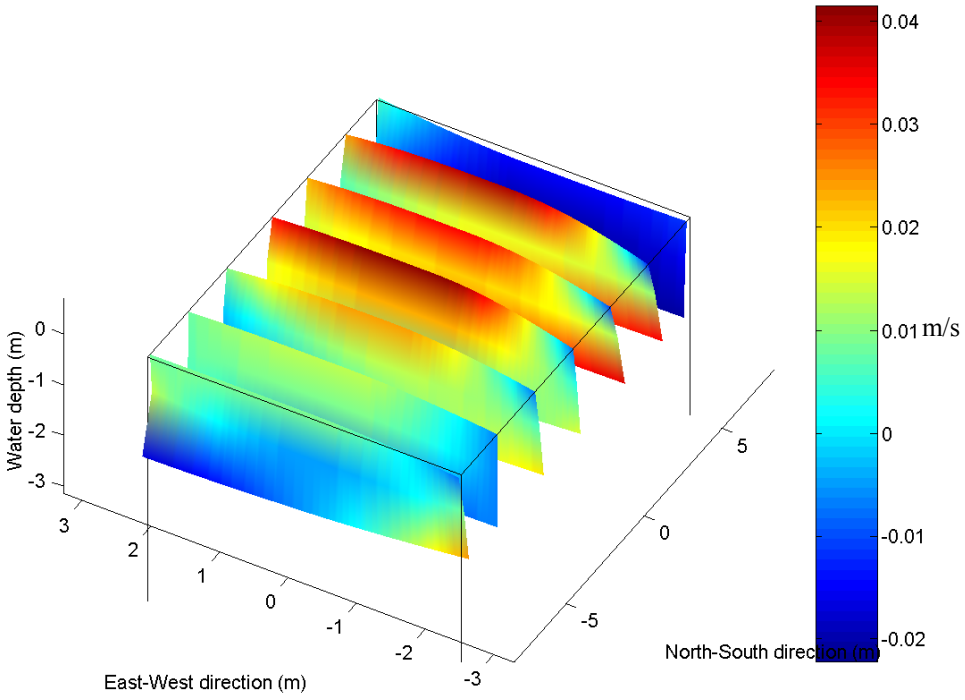

Figure B.41: Contours for *v* for a 3*3 array with a RG5 wave + current test at 100%

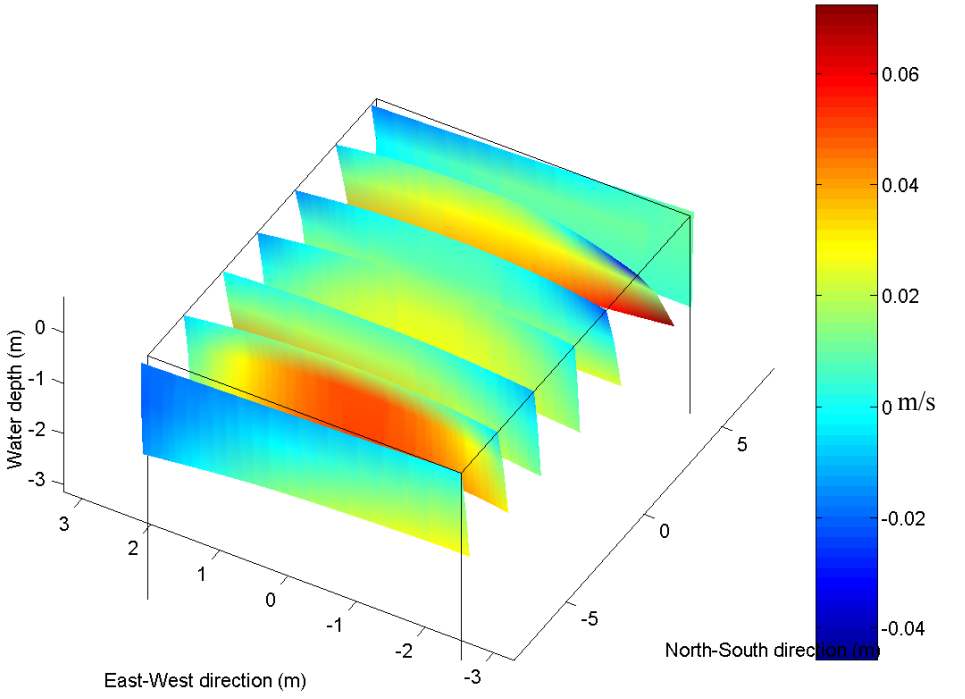

Figure B.42: Contours for *w* for a 3*3 array with a RG5 wave + current test at 100%

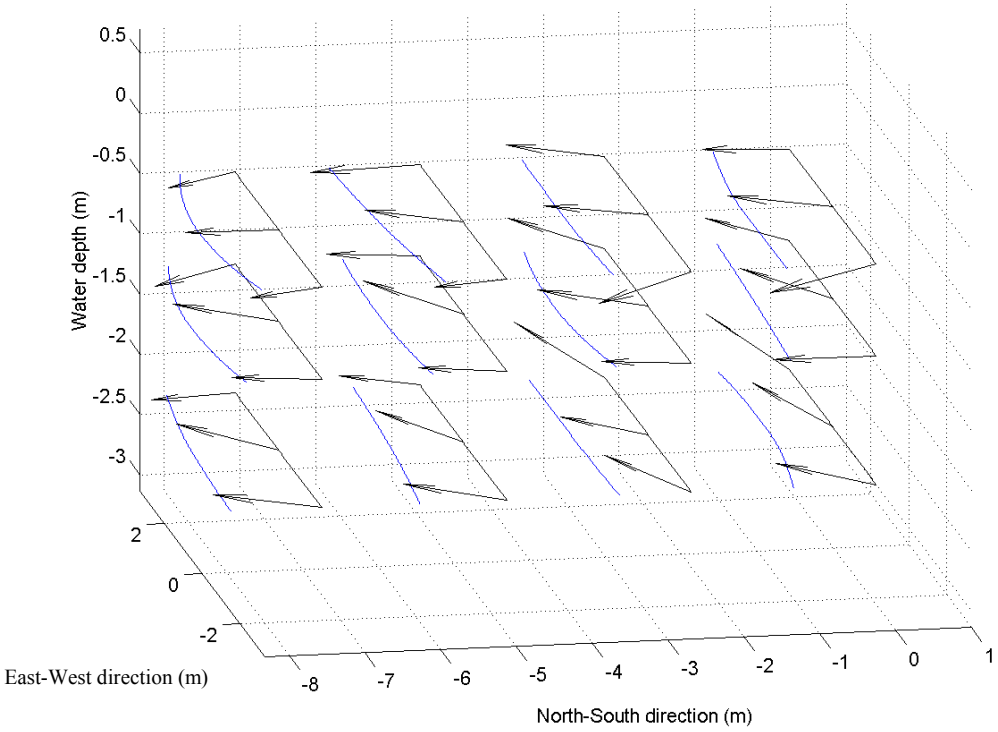

Figure B.43: Average Velocity for a 3*3 array with a RG5 wave + current test at 200%

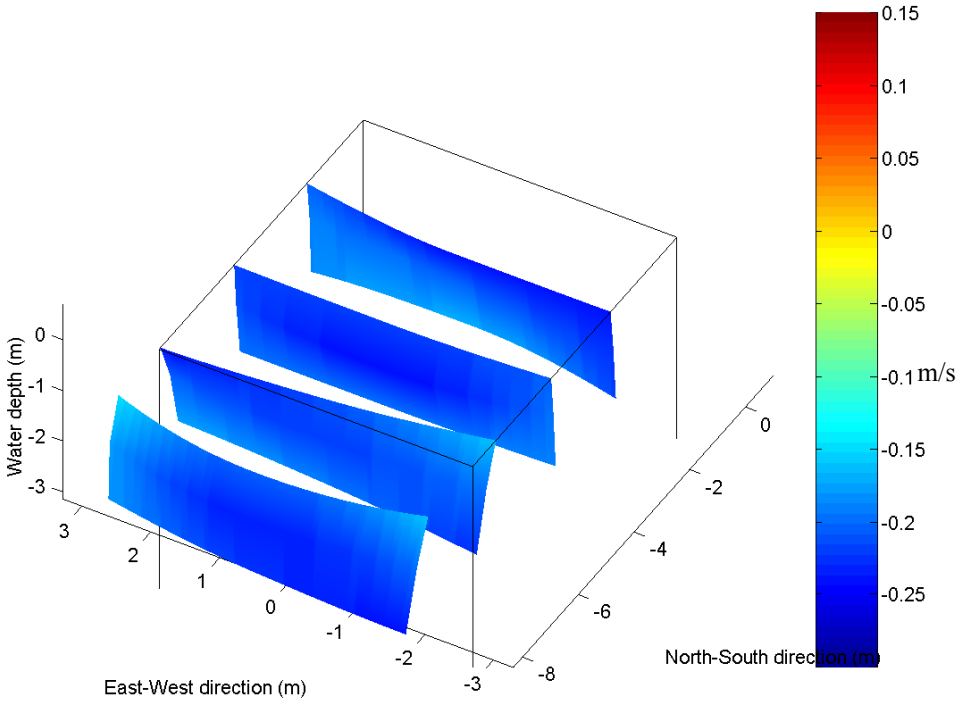

Figure B.44: Contours for *u* for a 3*3 array with a RG5 wave + current test at 200%

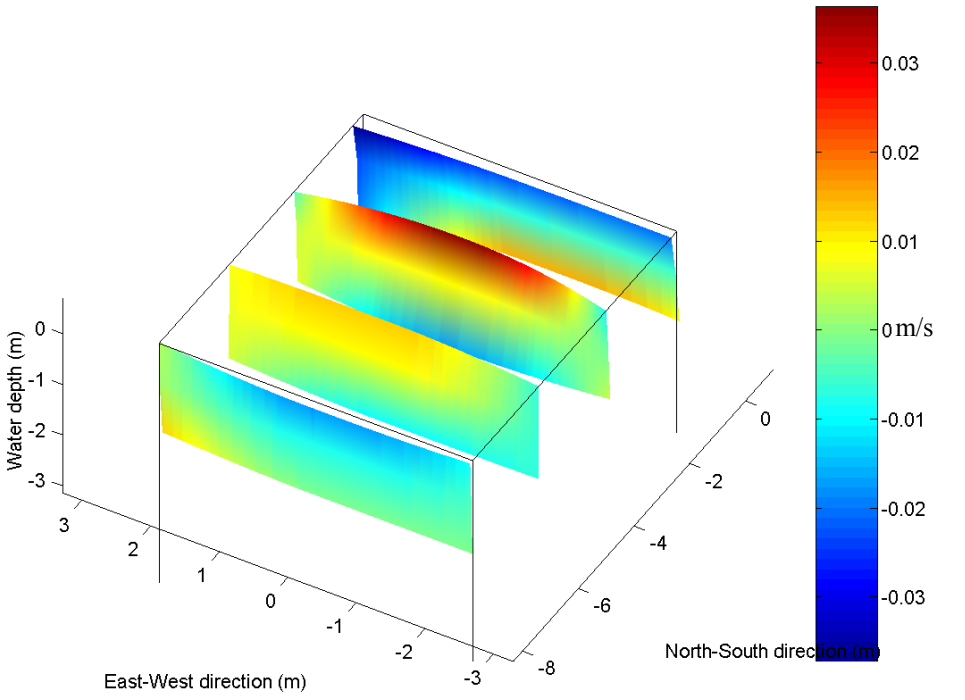

Figure B.45: Contours for *v* for a 3*3 array with a RG5 wave + current test at 200%

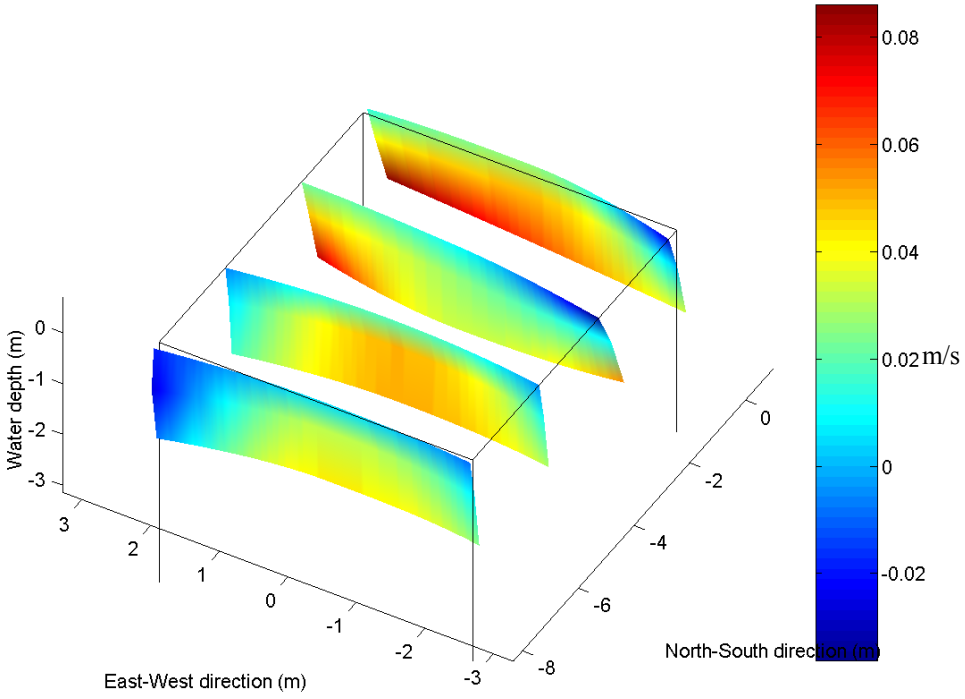

Figure B.46: Contours for *w* for a 3*3 array with a RG5 wave + current test at 200%

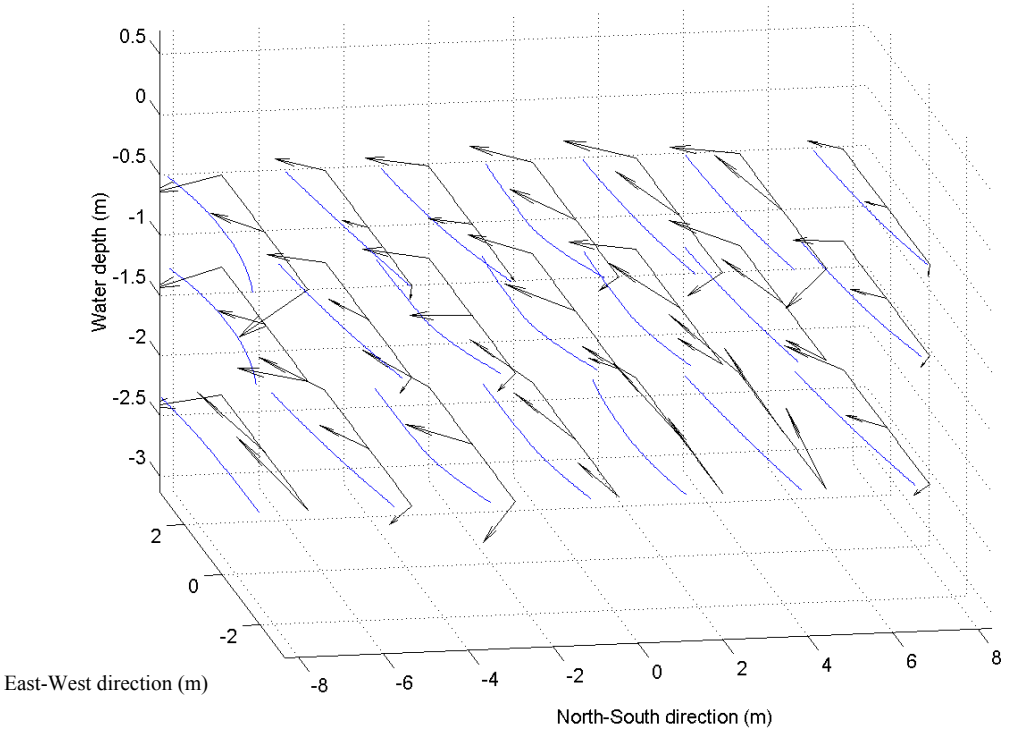

Figure B.47: Average Velocity for a 3*3 array with a RN wave + current test at 100%

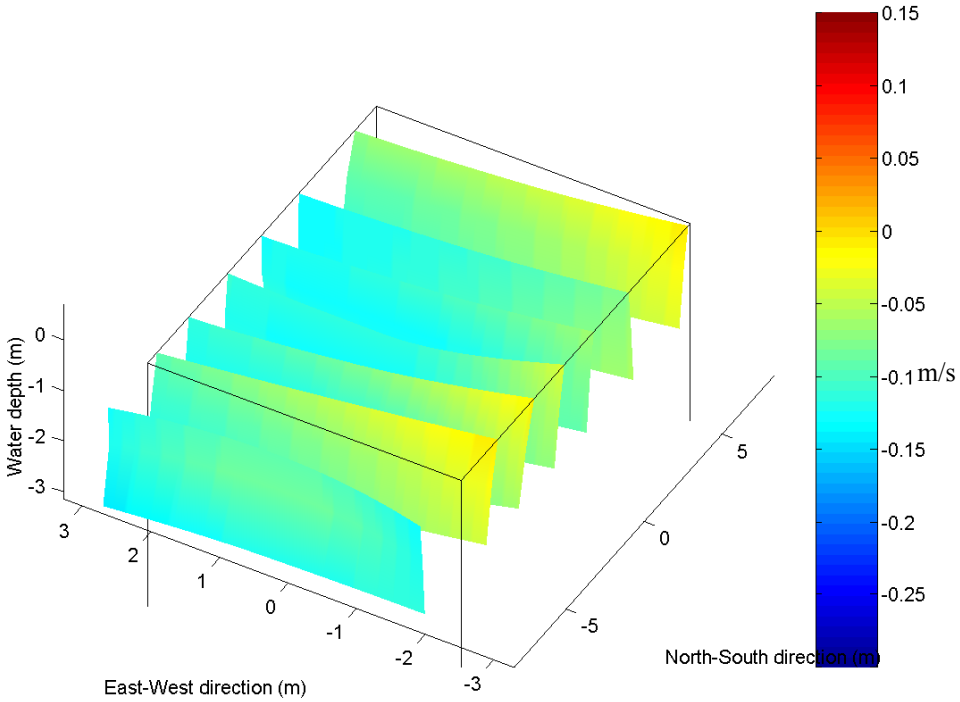

Figure B.48: Contours for *u* for a 3*3 array with a RN wave + current test at 100%

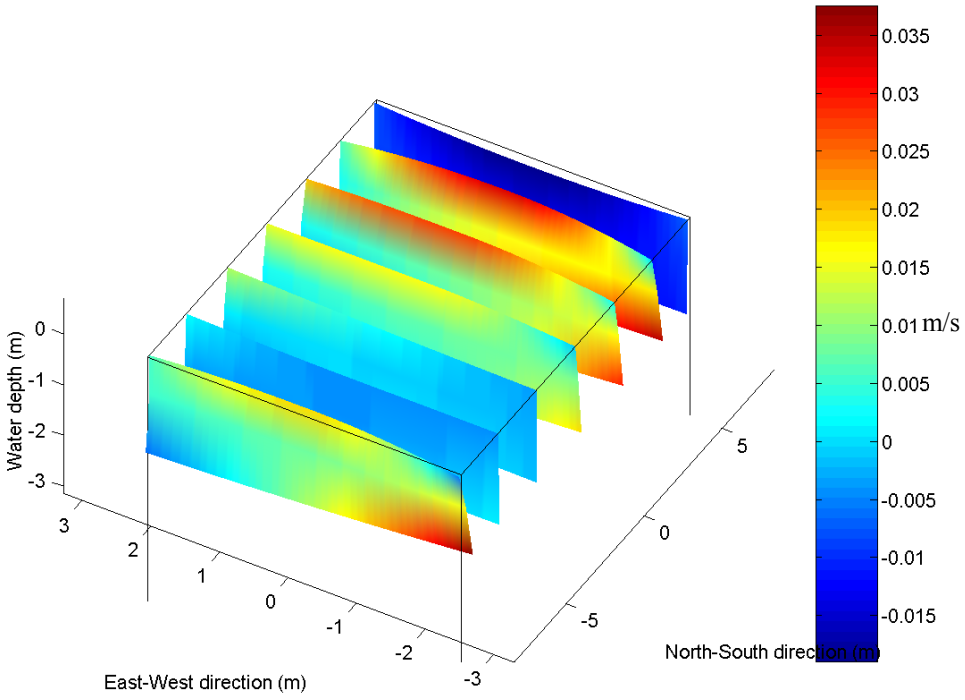

Figure B.49: Contours for *v* for a 3*3 array with a RN wave + current test at 100%

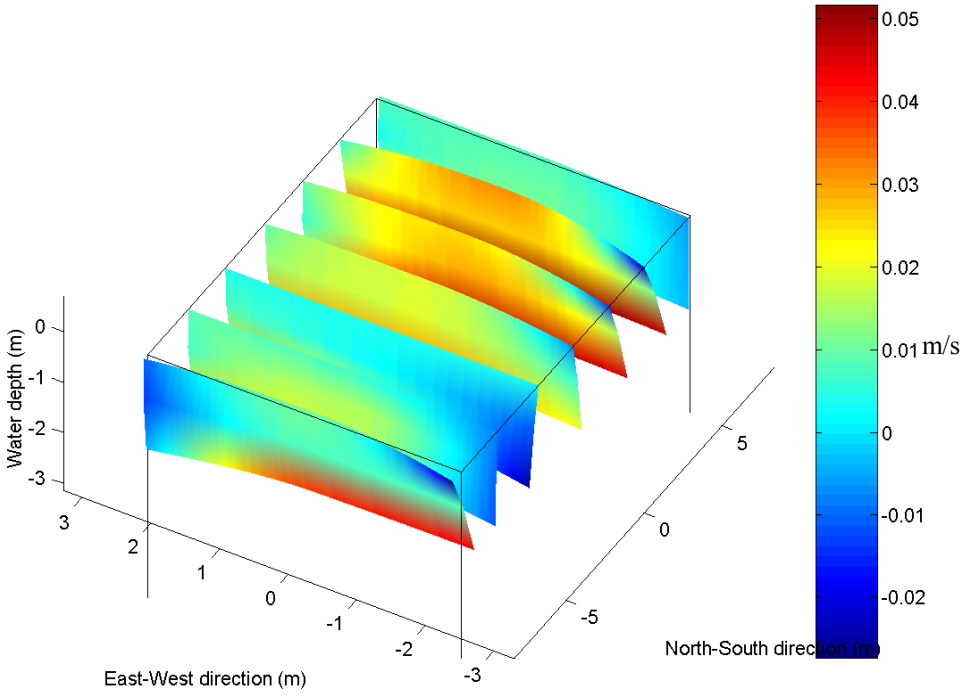

Figure B.50: Contours for *w* for a 3*3 array with a RN wave + current test at 100%

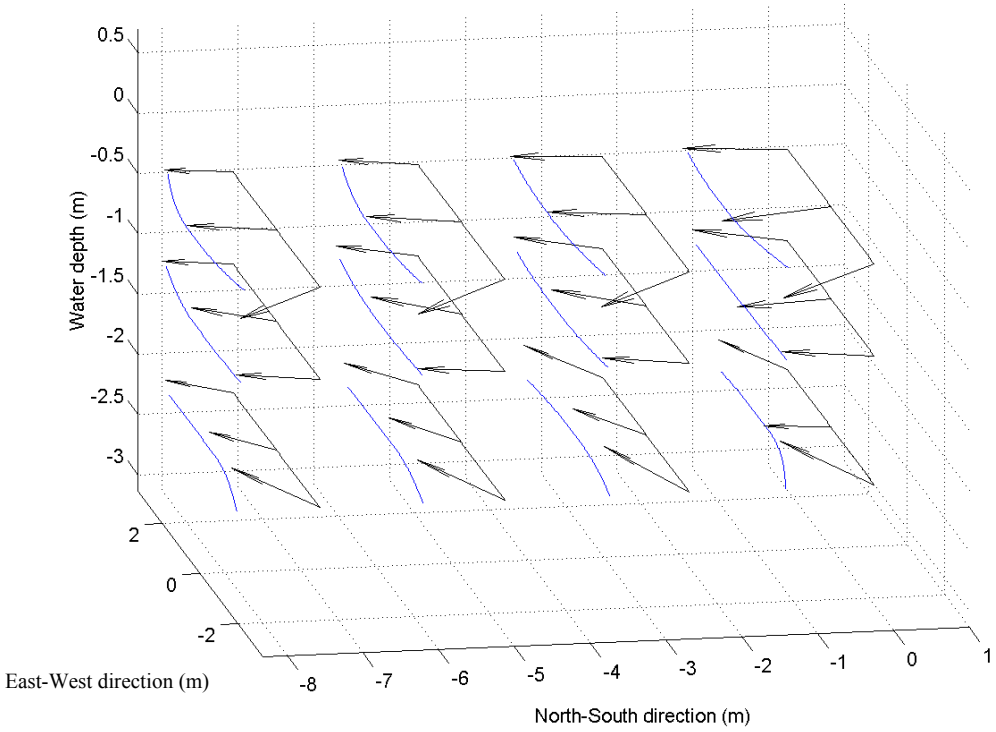

Figure B.51: Average Velocity for a 3*3 array with a RN wave + current test at 200%

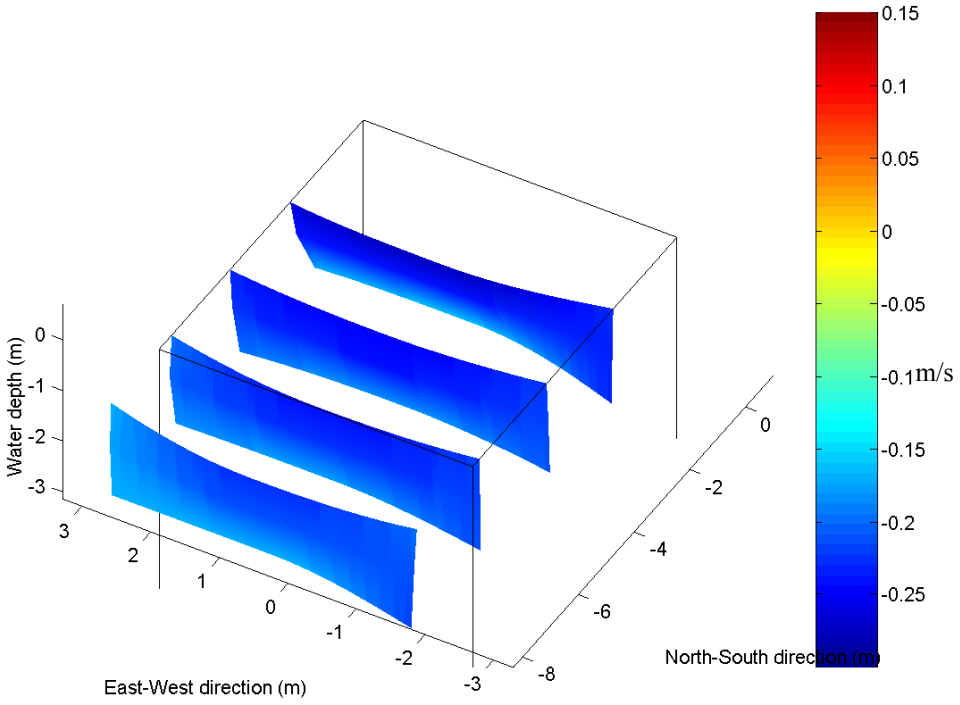

Figure B.52: Contours for *u* for a 3*3 array with a RN wave + current test at 200%

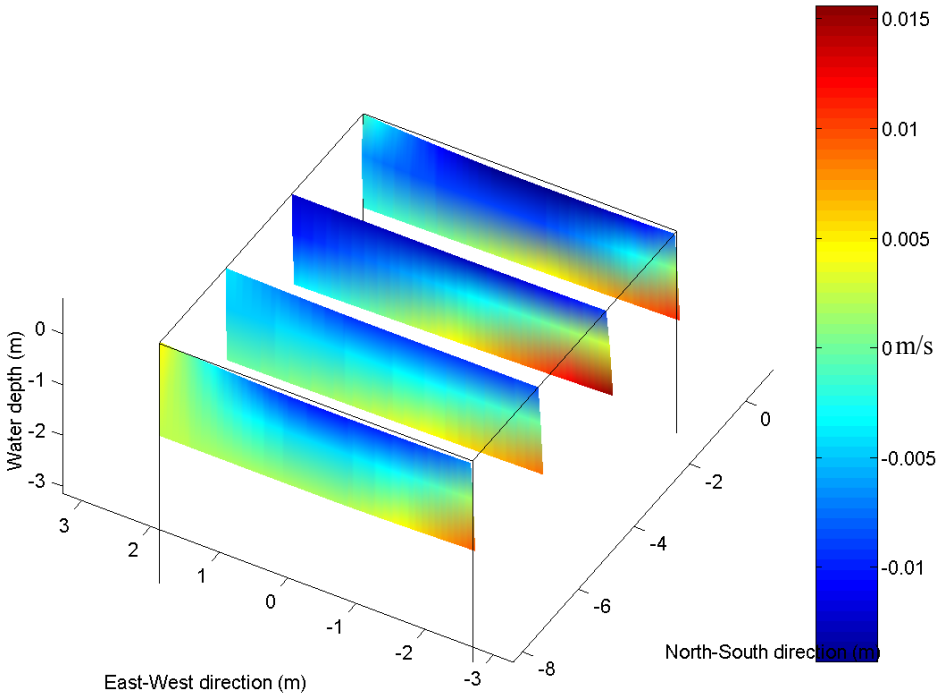

Figure B.53: Contours for *v* for a 3*3 array with a RN wave + current test at 200%

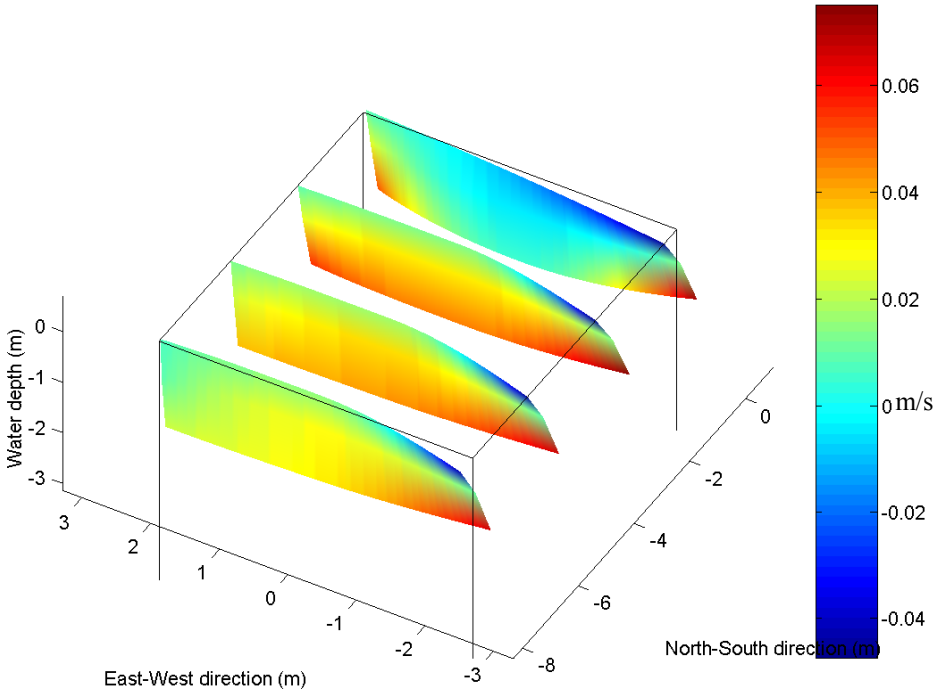

Figure B.54: Contours for *w* for a 3*3 array with a RN wave + current test at 200%

APPENDIX C

VELOCITY PROFILES

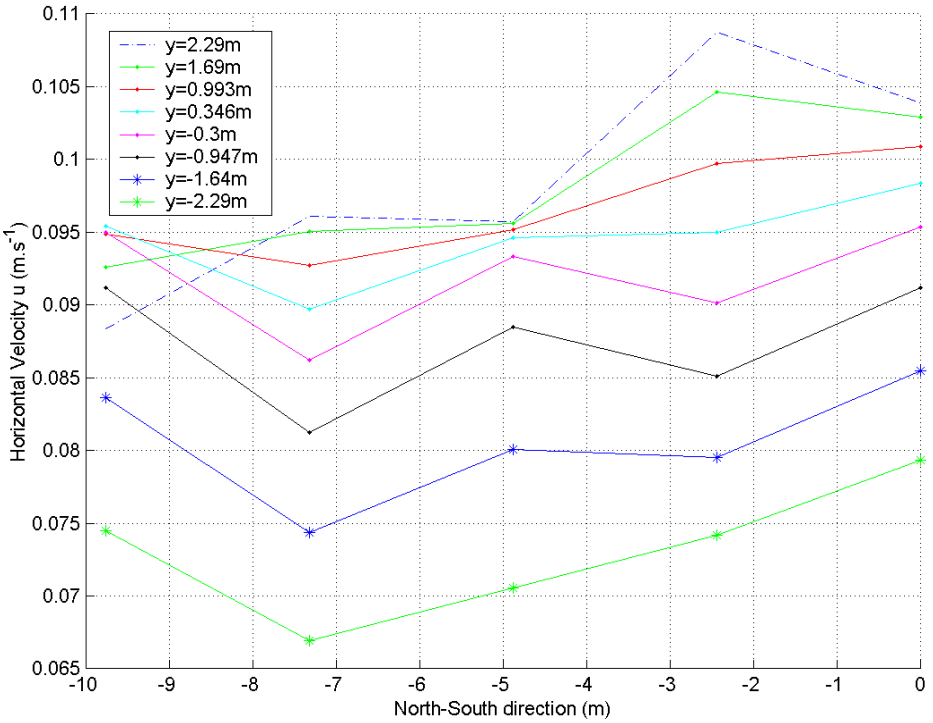

Figure C.1: Velocity profile along *x* at 100% in a 3*3 array for *x*-

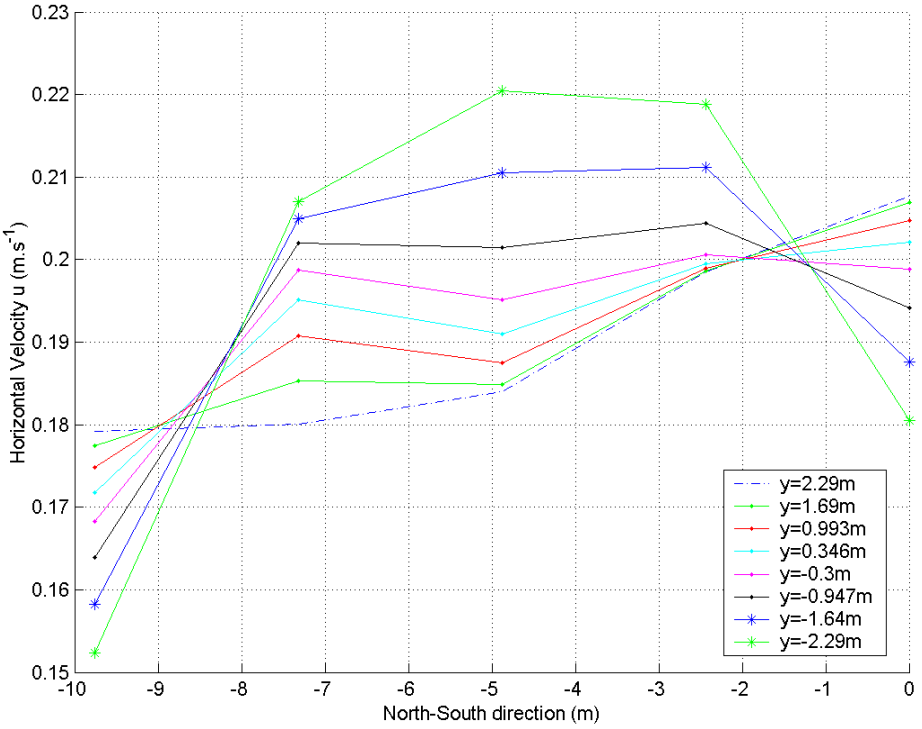

Figure C.2: Velocity profile along *x* at 225% in a 3*3 array for *x*-

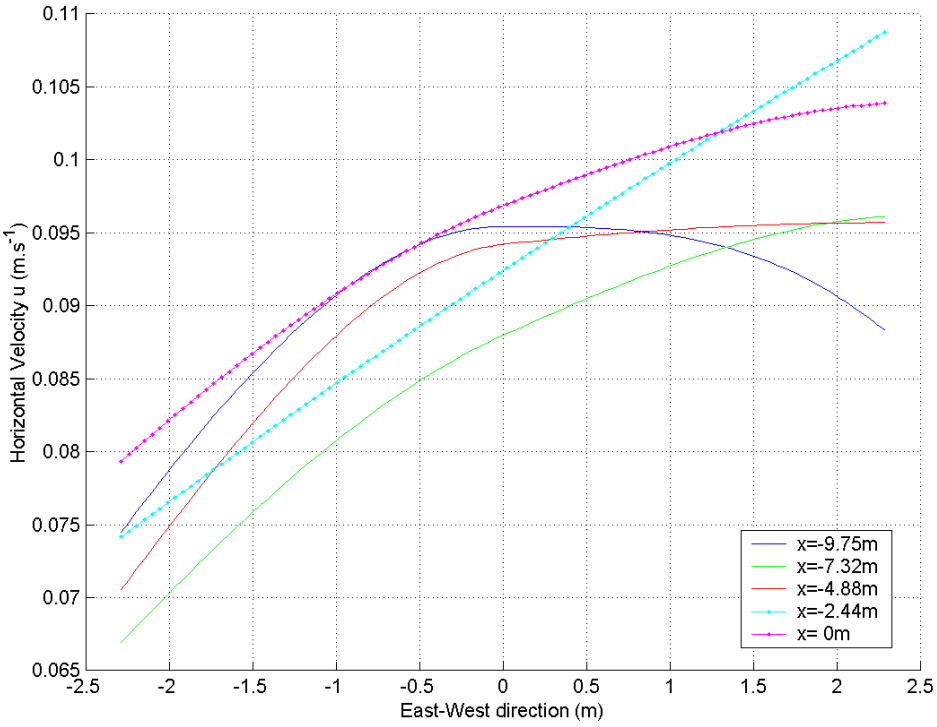

Figure C.3: Velocity profile along *y* at 100% in a 3*3 array for *x*-

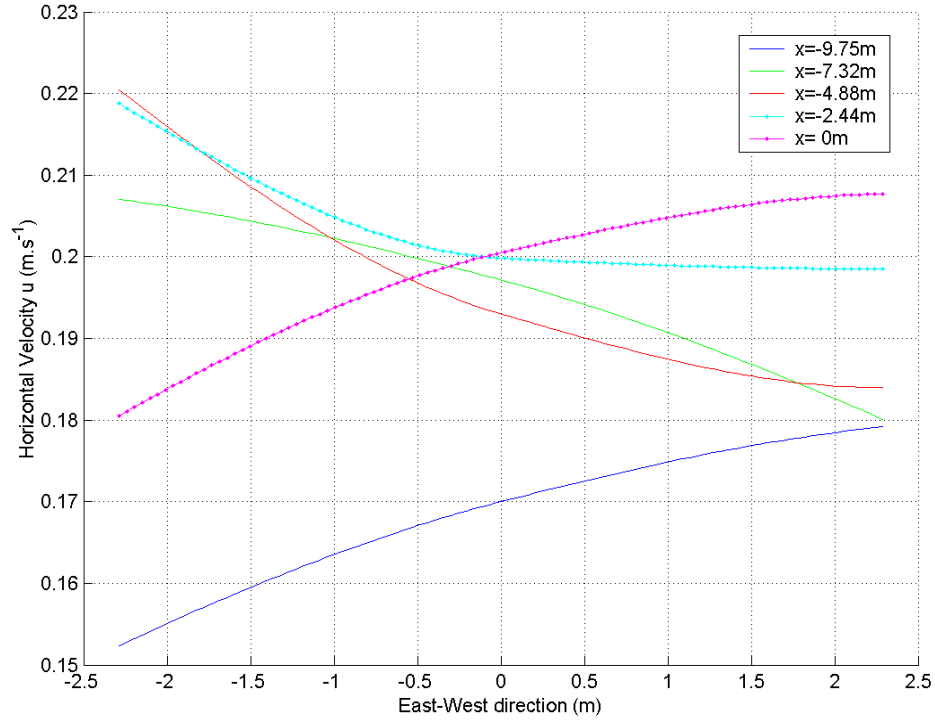

Figure C.4: Velocity profile along *y* at 225% in a 3*3 array for *x*-

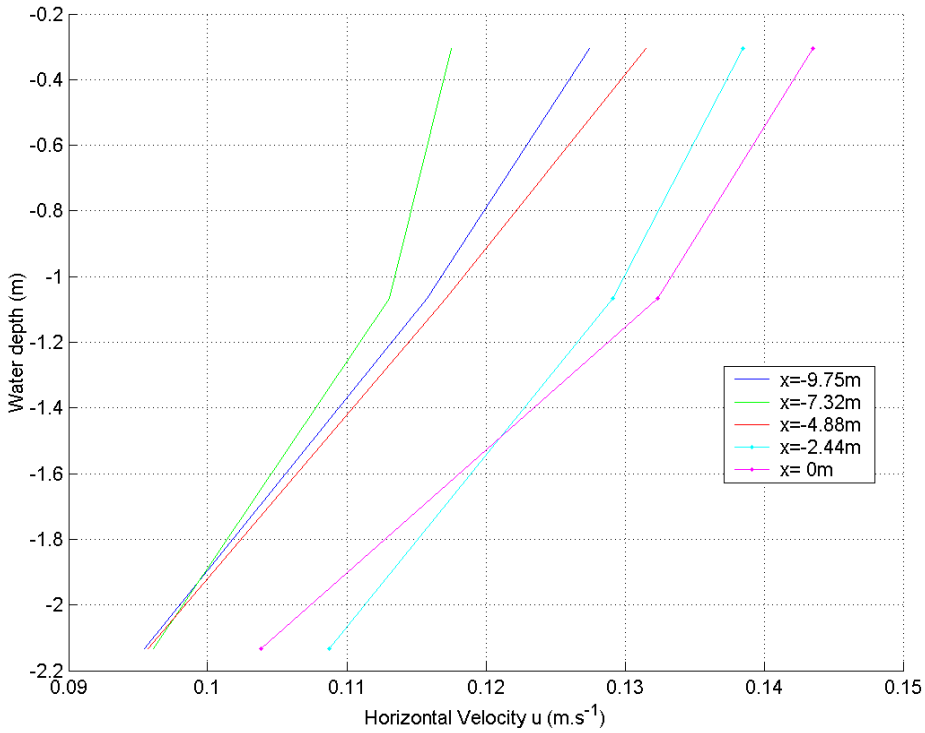

Figure C.5: Velocity profile along *z* at 100% in a 3*3 array for *x*-

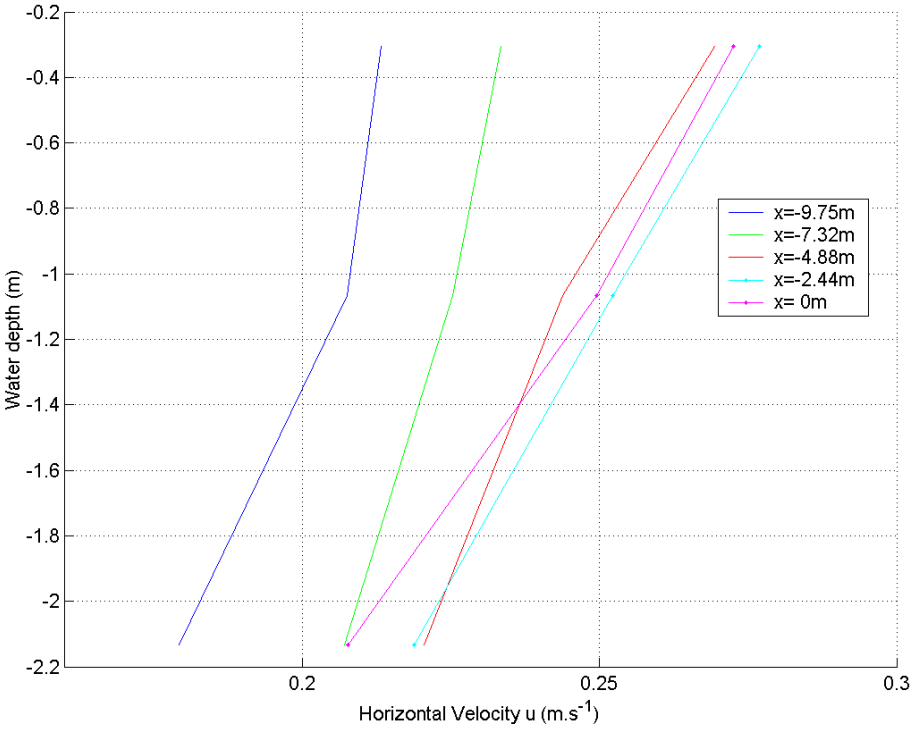

Figure C.6: Velocity profile along *z* at 225% in a 3*3 array for *x*-

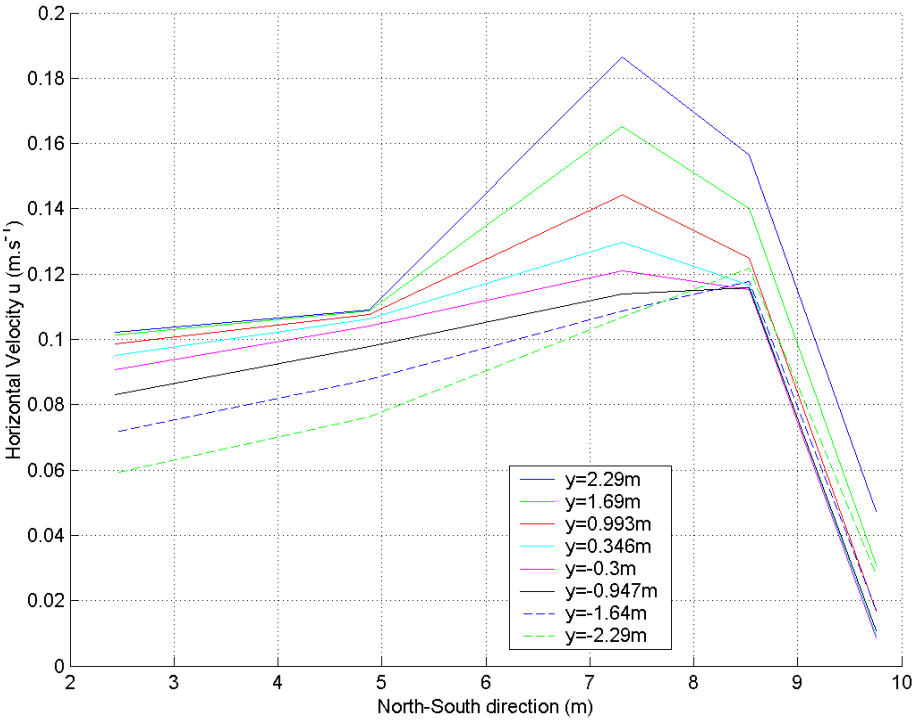

Figure C.7: Velocity profile along *x* at 100% in a 3*3 array for *x*+

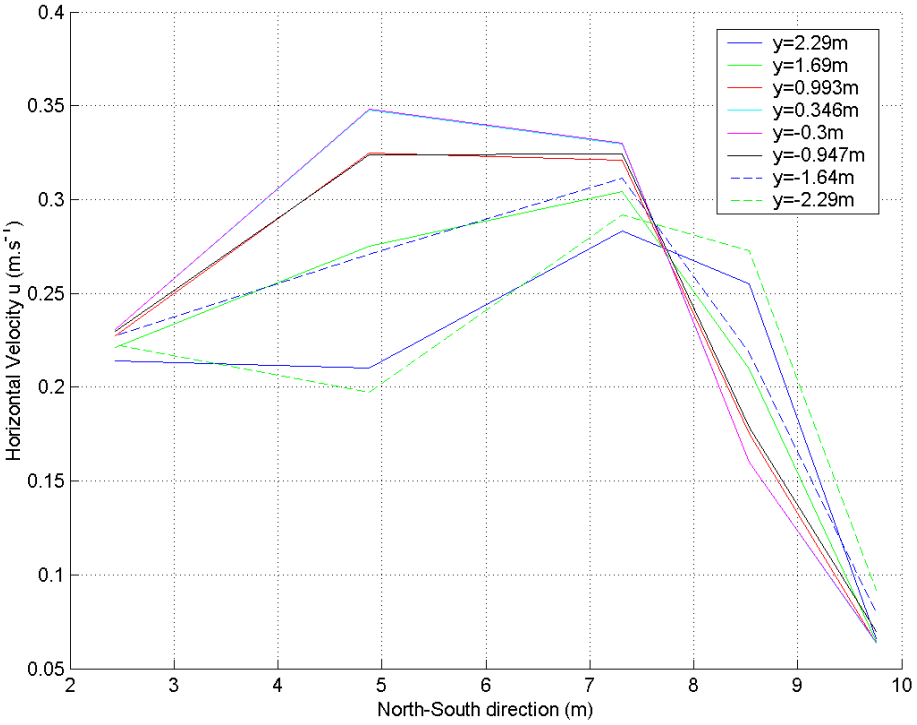

Figure C.8: Velocity profile along at 225% in a 3*3 array for *x*+

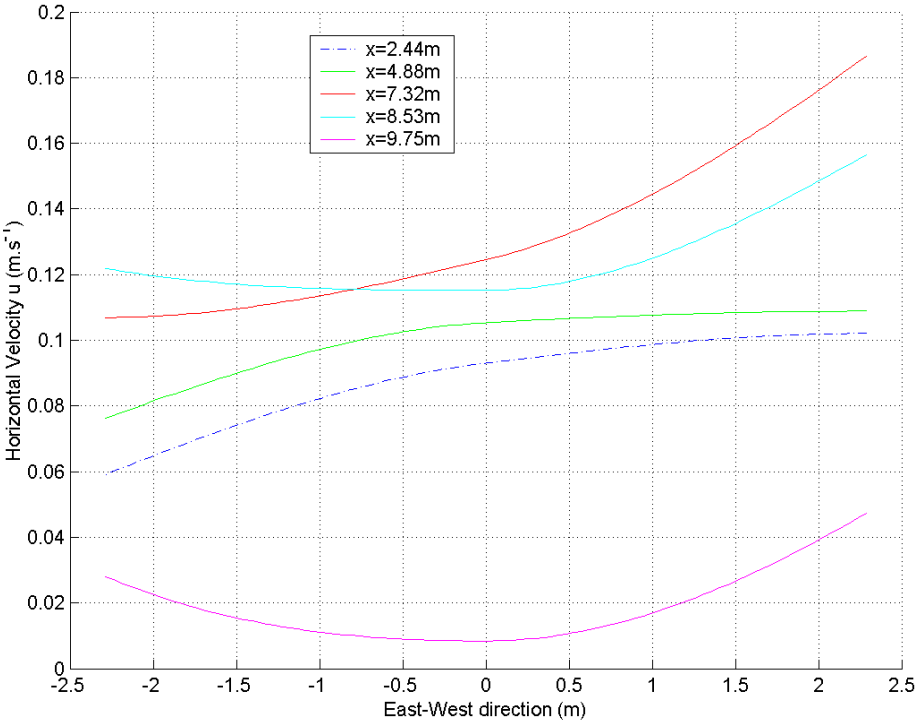

Figure C.9: Velocity profile along *y* at 100% in a 3*3 array for *x*+

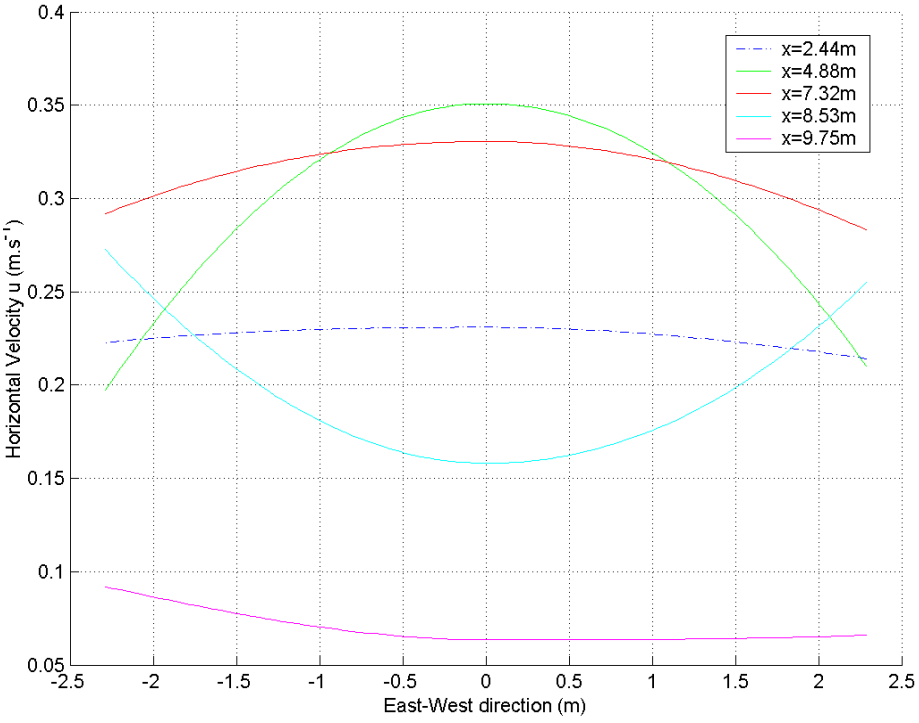

Figure C.10: Velocity profile along *y* at 225% in a 3*3 array for *x*+

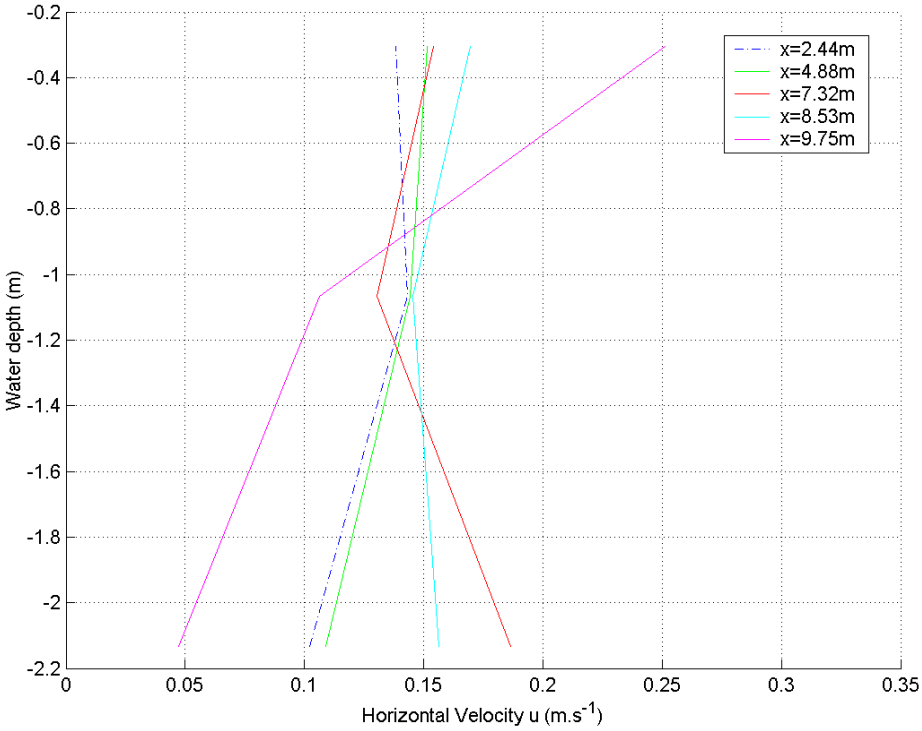

Figure C.11: Velocity profile along *z* at 100% in a 3*3 array for *x*+

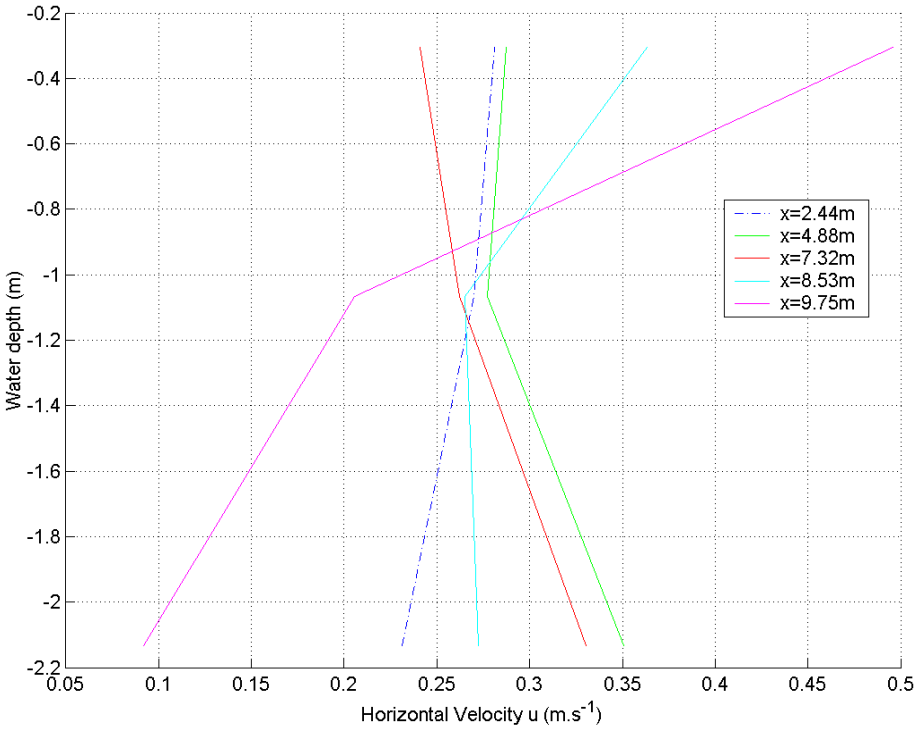

Figure C.12: Velocity profile along *z* at 225% in a 3*3 array for *x*+

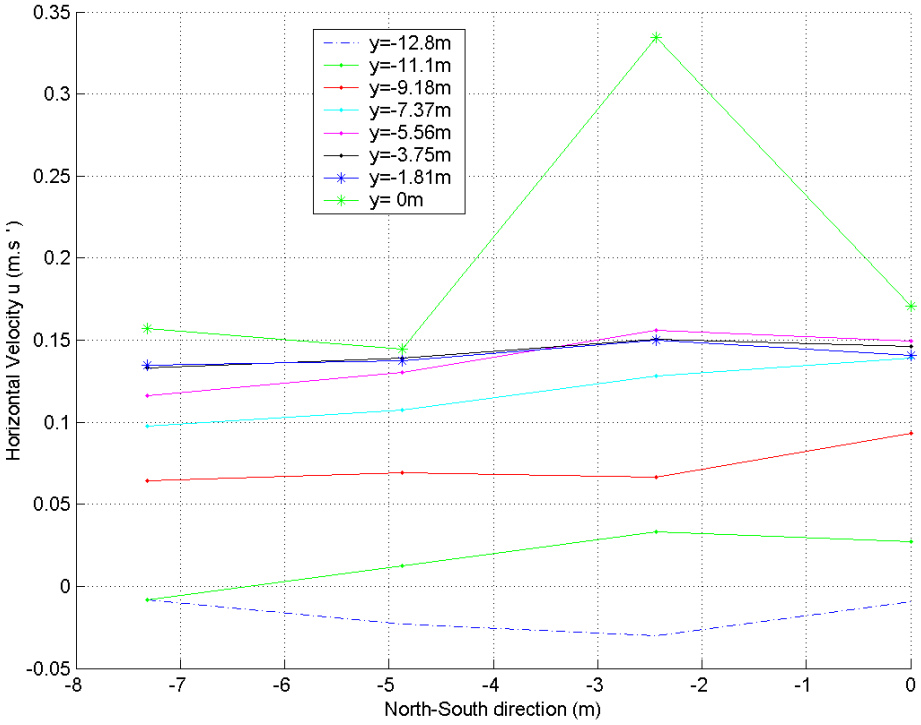

Figure C.13: Velocity profile along *x* at 100% in a Vertical array

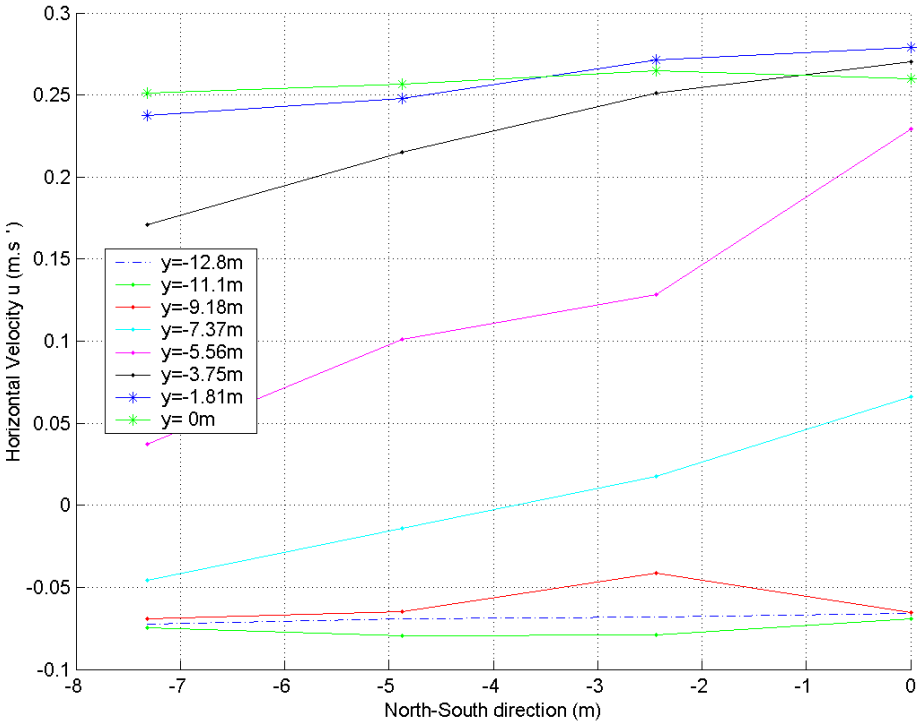

Figure C.14: Velocity profile along *x* at 200% in a Vertical array

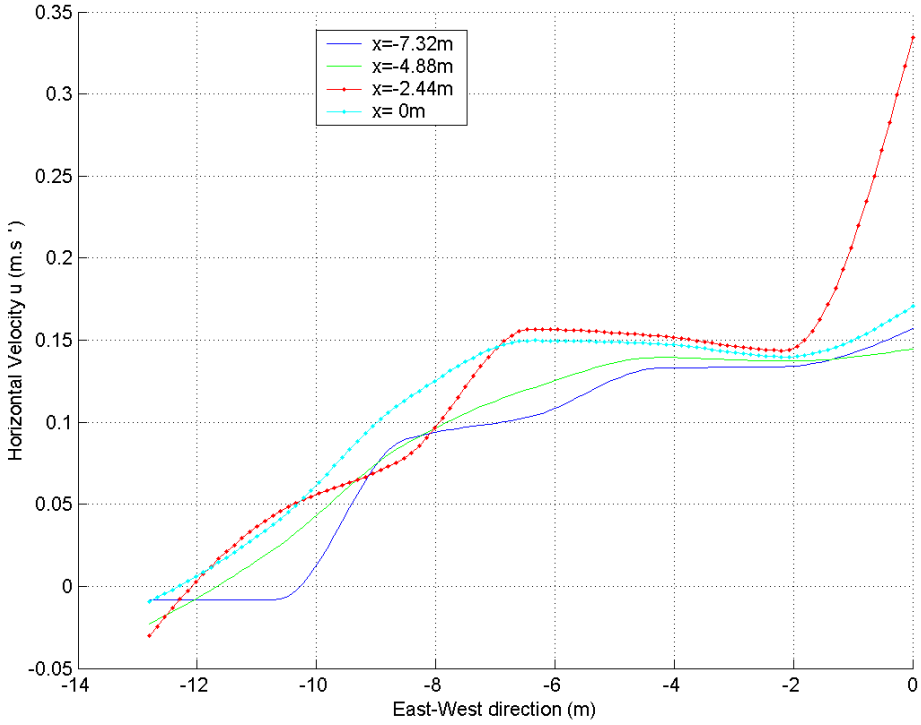

Figure C.15: Velocity profile along *y* at 100% in a Vertical array

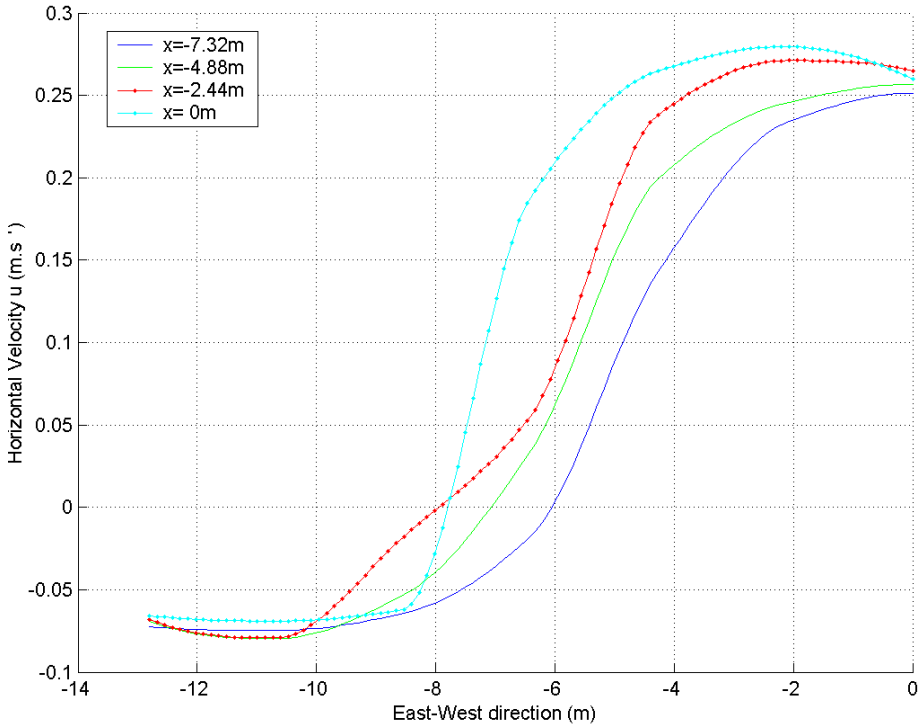

Figure C.16: Velocity profile along *y* at 200% in a Vertical array

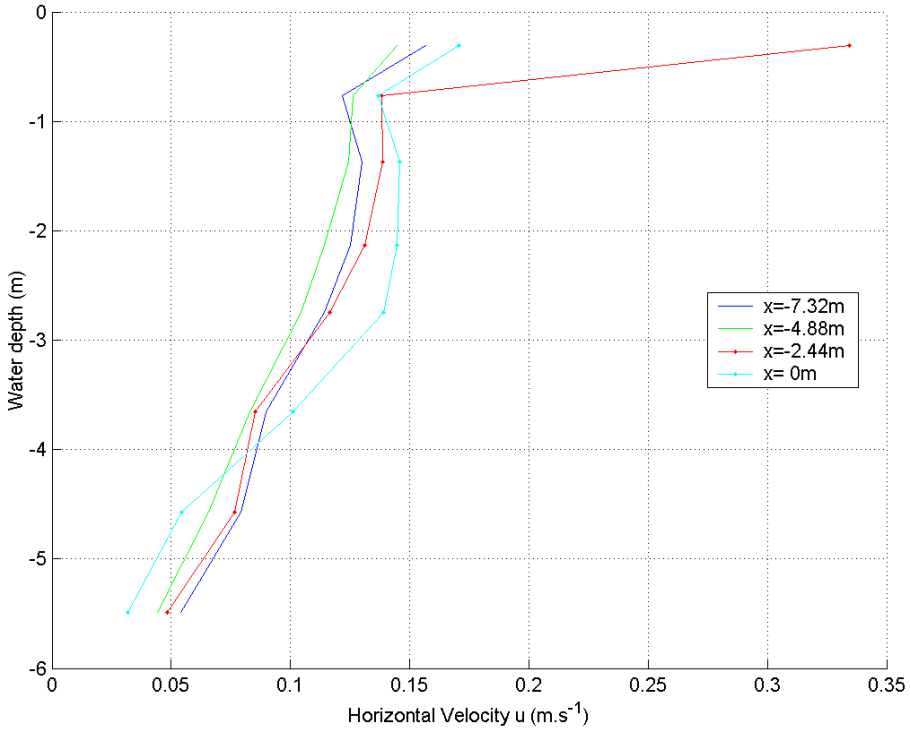

Figure C.17: Velocity profile along *z* at 100% in a Vertical array

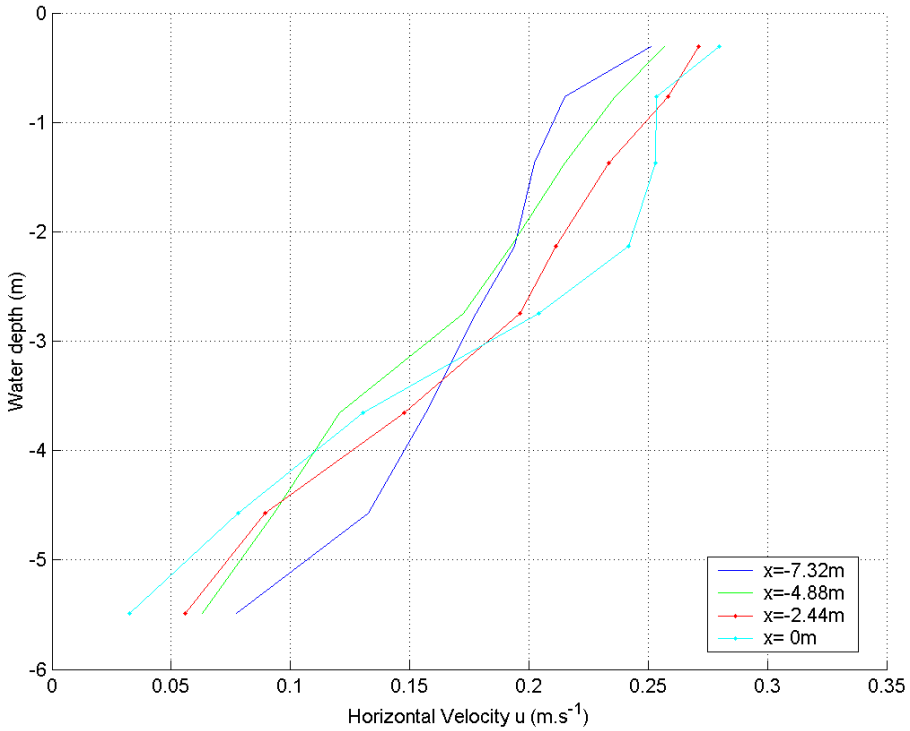

Figure C.18: Velocity profile along *z* at 200% in a Vertical array

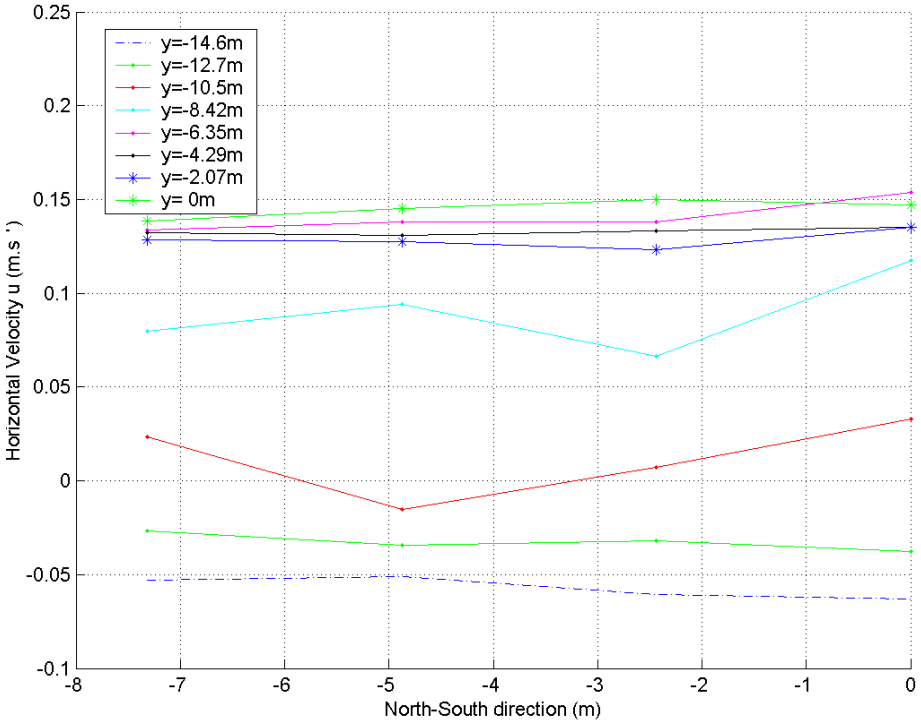

Figure C.19: Velocity profile along *x* at 100% in a Horizontal array

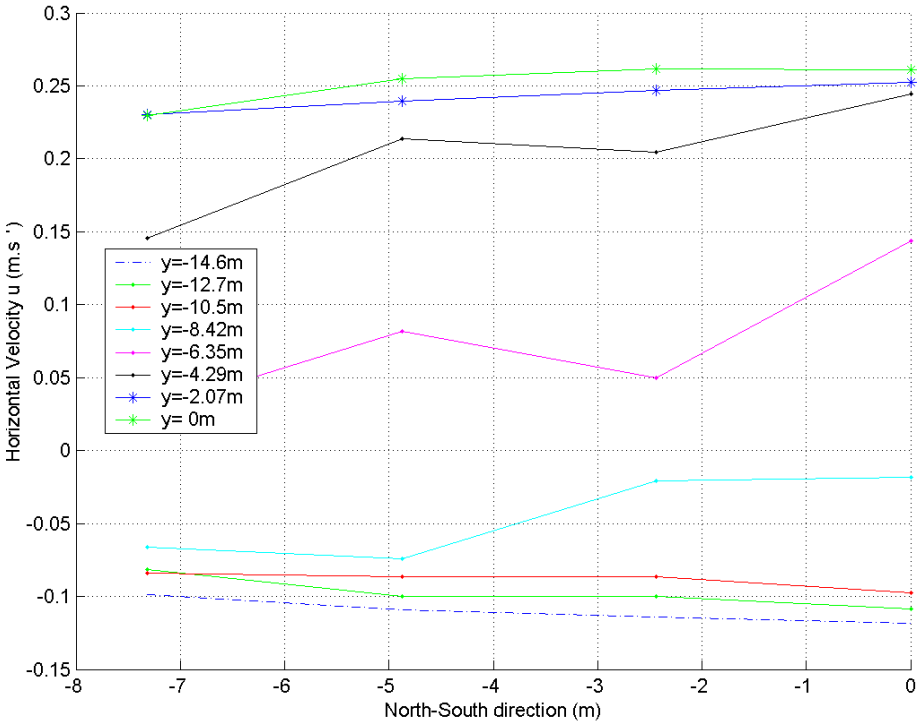

Figure C.20: Velocity profile along *x* at 200% in a Horizontal array

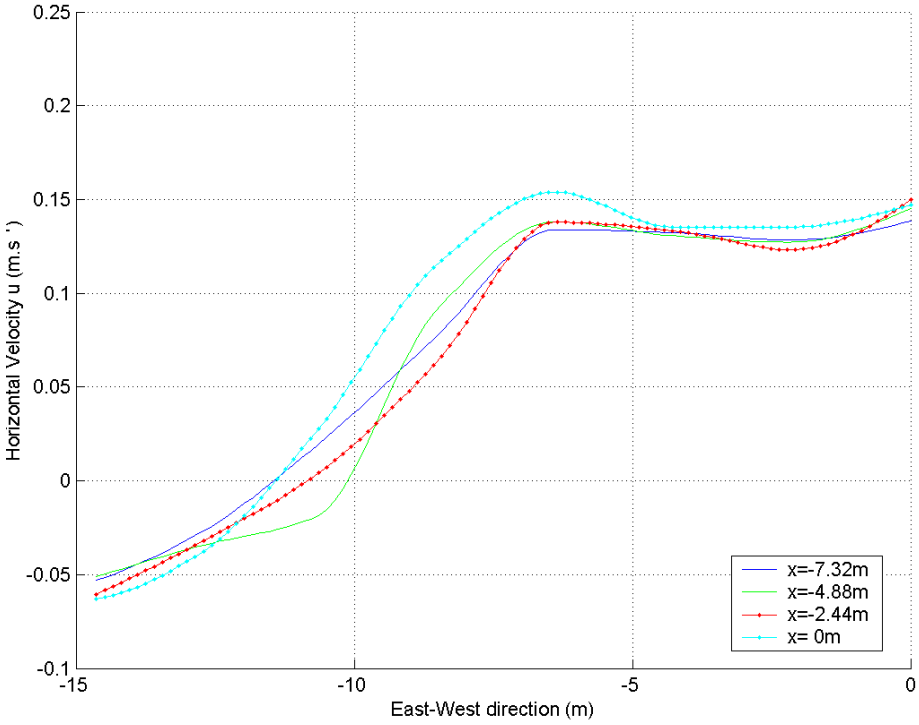

Figure C.21: Velocity profile along *y* at 100% in a Horizontal array

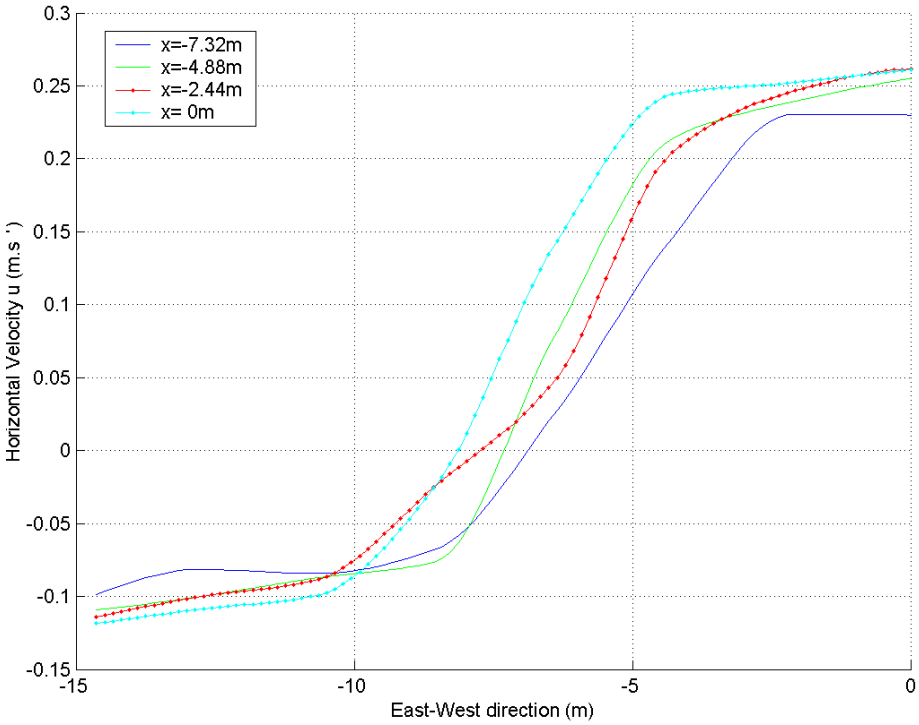

Figure C.22: Velocity profile along *y* at 200% in a Horizontal array

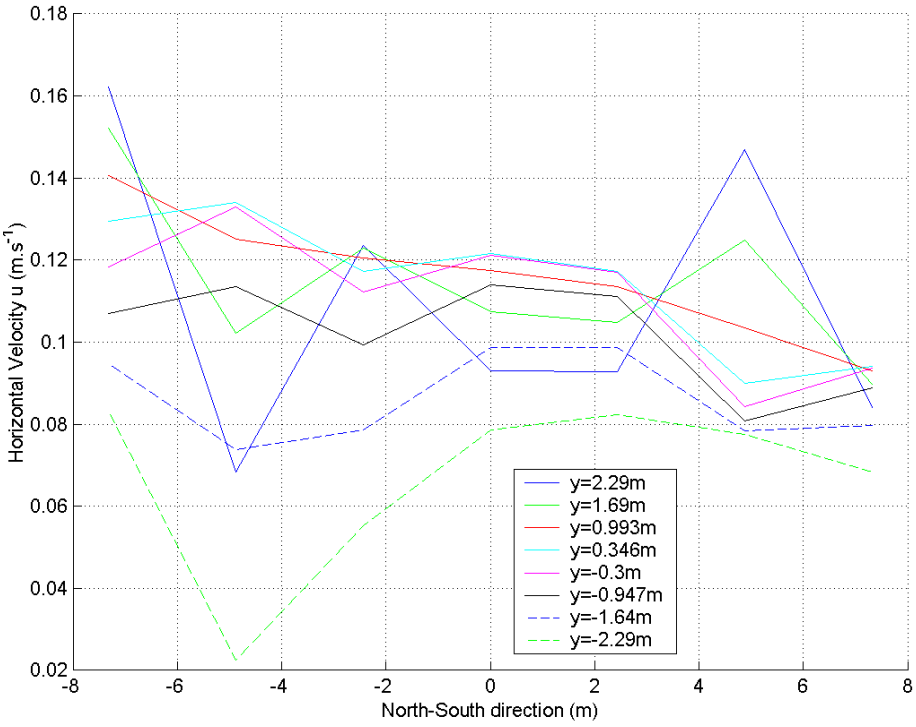

Figure C.23: Velocity profile along *x* for a RG2 + 100% in a 3*3 array

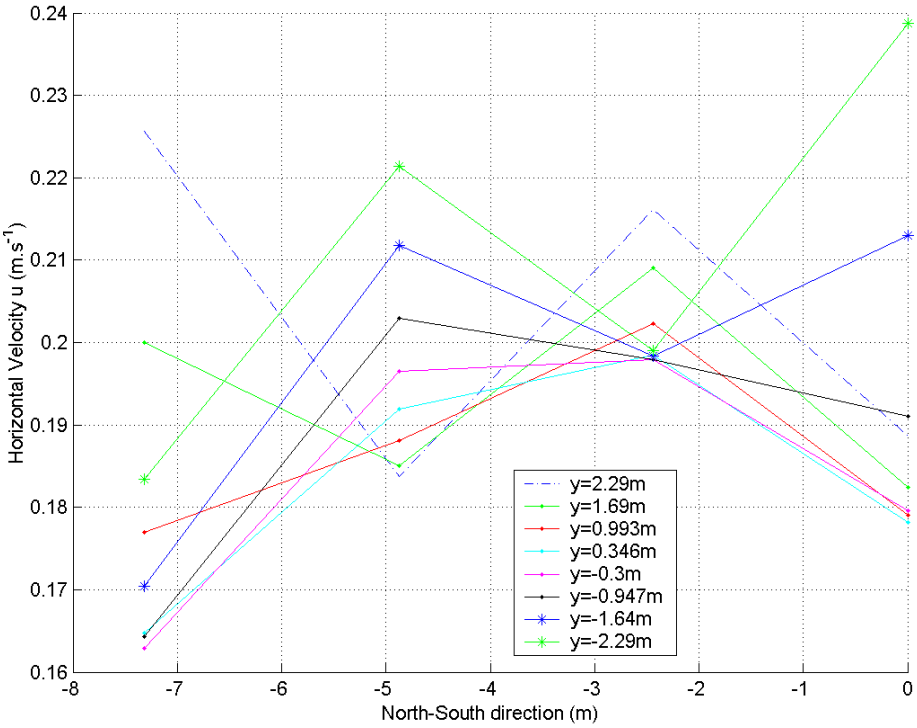

Figure C.24: Velocity profile along *x* for a RG2 + 200% in a 3*3 array

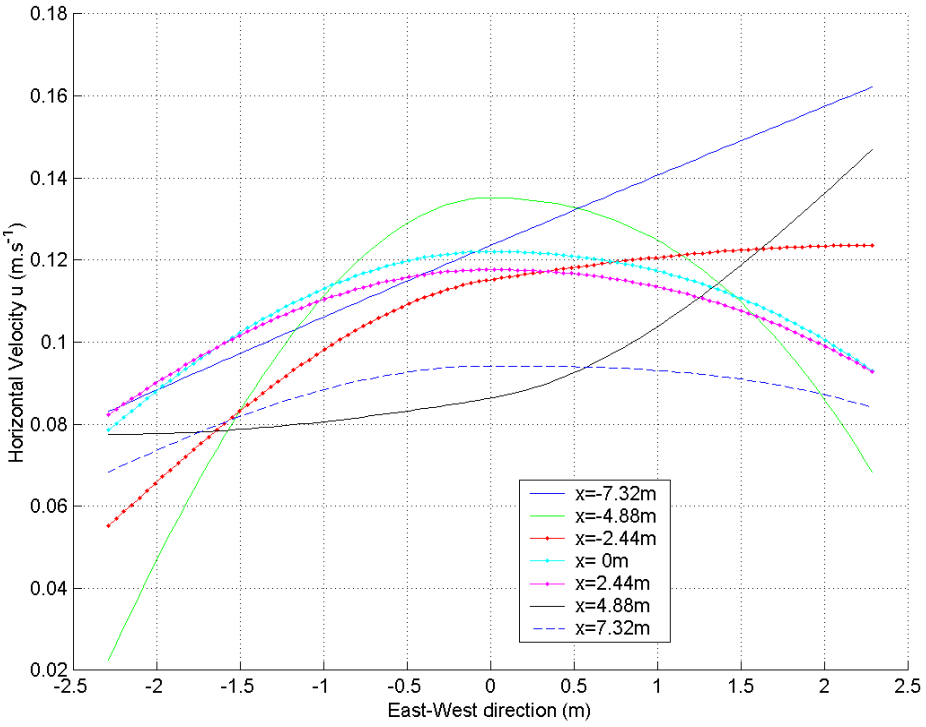

Figure C.25: Velocity profile along *y* for a RG2 + 100% in a 3*3 array

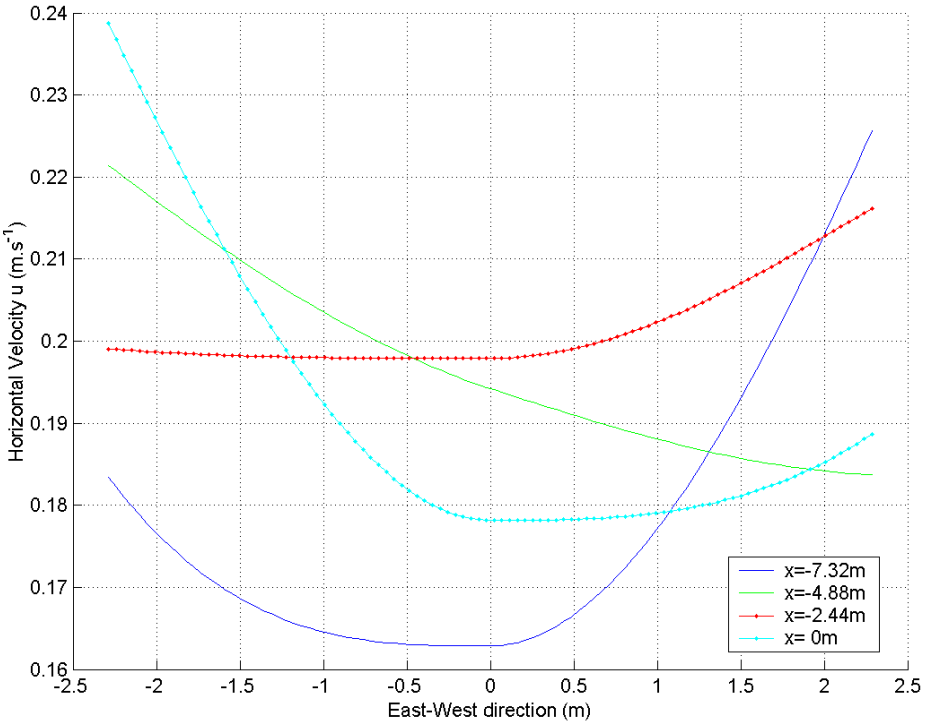

Figure C.26: Velocity profile along *y* for a RG2 + 200% in a 3*3 array

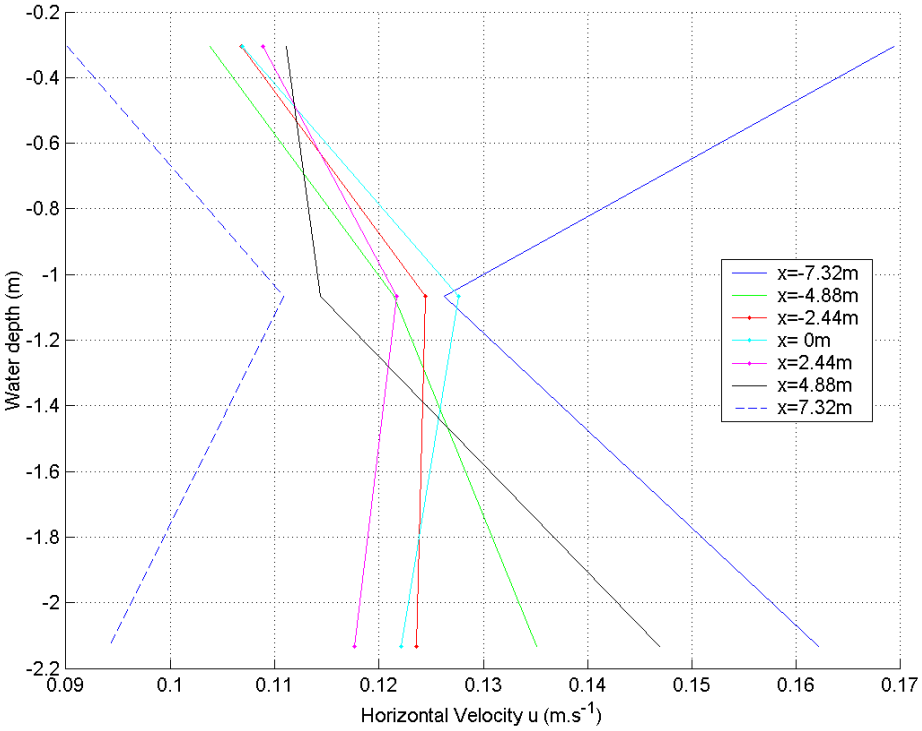

Figure C.27: Velocity profile along *z* for a RG2 + 100% in a 3*3 array

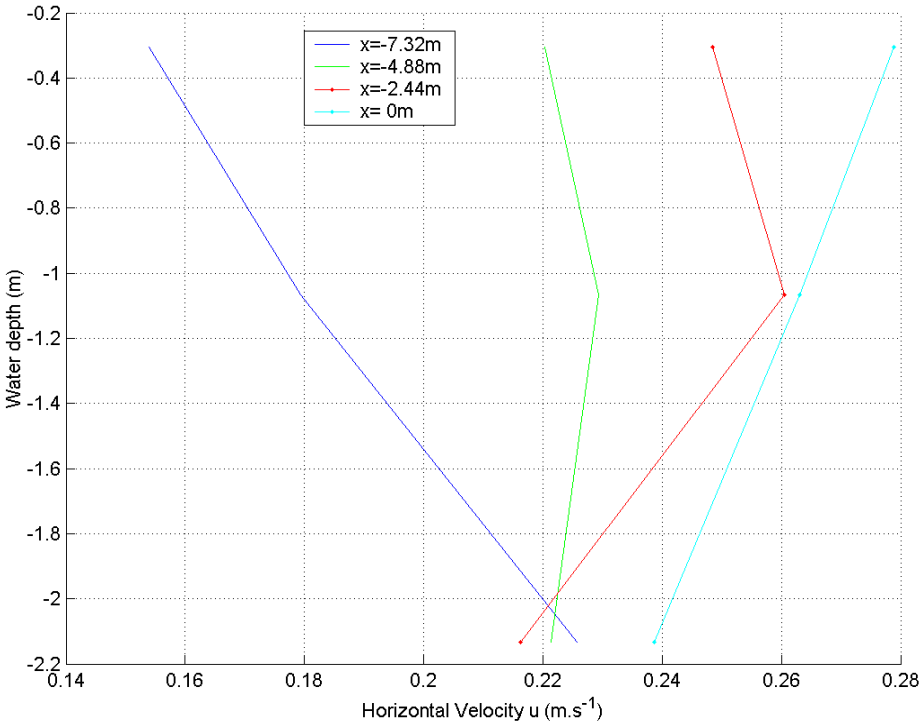

Figure C.28: Velocity profile along *z* for a RG2 + 100% in a 3*3 array

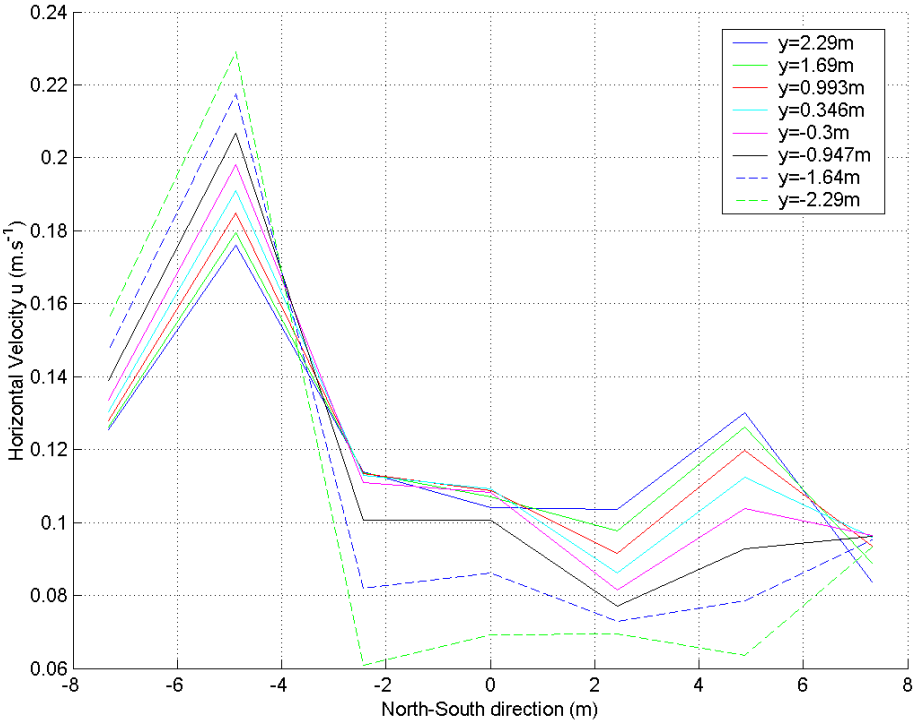

Figure C.29: Velocity profile along *x* for a RG5 + 100% in a 3*3 array

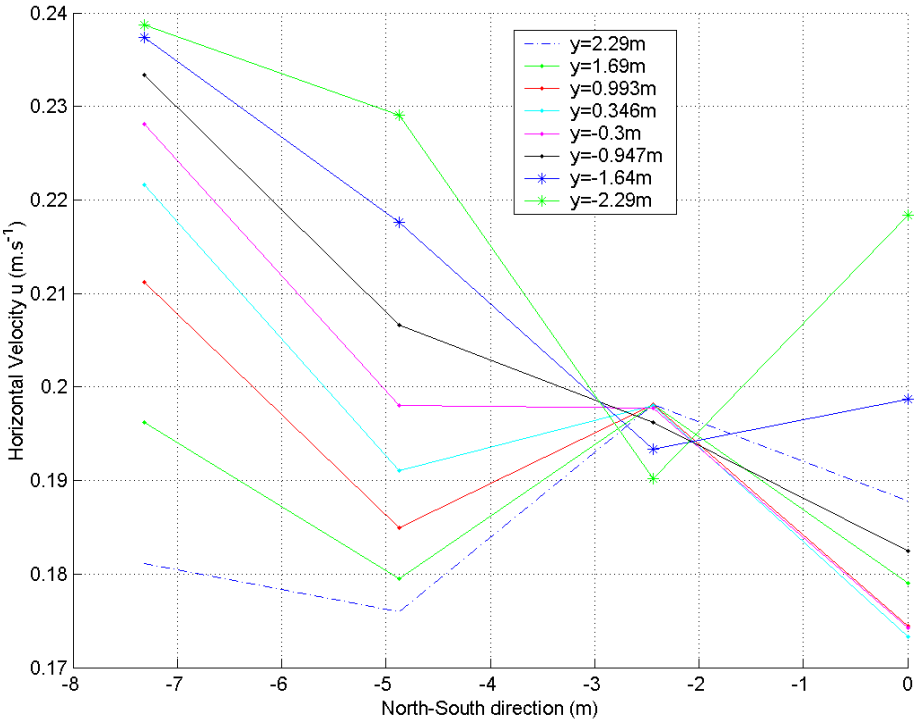

Figure C.30: Velocity profile along *x* for a RG5 + 200% in a 3*3 array

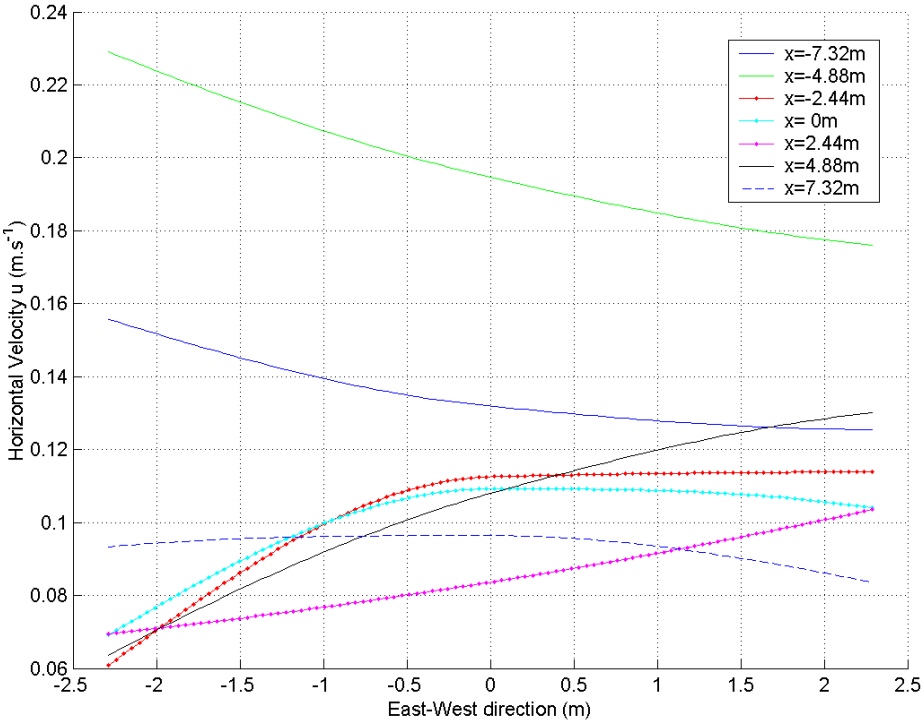

Figure C.31: Velocity profile along *y* for a RG5 + 100% in a 3*3 array

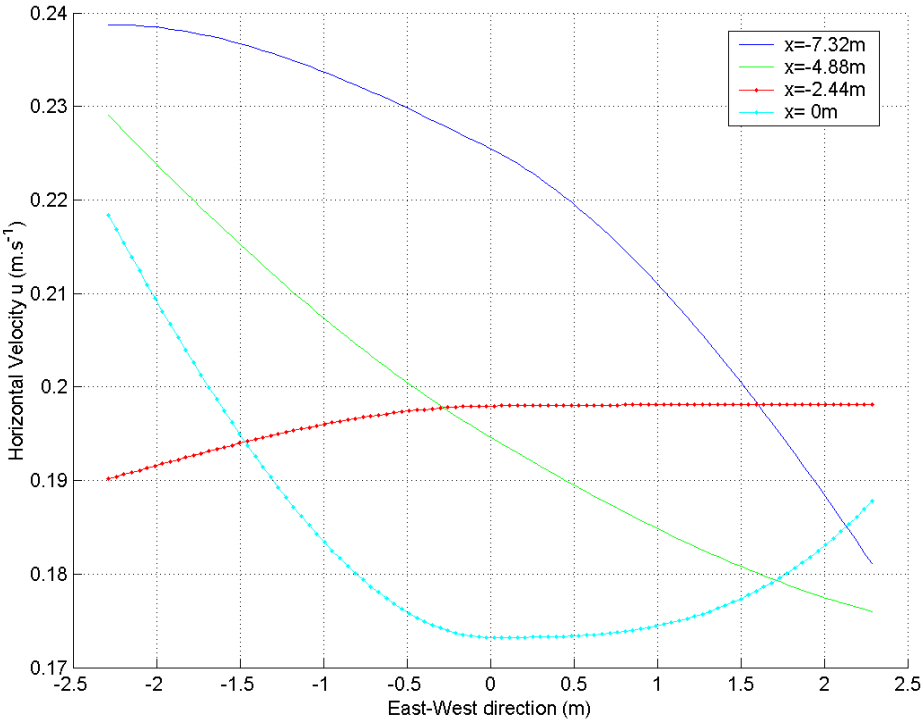

Figure C.32: Velocity profile along *y* for a RG5 + 200% in a 3*3 array

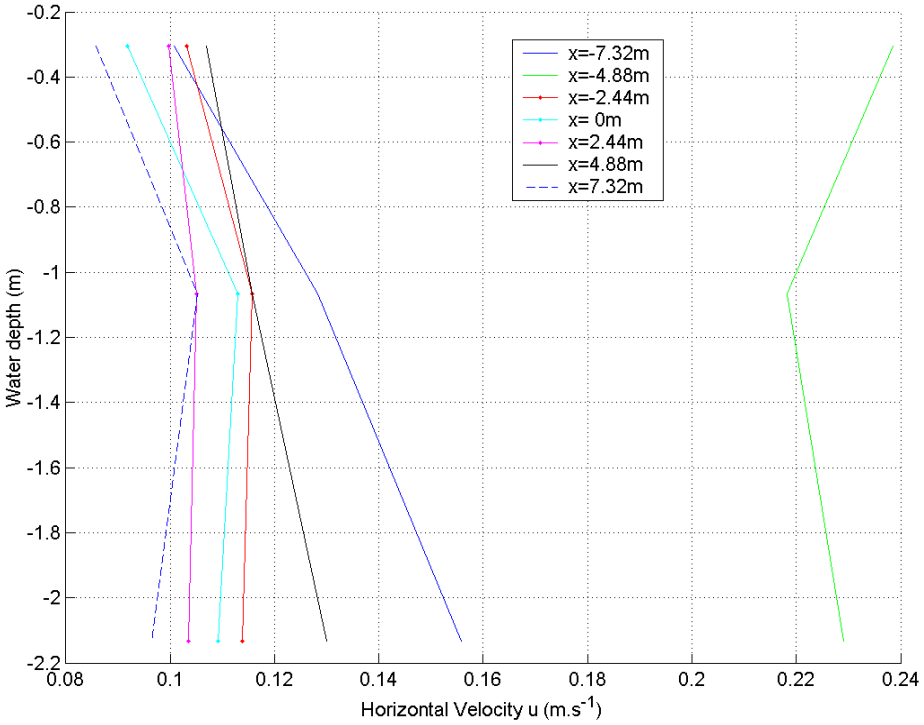

Figure C.33: Velocity profile along *z* for a RG5 + 100% in a 3*3 array

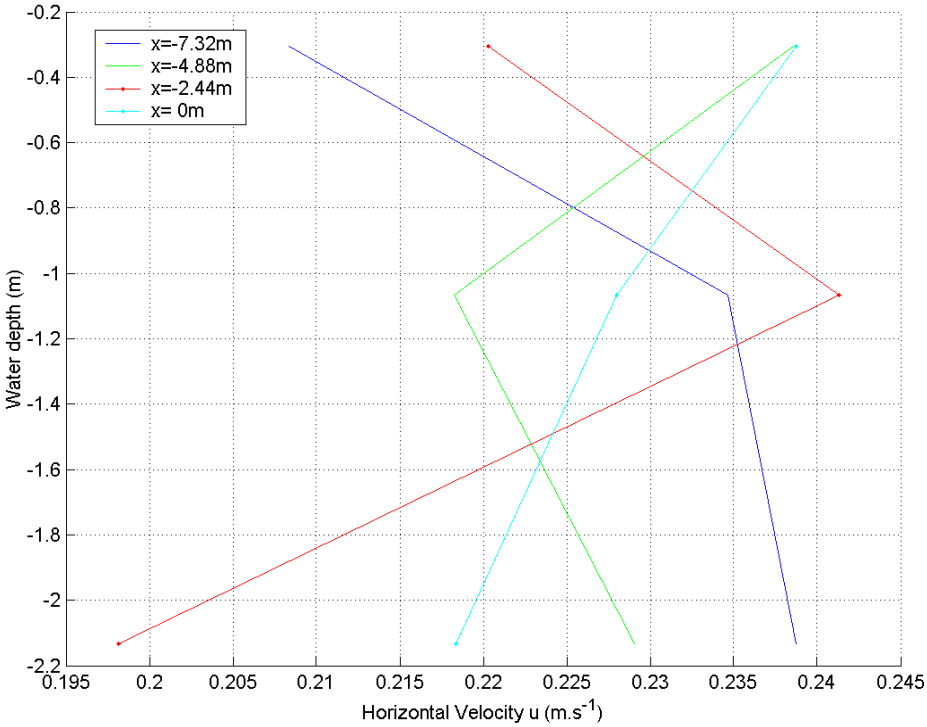

Figure C.34: Velocity profile along *z* for a RG5 + 200% in a 3*3 array

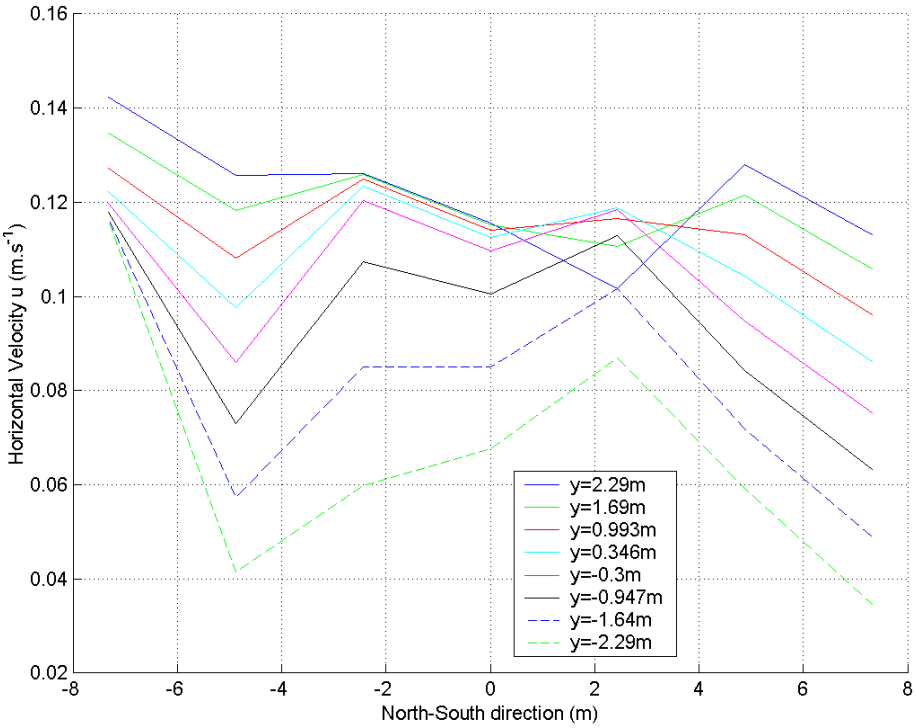

Figure C.35: Velocity profile along *x* for a RN + 100% in a 3*3 array

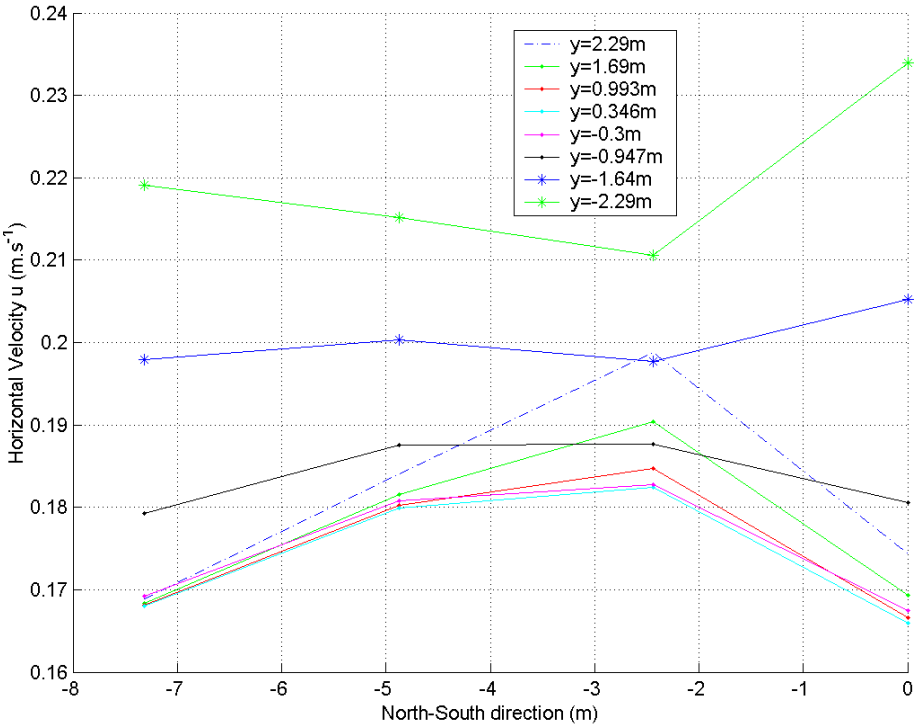

Figure C.36: Velocity profile along *x* for a RN + 200% in a 3*3 array

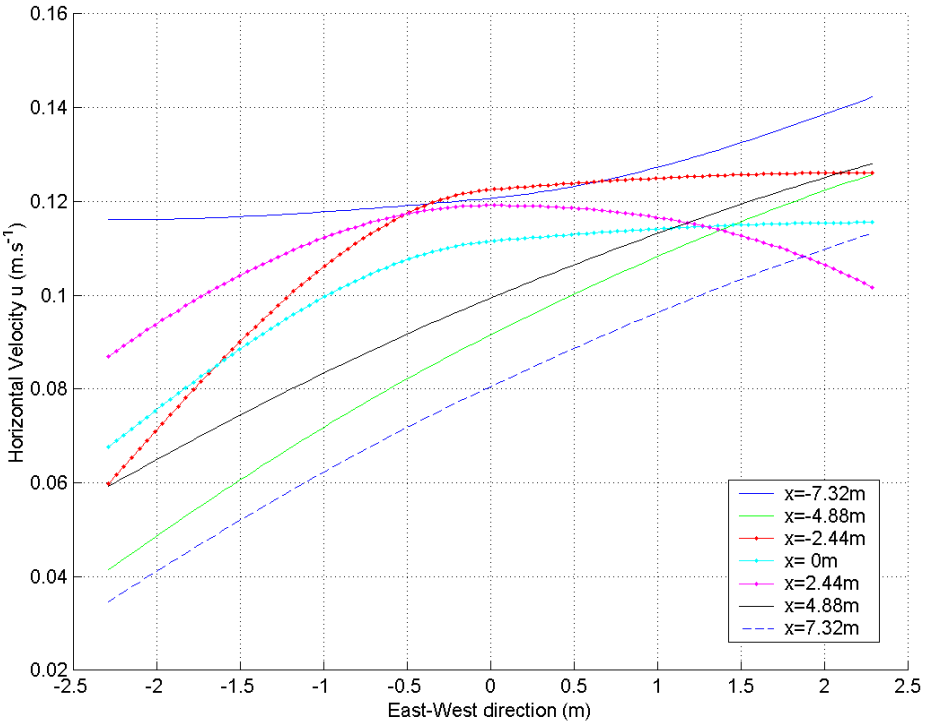

Figure C.37: Velocity profile along *y* for a RN + 100% in a 3*3 array

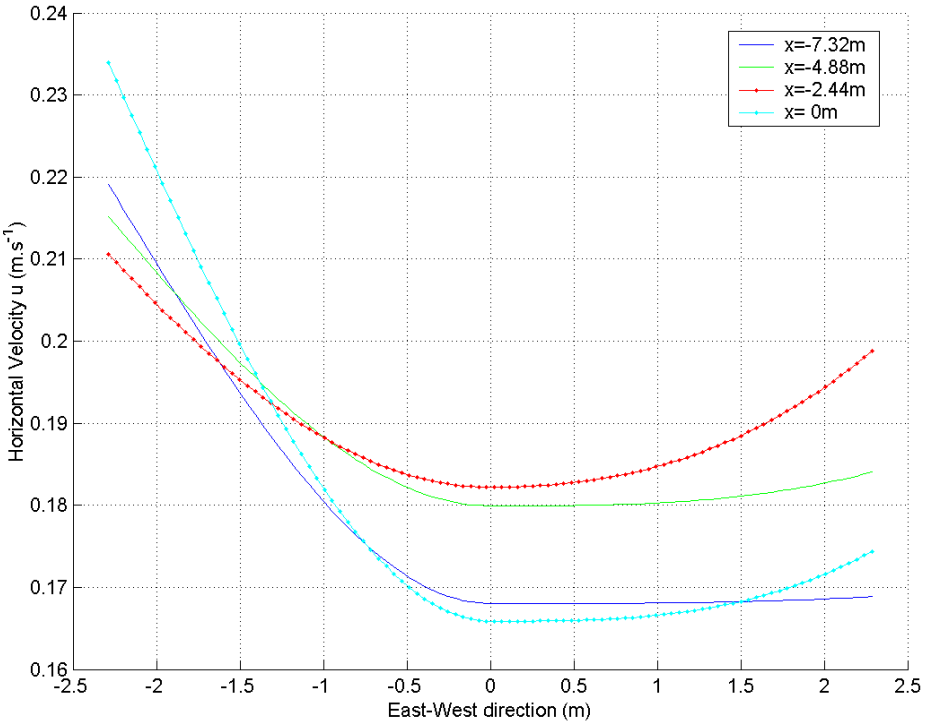

Figure C.38: Velocity profile along *y* for a RN + 200% in a 3*3 array

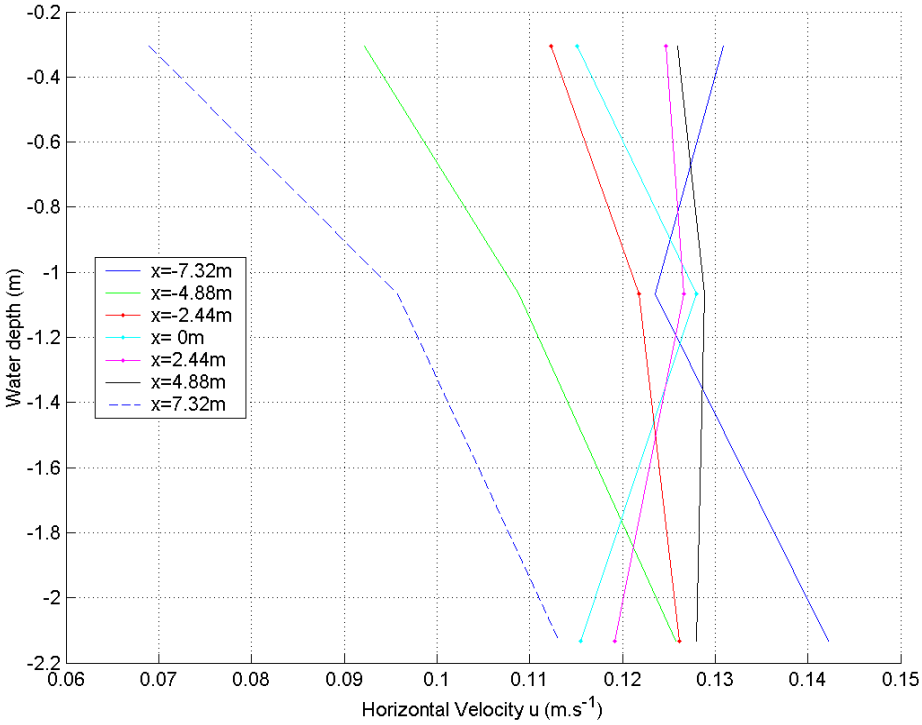

Figure C.39: Velocity profile along *z* for a RN + 100% in a 3*3 array

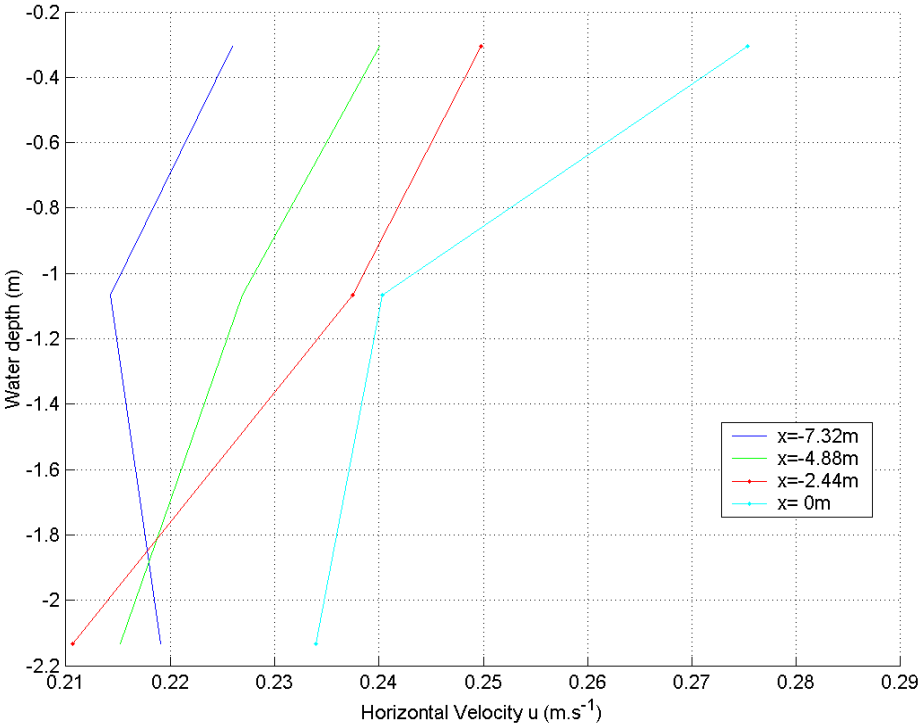

Figure C.40: Velocity profile along *z* for a RN + 200% in a 3*3 array

APPENDIX D

MAPPING OF THE TURBULENCE

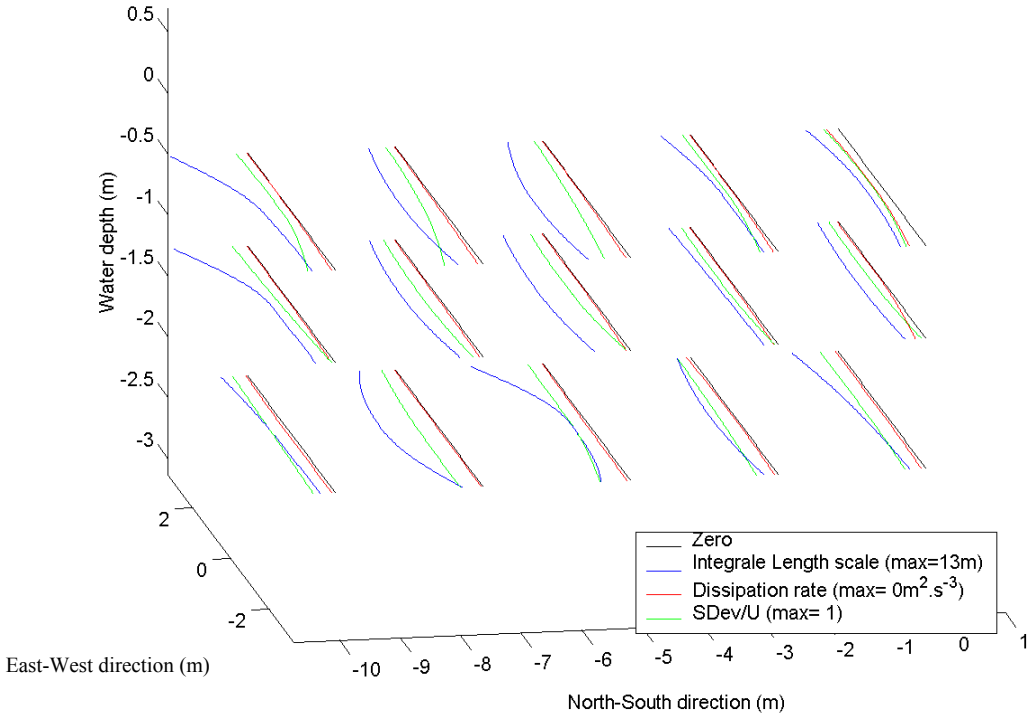

Figure D.1: L, ε and Sd/U for a 3*3 array current test at 100% for *x*-

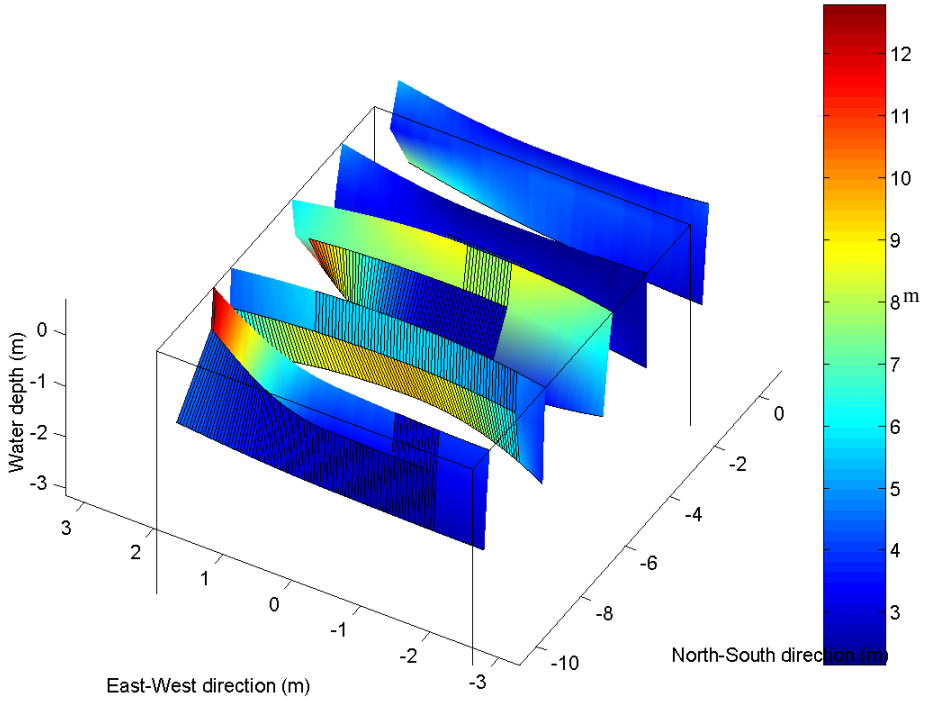

Figure D.2: Lx for a 3*3 array current test at 100% for *x*-

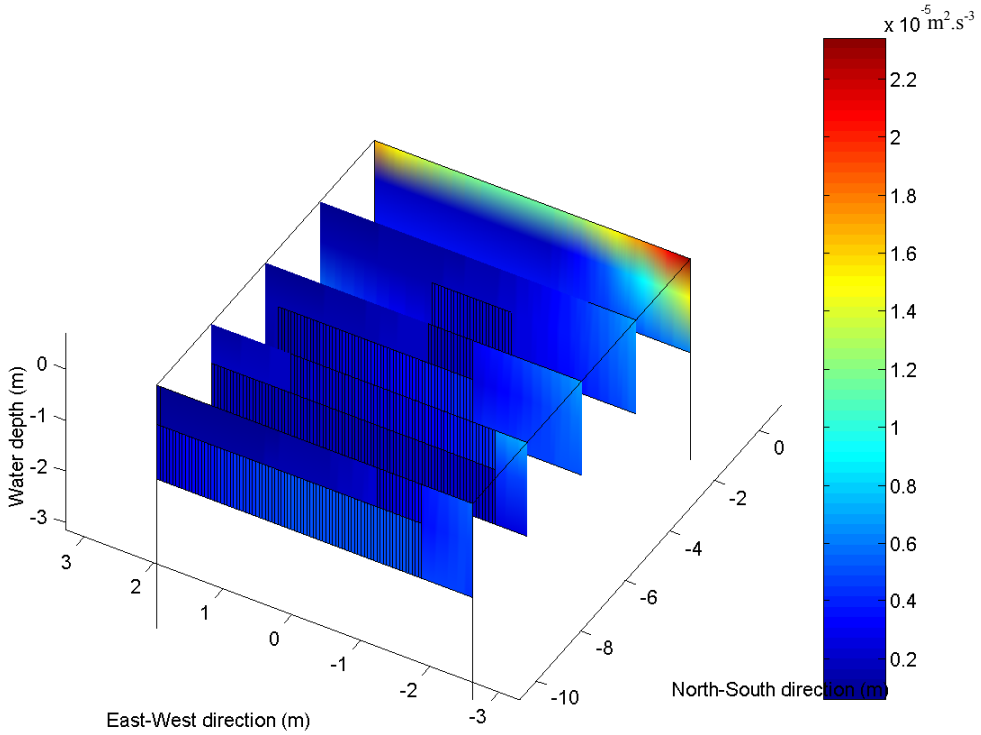

Figure D.3: ε for a 3*3 array current test at 100% for *x*-

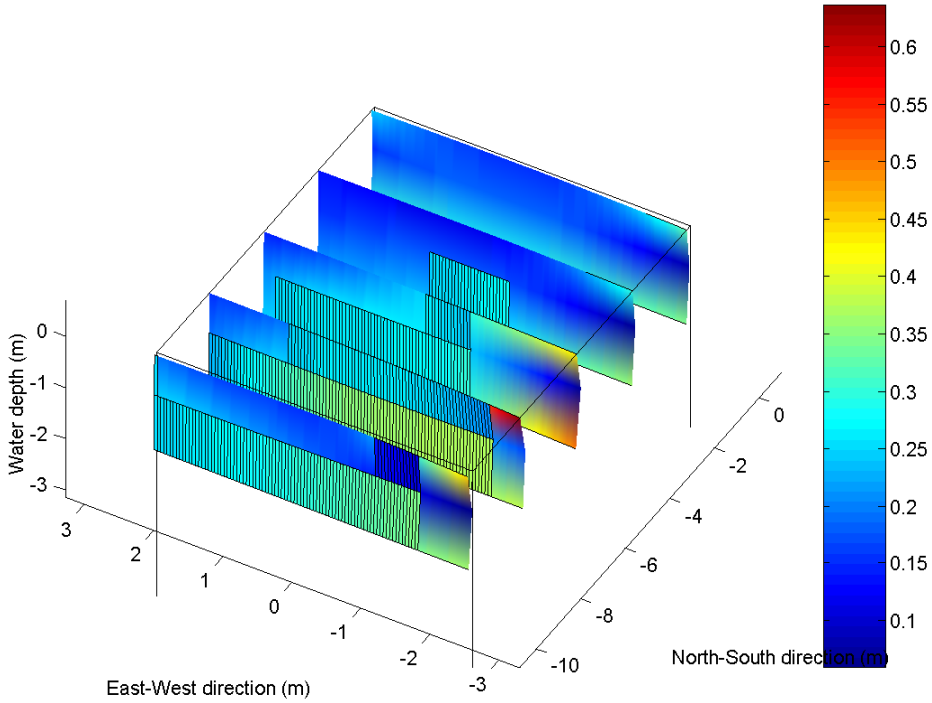

Figure D.4: Sd/U for a 3*3 array current test at 100% for *x*-

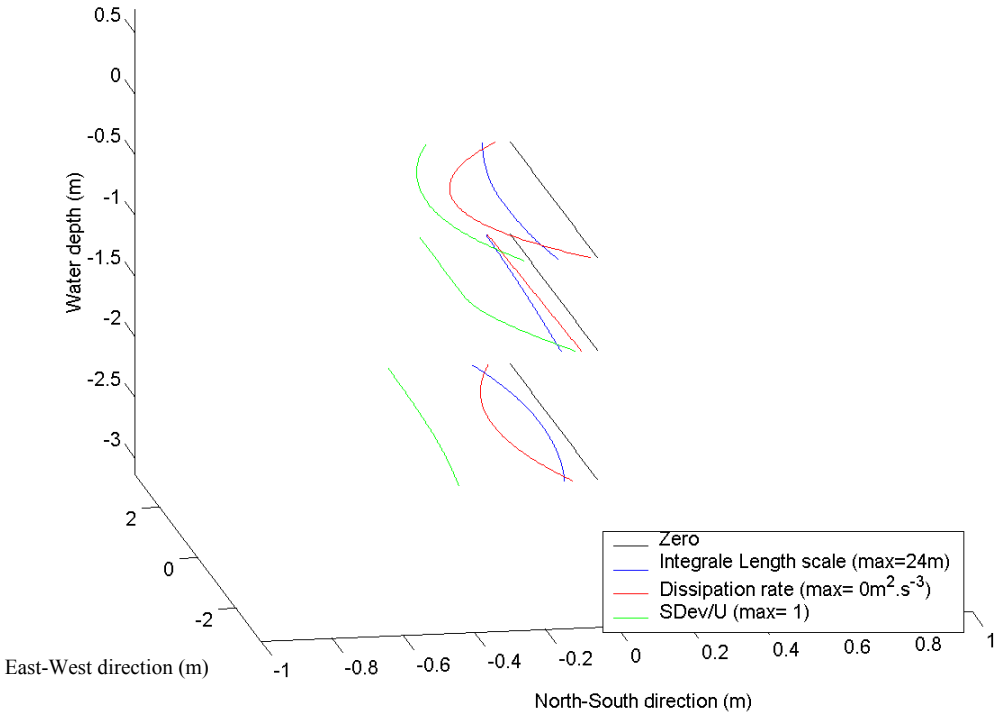

Figure D.5: L, ε and Sd/U for a 3*3 array current test at 200%

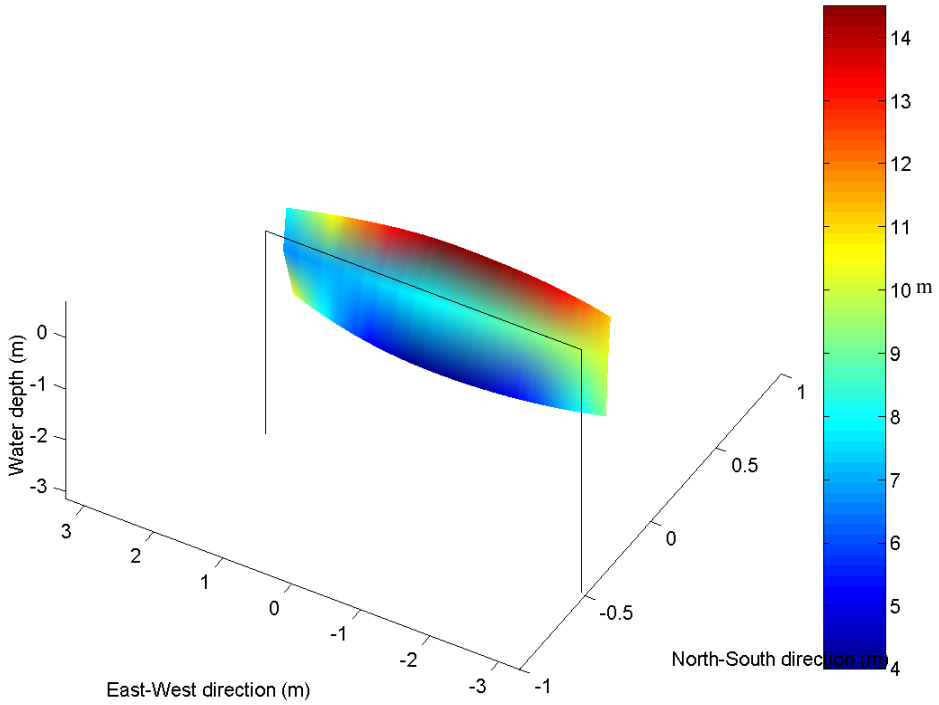

Figure D.6: L for a 3*3 array current test at 200%

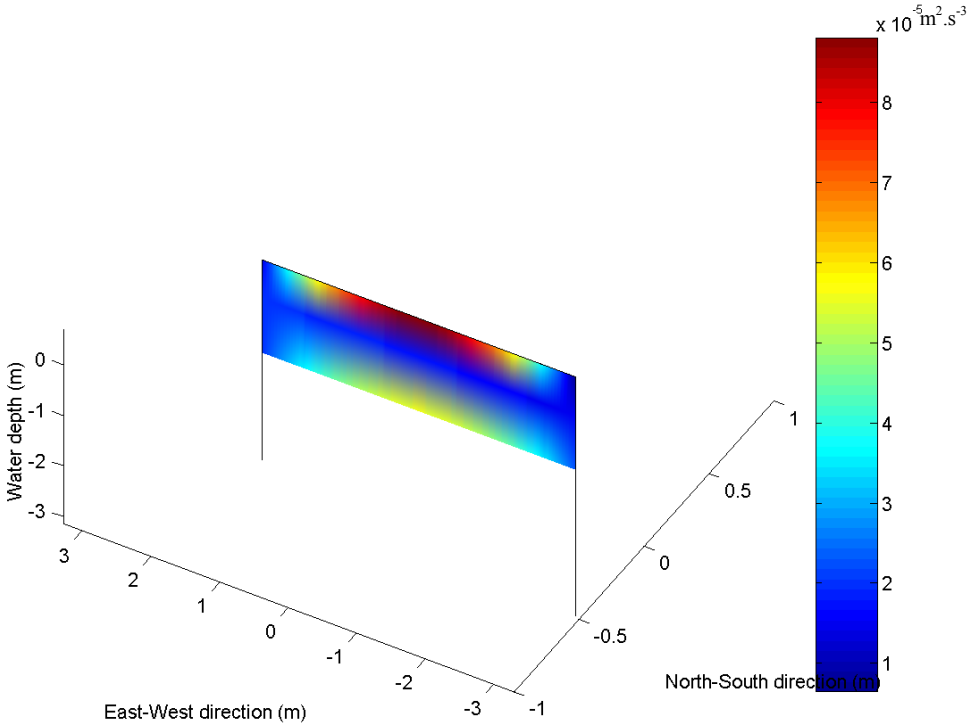

Figure D.7: ε for a 3*3 array current test at 200%

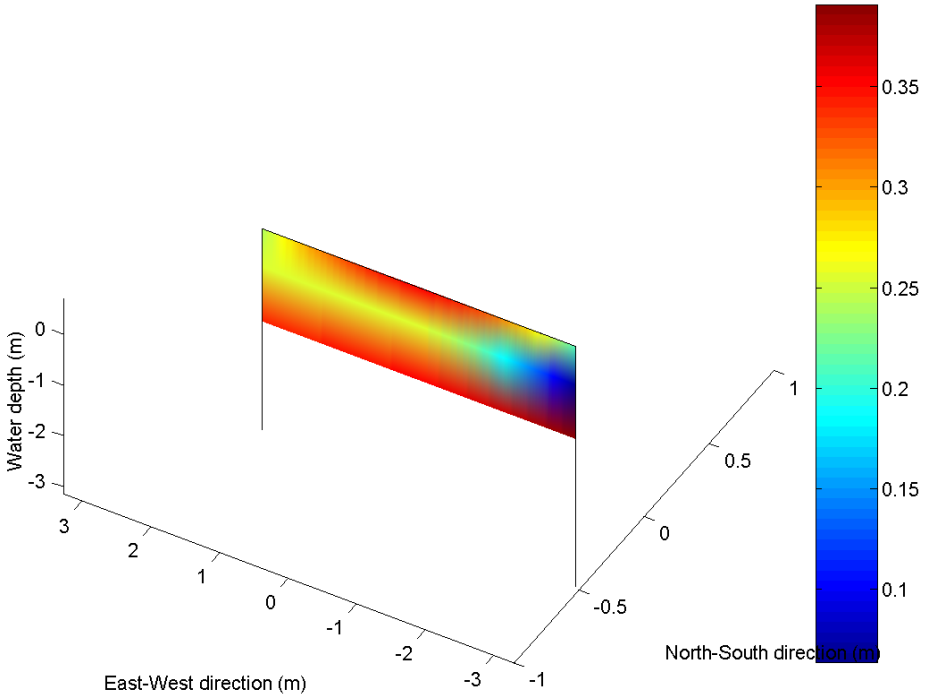

Figure D.8: Sd/U for a 3*3 array current test at 200%

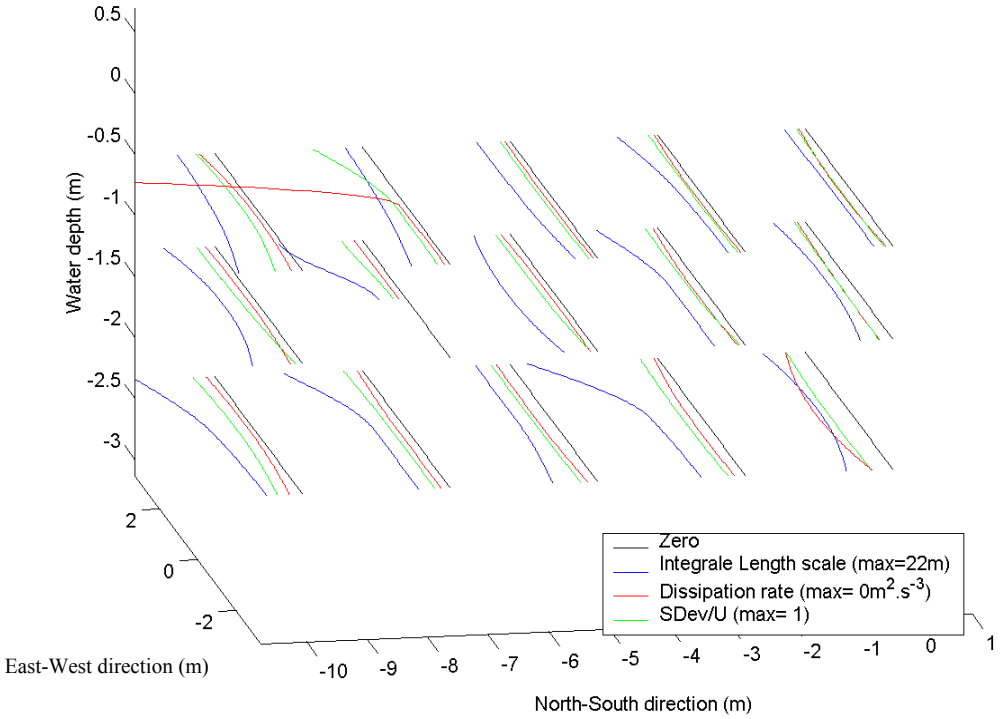

Figure D.9: L, ε and Sd/U for a 3*3 array current test at 225% for *x*-

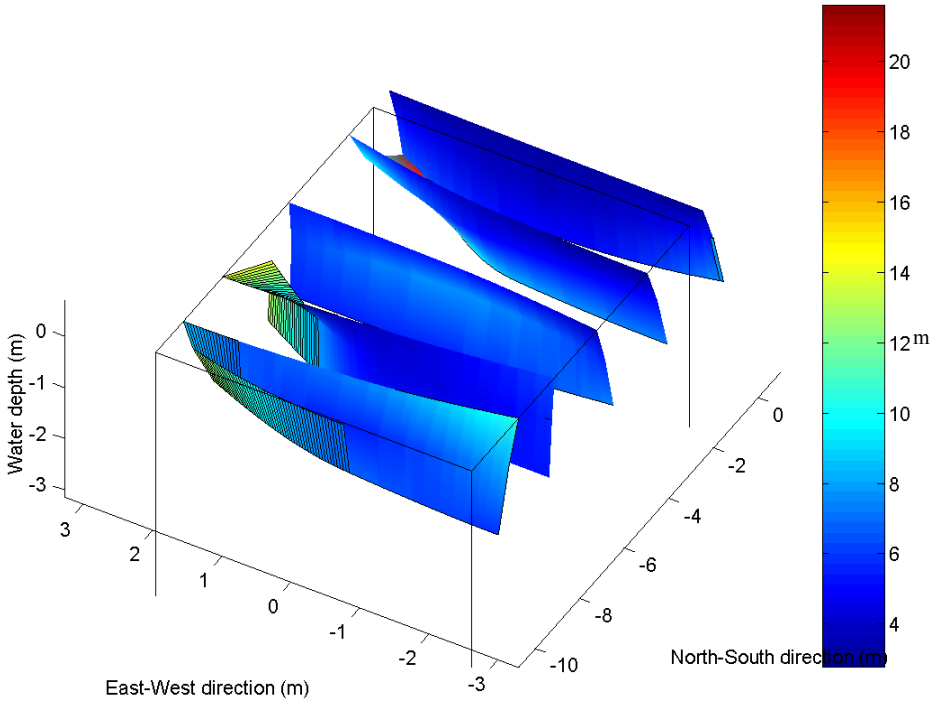

Figure D.10: L for a 3*3 array current test at 225% for *x*-

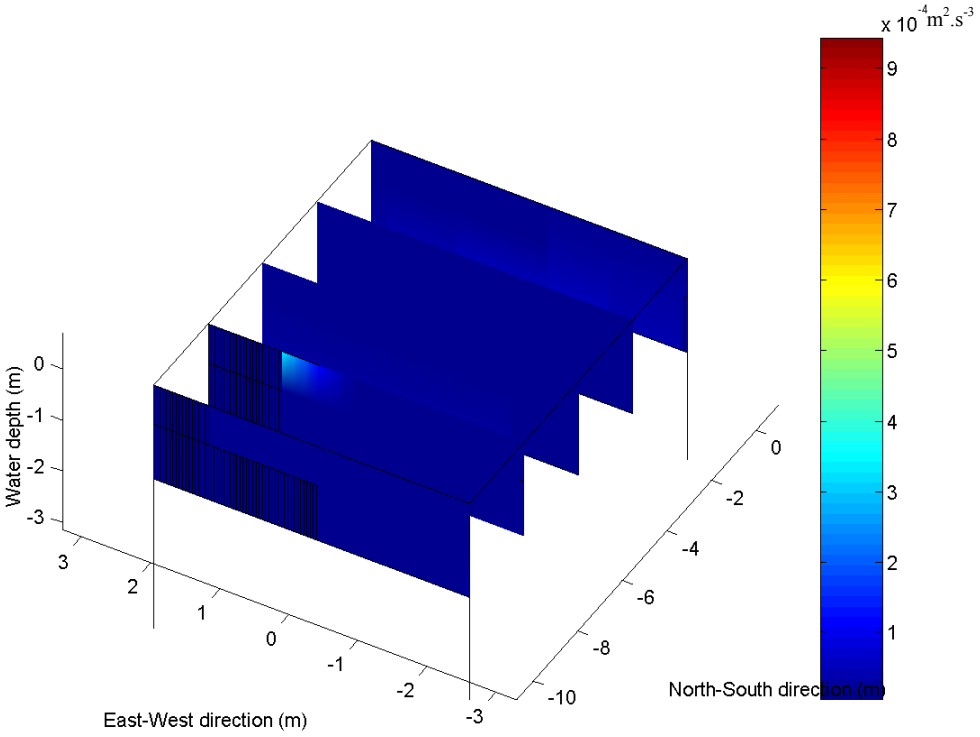

Figure D.11: ε for a 3*3 array current test at 225% for *x*-

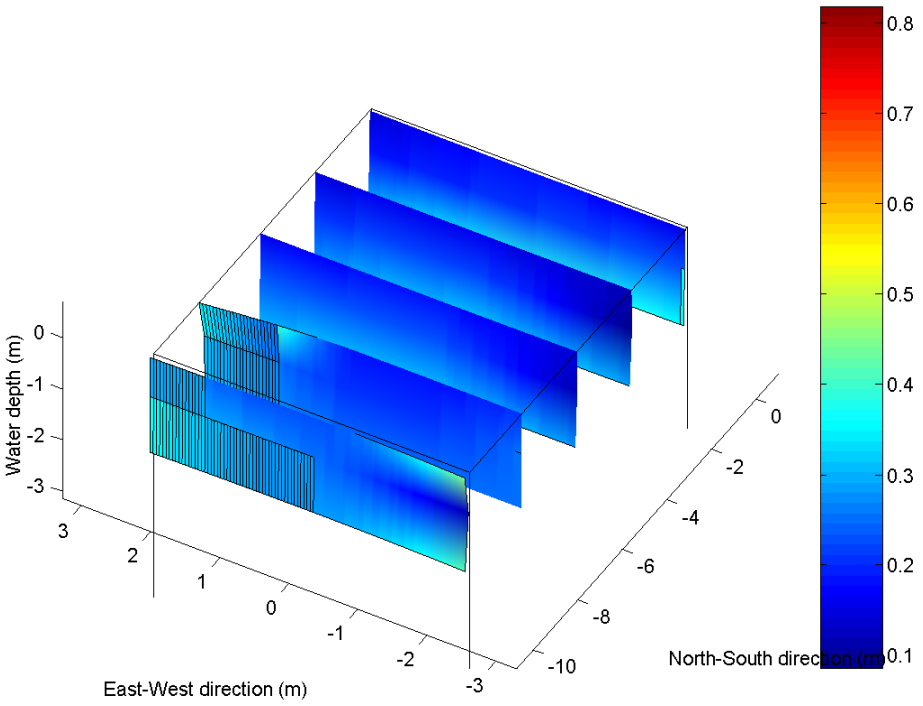

Figure D.12: Sd/U for a 3*3 array current test at 225% for *x*-

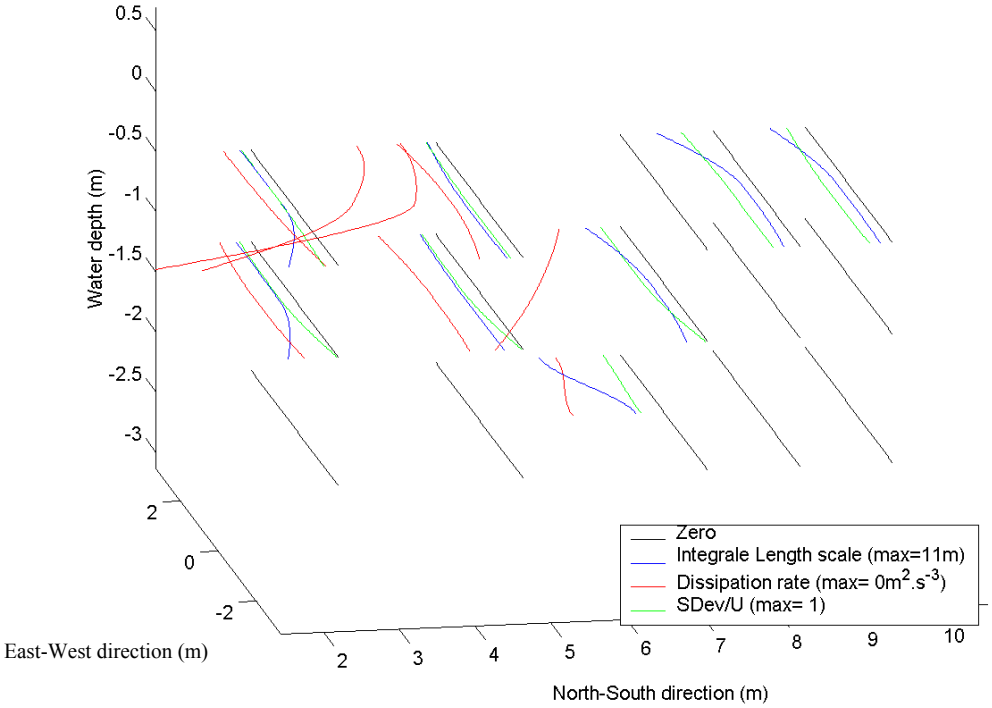

Figure D.13: L, ε and Sd/U for a 3*3 array current test at 100% for *x*+

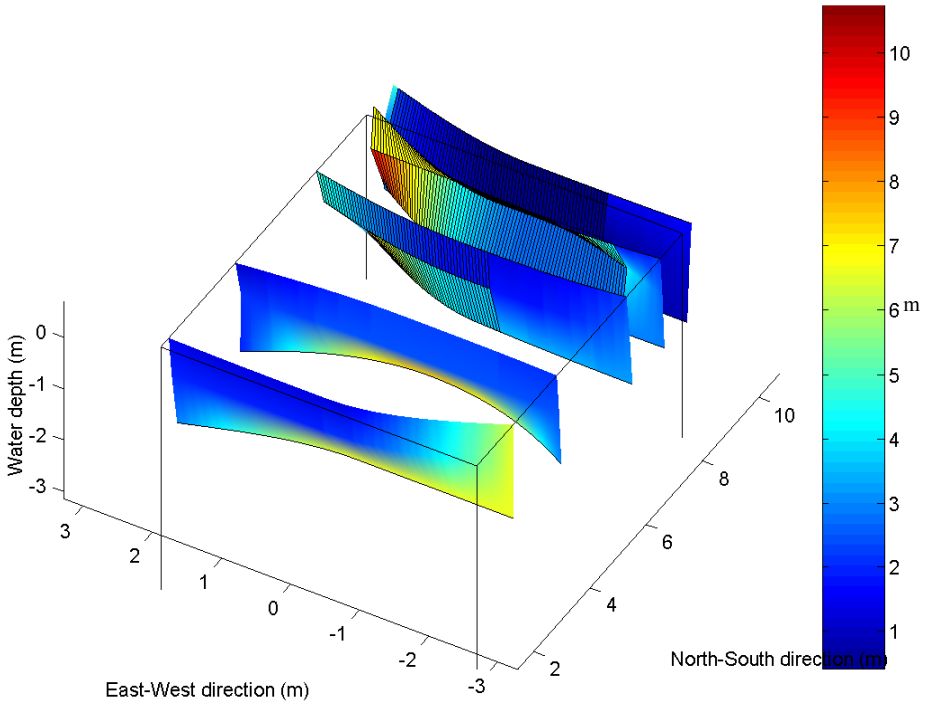

Figure D.14: L for a 3*3 array current test at 100% for *x*+

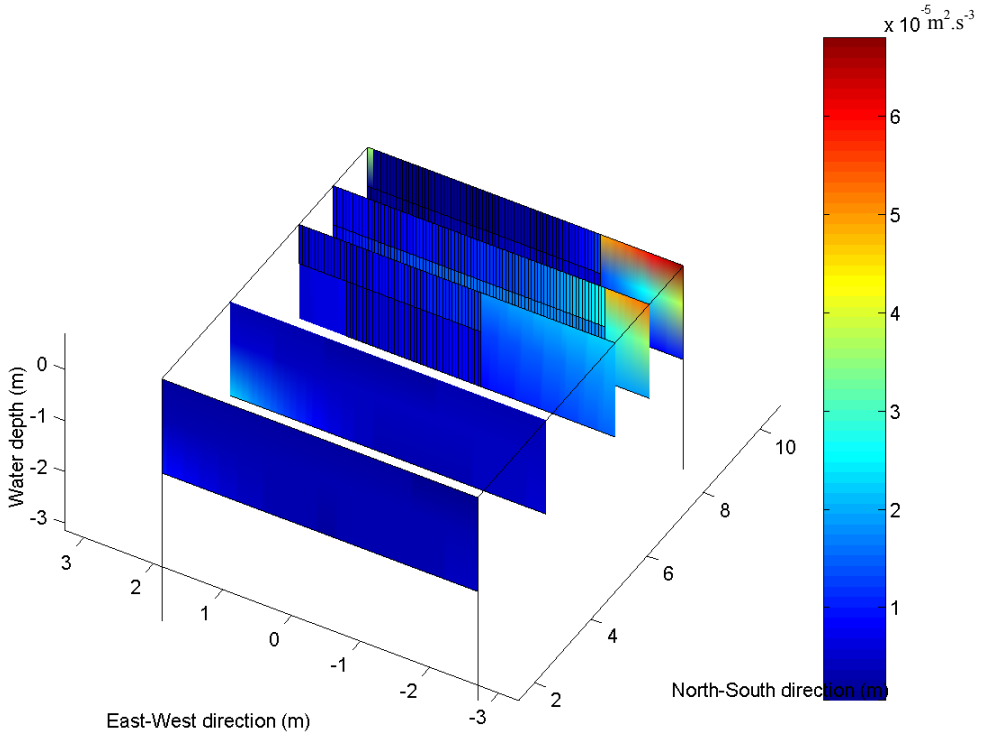

Figure D.15: ε for a 3*3 array current test at 100% for *x*+

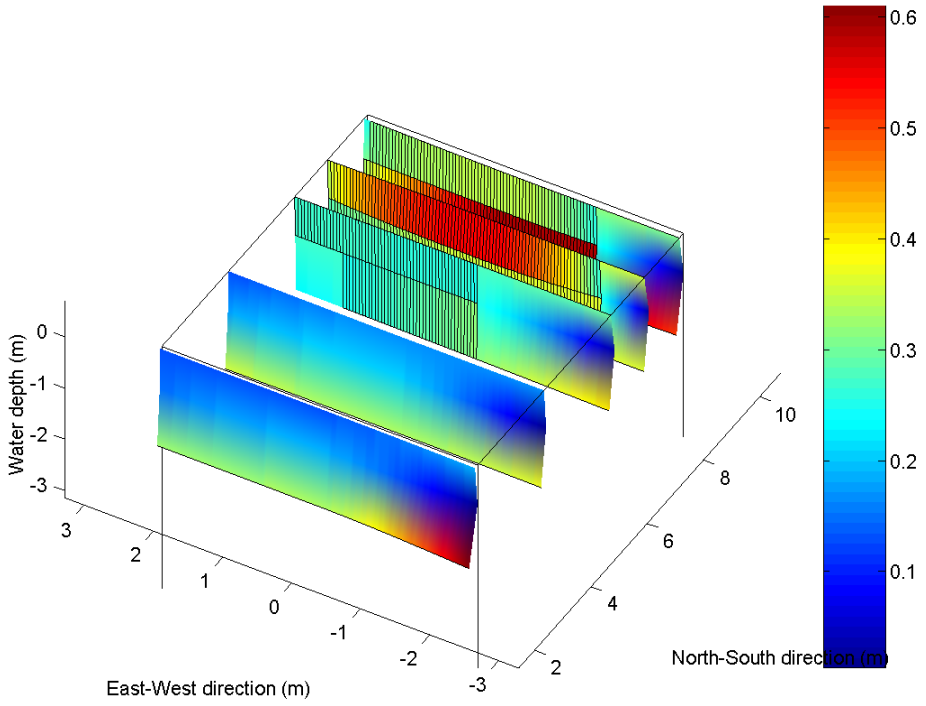

Figure D.16: Sd/U for a 3*3 array current test at 100% for *x*+

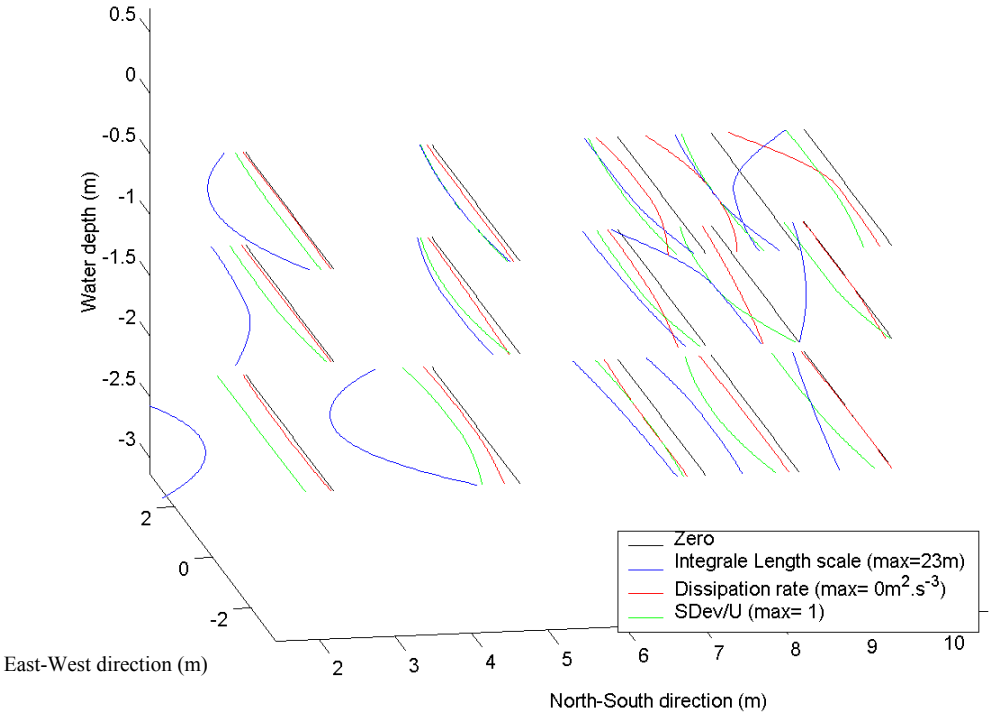

Figure D.17: L, ε and Sd/U for a 3*3 array current test at 225% for *x*+

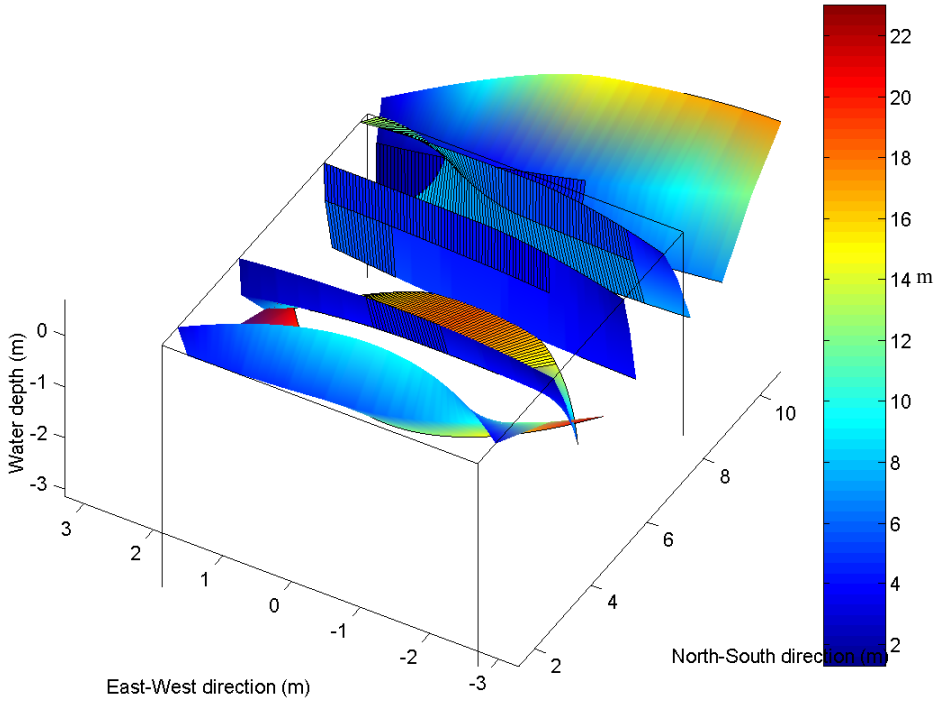

Figure D.18: L for a 3*3 array current test at 225% for *x*+

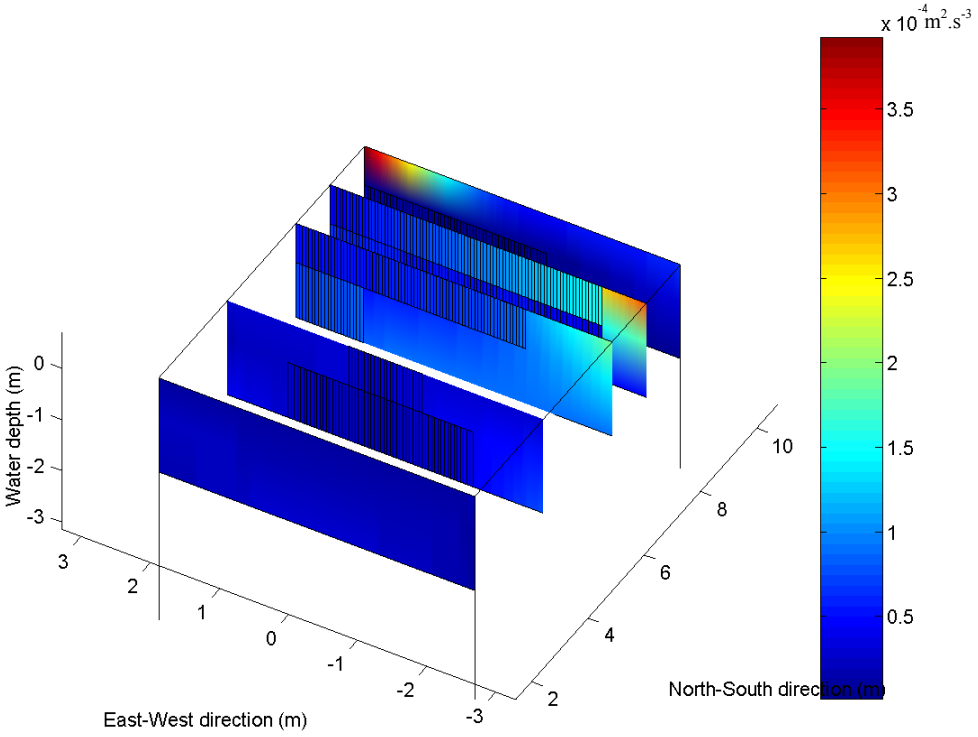

Figure D.19: ε for a 3*3 array current test at 225% for *x*+

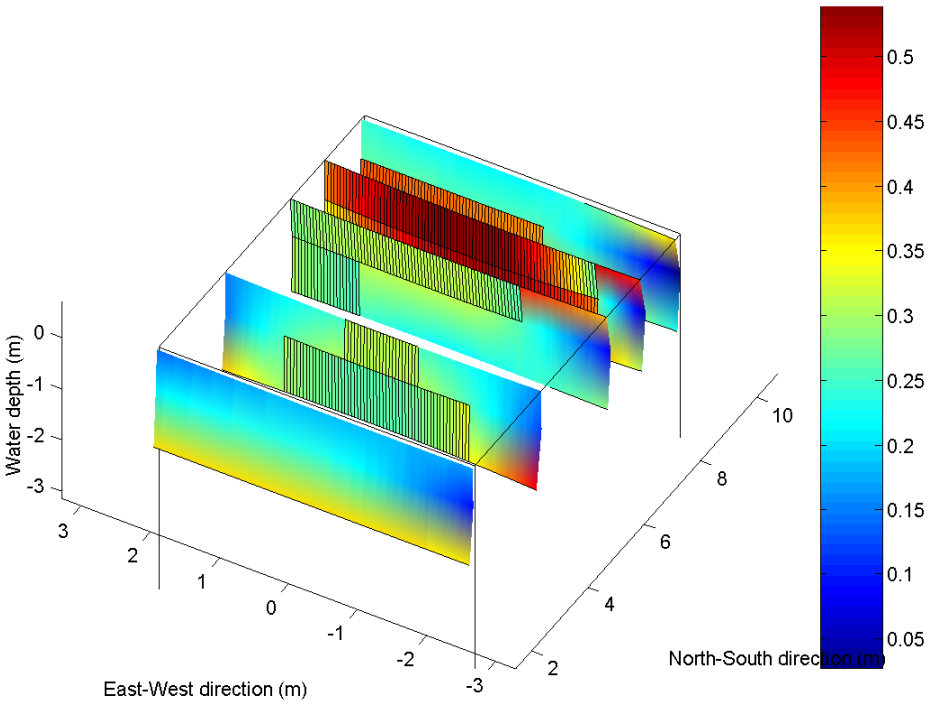

Figure D.20: Sd/U for a 3*3 array current test at 225% for *x*+

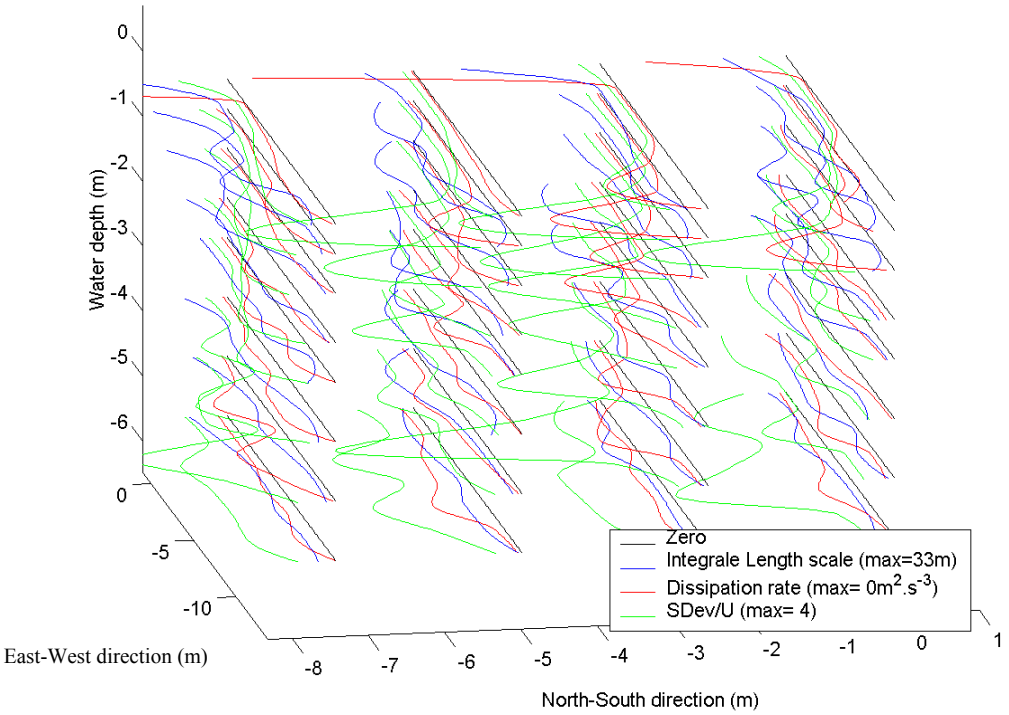

Figure D.21: L, ε and Sd/U for a Vertical array current test at 100%

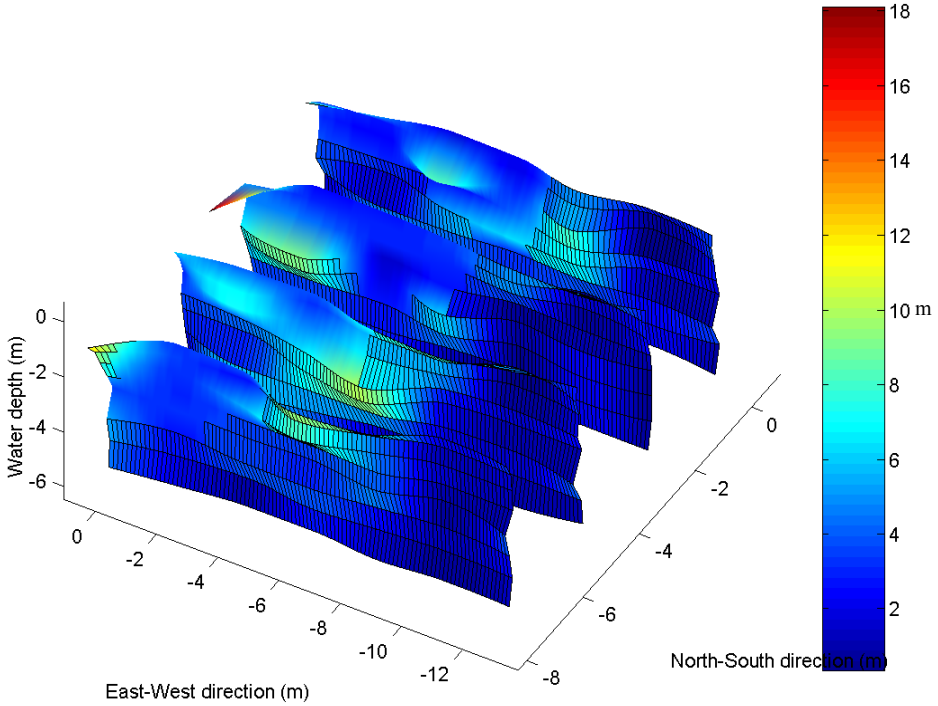

Figure D.22: L for a Vertical array current test at 100%

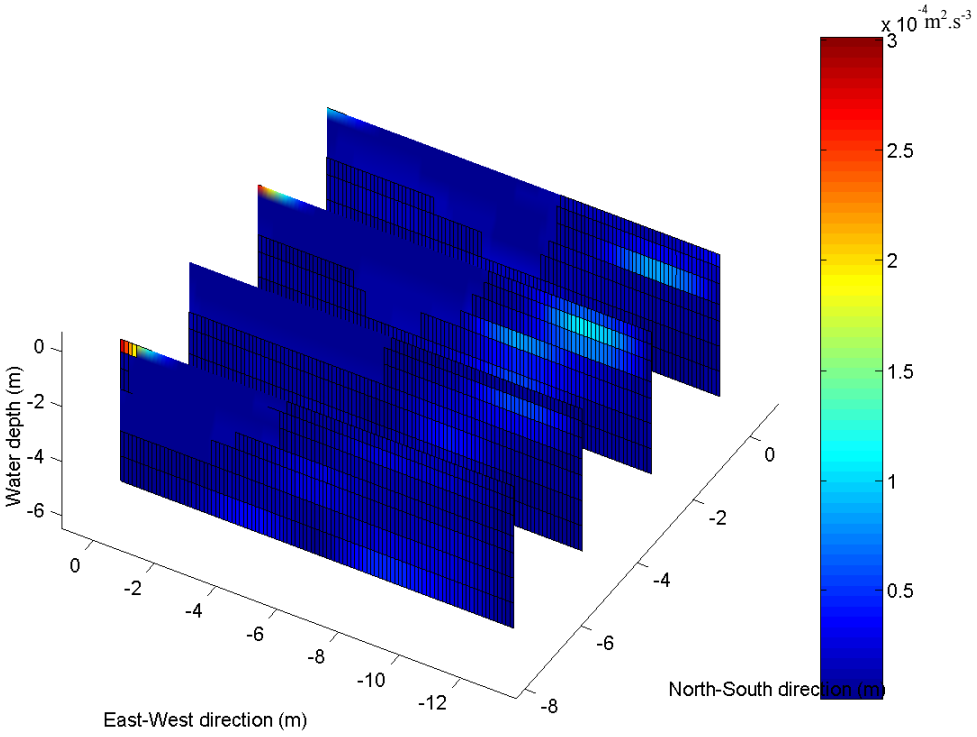

Figure D.23: ε for a Vertical array current test at 100%

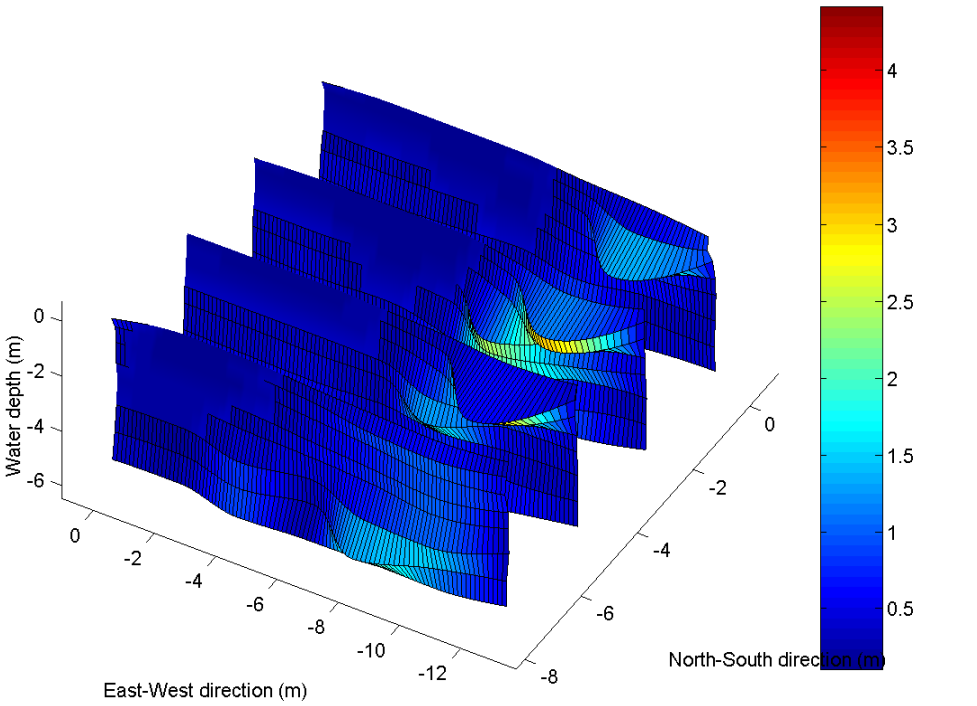

Figure D.24: Sd/U for a Vertical array current test at 100%

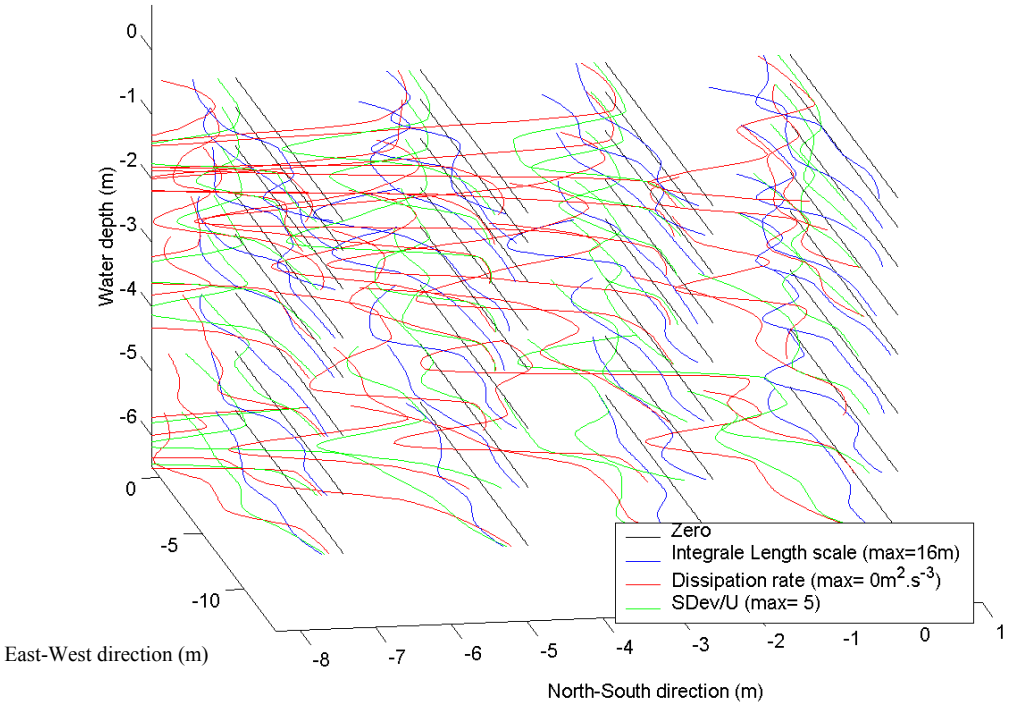

Figure D.25: L, ε and Sd/U for a Vertical array current test at 200%

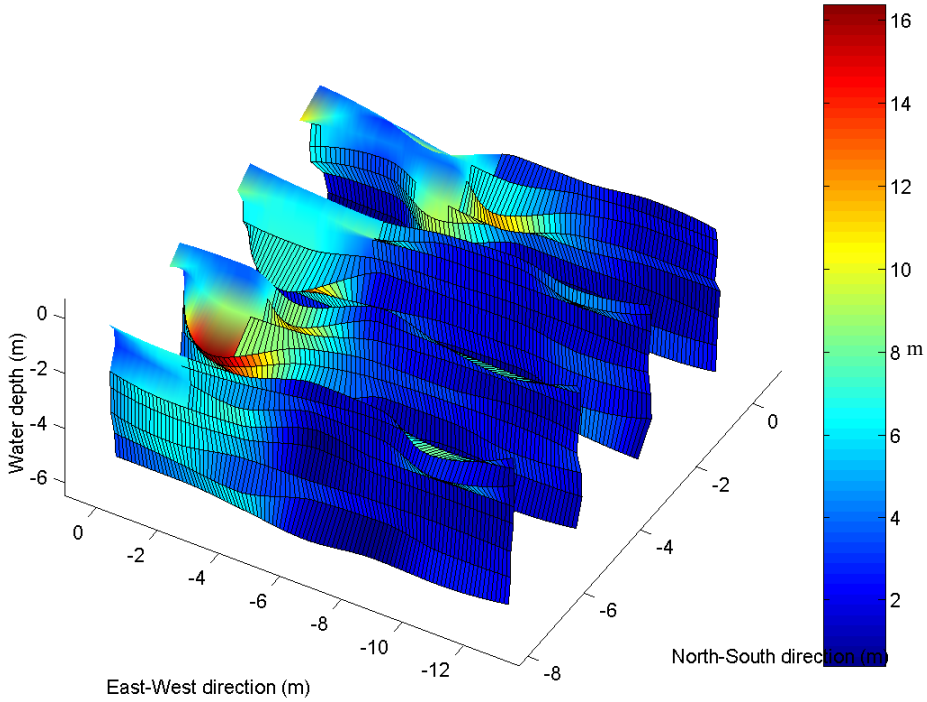

Figure D.26: L for a Vertical array current test at 200%

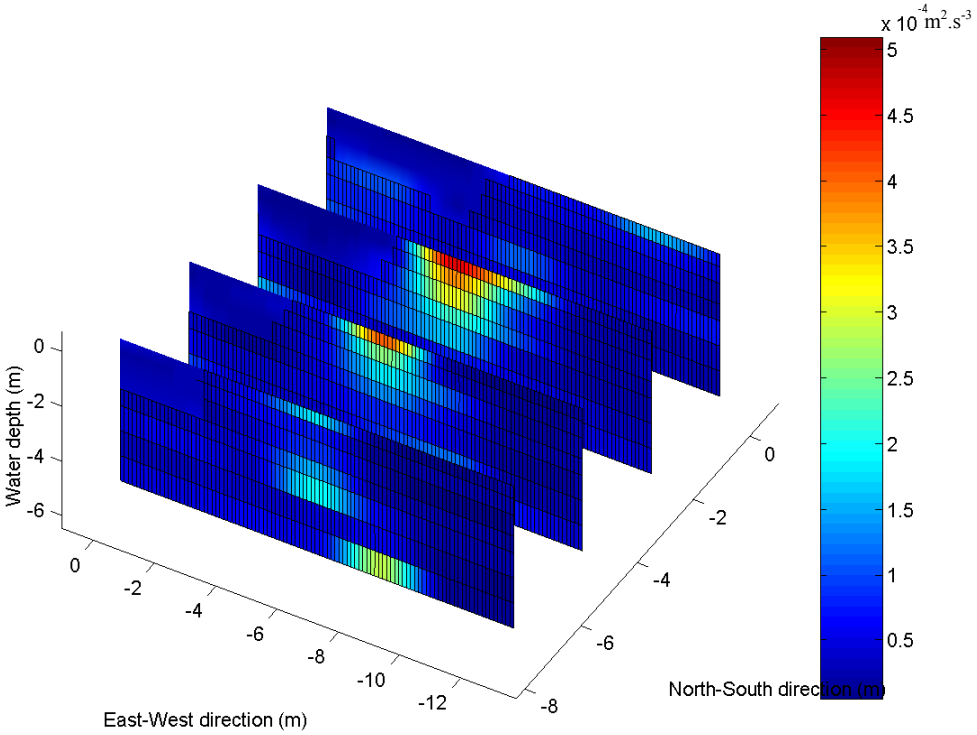

Figure D.27: ε for a Vertical array current test at 200%

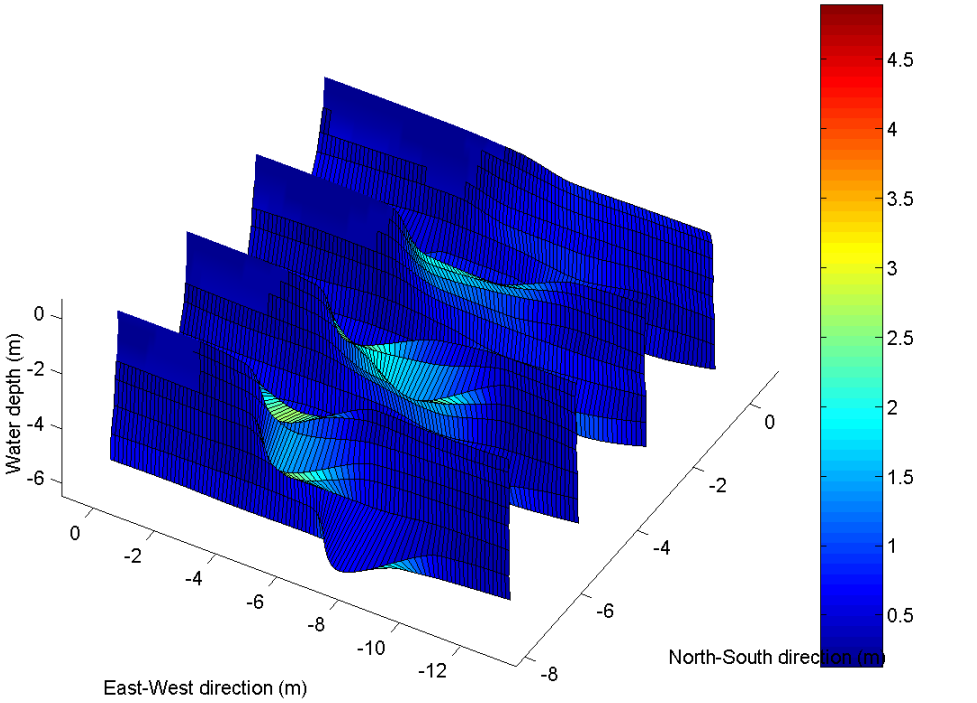

Figure D.28: Sd/U for a Vertical array current test at 200%

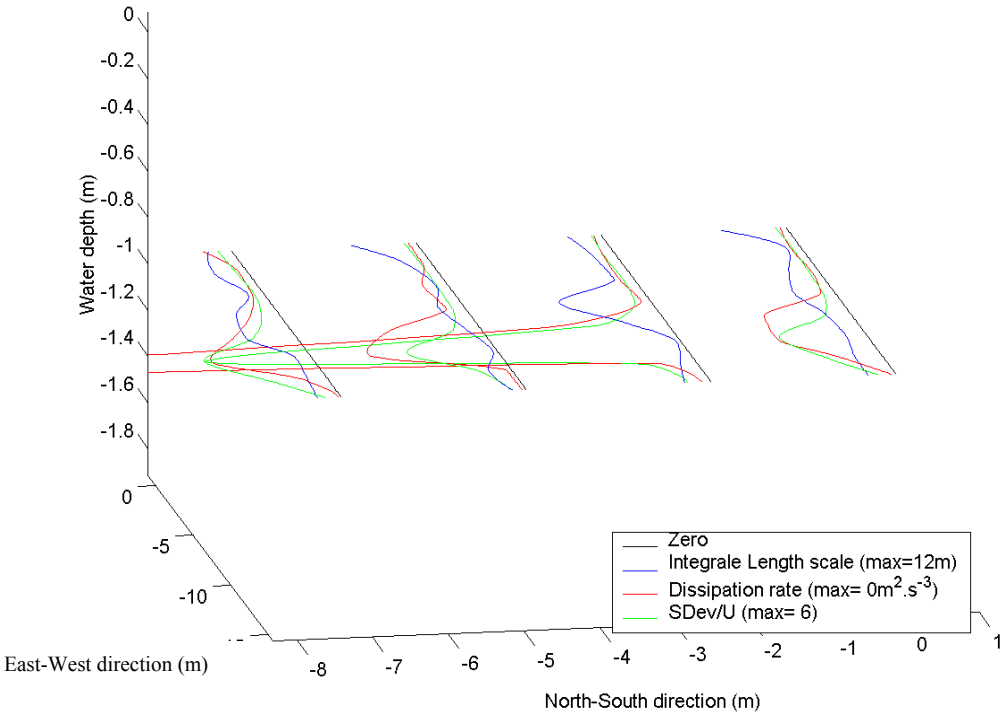

Figure D.29: L, ε and Sd/U for a Horizontal array current test at 100%

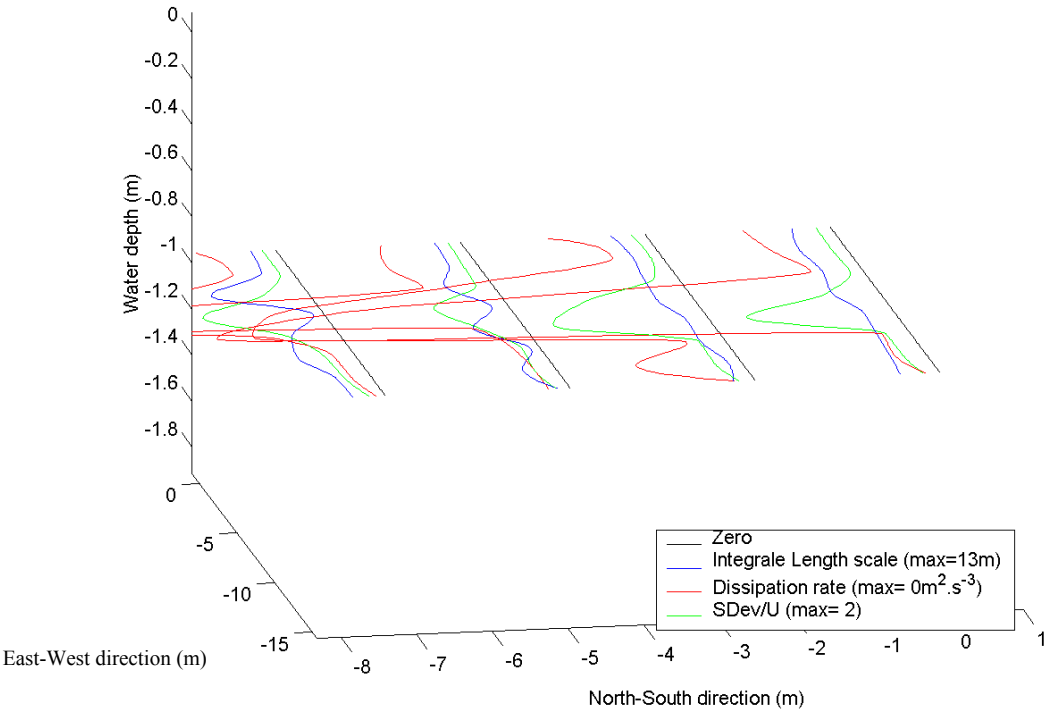

Figure D.30: L, ε and Sd/U for a Horizontal array current test at 200%

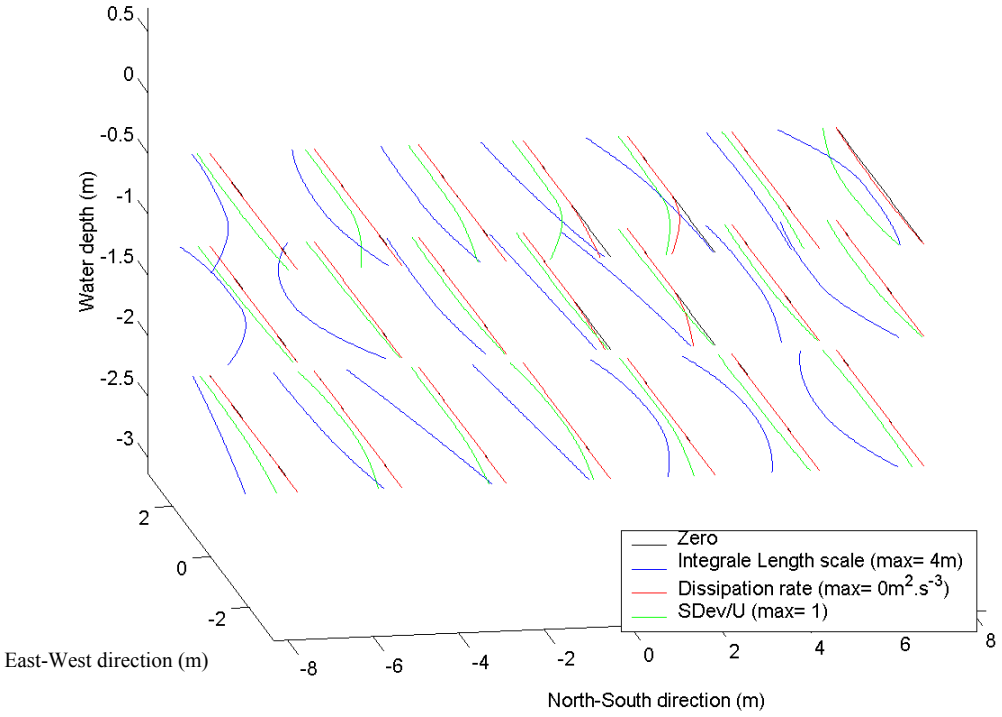

Figure D.31: L, ε and Sd/U for a 3*3 array with a RG2 wave + current test at 100%

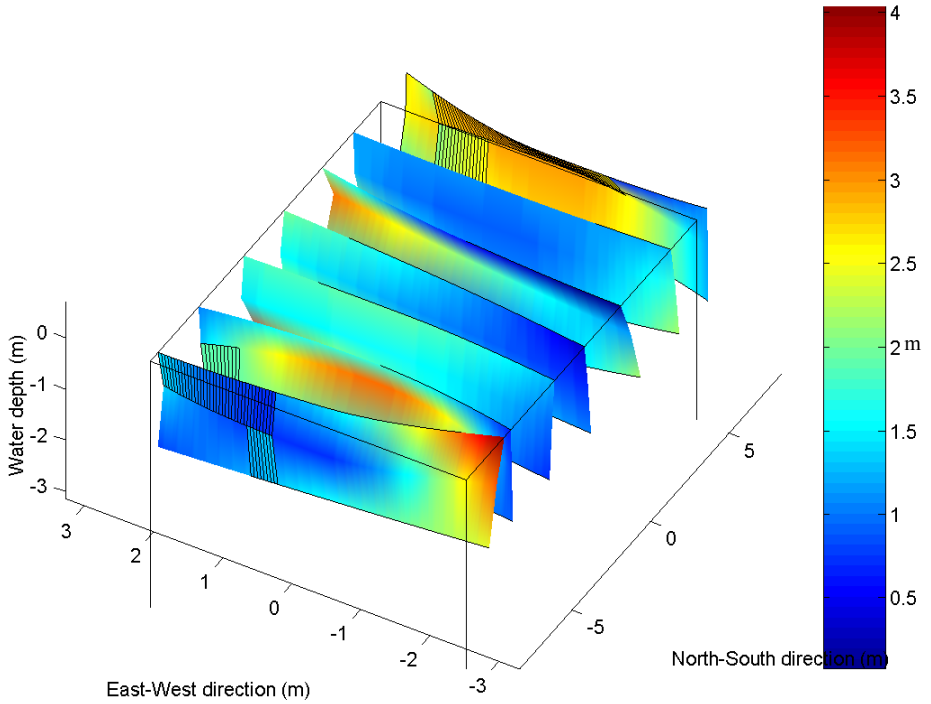

Figure D.32: L for a 3*3 array with a RG2 wave + current test at 100%

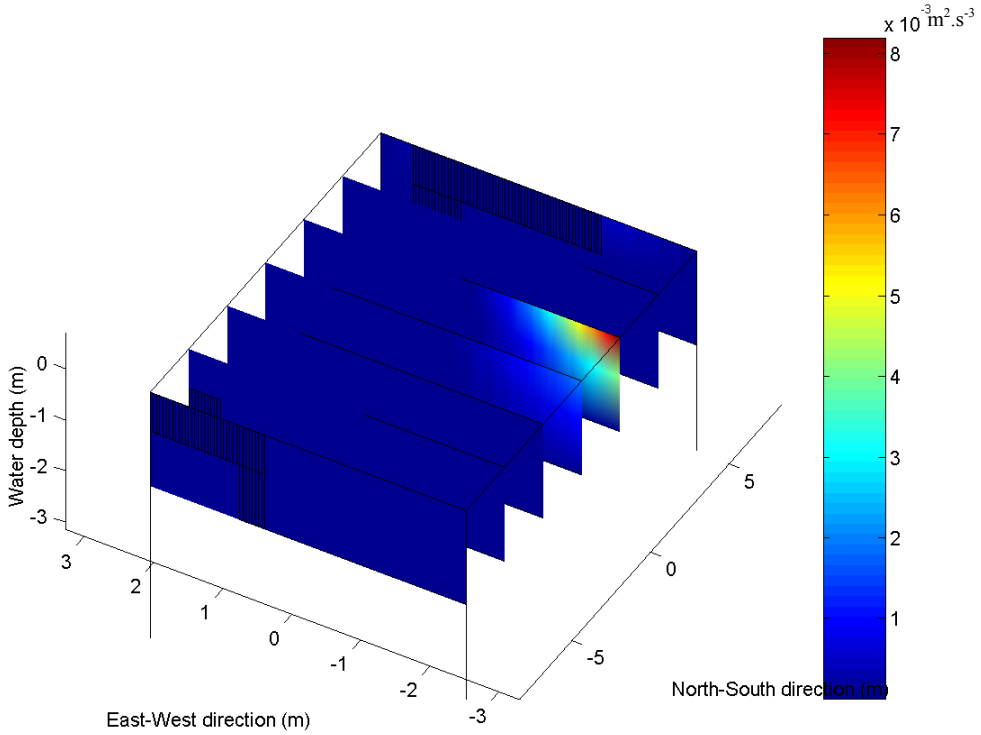

Figure D.33: ε for a 3*3 array with a RG2 wave + current test at 100%

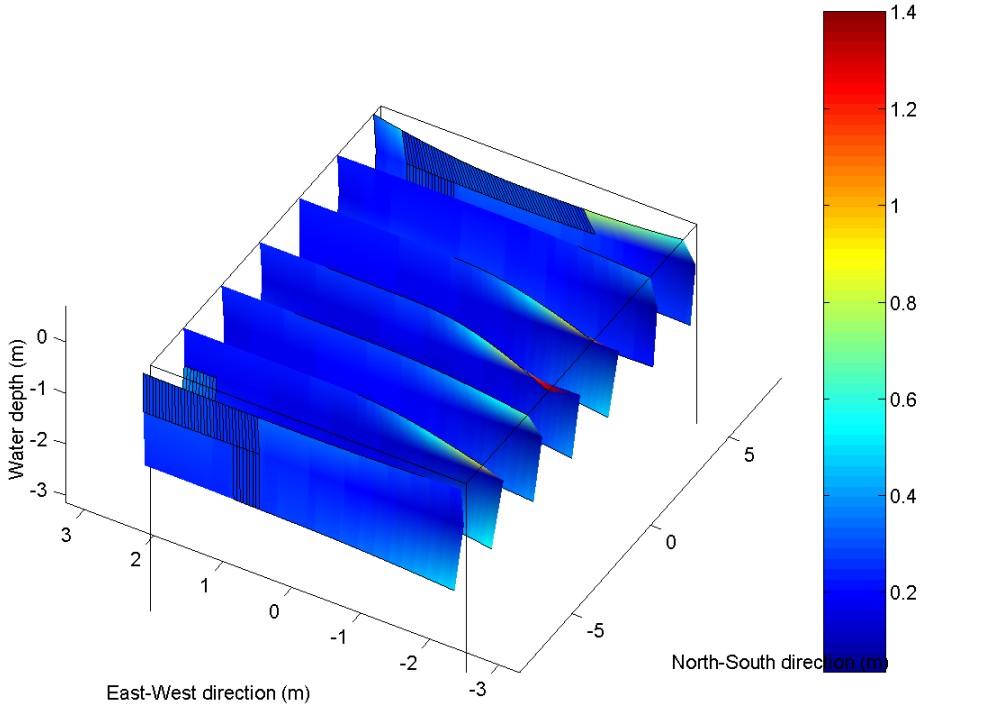

Figure D.34: Sd/U for a 3*3 array with a RG2 wave + current test at 100%

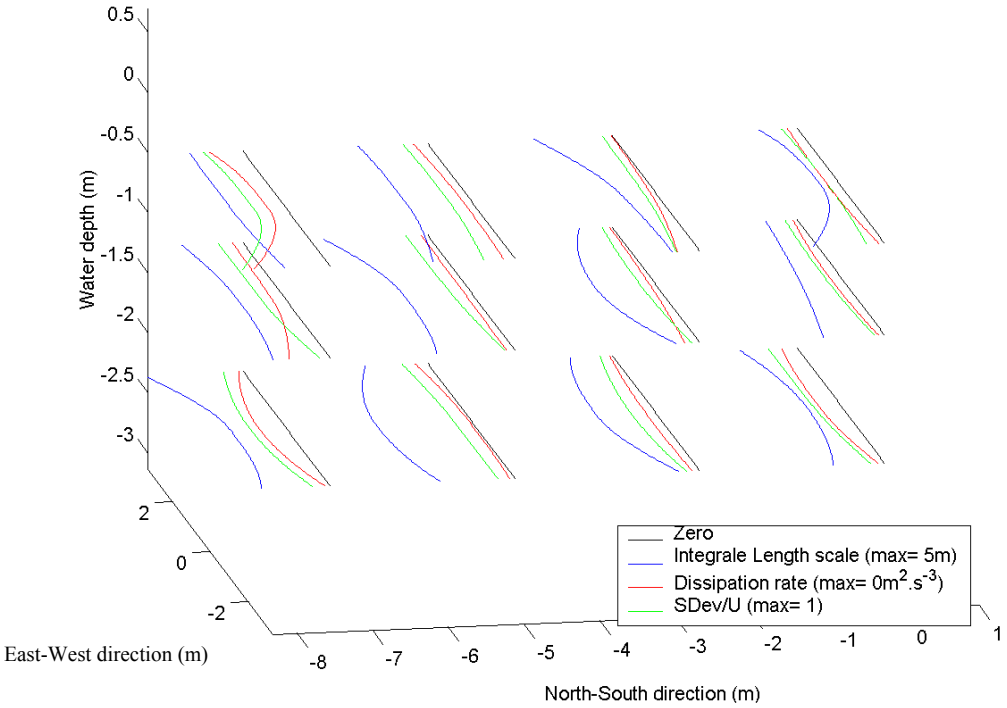

Figure D.35: L, ε and Sd/U for a 3*3 array with a RG2 wave + current test at 200%

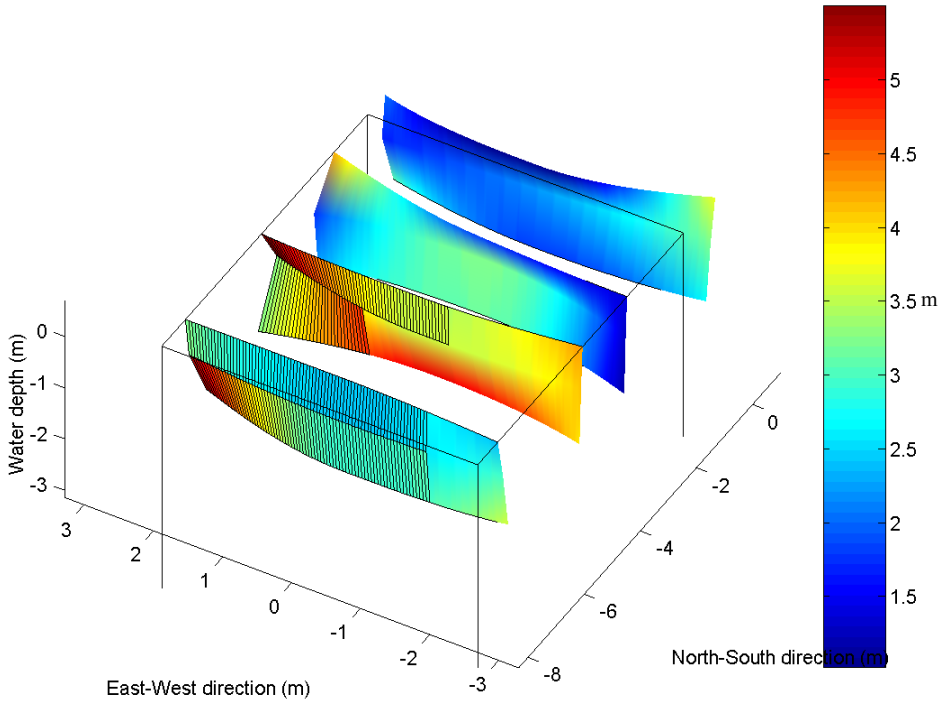

Figure D.36: L for a 3*3 array with a RG2 wave + current test at 200%

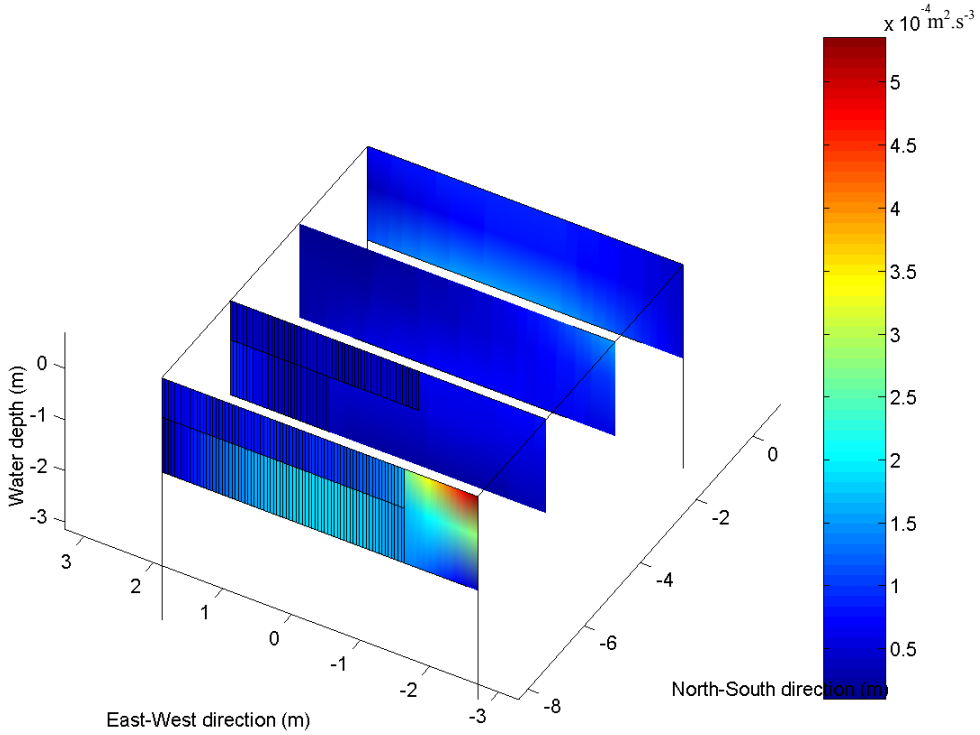

Figure D.37: ε for a 3*3 array with a RG2 wave + current test at 200%

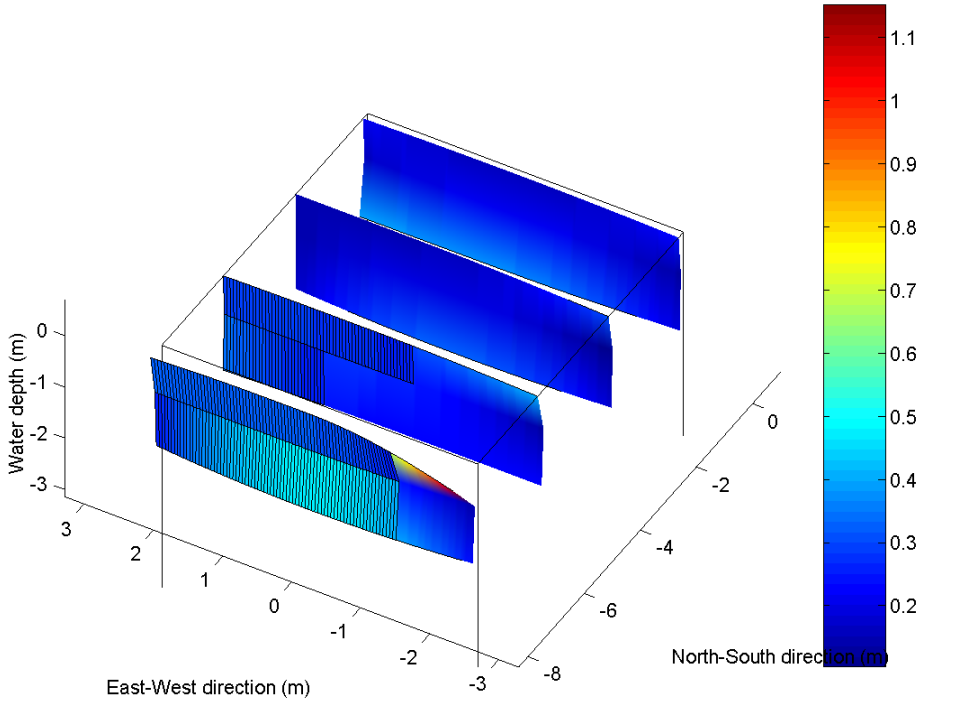

Figure D.38: Sd/U for a 3*3 array with a RG2 wave + current test at 200%

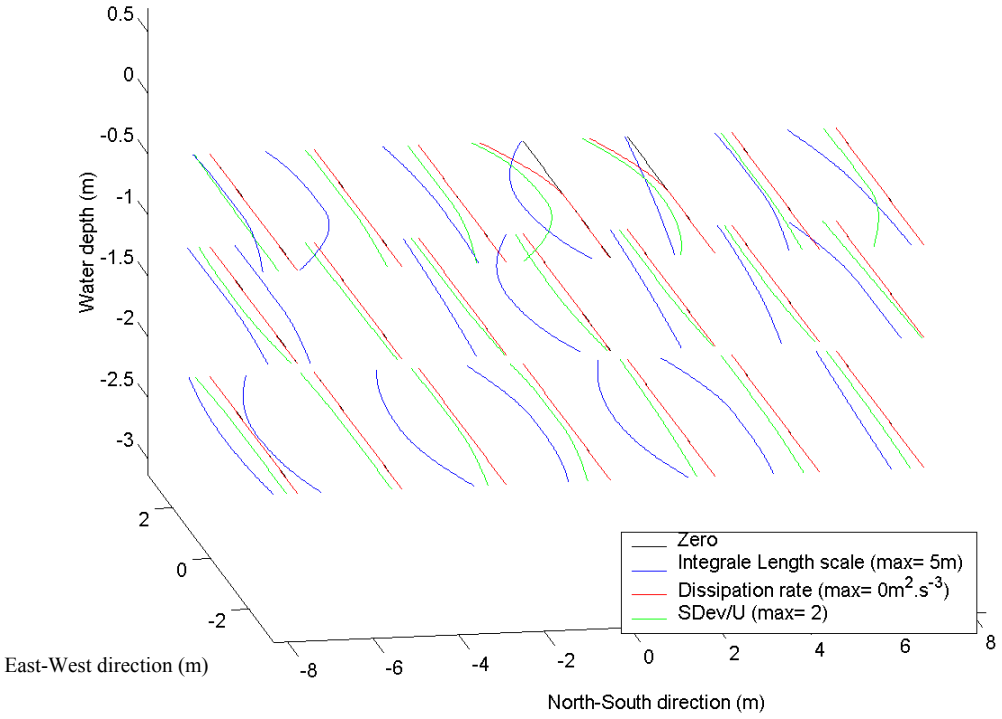

Figure D.39: L, ε and Sd/U for a 3*3 array with a RG5 wave + current test at 100%

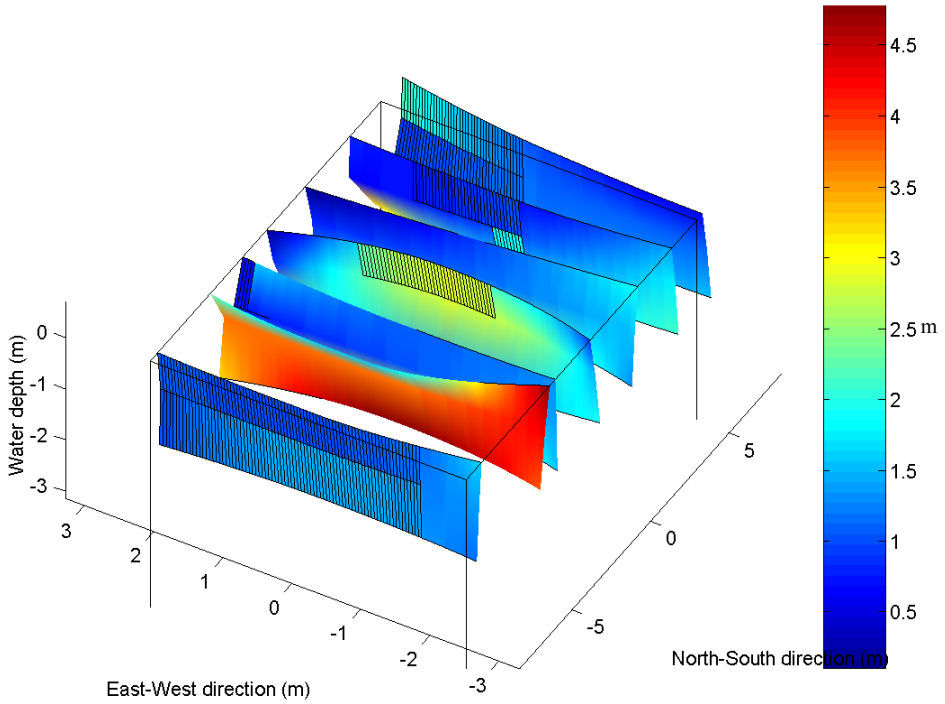

Figure D.40: L for a 3*3 array with a RG5 wave + current test at 100%

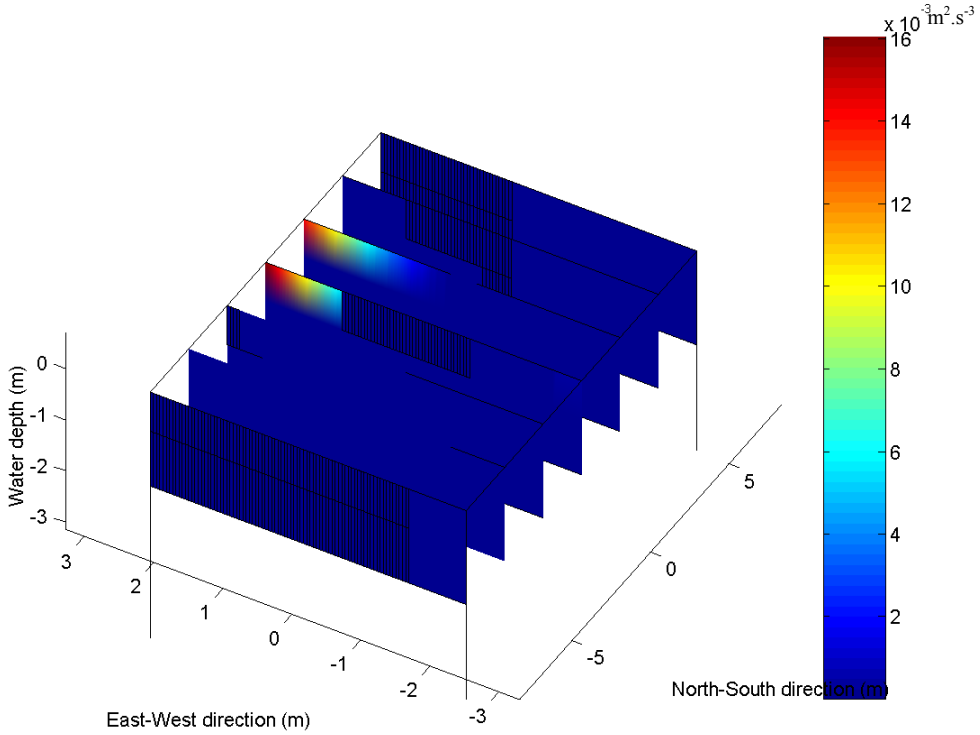

Figure D.41: ε for a 3*3 array with a RG5 wave + current test at 100%

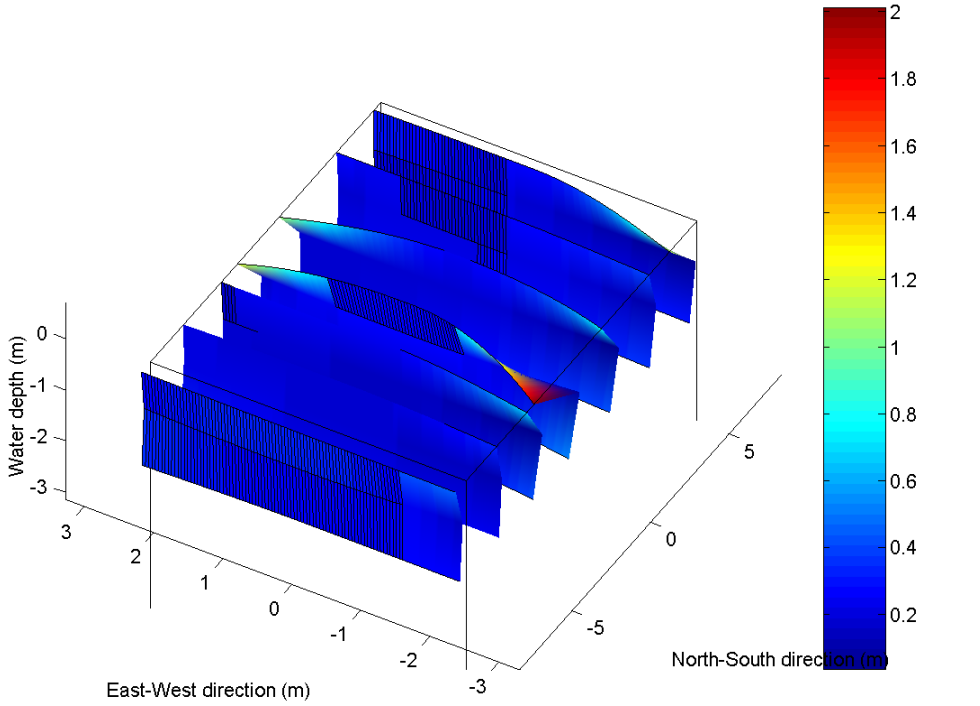

Figure D.42: Sd/U for a 3*3 array with a RG5 wave + current test at 100%

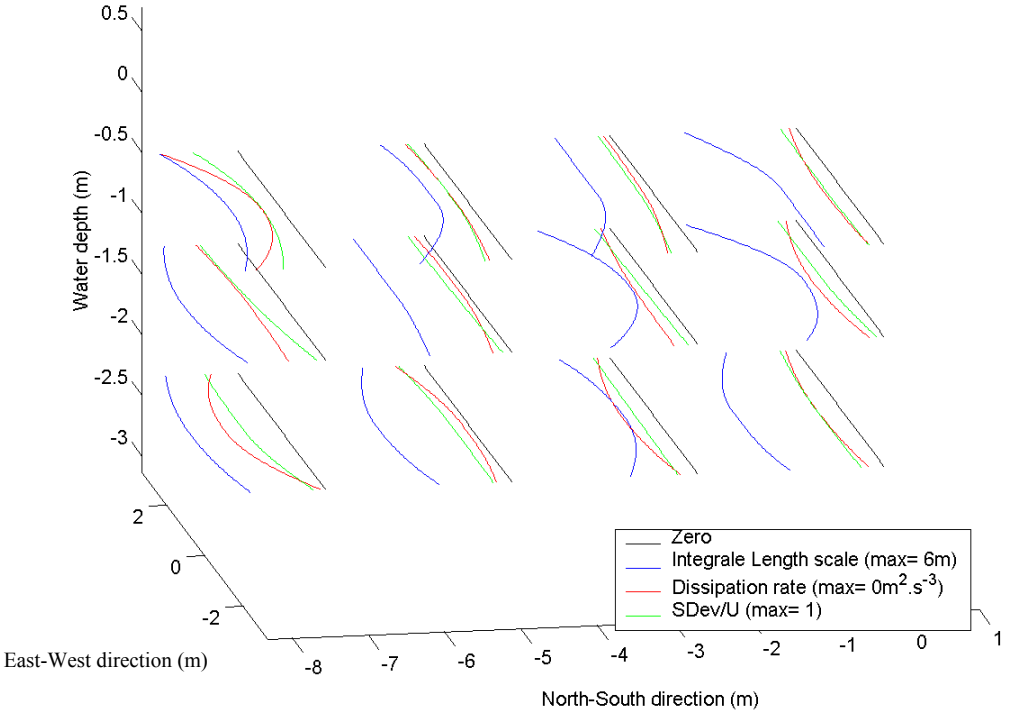

Figure D.43: L, ε and Sd/U for a 3*3 array with a RG5 wave + current test at 200%

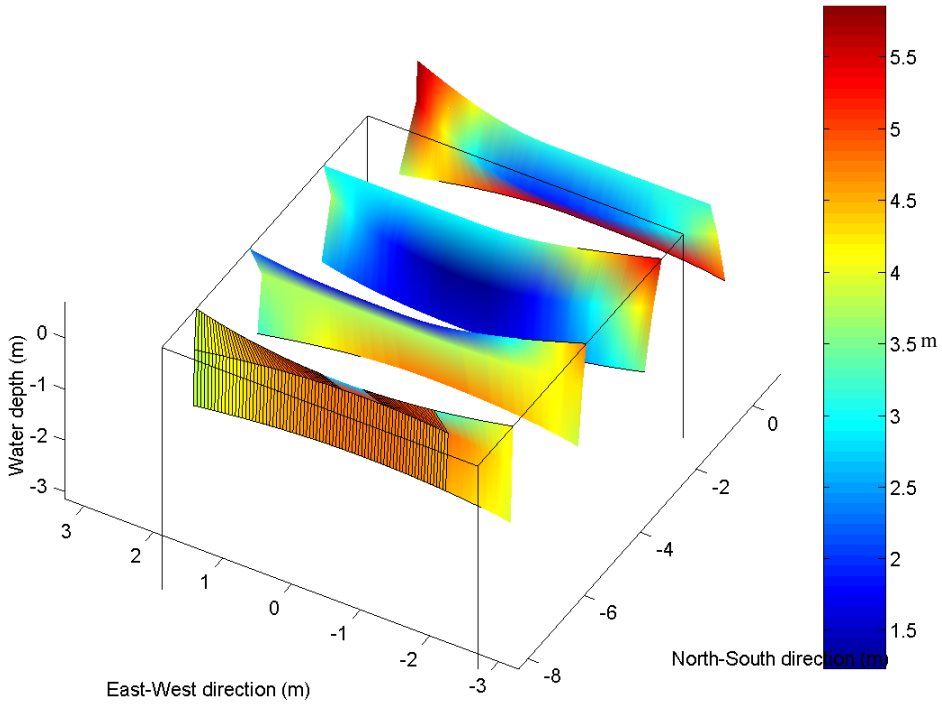

Figure D.44: L for a 3*3 array with a RG5 wave + current test at 200%

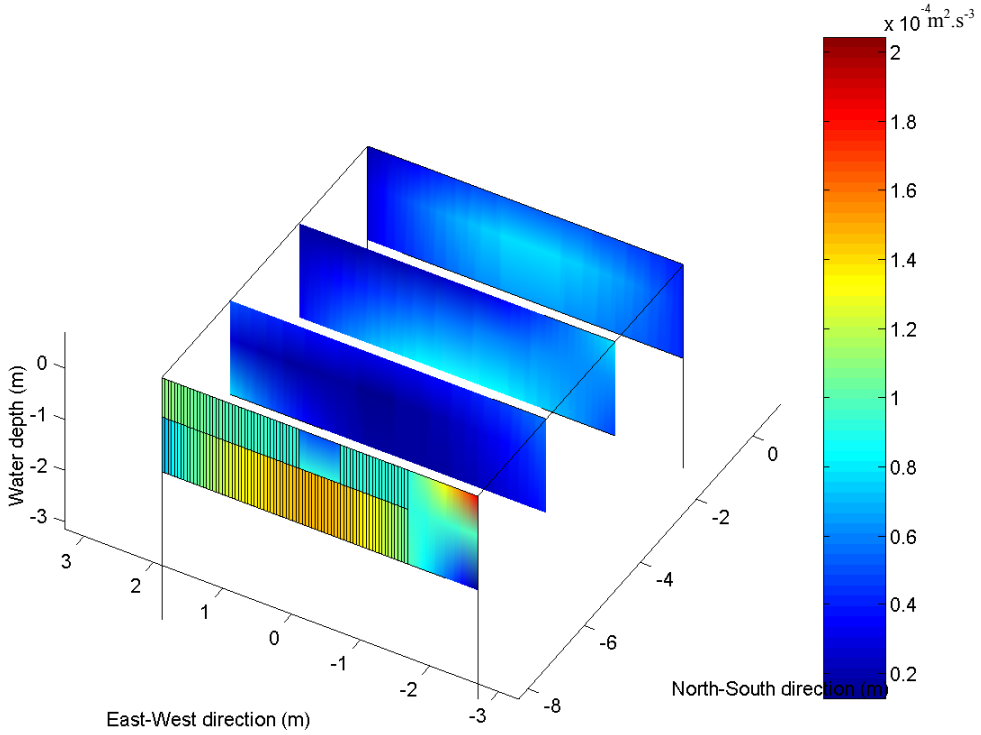

Figure D.45: ε for a 3*3 array with a RG5 wave + current test at 200%

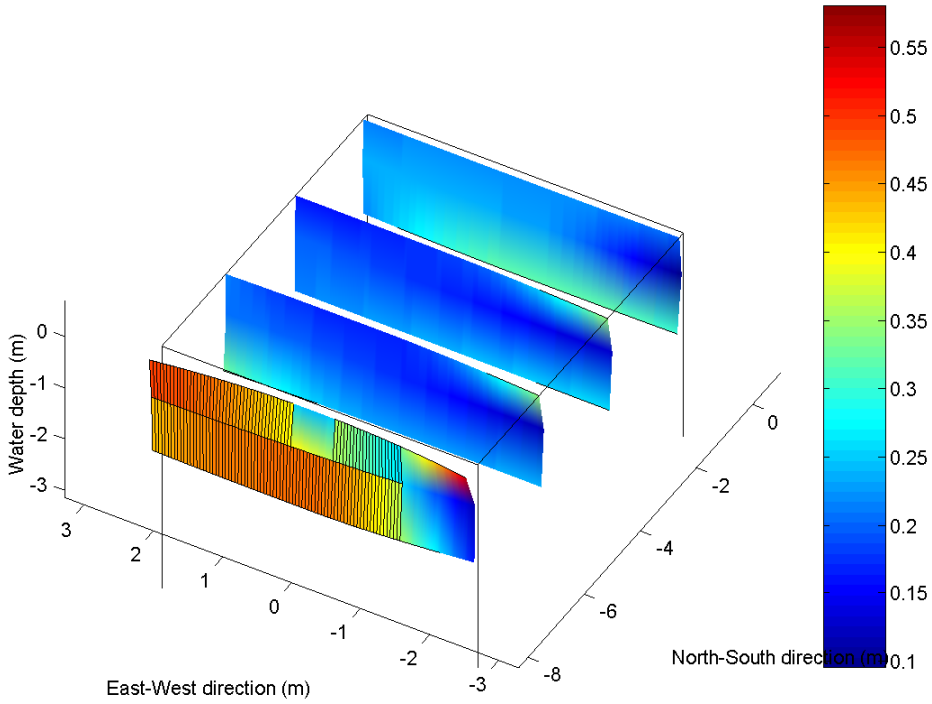

Figure D.46: Sd/U for a 3*3 array with a RG5 wave + current test at 200%

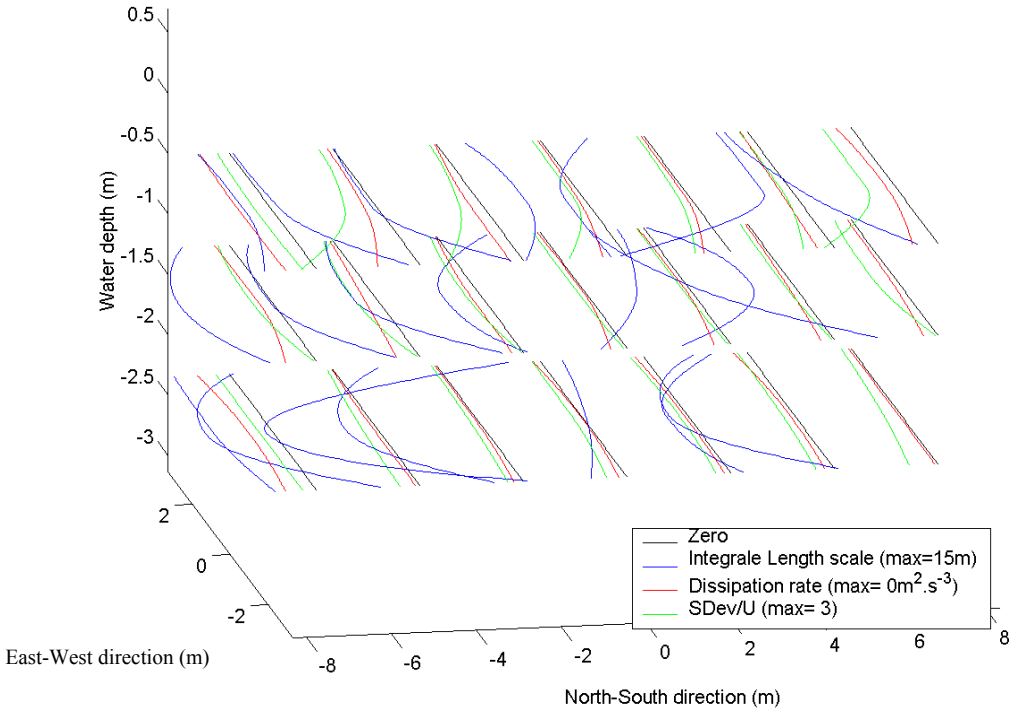

Figure D.47: L, ε and Sd/U for a 3*3 array with a RN wave + current test at 100%

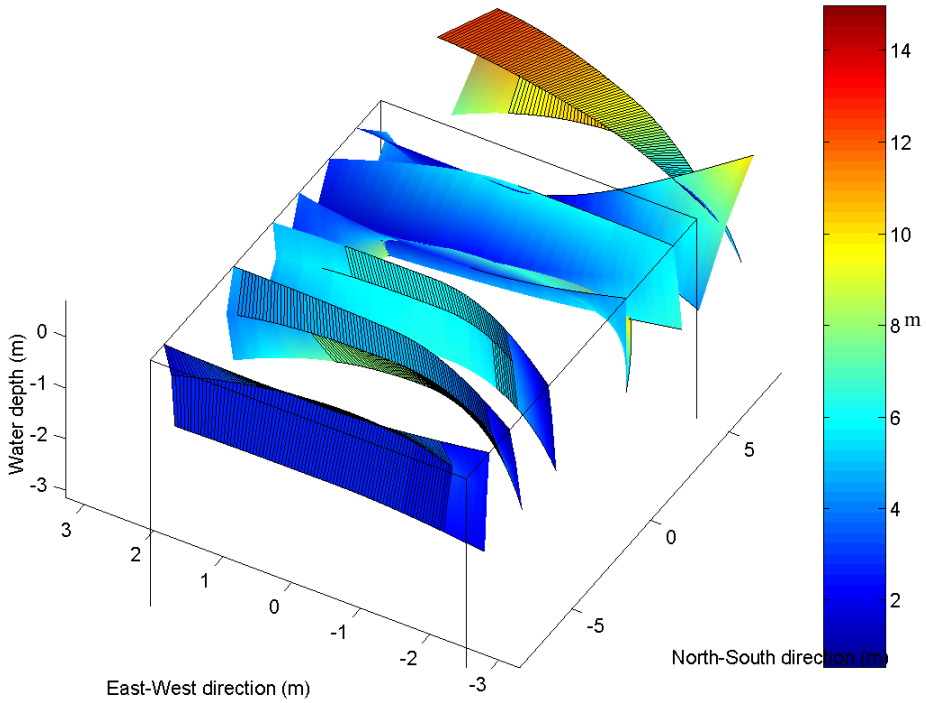

Figure D.48: L for a 3*3 array with a RN wave + current test at 100%

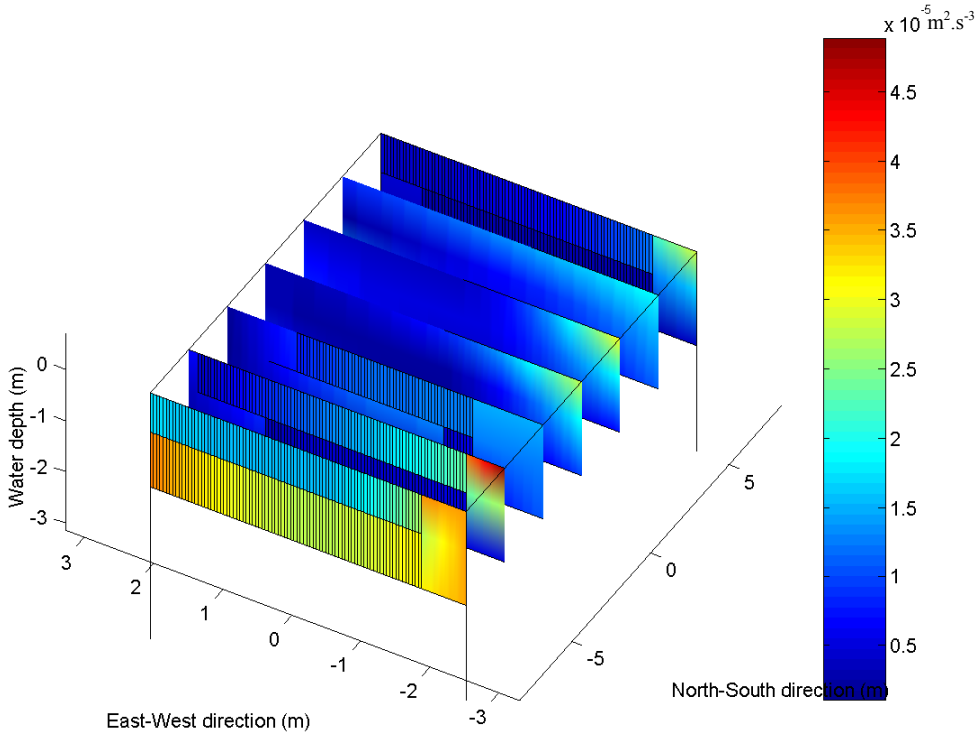

Figure D.49: ε for a 3*3 array with a RN wave + current test at 100%

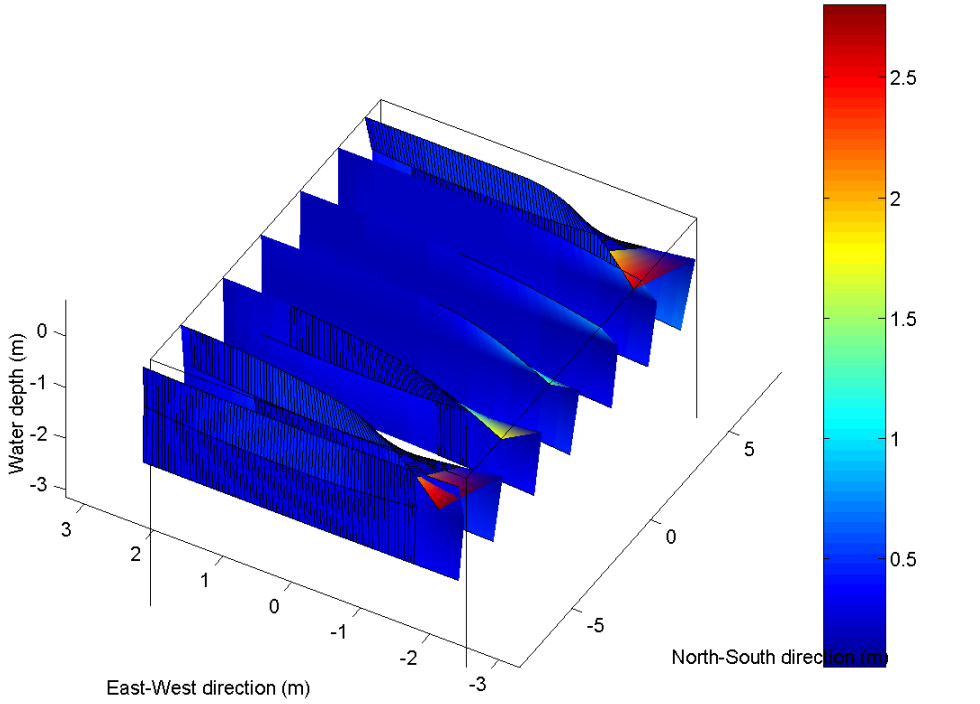

Figure D.50: Sd/U for a 3*3 array with a RN wave + current test at 100%

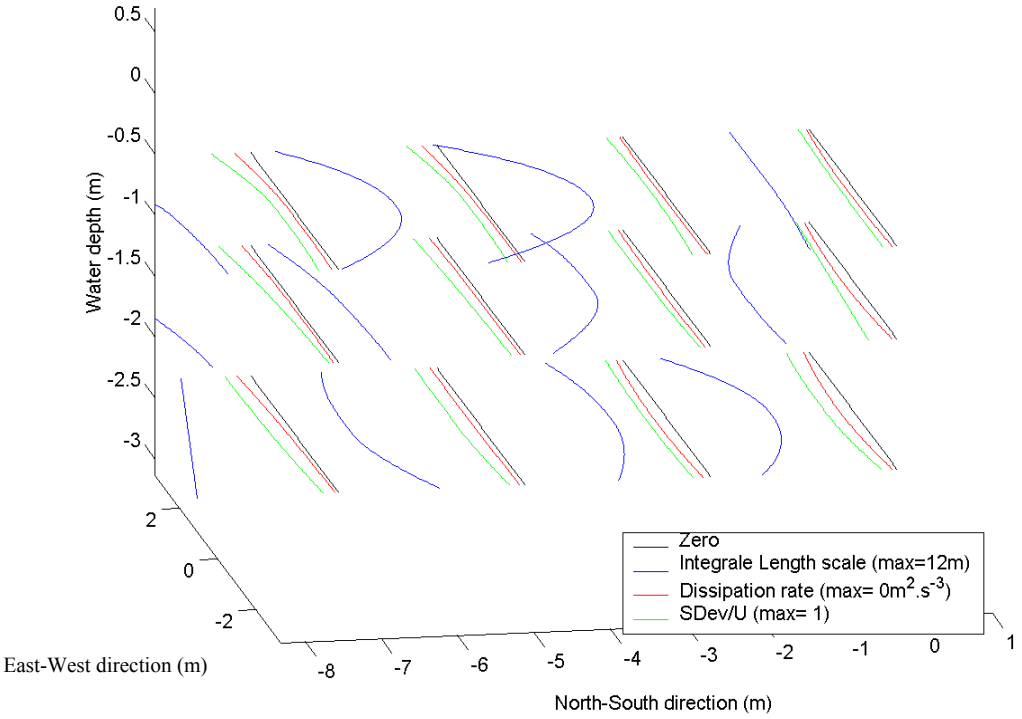

Figure D.51: L, ε and Sd/U for a 3*3 array with a RN wave + current test at 200%

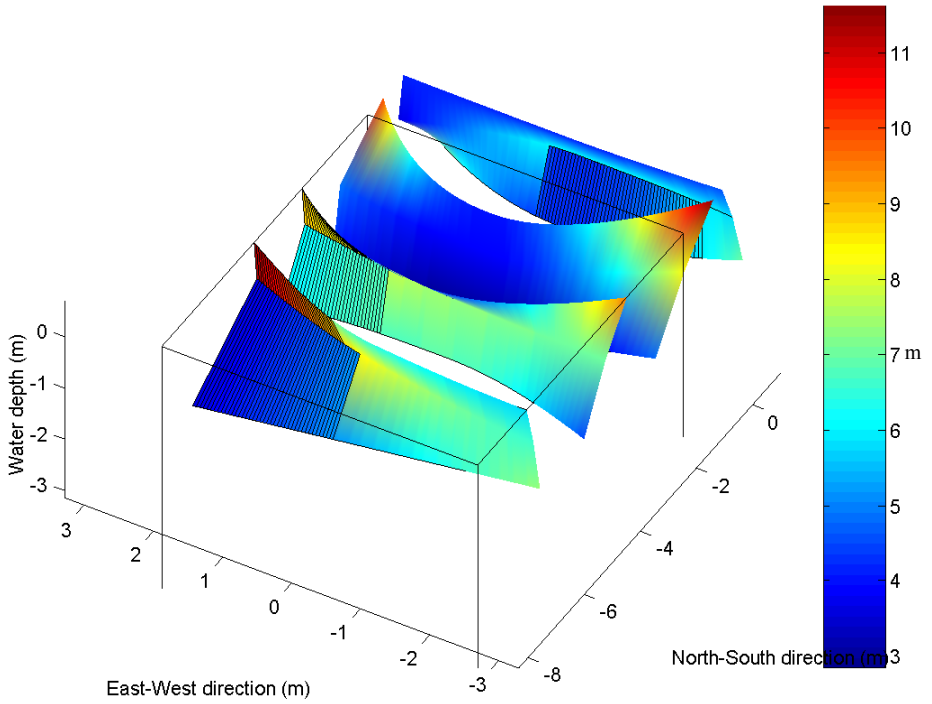

Figure D.52: L for a 3*3 array with a RN wave + current test at 200%

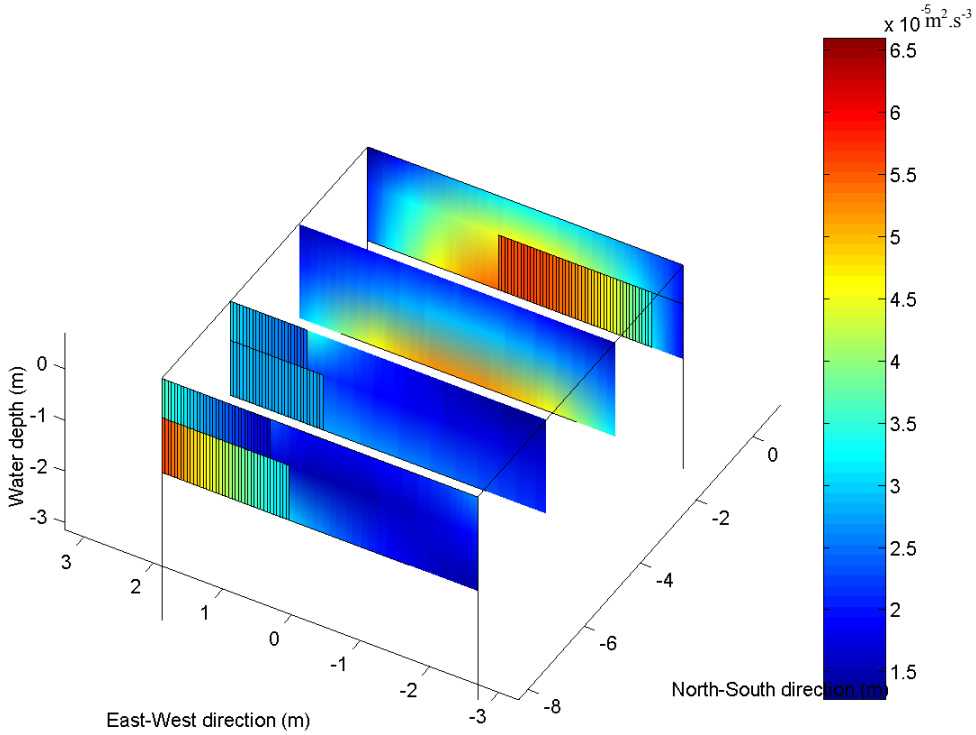

Figure D.53: ε for a 3*3 array with a RN wave + current test at 200%

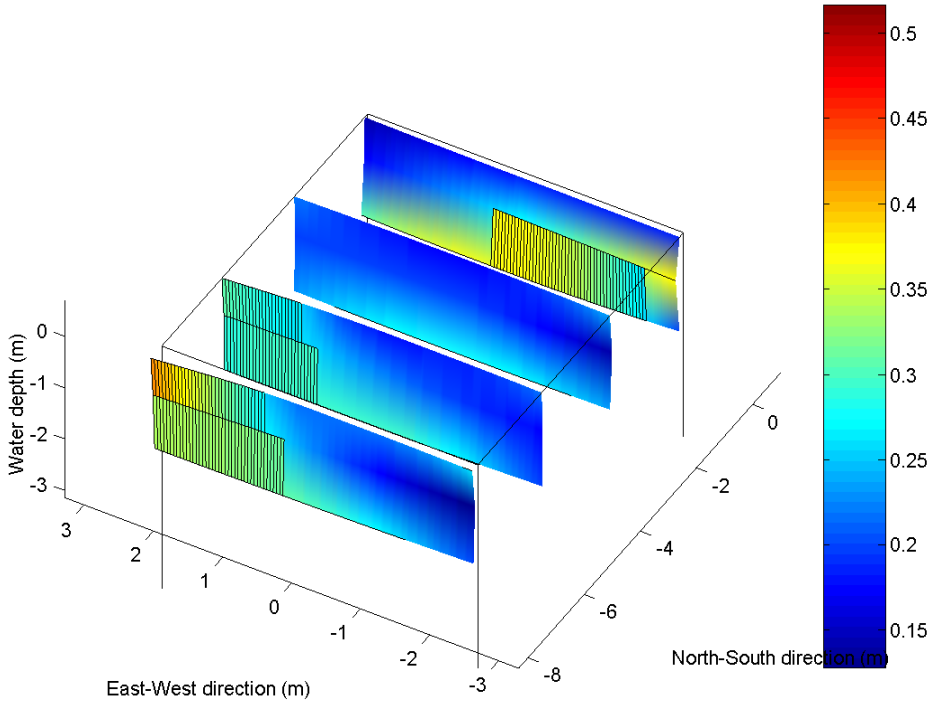

Figure D.54: Sd/U for a 3*3 array with a RN wave + current test at 200%

APPENDIX E

TEST PLAN

Phase	*Test Name*	*Test*	*Test Characteristic*	*Sensor Direction*	*Array Direction*	*Comments*
Phase 1	15HZ_001	Tow		VR	1 sensor only	Noisy due to shake of the Bridge
	30HZ_001					Junk test taken
	20HZ_001					no saturations
	30HZ_002					no saturations
	45HZ_001					
	CALM_011	Calm				
	15HZNS_001	Tow	60 sec.	NS		
	20HZNS_001		60 sec.			MAVS data acquisition stopped 5 sec. prior to end
	30HZNS_001		60 sec.			Neff data acquisition began 4.5 sec earlier than MAVS
	45HZNS_001		60 sec.			6 saturated samples on ch2(current *y*)
	CALM_012	Calm	60 sec.			
	15HZEW_001	Tow	60 sec.	EW		
	20HZEW_001		45 sec.			
	30HZEW_001		45 sec.			MAVS data acquisition stopped 5 sec. prior to end
	45HZEW_001		30 sec.			
	CALM_021	Calm	60 sec.			
	ST1_001	Current	Current at 200%, 5 min.			
	C1EW_001	Current	Current at 200%, 180 sec.	EW		
	C1NS_001		Current at 200%, 180 sec.	NS		
	C1VR_001		Current at 200%, 180 sec.	VR		
	C6VR_001		Current at 200%, 180 sec.	VR		
	C6NS_001		Current at 200%, 180 sec.	NS		
	C6EW_001		Current at 200%, 180 sec.	EW		

	CALM_031	Calm				1 wave probe calibrated ch.5 Wavemaker up & calibrated wave frequency = 0.7143s & amplitude = 2ft (meas +/- 3.5") Waveprobe deployed 18" W of MMB
	WVEW_001	Wave		EW		
	WV3E_001					
	WV3N_001			NS		
	WV1N_001					
	WV1V_001			VR		
	WV3V_001					
	WIND_001	Wind				Straight on and off
	WIND_002					Ground strap in and out of water
	WIND_003					Varying speeds strap out of water
	CALM_041	Calm	60 sec.			MAVS & MMB -3ft. apart, 16" E of CL VFD to 6 Hz then to 30 Hz
	V30V3_001			VR		
	V30N3_001			NS		Data 30 min too long
	V30E3_001			EW		
Phase 2	TOW1_001	Tow	0,2778 fps = 8.46cm/s	NS	N.A.	Bridge traveling 30ft in 1:48.00 MAVS #8 Broken => Unplugged
	TOW2_001		0,418 fps = 12.74cm/s			Bridge traveling 30ft in 1:11.72
	TOW3_001		0,561 fps = 17.10cm/s			Bridge traveling 30ft in 0:53.44
	TOW4_001		0,657 fps = 20.03cm/s			Bridge traveling 30ft in 0:45.69
	TOW5_001		0,987 fps = 30.08cm/s			Bridge traveling 30ft in 0:30.41
	TOW6_001		1,486 fps = 45.29cm/s			Bridge traveling 30ft in 0:20.19
	TOW7_001		1,972 fps = 60.11cm/s			Bridge traveling 30ft in 0:15.21
	TOW8_001		1,983 fps = 60.44cm/s			Bridge traveling 30ft in 0:15.13
	20HZ_004	Tow	20cm/s		3*3	
	45HZ_004		45cm/s			
	CALM_001	Calm				
	20HZ_005	Tow	20cm/s			
	CALM_002	Calm				
	45HZ_005	Tow	45cm/s			

CALM_003	Calm				
30HZ_004	Tow	30cm/s			
CALM_004	Calm				
30HZ_005	Tow	30cm/s			
CALM_005	Calm				
60HZ_004	Tow	60cm/s			
CALM_006	Calm				
60HZ_005	Tow	60cm/s			
CALM_007	Calm				
20HZ_006	Tow	20cm/s	NS+EW	3*3	MAVS 1-3 rotated 90° CCW from previous measurments
CALM_008	Calm				
30HZ_006	Tow	30cm/s			
CALM_009	Calm				
45HZ_006	Tow	45cm/s			
CALM_010	Calm				
60HZ_006	Tow	60cm/s			
CALM_011	Calm		NS	3*3	resampled internal offset in MAVS #1, calibration monitor for calm water
20HZ_007	Tow	20cm/s			
CALM_012	Calm				
30HZ_007	Tow	30cm/s			
CALM_013	Calm				
45HZ_007	Tow	45cm/s			
CALM_014	Calm				
60HZ_007	Tow	60cm/s			
CALM_015	0 Offset in a bucket		-		not all meters functioning, some need flush from bubble and redeploy
20HZ_008					
45HZ_008					
60HZ_008					
CALM_015	Calm		NS	3*3	
20HZ_008	Tow	20cm/s			
CALM_016	Calm				

60HZ_008	Tow	60cm/s			
CALM_017	Calm				
30HZ_008	Tow	30cm/s			
CALM_018	Calm				
45HZ_008	Tow	45cm/s			
CALM_019	Calm				
30HZ_009	Tow	30cm/s			
CALM_020	Calm				
45HZ_009	Tow	45cm/s			
CALM_021	Calm				
20HZ_009	Tow	20cm/s			
CALM_022	Calm				
60HZ_009	Tow	60cm/s			
C100P0_001	Current	#2 at100%	NS	3*3	
C200P0_001	Current	#2 & #3 at100%	NS	3*3	
C200P0_002					MAVS #4 Failed
C200P0_003					
CALM_023	Calm		NS	3*3	
C225P0_001	Current	#2 & #3 at100% & #1 at25%	NS	3*3	*x* = 0 15Hz Mode
C225P0_001					*x* = 0
C225P-32_001					*x* = -32ft
C225P-24_001					*x* = -24ft
C225P-16_001					*x* = -16ft
C225P-8_001					*x* = -8ft
C225P8_001					*x* = +8ft
C225P16_001					*x* = +16ft
C225P24_001					*x* = +24ft
CALM_024	Calm			3*3	
C225P24_002	Current	#2 & #3 at100% & #1 at25%	NS	3*3	*x* = +24ft
C225P32_001					*x* = +32ft
C225P28_001					*x* = +28ft

C100P28_001		Pump #2 at100%	NS	3*3	*x* = +28ft basin at0% for 45 min prior starting pump #2
C100P32_001					*x* = +32ft
C100P24_001					*x* = +24ft
C100P16_001					*x* = +16ft
C100P8_001					*x* = +8ft
C100P0_001					*x* = 0ft
CALM_025	Calm			3*3	
C100P0_003	Current	Pump #2 at100%	NS	3*3	*x* = 0ft
C100P-8_001					*x* = -8ft
C100P-16_001					*x* = -16ft
C100P-24_001					*x* = -24ft MAVS #4 glitched?
C100P-32_001					*x* = -32ft
CALM_026	Calm			3*3	Calibrate 3 wavprobes and deploy at the same *x* & y coordinates of the MAVS meters. Zero waveprobes & stokes Wavemaker up & calibrated
RG2A_001	Wave	15 min random & 2 min delay	NS	3*3	Wavetrains from FPSO2002
RE5_2_001					
RN2A_001					New calibration after that test
CALM_027	Calm		NS	3*3	
RG2A_002	Wave			3*3	Observe ringlet waves reflecting back from MAVS stg. Beams
RE5_2_002					
RN2A_002					
RNC1P0_001	Wave + Current	Current at 100%	NS	3*3	*x* = 0ft move instruments
RG2C1P0_001					*x* = 0ft
RG5C1P0_001					*x* = 0ft
RG5C1P8_001					*x* = +8ft move instruments
RG2C1P8_001					*x* = +8ft
RNC1P8_001					*x* = +8ft
RNC1P16_001					*x* = +16ft move instruments
RG2C1P16_001					*x* = +16ft wave maker up & calibrated
RG5C1P16_001					*x* = +16ft
RG5C1P24_001					*x* = +24ft move instruments

RG2C1P24_001					*x* = +24ft
RNC1P24_001					*x* = +24ft
RNC1P-8_001					*x* = -8ft move instruments
RG2C1P-8_001					*x* = -8ft
RG5C1P-8_001					*x* = -8ft
RNC1P-16_001					*x* = -16ft move instruments
RG5C1P-16_001					*x* = -16ft
RG2C1P-16_001					*x* = -16ft
RNC1P-24_001					*x* = -24ft move instruments
RG2C1P-24_001					*x* = -24ft
RG5C1P-24_001					*x* = -24ft
RNC2P-24_001					*x* = -24ft move bridge
RG2C-24_001					*x* = -24ft
RG5C2P-24_001					*x* = -24ft
RG5C2P-16_001					*x* = -16ft move instruments
RG2C-16_001					*x* = -16ft
RNC2P-16_001		Current at 200%	NS	3*3	*x* = -16ft
RNC2P-8_001					*x* = -8ft move instruments
RG2C2P-8_001					*x* = -8ft wave maker up & Calibrated
RG5C2P-8_001					*x* = -8ft
RG5C2P0_001					*x* = 0ft move bridge
RG2C2P0_001					*x* = 0ft
RNC2P0_001					*x* = 0ft
VCALM_028	Calm		NS	V	*x* = 0ft
VC1P0_001	Current				*x* = 0ft Air Bubbles collected on MAVS #1 after 7 min
VC1P0_002					*x* = 0ft
VC1P-8_001					*x* = -8ft Still bubbles in MAVS #1
VC1P-16_001		Current pump #2 at100%	NS	V	*x* = -16ft after flushing the bubbles
VC1P-24_001					*x* = -24ft MAVS #1 hampered with bubbles
VC1P-24_002					*x* = -24ft after flushing the bubbles
VC1P-8_002					*x* = -8ft

	VC2P-8_001		#2 & #3 at100%	NS	V	*x* = -8ft
	VC2P0_001					*x* = 0ft rinse the bubbles
	VC2P-16_001					*x* = -16ft
	VC2P-24_001					*x* = -24ft MAVS #1 collected bubbles
	VC2P-24_002					*x* = -24ft Concl. of the vert. array test phase: no return current up in the middle of basin
	V7C2P-24_001					*x* = -24ft & *y* = -7ft Vertical array moves 7ft east (maintain measurement depth while mapping in a horizontal direction)
	V7C2P-16_001					*x* = -16ft & *y* = -7ft
	V7C2P-8_001					*x* = -8ft & *y* = -7ft
	V7C2P0_001					*x* = 0ft & *y* = -7ft
	V14C2P0_001					*x* = 0ft & *y* = -14ft
	V14C2P-8_001					*x* = -8ft & *y* = -14ft
	V14C2P-16_001					*x* = -16ft & y = -14ft
	V14C2P-24_001					*x* = -24ft & *y* = -14ft
	V21C2P-24_001					*x* = -24ft & *y* = -21ft
	V21C2P-16_001					*x* = -16ft & *y* = -21ft
	V21C2P-8_001					*x* = -8ft & *y* = -21ft
	V21C2P0_001					*x* = 0ft & *y* = -21ft
	V28C2P0_001					*x* = 0ft & *y* = -28ft
	V28C2P-8_001					*x* = -8ft & *y* = -28ft
	V28C2P-16_001					*x* = -16ft & *y* = -28ft
	V28C2P-24_001					*x* = -24ft & *y* = -28ft
	V35C2P-24_001					*x* = -24ft & y = -35ft
	V35C2P-16_001					*x* = -16ft & *y* = -35ft
	V35C2P-8_001					*x* = -8ft & *y* = -35ft
	V35C2P0_001					*x* = 0ft & *y* = -35ft
	V42C2P0_001					*x* = 0ft & *y* = -42ft
	V42C2P-8_001					*x* = -8ft & *y* = -42ft
	V42C2P-16_001					*x* = -16ft & *y* = -42ft
	V42C2P-24_001					*x* = -24ft & *y* = -42ft
	V42C1P-24_001		Pump #2 at100%	NS	V	*x* = -24ft & *y* = -42ft

	V42C1P-16_001					x = -16ft & y = -42ft
	V42C1P-8_001					x = -8ft & y = -42ft
	V42C1P0_001					x = 0ft & y = -42ft
	V35C1P0_001					x = 0ft & y = -35ft
	V35C1P-8_001					x = -8ft & y = -35ft
	V35C1P-16_001					x = -16ft & y = -35ft
	V35C1P-24_001					x = -24ft & y = -35ft
	V28C1P-24_001					x = -24ft & y = -28ft
	V28C1P-16_001					x = -16ft & y = -28ft
	V28C1P-8_001					x = -8ft & y = -28ft
	V28C1P0_001					x = 0ft & y = -28ft
	V21C1P0_001					x = 0ft & y = -21ft
	V21C1P-8_001					x = -8ft & y = -21ft
	V21C1P-16_001					x = -16ft & y = -21ft
	V21C1P-24_001					x = -24ft & y = -21ft
	V14C1P-24_001					x = -24ft & y = -14ft
	V14C1P-16_001					x = -16ft & y = -14ft
	V14C1P-8_001					x = -8ft & y = -14ft
	V14C1P-16_002					x = -16ft & y = -14ft
	V14C1P0_001					x = 0ft & y = -14ft
	V7C1P0_001					x = 0ft & y = -7ft
	V7C1P-8_001					x = -8ft & y = -7ft
	V7C1P-16_001					x = -16ft & y = -7ft
	V7C1P-24_001					x = -24ft & y = -7ft
	HC1P-24_001				EW	8 MAVS deployed, 3 wave probes calibrated and deployed over MAV #5,6 & 7
	HC1P-16_001					
	HC1P-8_001					
	HC1P0_001					
	RG5HC1P0_001	Wave + Current				
	RNHC1P0_001					
	RG5HC1P-8_001					

	RNHC1P-8_001 RG5HC1P-16_001 RNHC1P-16_001 RG5HC1P-24_001 RNHC1P-24_001					
	HC2P-24_001 HC2P-16_001 HC2P-8_001 HC2P0_001	Current				
	RG5HC2P0_001 RNHC2P0_001 RG5HC2P-8_001 RNHC2P-8_001 RG5HC2P-16_001 RNHC2P-16_001 RG5HC2P-24_001 RNHC2P-24_001	Wave + Current	#2 & #3 at100% & #1 at25%	NS	EW	
Phase 3	CALM_028	Calm		NS	EW	AVS #7 is reading negative polarity
	20HZ_101	Tow	20.025cm/s			avg = 15,5cm/s => 22,968% low
	30HZ_101		30.084cm/s			avg = 23,666cm/s => 21,335% low
	45HZ_101		45.293cm/s			avg = 35,183cm/s => 22,968% low
	60HZ_101		60.107cm/s			avg = 46,671cm/s => 22,32% low
	CALM_029	Calm		V		
	20HZ_102	Tow	20.025cm/s			avg = 19,05cm/s => 4,369% low
	30HZ_102		30.084cm/s			avg = 28,453cm/s => 5,42% low
	45HZ_101		45.293cm/s			avg = 42,611cm/s => 5,921% low
	60HZ_101		60.107cm/s			avg = 56,16cm/s => 6,567% low
Phase 4	ZERO_101	Calm		NS	EW	MAVS #1-5 left alone, MAVS #6-9 with a 30Hz sample rate
	30S20HZ_101	Tow	20.025			
	30S30HZ_101		30.084			#7 alone is 10.45% low. With a sample rate at40Hz, it was 2.54% low

	30S45HZ_101		45.293			
	30S60HZ_101		60.107			
	ZERO_102	Calm				Remove #7, replace #8 mount with slimline, meausre "z" #8
	30S20HZ_102	Tow	20.025			7 has weird results (results in 3 directions, took the Vy line)
	30S30HZ_102		30.084			
	30S45HZ_102		45.293			7 has weird results (results in 3 directions => didn't take it into account)
	30S60HZ_102		60.107			
	ZERO_103	Calm				Remove #7, replace #8 mount with slimline, measure "z" #8
	30S20HZ_103	Tow	20.025			7 has weird results (results in 3 directions => didn't take it into account)
	30S30HZ_103		30.084			
	30S45HZ_103		45.293			
	30S60HZ_103		60.107			

APPENDIX F

SUBROUTINES INTERACTIONS

Processing

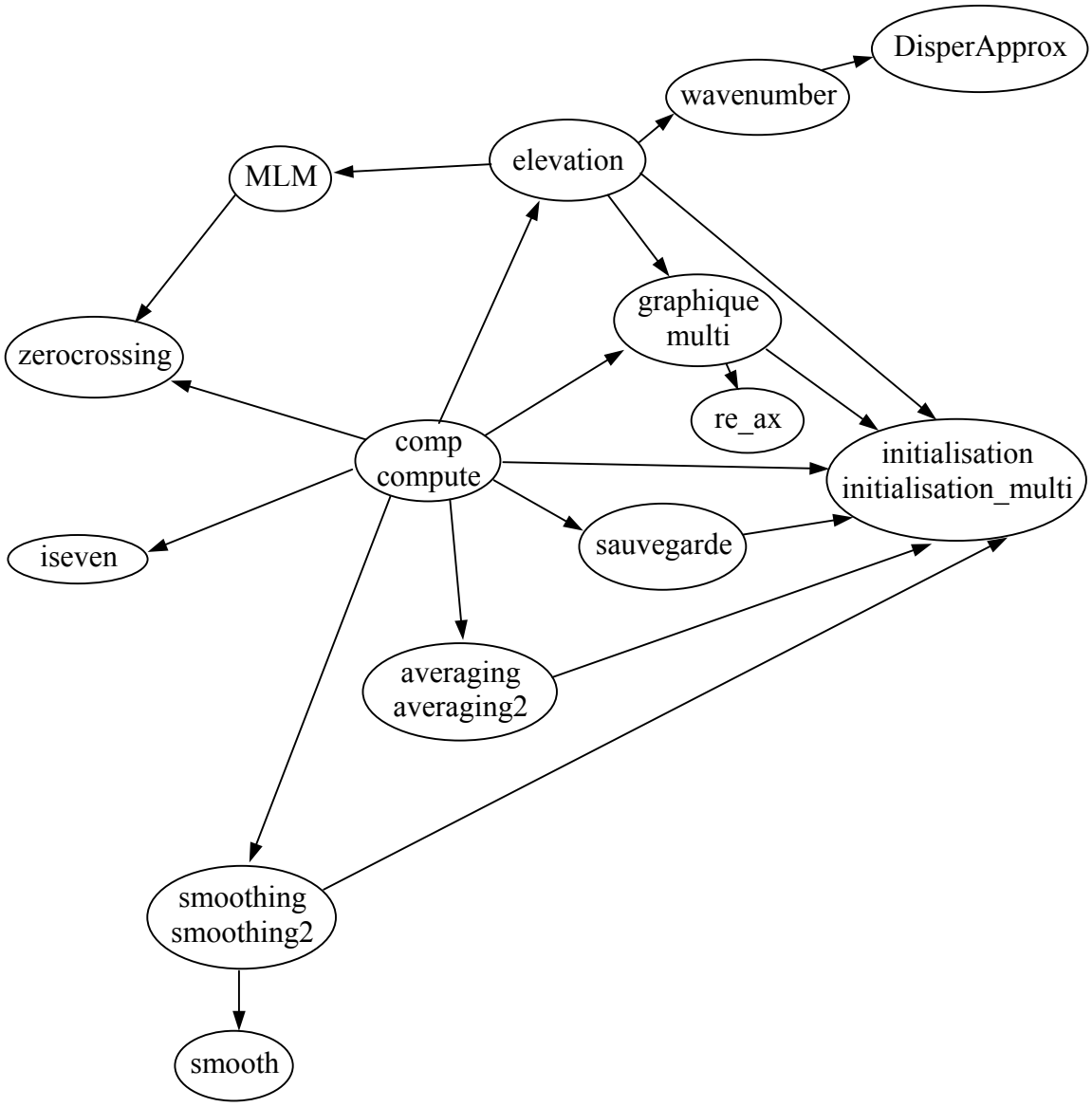
DisperApprox
wavenumber
elevation
MLM
graphique
multi
zerocrossing
re_ax
comp
compute
initialisation
initialisation_multi
iseven
sauvegarde
averaging
averaging2
smoothing
smoothing2
smooth

Post-Processing

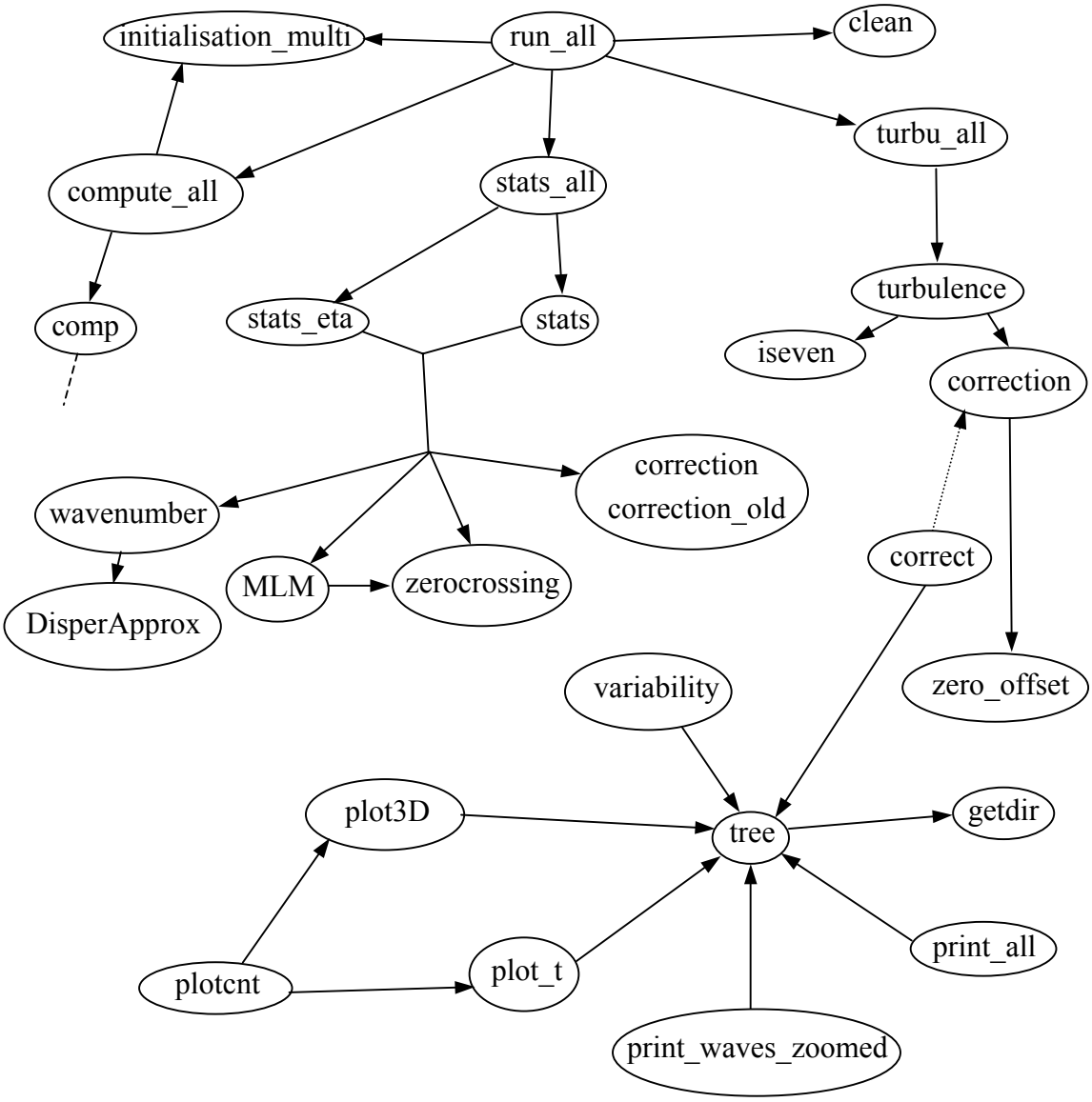

Pre-Processing

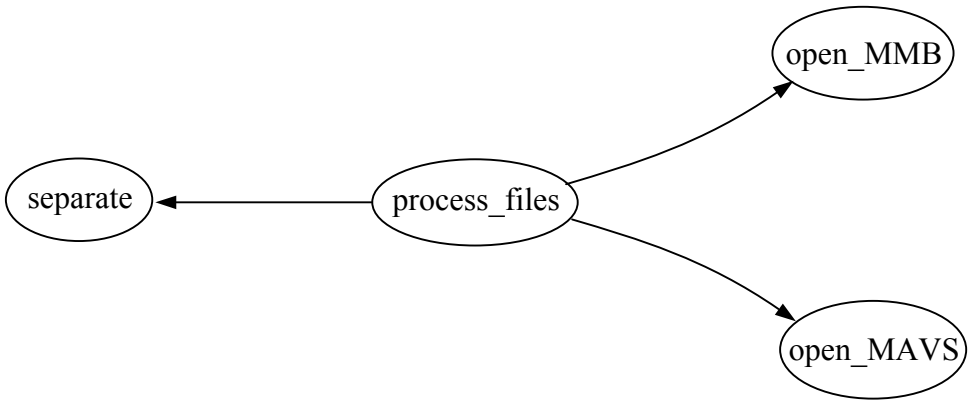

	Name	*Definition*
Pre-process	open_MAVS	Read the data from the MAVS files
	open_MMB	Read the data from the March-Mc Byrney files
	process_files	Converts from raw data to data possible to process in Matlab
	separate	Separates the 4 velocities of the sensor into a 3 dimensional velocity
Processing	amplitude	Computes the amplitude from the elevation
	averaging	Averages the signal
	averaging2	Averages the signal
	avgmax	Computes the average extrema over a time period
	comp	
	compute	
	compute_all	Automates of the computation
	DisperApprox	
	elevation	Computes the linear wave theory
	enveloppe	Finds the envelope of the signal
	enveloppe2	Finds the envelope of the signal

	extremum	Finds the local extrema (works even if there is a low frequency signal above but slower than the other one)
	extremum_old	Finds the global extrema
	findmax	Finds the maxima
	findmin	Finds the minima
	graphique	Plot for the case of a single sensor
	initialisation	Initializes the variables for a case of a single sensor
	initialisation_multi	Initializes the variables for a case of multiple sensors
	iseven	Test if a number is even or odd
	MLM	Computes the Maximum Likelihood method on the window of a signal
	multi	execute the plot for the cases of multiple sensors
	NL	Computes the NL phase from the elevation (out of date)
	NL_phase	Computes the NL phase from the elevation (out of date)
	phase	Computes the phase from the elevation phi=acos(signal./A) (out of date)
	phaseMLM	Computes the phase from the MLM (finds the period) (out of date)
	phaseNL	Computes the phase from the elevation (out of date) (not NL phase though because of the troubles developed in the thesis)
	re_ax	Calibrate the axis
	sauvegarde	Save the plots and the results of the computation
	smooth	Smoothing function
	smoothing	Smooth the logarithm of the spectrum
	smoothing2	Idem than previous one
	wavenumber	Finds the wavenumber
	zerocrossing	Finds the up or downcrossing with n number of points of accuracy
Post-processing	clean	Resets matlab
	correct	Creates the correction factors
	correction	Corrects the signal (needs correct to be run once before)
	correction_old	Corrects the signal (coefficients included)
	getdir	Gets all the content of a directory
	plot_t	Plots the turbulence in the wave basin
	plot3D	Plots the average current in the wave basin
	plotcnt	Plots the average current and the turbulence
	print_all	Prints any type of plot under any orientation using the postscript
	print_waves_zoomed	Prints a window of the time series of the waves using the postscript files
	run_all	Runs all the automated files
	stats	Extracts the main characteristics of the signal
	stats_all	Automates the statistics
	stats_eta	Extracts the statistics of the water surface elevation
	tree	Finds the tree of directories
	turbu_all	Automated turbulence
	turbulence	Computes the integral length scale and dissipation rate

	variability	Finds the variation of the current and plot the area
	zero_offset	Finds the calm file associated with a test
Validation and stand alones	valid_enveloppe	
	valid_eta	
	valid_extrema	
	valid_kh	
	valid_linearity	
	valid_phase	
	test_correction	
	check_MLM	
	check_NL	
	check_process	
	Etc…	Miscellaneous other checking and validation files
	Amp	Displays the characteristics of the amplitudes from a signal
	displacement	Plots the water displacement corresponding to our plots.
	err	Plots the errors of the tests (out of date)
	errors	Plots the errors of the tests (out of date)
	fit	First regression method (out of date)
	localisation	Generates a localization file (in meters) of the array for latter computation
	resample	Resample the signal to see the differences
	proof_nonlinear	Computes the amplitude of a non linear wave from the potential theory

VITA

Stéphane Besnard was born in Evreux, France, on May 7th, 1979. After moving to Mont-de-Marsan and finally to Blagnac close to Toulouse in the South of France, he obtained his Baccalauréat (High School Diploma) in June 1997 from the Lycée Pierre de Fermat in Toulouse in applied Biology, Mathematics and Physics. Admitted in Classes Préparatoires aux Grandes Ecoles in the Lycée Saliège in Balma close to Toulouse during the Fall 1997 in a Physique et Science de l'Ingénieur program (math, physics and scientifically oriented subjects), he was accepted to the Ecole Spéciale des Travaux Publics, du Bâtiments et de l'Industrie (E.S.T.P.) in Paris in Fall 2000 after competitive exams for the entrance in schools of engineering. Along his studies there, he chose the option to study abroad for a Master of Science degree in ocean engineering instead of a the regular third year. For that, he was admitted in Fall 2002 to Texas A&M University where he worked toward his graduation while working as a research assistant at the Offshore Technology Research Center under the responsibility of Dr. Richard Mercier.

Stéphane can be reached at the following address:

Monsieur Stéphane Besnard
4, rue des tamaris
31700 Blagnac
FRANCE